Group 4 and 12 complexes bearing guanidine–phenolate or amidine–phenolate ligands: coordination chemistry and polymerization studies

Victor Flores Romero

A Dissertation submitted to the Faculty of Graduate Studies in Partial Fulfillment of the Requirements for the Degree of Doctor of Philosophy

Graduate Program in Chemistry
York University
Toronto, Ontario

June 2025

Abstract

This dissertation explored the synthesis of Group 4 and Zn catalysts bearing guanidine–phenolate or amidine–phenolate ligands and their ability to catalyze chemical transformations. Group 4 diisopropoxide and Zn complexes were evaluated for the homopolymerization of lactide, while titanium dichloride complexes were assessed for their ability to polymerize ethylene.

Group 4 diisopropoxide catalysts were active towards the ring-opening polymerization (ROP) of lactide, in the absence of any solvent, at 130°C. All Zr complexes were more active than the corresponding titanium homologues. The rate constant of the bis(guanidine–phenolate) group 4 systems (1.17—3.21 × 10^{-4} s^{-1}) were higher than those displayed with $Ti(O^iPr)_4$ (5.34 × 10^{-5} s^{-1}), and $Zr(O^iPr)_4 \cdot {}^iPrOH$ (2.79 × 10^{-5} s^{-1}). Polylactic acid produced by guanidine-based catalysts exhibited similar molecular weights and dispersity (Đ) values to those of the industrial standard catalyst $Sn(Oct)_2$, as well as to the precursors $Ti(O^iPr)_4$ and $Zr(O^iPr)_4$. The guanidine–phenol ligand proved to be active for the ROP of lactide with a larger rate constant than the most active Zr-based catalysts. The bis(guanidine–phenolate) titanium dichloride complexes were successfully synthesized and evaluated for the homopolymerization of ethylene. The low activity (up to 1.1 kg_{PE} $mol^{-1}h^{-1}$) of the titanium dichloride complexes was ascribed to the electron-donating ability of the guanidine fragment and the stereoarrangement imparted by the guanidine–phenolate ligand about the Ti center.

Zn catalysts bearing guanidine– and amidine–phenolate ligands were synthesized and evaluated for the ROP of lactide under solvent-free conditions at 130°C. The catalyst with the best performance was only 3 times slower than the industrial standard $Sn(Oct)_2$ when a 100 to 1 monomer to catalyst ratio was used. Most catalysts displayed heterotactic bias in the polylactic acid generated with molecular weights up to 4900 Da. Dispersity values (Đ) ranged from 1.2 to 2.3 and were considered acceptable. Proligands were tested for the ROP of lactide, proving that their participation in the polymerization process cannot be ruled out. This new class of ligands and the corresponding complexes offer great potential and have a great deal of room for improvement.

Lay Summary

This project focuses on developing new metal-based chemical compounds (catalysts) that can create biodegradable polymers, also known as bioplastics, more efficiently. These systems are based on metals such as titanium, zirconium, and zinc, and they are designed with molecules attached to them (ligands) that affect their performance.

Polylactic acid was the main polymer studied in this project, as it's considered a biodegradable polymer and made from renewable resources. The performance of these catalysts in producing polylactic acid at high temperatures in the absence of solvent was explored, where the zirconium-based catalysts were better than the titanium systems. Moreover, the zinc-based systems came close to matching the performance of the industrial-standard catalyst. This work also explored how titanium-based catalysts could help make other plastics, such as polyethylene, and pointed out areas where more improvement is needed.

This study shows that these metal-based systems have the potential to make biodegradable polymers more efficiently, which could benefit industries currently focusing on developing environmentally friendly materials.

Acknowledgment

First of all, I would like to thank the “Consejo Nacional de Humanidades, Ciencias y Tecnología” of Mexico for the scholarship I received while at York University. I am also grateful to my supervisor, Professor Gino Lavoie, for his guidance, patience, support, and the opportunity to be part of his research group. I would also like to thank my thesis committee members, Dr. Thomas Baumgartner and Dr. Arturo Orellana, for their patience and time invested during evaluations of this project. Special appreciation to Dr. Matthew George and Dr. Parisa Mehrkhodavandi for their participation in my defense committee. Many thanks to Dr. Howard Hunter for his help, guidance, and advice with NMR experiments.

I want to express my gratitude to the current and past members of the Lavoie Group, Brandon Khan, Jesse LeBlanc, Lya Campos Rivera, and Nicolas Miceli. You all supported me professionally and personally when I needed it, and no words can express how grateful I am to have met you. To my friends from the Caputo Group, Casey Lenart, Lucas Torres, Taylor Cosby, Avik Bhattacharjee, Charley Garrard, and Madeleine Agostino, thanks for spending time with me; seeing you always made me smile. I would also like to thank other friends and colleagues from York, Andrea Angelucci, Lisa Azzarello, Alessia Colussi, Dylan James, Natalie Khamissi, Ian Frankel, and Mayré Rodríguez, I will miss our little talks.

To my mom, Margarita Romero Avila, your support has been invaluable throughout my years away from home. Lastly, I thank my beautiful wife, Beatriz Herrera Gutierrez. My life only makes sense when you are by my side. Thank you for your support and for allowing me to be a father, Victoria, daddy loves you.

Dedication

Esta tesis está dedicada a los seres queridos que perdí durante mi estancia en Canadá.

A mis abuelos, Margarita Ávila Bello y Salvador Romero Vargas, siempre fueron un ejemplo para mí y quiero creer que de alguna manera me siguen cuidando.

A mi padre, Blas Flores Pérez, tu apoyo siempre fue invaluable y espero que donde quiera que estes, te sientas orgulloso de mi.

Table of Contents

List of Figures

List of Tables

List of Schemes

List of abbreviations

Symbols	Definitions
ADC	Acyclic diamino carbene
AMM	Activated Monomer Mechanism
Ar	Aryl
BONHMe	2-methylamino-benzoxazole
CAAC	Cyclic(alkyl)(amino) carbene
CIM	Coordination-Insertion Mechanism
δ	Chemical shift
DCM	Dichloromethane
DFT	Density Functional Theory
DP	Degree of Polymerization
Equiv.	Equivalent
HMDS	Hexamethyldisilazide
^{i}Pr	Isopropyl
LDA	Lithium diisopropylamide
L_n	Ligands
LDPE	Low density polyethylene
MALDI-TOF	Matrix-Assisted Laser Desorption/Ionization-Time of Flight
MeCN	Acetonitrile
Mes	Mesityl
M_n	Number-average molecular weight
M_w	Weight-average molecular weight
NHC	N-heterocyclic carbene
NHIs	N-heterocyclic imines
NIPOx	N-isopropyl oxamate
NMR	Nuclear Magnetic Resonance
Oct	Octoate
PE	Polyethylene
PET	Polyethylene Terephthalate
PCL	Polycaprolactone
PLA	Poly(lactic)acid
PP	Polypropylene
ROP	Ring-opening polymerization
R	Alkyl or aryl fragment
SHARCNET	Shared Hierarchical Academic Research Computing Network
THF	Tetrahydrofuran
^{t}Bu	*tert*-butyl
VT	Variable Temperature

Chapter 1 Introduction

The catalytic performance of transition metal complexes, such as those based on Ti, Zr, and Zn, in the production of polymers is critically influenced by the ligand design. Well-designed ligands can effectively modify the electronic and steric environment around the metal center, thereby enhancing the polymerization process. In particular, guanidines and amidines are systems where the donating capability of the N-donor atom can be fine-tuned by modifying the carbene moiety used as a building block. The utilization of bidentate ligands containing neutral guanidine or amidine fragments offers excellent opportunities to optimize catalyst performance.

1.1 Olefin polymerization

Polyolefins are polymers that have a huge relevance in the daily life of modern society as they present chemical stability and versatile properties, allowing their application in medicine, packaging, automotive parts, rubbers, textiles, and insulators.[1] These polymeric materials are produced from alkenes such as ethylene, propylene, and other α-olefins, with polyethylene (PE) and polypropylene (PP) being the most used polyolefins. Since 1930, when low-density polyethylene (LDPE) was made through free radical polymerization, several advances have occurred primarily in metal-mediated olefin polymerization methods. These systems produced polyethylene with different properties from those obtained through free radical polymerization, with greater melting point, densities, and crystallinity.[2] Moreover, these catalysts have shown stereochemical control with α-olefins, generating either isotactic or syndiotactic polymers (Figure 1.1), imparting different bulk properties without a chemical modification of the structure of the macromolecule.

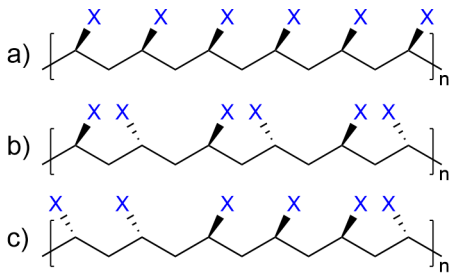

Figure 1.1 Stereochemical forms of polyolefins a) isotactic, b) syndiotactic, and c) atactic

1.1.1 Ziegler-Natta catalyst

The history of olefin polymerization began around 1930 in England when LDPE was made by Imperial Chemical Industries (ICI) through free radical polymerization. This method required high-pressure (350–3000 atm) and temperature (150–375 °C) conditions to generate polymers with molecular weights up to 100 kDa. The free radical polymerization method was also applied to produce copolymers such as poly(ethylene-vinyl acetate) and poly(ethylene-acrylic acid), materials that found applications in food packaging and sealants.[2–4] Although free radical polymerization showed the capability of producing LDPE and copolymers, there is poor control over the molecular weight distributions (Đ) and homopolymerization of α-olefins is limited. Moreover, polymers obtained through this method are semi-crystalline, a consequence of intermolecular and intramolecular chain transfer over the polymer backbone, which has a detrimental effect on the physical and mechanical properties of the final material.[2] Further development in the olefin polymerization occurred with the utilization of metal-based catalysts.

Karl Ziegler, while working at the Max Planck Institute for Coal Research in Germany, prepared high-density polyethylene (HDPE) by heterogeneous catalysis using aluminum alkyl compounds (e.g., $AlEt_3$, $AlEt_2Cl$, and $Al_2Et_3Cl_3$ and transition metal halides (e.g., $TiCl_4$, VCl_4, and $VOCl_3$ as catalysts. This was accomplished at atmospheric pressure and with a catalytic amount of the transition metal halide (Figure 1.2).[5,6] HDPE presented increased tensile strength, stiffness, chemical resistance, and higher thermal stability compared to LDPE. Following Ziegler´s research, Giulio Natta, during his stay at the Polytechnic University of Milan (Italy), worked with propylene and developed highly isotactic polypropylene. These contributions led both scientists to receive the Nobel Prize in Chemistry in 1963. Although Ziegler-Natta catalysts have been applied mainly for the production of PE and PP, their use is not limited to polymerizing α-olefins such as but-1-ene, hex-1-ene, and oct-1-ene and vinyl aromatic compounds, such as styrene.[6] Ziegler-Natta catalysts were a breakthrough in the polymer area. However, it presented some drawbacks: the productivity of the catalysts decreased in the presence of Lewis basic impurities. Additionally, it was necessary to extract the atactic polymer due to the insufficient stereospecificity of the catalyst.[6]

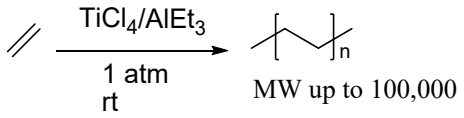

Figure 1.2 Polyethylene production using a Ziegler-type catalyst system

Nowadays, Ziegler-Natta catalysts are expected to have high productivity while offering control over polymer features such as molecular weight, chemical composition, tacticity, and particle morphology. Modern versions of these heterogeneous systems comprise four components to enhance their performance in the polymerization process and obtain the aforementioned characteristics. Firstly, a support, such as $MgCl_2$, is used to increase the availability of active sites (higher productivity) and allows easier separation (if needed) of the final material from the reaction medium. Secondly, electron donors, such as esters, ethers, and alkoxysilanes, increase stereospecificity and control of the molecular weight distribution of the polymer. Thirdly, aluminum alkyl reagents activate transition metal catalysts such as titanium ($TiCl_4$) or vanadium compounds ($VOCl_3$).[6] Despite the excellent performance of these systems, there are still limitations that must be addressed. Particularly, Ziegler-Natta catalysts are ineffective at copolymerizing olefins with polar monomers as the latter interact with the active site, leading to deactivation.

1.1.2 Group 4 metallocenes in olefin polymerization

Walter Kaminsky and coworkers discovered that group 4 homogeneous metallocene catalytic systems were highly active in polymerizing α-olefins larger than propylene in the presence of methylaluminoxane (MAO). MAO is an ill-defined aluminum alkyl oligomer used as both a co-catalyst to generate an active species and as an impurity scavenger.[7] Initial studies were performed with $Cp_2Zr(CH_3)_2$. However, due to its poor stability, Cp_2ZrCl_2 was found to be a better option as a catalyst. This Cp_2ZrCl_2/MAO system produces 40 metric tonnes of PE per gram of catalyst in 1 h (this corresponds to 4×10^8 $mol_{C_2H_4}$ mol_{Zr}^{-1} h^{-1}) at 95 °C and 8 bar of ethylene pressure, up to two orders of magnitude greater than that of the classic Ziegler-Natta catalysts.[7] Moreover, polymers with high molecular weights and narrow molecular distributions were observed.

In contrast to Ziegler-Natta catalysts, Cp_2ZrCl_2/MAO systems produce atactic polypropylene. The stereoselectivity polymerization was achieved with bridged metallocenes, also called *ansa*-metallocenes (Figure *1.3*b). Variations in the ligand allowed the production of syndiotactic and

atactic polypropylene.[7–9] In contrast to Ziegler-Natta systems, these metallocenes effectively mediate the homopolymerization of cyclic olefins, such as cyclobutene, cyclopentene, and norbornene. In addition, these catalysts are suitable to produce copolymers of cyclic olefins with ethylene, resulting in a new class of materials known as Cyclic Olefin Copolymers (COC).[7]

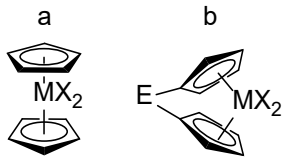

Figure 1.3 a) Bis(cyclopentadienyl) metal complex b) *ansa*-metallocene complex

1.1.3 Group 4 imine–phenolate systems (FI catalysts)

In 1998, Fujita and coworkers reported post-metallocene catalysts with salicylaldimine-based ligands coordinated to group 4 metals (Figure *1.4*). These complexes are prepared from readily available metal precursors, such as MCl_4, $MCl_4(THF)_2$, MO^iPr_4, and $M(NMe_2)_4$. When MCl_4 or $MCl_4(THF)_2$ are employed, the phenol–imine ligand must be deprotonated prior to complexation with bases such as KO^tBu, NaH, lithium diisopropylamide (LDA), and sodium hexamethyldisilazide (NaHMDS). In contrast, the phenol can be employed directly if MO^iPr_4 or $M(NMe_2)_4$ is the metal source. These bis(imine–phenolate) group 4 complexes display an octahedral geometry around the metal center, with five possible isomers (Figure *1.5*). These complexes mainly adopt a *cis*-X framework and *cis*-N,N-*trans*-O,O geometry (Isomer A) in the solid state, except when bulky R^1 substituents are present (e.g., tertiary alkyls), which results in a cis-X and *cis*-N,N-*trans*-O,O (Isomer C) structure.[10]

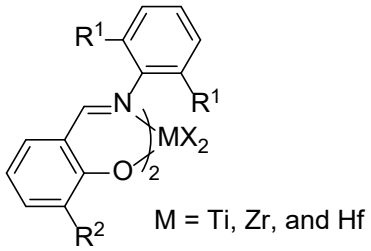

Figure 1.4 Imine–phenolate catalysts (FI catalysts) for group 4 complexes

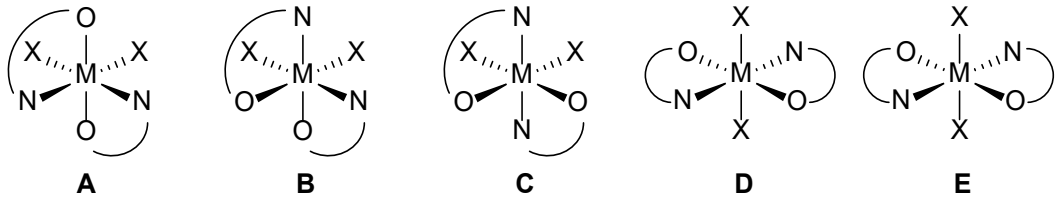

Figure 1.5 Possible isomers (excluding enantiomers) for bis(imine–phenolate) six-coordinate complexes

These imine–phenolate systems, with MAO as a co-catalyst, display higher activities than those observed with metallocenes. The diversity and tuneability of these catalysts have been well studied, allowing a deep understanding of the influence of ligand structure on catalytic activity.[10] Fujita demonstrated that increasing the size of the R^2 substituents produced a marked improvement in the activity (Figure *1.4*). The polymerization activity of titanium complexes increased with increasing R^2 substituents (H (0.038 kg_{PE} $mmol_{Ti}^{-1}$ h^{-1}) < Me (0.25 kg_{PE} $mmol_{Ti}^{-1}$ h^{-1}) < ^{t}Bu (3.2 kg_{PE} $mmol_{Ti}^{-1}$ h^{-1}); (Table 1.1), due to bulky groups lowering the energy barrier for olefin insertion and protecting the phenolic oxygen from side reactions. On the other hand, larger R^1 substituents (from H to Me, ^{i}Pr, and ^{t}Bu) had a negative impact on the activity of these catalysts (Figure *1.4*).[10] The decrease in activity was attributed to more steric congestion, hampering the coordination of ethylene.[11] In the context of stereospecificity, these catalysts produced highly syndiotactic polymer with Ti, and slightly syndiotactic and atactic polypropylene with the larger 4*d* and 5*d* metals, Zr and Hf. However, all showed poor stereoselectivity with higher α-olefins, such as 1-hexene. Furthermore, while these catalysts can copolymerize ethylene and polar monomers, such as 10-undecen-1-ol and 5-hexen-1-ol, up to only 3 mol% of the polar monomers were incorporated in the polymer.[10]

Table 1.1 Effect of R^1 and R^2 substituents for FI catalysts in the polymerization of ethylene

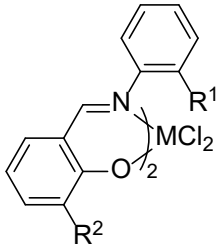	**Activity (kg_{PE} $mmol_M^{-1}$ h^{-1})**	
	Ti	**Zr**
$R^1 = R^2 = H$	0.038	0
$R^1 = H$ $R^2 = Me$	0.25	0.40
$R^1 = H$ $R^2 = {}^tBu$	3.2	540
$R^1 = Me$ $R^2 = {}^tBu$	0.30	40
$R^1 = {}^iPr$ $R^2 = {}^tBu$	0	58

1.1.4 Mechanism of olefin polymerization

Olefin polymerization involves three steps: (1) initiation, (2) propagation, and (3) termination (Figure *1.6*). The first step is related to the formation of the active species, either by using a cocatalyst or by the dissociation of a ligand, leaving one vacant coordination site. The second step involves the coordination of the olefin and migratory insertion of the alkyl, regenerating the vacant site, and growing the polymer chain by one monomeric unit. This process repeats until the chain growth terminates either by chain transfer or through β-hydrogen elimination.[12]

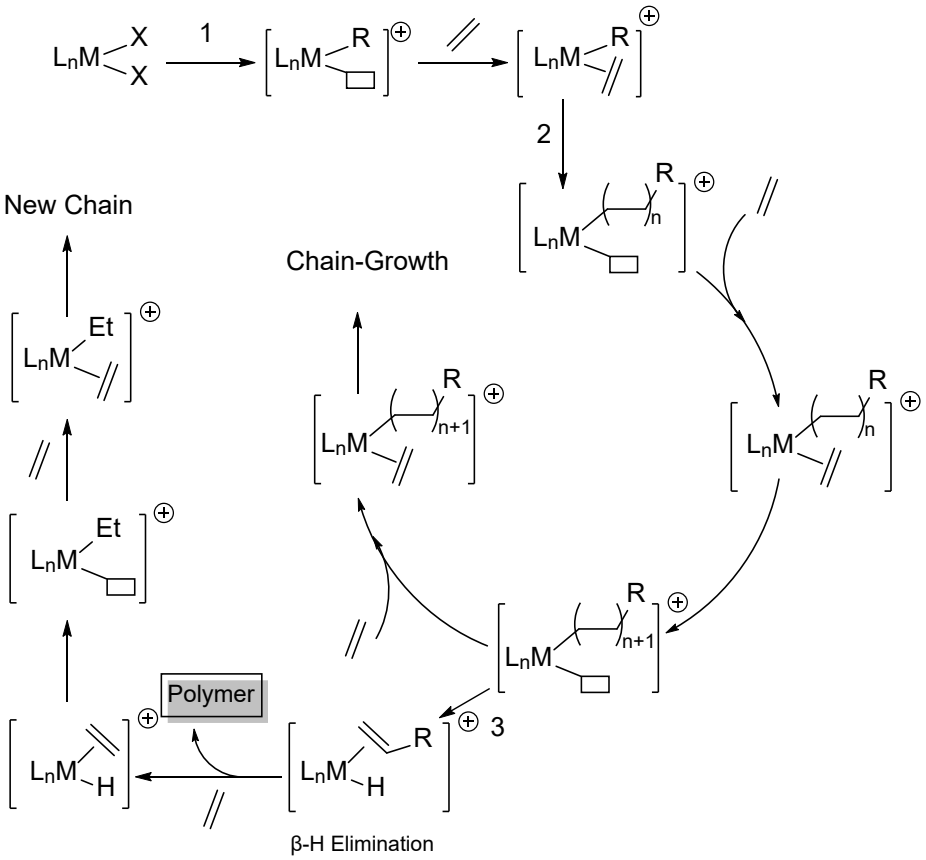

Figure 1.6 General mechanism for olefin polymerization, (1) initiation, (2) propagation, and (3) termination

1.2 Poly(lactic acid) (PLA)

Poly(lactic acid) (PLA) is a polyester considered green, nontoxic, and biodegradable, derived from lactic acid (Figure *1.7*). Lactic acid contains a stereogenic center, leading to two possible stereoisomers, the L and D enantiomers. Typically, lactic acid is obtained by bacterial fermentation of renewable resources such as corn, sugar, and other feedstocks. The PLA production in the USA in 2002 was 70,000 metric tons and increased to 150,000 metric tons by 2015. In 2019, PLA represented approximately 14% of all global bioplastics produced and is expected to keep growing.[13,14] Furthermore, the synthesis of these polymers is expected to reduce the environmental pollution of petroleum-based plastics.

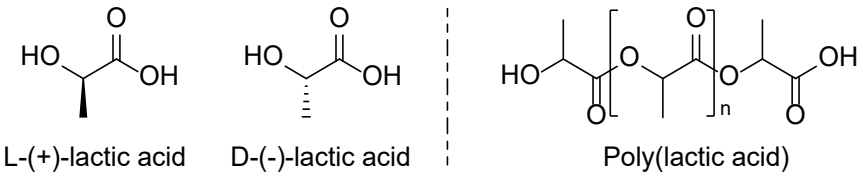

Figure 1.7 Structure of L-(+) and D-(-) lactic acid, and of poly(lactic acid)

1.2.1 PLA: Properties, applications, and synthetic methods.

PLA is very attractive in part thanks to its properties such as mechanical strength, biocompatibility, biodegradability, transparency, and easy processing. All these features have allowed for the application of PLA in different fields.[15] The medical industry has implemented PLA in nanocomposites, which can be used as synthetic bone, drug delivery systems, and medical implants. More recently, copolymers of PLA and polyglycolic acid (PGA) have emerged in the area of tissue engineering, with the polymer acting as a cell adhesive and growth carrier.[15,16] PLA presents low solubility in water, high molecular weights, and a tensile strength modulus similar to that of PE and polyethylene terephthalate (PET), making it a great alternative to conventional fossil fuel-based plastics commonly used for packaging, such as shopping bags, chip bags, yogurt cups, and fruit or salad containers.[15,17] [16] PLA can also be found in car interior parts, such as carpets, mats and trim parts. Using biopolymers-based materials is expected to reduce vehicle weight, which translates into either a greater fuel efficiency (with a decrease in CO_2 emissions) for internal combustion engine vehicles or a greater range for electric vehicles.

There are three main methods to produce PLA: direct condensation polymerization, azeotropic condensation polymerization, and ring-opening polymerization of lactide (ROP). These methods are illustrated in Figure *1.8*.

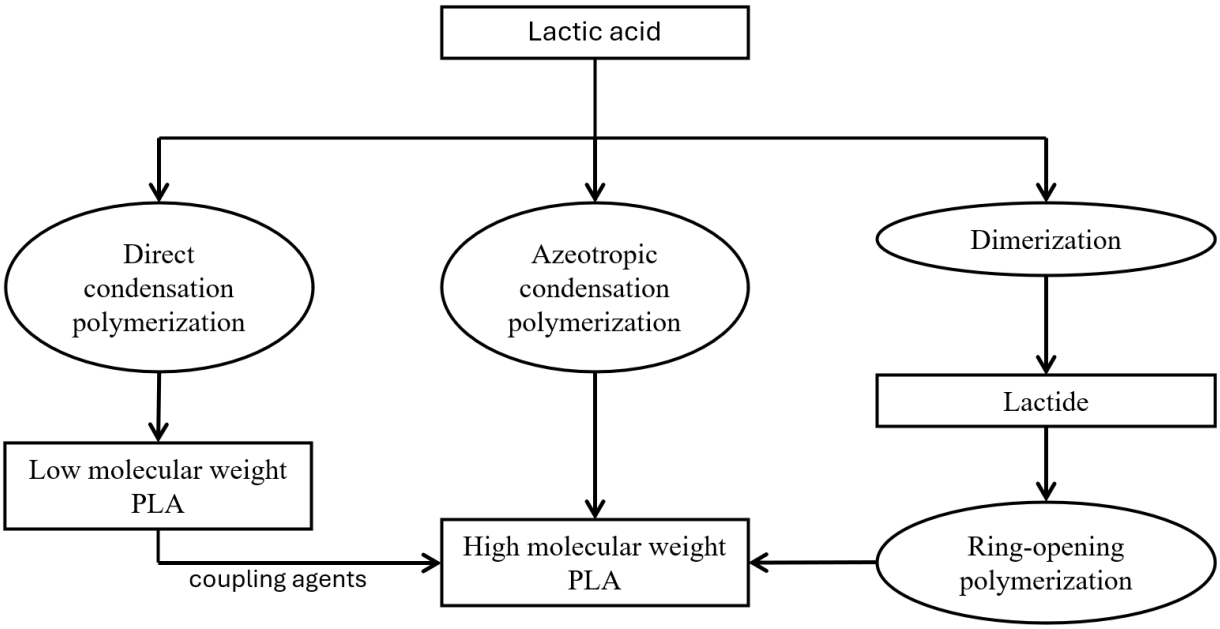

Figure 1.8 PLA synthetic methods. Adapted from literature.[16]

Two types of polycondensation of lactic acid can be used to produce PLA: direct condensation and azeotropic condensation. The former is the cheapest method to produce PLA. Low molecular weight polymers (< 5000 Da) are normally obtained. High molecular weight PLA can, however, be produced at a temperature range of 180–200 °C, under vacuum (5 mm Hg), with long reaction times, and using coupling agents. In contrast, azeotropic condensation relies on the removal of the water produced by azeotropic distillation to generate high molecular weight polymers. This, however, requires the use of solvents such as toluene, xylene, and diphenyl ether, making the process costly.[15,16]

The most common process to produce PLA is, however, by ring-opening polymerization (ROP) of lactide, the cyclic dimer of lactic acid. Due to its two stereogenic centers, three stereoisomers are generated: D-, L-, and *meso*-lactide (Figure *1.9*). ROP allows the production of high molecular weight PLA at short reaction times and under relatively mild conditions (130 °C–180 °C). This method commonly uses metal-based catalysts with tin(II) octoate ($Sn(Oct)_2$) being the preferred one for the industry. Other initiators, such as aluminum isopropoxide ($Al(O^iPr)_3$) and zinc lactate ($Zn(C_3H_5O_3)_2$), are used when polymers are produced for biomedical applications, as tin compounds (especially organotin) present stricter restrictions.[15,18,19] Given the important role of metal-based initiators, several studies of the polymerization mechanism have been conducted.

Nowadays, the most accepted mechanisms for the ROP of lactide using metal-based initiators are the coordination insertion mechanism (CIM) and the activated monomer mechanism (AMM).

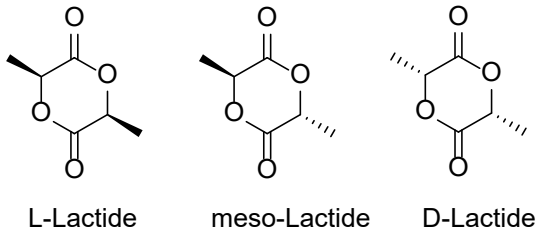

Figure 1.9 Lactide stereoisomers

1.2.2 Coordination insertion mechanism (CIM) and activated monomer mechanism (AMM)

Generally, metal–alkoxide and amide catalysts operate through CIM. While metal–alkyl or halide species can also be used, they necessitate the addition of a proper co-catalyst or react with polar impurities in the monomer, such as water, alcohols, and lactic acid, to initiate the ROP. Kricheldorf and Dubois performed initial mechanistic studies using $Al(O^iPr)_3$ in the 1980s, where the isopropyl ester was observed as a chain end by ^1H spectroscopy.[20,21] More recently, theoretical and experimental studies have been performed, allowing a better understanding of the overall process.[22,23] ROP initiates with the coordination of the monomer to the metal center, followed by the addition of the nucleophilic ligand on the activated carbonyl, causing the ring-opening of the monomer and extending the alkoxide propagating chain by one lactide monomer unit or by two lactic acid building blocks (Figure *1.10*, A). Metal-based catalysts can also operate through AMM, where the cyclic ester is activated once coordinated to the metal center, and the ring opening occurs by the nucleophilic addition of an external nucleophile, such as alcohols. The new terminal alcohol formed after the ring opening of lactide can now act as the nucleophile, allowing polymer growth by one lactide monomer unit (Figure *1.10*, B).[24–26]

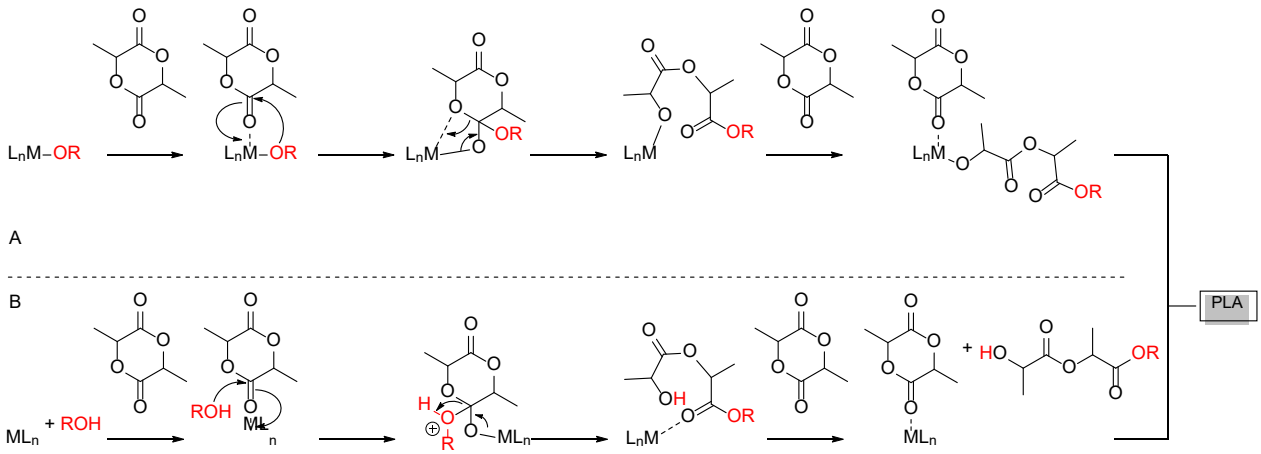

Figure 1.10 ROP of lactide by the A) coordination insertion and B) activated monomer mechanisms

For both mechanisms, the control over the molecular weight of the polymer is affected by side reactions, such as chain transfer and/or transesterification. The latter can be subdivided into two types: intramolecular and intermolecular transesterification. Intramolecular transesterification, also known as backbiting, produces macrocycles (Figure *1.11*, top). Typically, these cyclic polyesters present low-molecular weight (< 2000 Da) unless ring-expansion techniques were used.[27–29] In contrast, in intermolecular transesterification, the alkoxide group of a polymer chain forms a new ester bond by cleaving the ester bond of another polymer chain (Figure *1.11*, bottom).

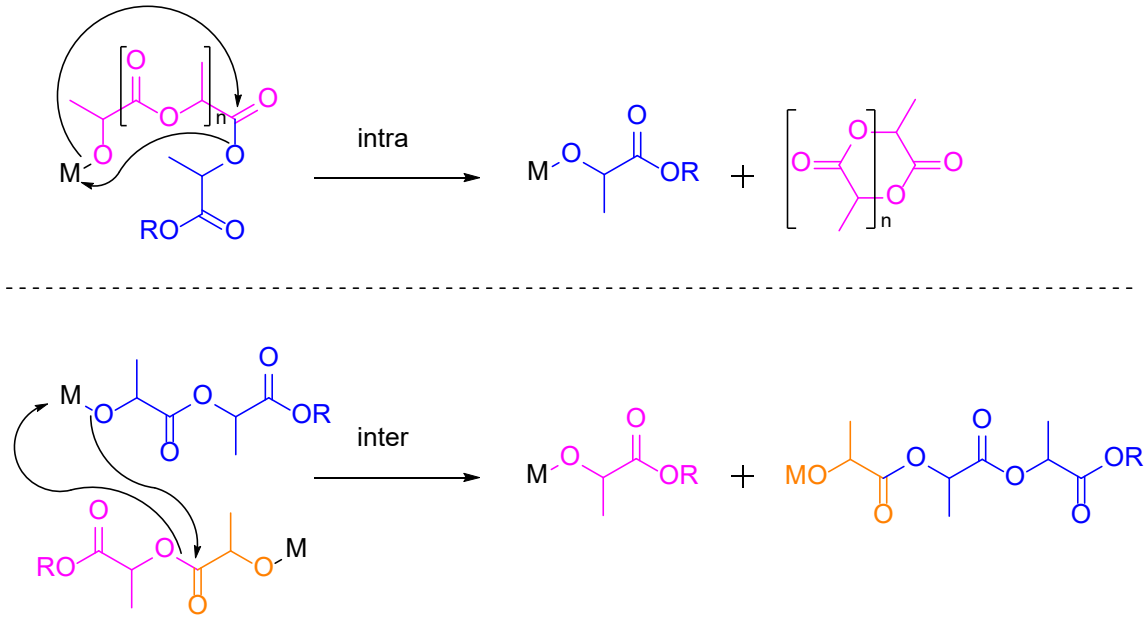

Figure 1.11 Representation of intramolecular (top) and intermolecular (bottom) transesterification

Both types of transesterification broaden the molecular weight distribution.[20,30] It should be considered that transesterification processes are affected by temperature, reaction time, metal center, and type of monomer.[31,32] The presence of transesterification during the polymerization is easily identified by mass spectrometry measurements of the polymer, such as Matrix-Assisted Laser Desorption/Ionization-Time of Flight mass spectrometry (MALDI-TOF), where an m/z value of 72 amu between peaks is observed (Figure 1.12).[33]

Figure 1.12 Expected peak separation in MALDI-TOF

1.2.3 Stereocontrol of lactide (microstructures in PLA)

As a consequence of the stereogenic centers in either lactic acid or lactide, the PLA main chain has different microstructures, such as isotactic, syndiotactic, atactic, heterotactic, and stereo-block (Figure *1.13*). The tacticity impacts both the mechanical and physical properties of the polymer, including its biological degradation. As an example, isotactic PLA from L-lactide, also called poly(L-lactide) (PLLA), presents a melting point temperature (T_m) of 170–180 °C and a glass transition temperature (T_g) of 50–65 °C. In contrast, the T_m and T_g values for syndiotactic PLA are 102–154°C and 33–39°C, respectively.[13,34–36]Heterotactic PLA presents a T_m of 120°C and a T_g of 38–46°C. The stereoblock PLA, which is a polymer composed of distinct blocks of PLLA and PDLA organized within a single chain, presents enhanced thermal properties (T_m = 220–240 °C and T_g = 65–72 °C) compared to those for pure PLLA and PDLA.

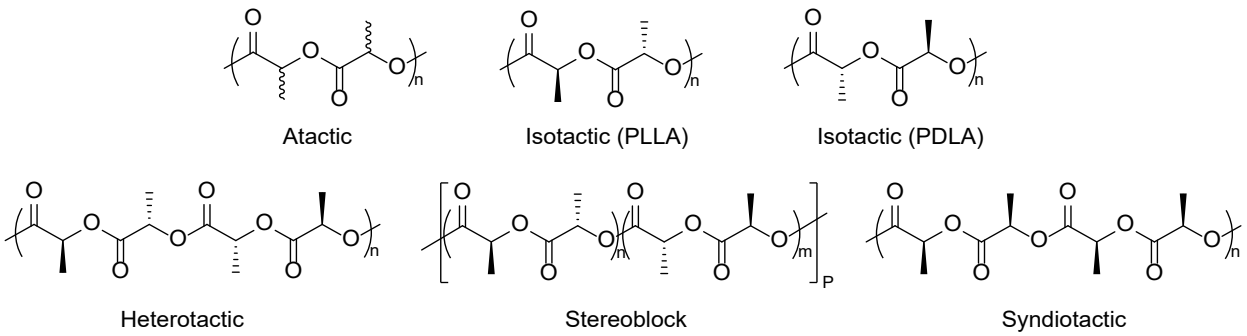

Figure 1.13 Microstructures of PLA

These microstructures can be obtained depending on the monomer used. In the absence of epimerization, pure L-lactide and D-lactide will lead to isotactic-PLLA and isotactic PDLA, respectively. *rac*-Lactide (50:50 mix of D- and L- lactide) gives either atactic, stereoblock or syndiotactic PLA. In the case of *meso*-lactide, heterotactic and syndiotactic microstructures are possible.[30]

The degree of stereoregularity is commonly reported as the probability of forming *racemic*/syndiotactic (P_r) or *meso*/isotactic ($P_m = 1 - P_r$) diad. Atactic polymer is described by $P_r = 0.5$. If *rac*-lactide is the monomer, $P_r = 1$ indicates the formation of a heterotactic polymer, while a P_r value of 0 indicates an isotactic PLA, or more accurately, a stereoblock PLLA-PDLA polymer. In the case of *meso*-lactide, $P_r = 1$ ($P_m = 0$) and $P_m = 1$ ($P_r = 0$) represent syndiotactic and heterotactic, respectively. To determine the P_r value, a proton-proton homonuclear decoupling nuclear magnetic resonance (NMR) experiment is employed, with irradiation of the CH_3 resonance. This leads to the observation of tetrads that are unique for each microstructure. The P_r value is obtained using the equation below, wherein I_1 and I_2 are the relative integrations between δ 5.25–5.20 ppm (in $CDCl_3$) and δ 5.20–5.13 ppm (in $CDCl_3$), respectively.[37]

$$P_r = \frac{2I_1}{I_1 + I_2}$$

As previously mentioned, tacticity influences the mechanical properties (e.g., tensile strength, stiffness, and elongation at break) of PLA. By measuring the P_r value, the aforementioned mechanical properties can be predicted.[38] This is illustrated in Table 1.2.

Table 1.2 Effect of tacticity of polylactic acid on its mechanical properties

Tacticity	Tensile strength (MPa)	Young Modulus/Stiffness (GPa)	Elongation at break (%)	P_r values expected (monomer used)
Isotactic	60–70	3.5–4.0	2–5	$P_r = 0$ (*rac*-lactide)
Syndiotactic	50–60	3.0–3.5	5–10	Pr = 1 (*meso*-lactide)
Heterotactic	55–65	3.2–3.8	6–12	Pr = 1 (*rac*-lactide) $P_r = 0$ (*meso*-lactide)
Atactic	30–50	2.0–2.5	10–20	$P_r = 0.5$

1.2.4 Group 4 metal complexes containing nitrogen-oxygen bidentate ligands for ROP of lactide

Over the past decade, the development of Ti(IV), Zr(IV), and Hf(IV) complexes capable of polymerizing lactide via ROP has generated great attention. Different group 4 metal alkoxy complexes supported by [N,O] phenolate ligands such as amine–phenolate, imine–phenolate, and benzoxazole–phenolate (Figure *1.14*) have proven to be active for high molecular weight PLA generation.[39]

Group 4 imine–phenolate metal alkoxide complexes were reported by Davidson. The Zr catalysts polymerize *rac*-lactide either in solution (toluene, 80 °C) or in the melt (130 °C) in the absence of any solvent, producing moderately-heterotactic PLA. In contrast, the titanium analogues were only active in the melt and produced atactic polymer.[40] Other group 4 imine–phenolate systems, tested by Chakraborty, included a second imino group not coordinated to the metal center. These catalysts produce PLA faster and present better control in the tacticity than the systems developed by Davidson. Additionally, Ti complexes were more active than Zr catalysts, a result that contrasts with most of the group 4 catalysts.[41,42] The ROP of *rac*-lactide with group 4 complexes of amine–phenolate ligands proved to be successful in the melt at 130°C. Moreover, both Zr and Hf complexes produced polymers with an isotactic bias, contrary to the Ti initiator which only yielded atactic polymers.[39,43] Group 4 catalysts bearing benzoxazole–phenolate ligands polymerize *rac*-lactide under solventless conditions with the Zr and Hf complexes showing better activity than Ti complexes and producing isotactic PLA.[44,45]

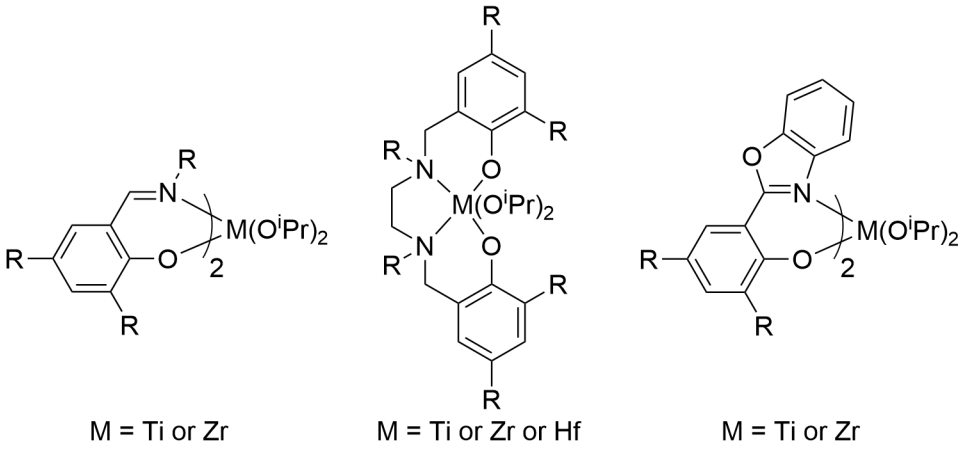

Figure 1.14 imine– (left), amine– (middle), and benzoxazole– (right) phenolate group 4 catalysts.

1.2.5 Zn metal complexes containing nitrogen-oxygen bidentate ligands for ROP of lactide

Zinc catalysts have generated much interest due to their non-toxic properties, low-cost production, and good activities in lactide polymerization. Some of the most attractive ligands are those incorporating a nitrogen donor atom, such as *β*-diiminate, amine–phenolate, and imine–phenolate type ligands (Figure *1.15*).

A zinc alkoxide catalyst bearing a β-diiminate ligand (Figure *1.15*), reported by Coates, is active for the polymerization of *rac*-lactide, yielding heterotactic PLA. The catalyst produces polymers with a molecular weight of 38,000 Da and a narrow molecular weight distribution ($Đ$ = 1.1) within 6–30 min at room temperature in CH_2Cl_2 (97% conversion).[46] Shortly thereafter, Tolman reported a zinc catalyst of a tridentate diamino-phenolate ligand (Figure *1.15*) with similarly high activities under similar conditions. The polymerization yielded atactic PLA with a molecular weight of 130,000 Da and a narrow molecular weight distribution.[47] More recently, Herres-Pawlis reported a zinc catalyst bearing an imine-phenolate ligand (Figure *1.15*) that produces PLA from *L*-lactide under industrial conditions commonly used for $Sn(Oct)_2$ (150 °C, solvent-free), demonstrating the applicability of these ligands to metals other than those from group 4. The catalyst showed a 54% conversion after 1 h with a 1000:1 monomer to initiator ratio, yielding polymers with a molecular weight of 64,000 Da with low dispersity.[48] Another L_2Zn-type zinc initiators supported by an imine–phenolate ligand (Figure *1.15*) also have good activities for the ROP of lactide, generating PLA with a molecular weight of 27,000 Da with a heterotactic bias at room temperature.[49]

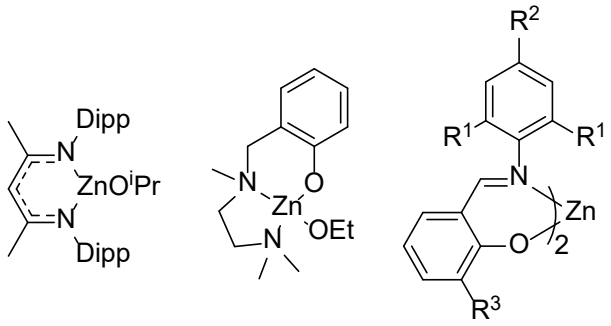

Figure 1.15 Zinc complexes of β-diiminate (left), b) diamine–phenolate (middle) and, imine–phenolate ligands (right).

1.3 N-heterocyclic Carbenes and Cyclic (Alkyl)(Amino)Carbenes-based scaffolds.

1.3.1 N-heterocyclic imine/iminate compounds

N-heterocyclic imines (NHIs) and the corresponding iminates are a category of guanidines and guanidinates that can be obtained through *N*-heterocyclic carbenes (NHCs).[50] Two mesomeric forms of NHIs (Figure *1.16*) show the donating character of these guanidines. The electron-donating capacity of the exocyclic nitrogen can easily be modulated by the substituents R^1, R^2, and R^3 or the modification of the NHC structure itself.[51]

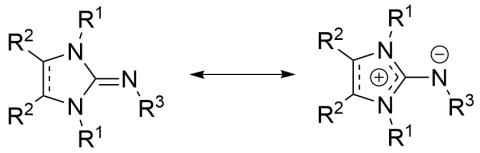

Figure 1.16 Mesomeric forms of cyclic guanidines

These cyclic guanidines have been used as ligands with early and late transition metals, generating several compounds that have been applied in homogeneous catalysis. One of the first examples based on an imidazoline-2-iminato scaffold was Ti(IV) complexes synthesized by Tamm. The catalyst $TiLCl_3$ and its analogous $CpTiLCl_2$ (Figure *1.17*) showed moderate activities in the polymerization of ethylene even at low ratios of the aluminoxane co-catalyst. The Lavoie group has previously reported the reactivity of group 4 complexes bearing a ligand that combines a neutral guanidine fragment and an enolate (Figure *1.17*). This first-generation Ti(IV) complex proved to be active in polymerizing ethylene.[52]

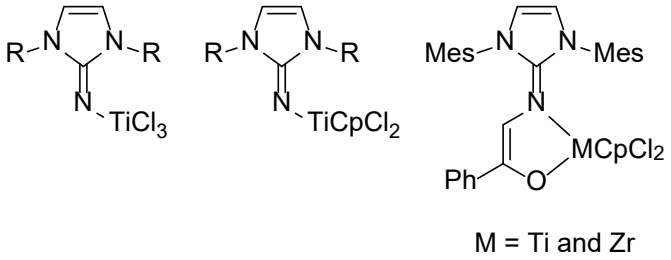

Figure 1.17 Imidazole-2-iminato titanium complex (left), half-sandwich imidazole-2-iminato titanium complexes (middle) and c) guanidine-ethenolate (right) group 4 complexes.

Zinc complexes bearing these guanidines have also been synthesized and tested towards the ROP of lactide. Herres-Pawlis has incorporated neutral ligands to Zn-based catalysts (Figure *1.18*) that display good activities for the ROP of unpurified *rac*-lactide at 150 °C under solvent-free conditions, yielding atactic PLA with molecular weights of 69,000 Da.[53] More recently, the Lavoie group prepared a series of zinc complexes of neutral bidentate ligands with an acylated cyclic guanidine donor (Figure *1.18*). These catalysts were tested for the ROP of *rac*-lactide at 135 °C in the absence of solvent, resulting in polymers with a slight heterotactic bias.[54] A monoanionic system containing a guanidine moiety was also developed by Pellechia (Figure *1.18*). These guanidinate Zn(II) complexes proved to be effective for the ROP of L-lactide under mild and industrial conditions (>130°C), showing activities comparable to the $Sn(Oct)_2$ industrial standard. Studies with *rac*-lactide were however, not reported.[55]

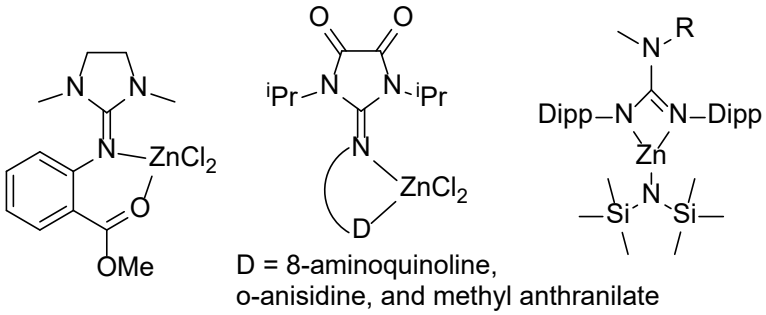

Figure 1.18 Zinc complexes of imidazoline-2-imine (left), acylated cyclic guanidine (middle), and guanidinate ligands (right).

1.3.2 Cyclic (Alkyl)(Amino)Carbenes (CAAC) imino ligands (CAAC=N⁻)

Cyclic(Alkyl)(Amino) carbenes (CAAC) are another class of cyclic carbenes that are more σ-donating and more π-accepting than NHCs (Figure *1.19*). Moreover, the quaternary carbon adjacent to the carbenoid carbon offers different steric effects than other carbene systems, such as NHCs and acyclic diamino carbenes (ADCs). [56] The features of CAACs have been explored with a Ti(II)

complex containing a carbene ligand, in which the titanium center shows π-bonding with the carbenoid carbon, further demonstrating the π-accepting properties of the CAAC systems.[57] The coordination chemistry of CAACs has also been studied for other transition metals, including vanadium,[58] group 6,[59], ruthenium,[60] rhodium,[61] group 10,[62,63] and gold.[64]

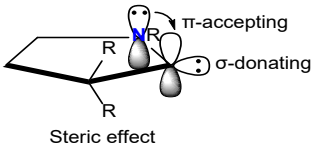

Figure 1.19 CAAC structure

The π-accepting property of the CAACs and NHCs can be estimated through the ^{31}P NMR chemical shift of the phenylphosphinidene-carbene adducts (Figure *1.20*). These adducts have two resonance structures: **A**, in which there is full π-back-donation generating a P=C bond and presenting a downfield ^{31}P NMR chemical shift, and **B**, in which the lone pair (with no π-back-donation) remains on the phosphorus atom, with an upfield ^{31}P NMR chemical shift.[65]

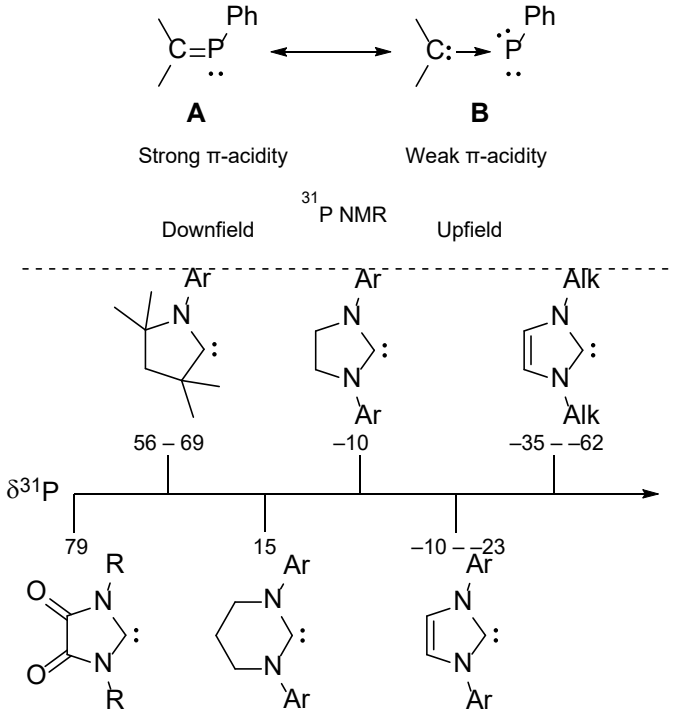

Figure 1.20 ^{31}P NMR chemical shifts of carbene-phosphinidene adducts.

Recently, Braunschweig reported the synthesis of a CAAC imino ligand by reacting 1-(2,6-diisopropylphenyl)-3,3,5,5-tetramethylpyrrolidin-2-ylidene ($CAAC^{Me}$) with trimethylsilyl azide ($TMSN_3$) to give the $CAAC^{Me}$=$NSi(CH_3)_2$ (Scheme 1.1). These new cyclic (alkyl)(amino)imines (CAAIs) are cyclic amidines that are expected to be a stronger σ-donor than NHIs, conversely less π-donating. Due to the similarities between CAAIs and NHIs systems, Braunschweig tested the coordination of $CAAC^{Me}$=$NSi(CH_3)_2$ with titanium (IV) precursors, such as $TiCl_4$ and $CpTiCl_3$ (Scheme 1.1). While the authors mentioned that these new titanium complexes are expected to be used in olefin polymerization, no results have been reported thus far.[66] Additionally, Density Functional Theory (DFT) calculations on diboranes of the anionic ligand proved that CAAIs are indeed stronger σ-donors but less π-donating than unsaturated NHIs.[67]

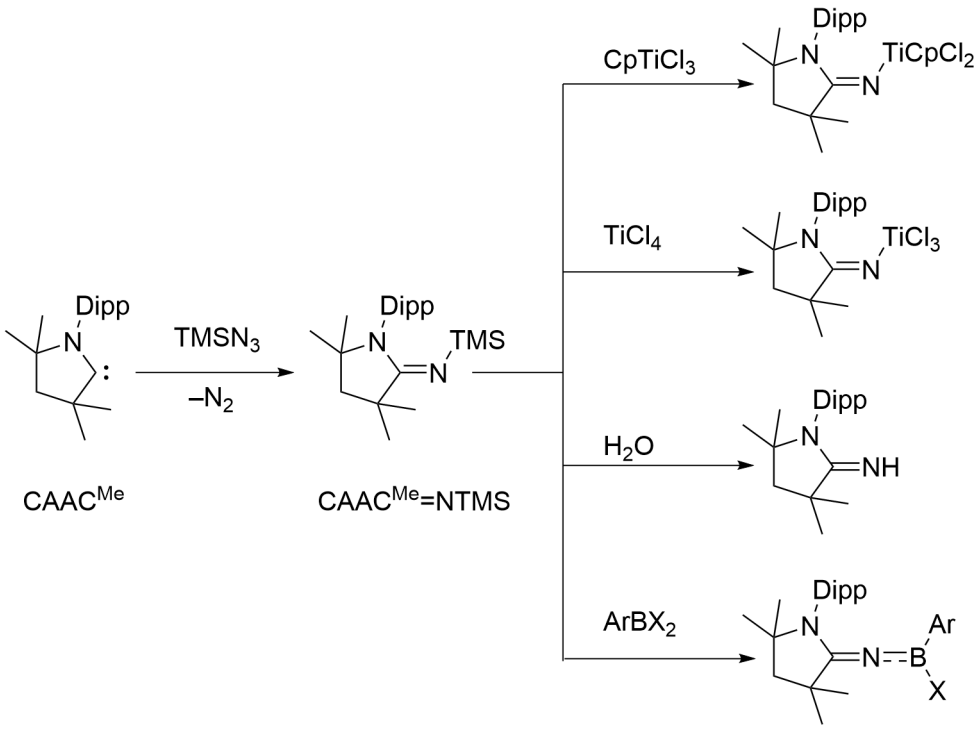

Scheme 1.1 Reactivity of CAACMe=NTMS

Proposed work

In 2013, the Lavoie group reported a first generation of monoanionic imidazol-2-imine–ethenolate ligands and their corresponding group 4 complexes.[52] Following that, several metal complexes containing guanidine ligands, mainly with non-cyclic and imidazolidine-2-imine guanidides,[53,55,68–70] have emerged as catalysts for olefin and lactide polymerizations. The guanidine–phenolate ligands developed by Eisen are of particular interest as they resemble the imine–phenolate ligands used in group 4 and Zn metal complexes involved in the aforementioned catalytic transformations.[68]

This project aims to expand the scope of the guanidine and amidine systems by developing a series of catalysts based on group 4 (Ti, Zr; Chapter 2) and 12 (Zn; Chapter 3) metals stabilized by monoanionic bidentate ligands that incorporate a neutral guanidine or amidine donor and an anionic phenolate donor (Figure *1.21*). The tuneability of the neutral guanidine/amidine donor and its impact on the catalytic activity will be investigated by modifying the building block of the NHC/CAAC itself to different fragments, such as diacyl and amidines. These NHC/CAAC scaffolds were selected to cover a broad range of electronics, as observed in Figure *1.20*. A ^{t}Bu substituent ortho to the phenolic oxygen will also be introduced to explore the influence of the added steric bulk on the catalyst performance. Similarly, the donating ability of the anionic oxygen will be modified by adding a -NO_2 or -OMe in the para position to the phenoxide group. DFT calculations are performed to get a better insight into the structure of these new series of catalysts and to investigate how it influences their catalytic performance. Group 4 bis(isopropoxide) and zinc complexes are studied as catalysts for the ROP of lactide, while titanium dichloride compounds are assessed for their ability to polymerize ethylene.

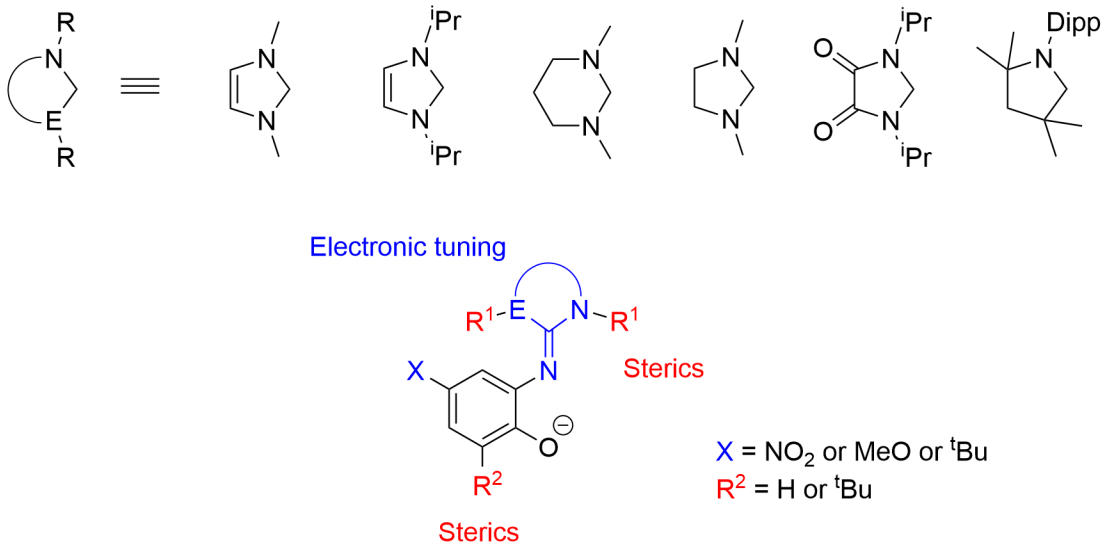

Figure 1.21 The design strategy of the guanidine– and amidine–phenolate ligands

Chapter 2 Group 4 complexes bearing guanidine–phenolate ligands: synthesis, coordination chemistry, and polymerization studies

2.1 Introduction

Modern society relies on fossil-fuel-based polymers designed as single-use materials, which generate environmental concerns. Biodegradable polymers such as polylactic acid are an attractive alternative to replace these fossil-fuel-based polymers. Over the past decade, the development of group 4 complexes capable of polymerizing lactide via ring-opening polymerization (ROP) has generated great attention as it avoids the use of tin octanoate. However, the challenge remains to develop initiators capable of polymerizing lactide under industrial conditions (neat, above 130°C). This chapter describes the synthesis and characterization of titanium and zirconium bis(isopropoxide) and dichloride complexes containing bidentate guanidine-based ligands. The variation of the guanidine moiety with imidazole-, imidazolidine-, and tetrahydropyrimidine-based backbones offers the opportunity to have a better understanding of the steric and electronic effects and study the catalytic performance in the polymerization of both lactide and ethylene.

2.2 Results and Discussion

2.2.1 Synthesis of the NHC scaffold

In order to prepare the guanidine–phenol systems, it is necessary to synthesize the NHC scaffold. The synthesis of the chloro iodide salt **1Cl** was accomplished by reacting 2-chloro-1-methylimidazole with CH_3I in dichloromethane (DCM) (Scheme *2.1*, a), whereas **2Cl** synthesis was explored by reacting 1,3-diisopropylimidazol-2-ylidene with hexachloroethane (Scheme *2.1*, b). The protons of **1Cl** and **2Cl** resonated more downfield with respect to the starting material, consistent with the addition of the chloride electron-withdrawing group and the redistribution of the electronic density. The chemical shifts of the azole backbone protons (δ = 7.97 (**1Cl**) and δ = 8.38 (**2Cl**)) have a similar value to the analogous compound 1,3-bis(2,6-diisopropylphenyl)-2-chloroimidazolium chloride (δ = 8.40).[68]

Following literature procedures **3Cl**, and **4Cl** can be prepared by the reaction of 1,3-dimethyl-2-imidazolidinone and 1,3-Dimethyl-3,4,5,6-tetrahydro-2(1H)-pyrimidinone, respectively, with oxalyl chloride (Scheme *2.1*, c).

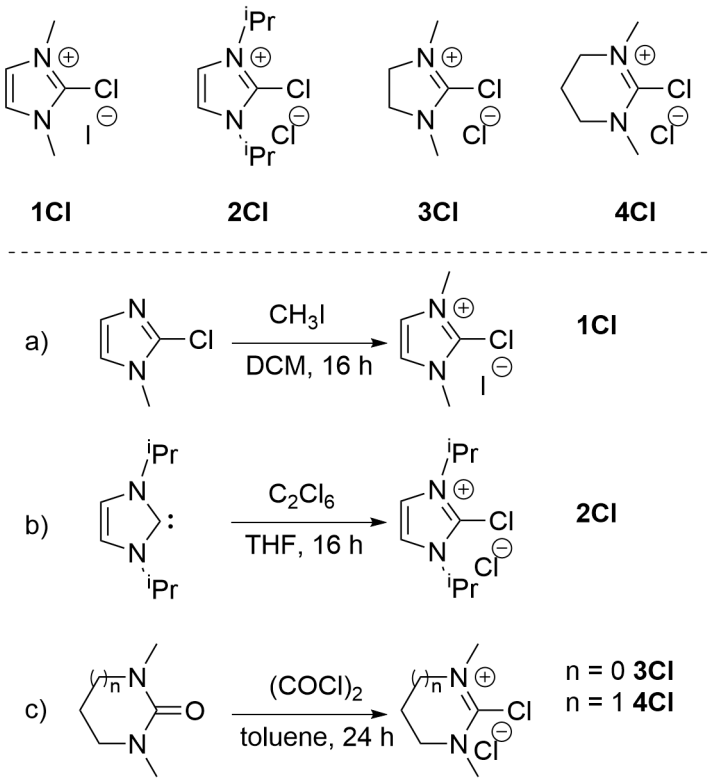

Scheme 2.1 Synthesis of chloro halide salts **1Cl**, **2Cl**, **3Cl**, and **4Cl**

2.2.2 Synthesis of guanidine–phenol proligands

The phenol–guanidinium hydrochloride salts were prepared by reacting the chloro halide salt (**1–4Cl**) with 2-aminophenol or the corresponding *tert*-butyl derivative in the presence of triethylamine. The phenol–guanidine **Lx**H is obtained by deprotonation of the guanidinium salt **Lx**H·HCl with KOH (Scheme *2.2*). NMR spectra of both the phenol and the hydrochloride salts showed magnetically-equivalent aliphatic substituents, consistent with free rotation about the C=N_{exo} due to electron delocalization from the N_{endo} lone pairs. This differs from what is observed in our related systems with diacylated imidazolidine-based ligands, wherein the acyl groups withdraw π-electron density, resulting in greater double bond character and restricted rotation of the C=N_{exo} double bond.[54]

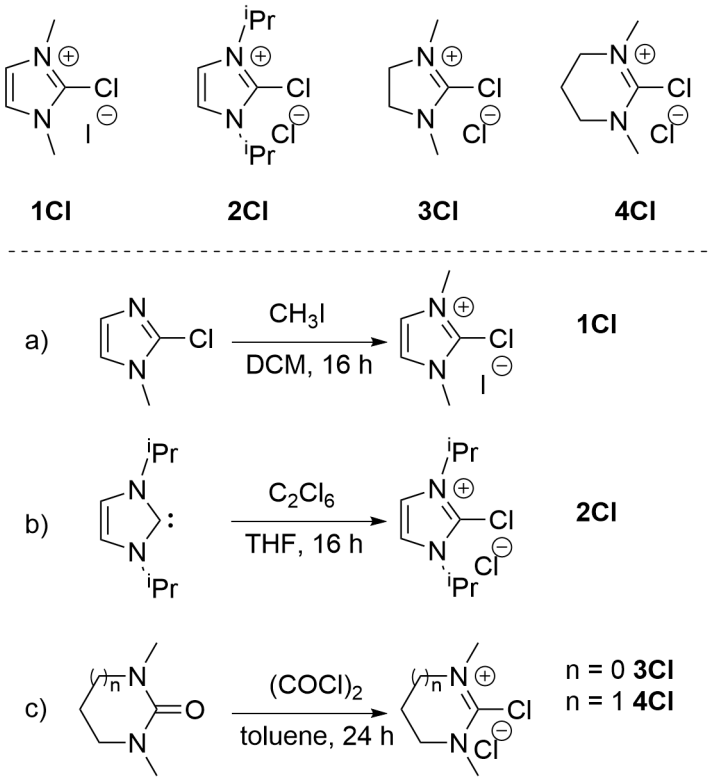

Scheme 2.2 Synthesis of the guanidine–phenol proligands **Lx**H

Variable-temperature (VT) ^{1}H NMR spectroscopy experiments were performed for ligand **L2**H in CD_2Cl_2 from –90 °C to 25 °C, to determine the Gibbs free energy of activation ($\Delta G^{\ddagger}$) for the rotational barrier about this bond. The experiment focused on the changes observed for the CH_3 isopropyl groups signals (1–1.5 ppm). Based on these NMR data, free rotation about the C–$N_{exocyclic}$ bond exists at room temperature and at temperatures as low as –55 °C. The experiment showed coalescence of the two CH_3 resonances from the isopropyl group (Figure *2.1*) at –65 °C. The energy barrier for this rotation was calculated to be 43 kJ mol^{-1} (10 kcal mol^{-1}), using equation 1 ($\delta\upsilon$ = 36 Hz obtained from the NMR spectrum recorded at –90 °C, T_c = 208.15 K). Similar $\Delta G^{\ddagger}$ values have been reported by Kessler for related cyclic guanidines.[71] This is consistent with the higher donating properties of systems that contain an unsaturated imidazole backbone versus their saturated analogues,[72] with a low $\Delta G^{\ddagger}$ implying higher single bond character and electron-donating properties. Compound **L2a**H can thus be represented more accurately by the resonance structure shown in Figure *2.1*.

$$\Delta G^{\ddagger} = RT_c\left[22.96 + \ln\left(\frac{T_c}{\delta v}\right)\right] \quad (1)$$

T_c = coaslescence temperature (K)

$\delta\upsilon$ = differrence in frequency between the maximum peak separation in the low − temperature limit (Hz)

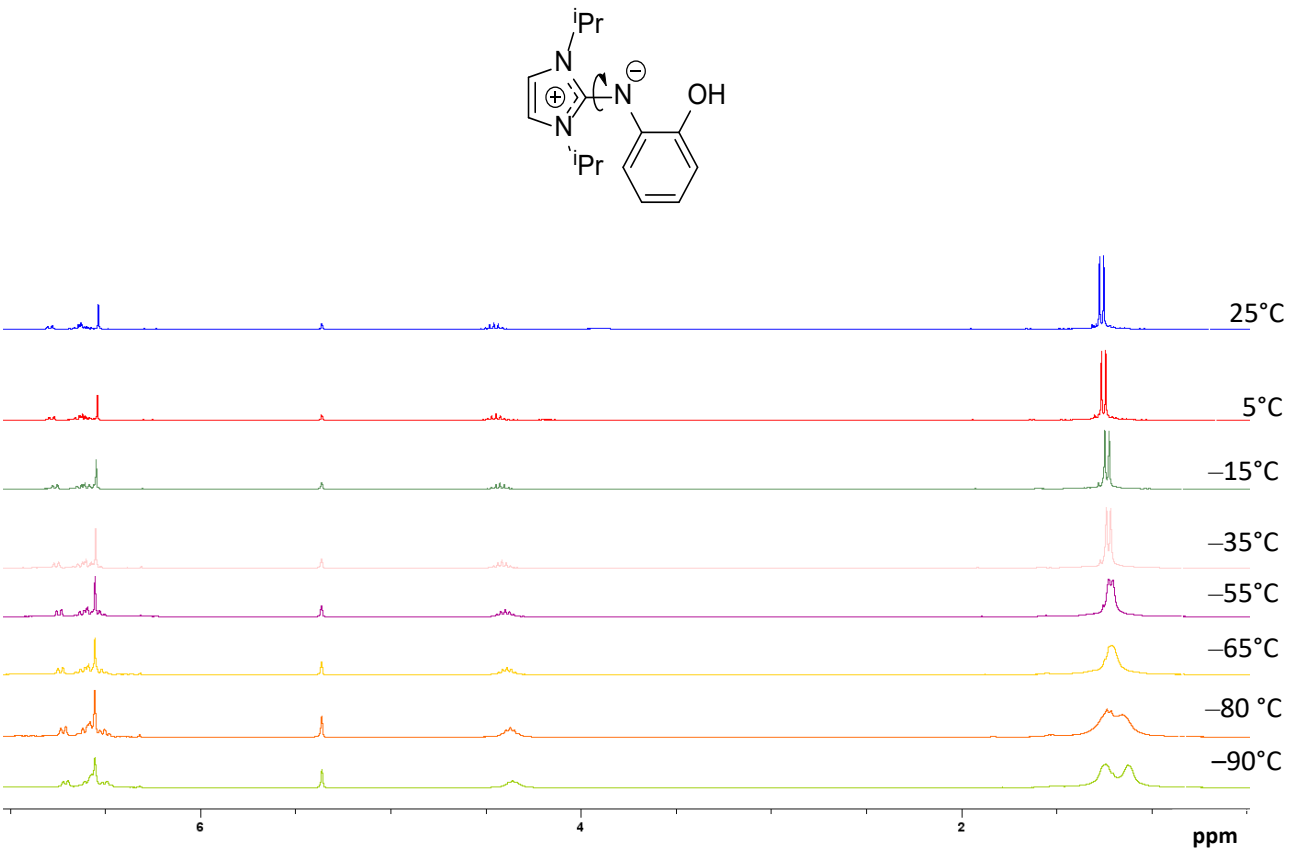

Figure 2.1 Mesomeric form (top) and variable-temperature NMR spectra of **L2a**H (CD_2Cl_2 300 NMR) (bottom).

2.2.3 Synthesis of Group 4 alkoxide complexes

Group 4 bis(isopropoxide) complexes M(**Lx**)$_2$(O^iPr)$_2$ were prepared in excellent yields (>85%) at 60 °C by the addition of 2 equivalents of the guanidine–phenol **Lx**H to Ti(O^iPr)$_4$ or Zr(O^iPr)$_4$·^{i}PrOH (Scheme *2.3*). The ^{1}H NMR spectra of all complexes are consistent with the structure proposed and show only one set of resonances, consistent with the generation of one single isomer. Most titanium complexes showed broad resonances for the aliphatic protons, due to a sterically crowded coordination sphere.

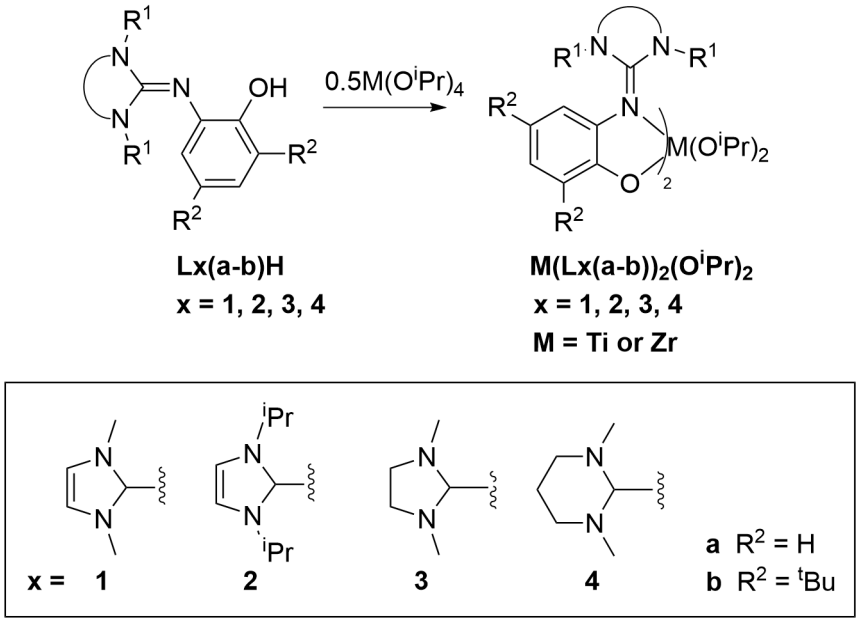

Scheme 2.3 Synthesis of bis(guanidine–phenolate) group 4 alkoxide complexes

X-ray quality crystals of Ti(**L3a**)$_2$(O^{i}Pr)$_2$, Zr(**L3a**)$_2$(O^{i}Pr)$_2$, and Ti(**L4a**)$_2$(O^{i}Pr)$_2$ were grown, and the solid-state molecular structures were determined (Figure *2.2*). All complexes are six-coordinate with the isopropoxide groups in a cis arrangement. Selected bond distances and angles are given in Table *2.1*. The guanidine–phenolate binds to the metal in a bidentate fashion to give the *cis*-N,N-*trans*-O,O diastereomer with average bite angles of 74.96° and 75.48° for Ti(**L3a**)$_2$(O^{i}Pr)$_2$ and Ti(**L4a**)$_2$(O^{i}Pr)$_2$, respectively. As expected, a smaller bite angle of 71.79° was observed in the corresponding zirconium complex Zr(**L3a**)$_2$(O^{i}Pr)$_2$. The O1–M–O2 bond angles deviates from linearity, at 158.35(6)°, 158.03(15)° and 151.00(10)° for Ti(**L3a**)$_2$(O^{i}Pr)$_2$, Ti(**L4a**)$_2$(O^{i}Pr)$_2$, and Zr(**L3a**)$_2$(O^{i}Pr)$_2$, respectively. The M–O^{i}Pr bond lengths range from 1.809(3) to 1.971(3) Å, consistent with analogous group 4 complexes of imine–phenolate ligands with the same stereo-arrangement.[73] The charge delocalization within the guanidine fragment can be expressed by the structural parameter ρ and is defined as ρ = 2a/(b + c) where a and (b, c) are the C=N$_{exo}$ and the two C–N$_{endo}$ bond distances, respectively.[74] The ρ values of 0.97–0.99 indicate extended electron delocalization within the guanidine moiety.

Table 2.1 Selected bond distances [Å] and angles [°] of Ti(**L3a**)$_2$(O^{i}Pr)$_2$, Zr(**L3a**)$_2$(O^{i}Pr)$_2$, and Ti(**L4a**)$_2$(O^{i}Pr)$_2$

M(**Lx**)$_2$(O^{i}Pr)$_2$			
	Ti(**L3a**)$_2$(O^{i}Pr)$_2$	Zr(**L3a**)$_2$(O^{i}Pr)$_2$	Ti(**L4a**)$_2$(O^{i}Pr)$_2$
Bond distances (Å)			
M–O1	1.9182(12)	2.061(3)	1.939(3)
M–O2	1.9245(14)	2.061(3)	1.937(3)
M–O3	1.8103(14)	1.944(3)	1.809(3)
M–O4	1.8466(13)	1.971(3)	1.850(3)
M–N1	2.3724(14)	2.386(3)	2.281(4)
M–N4	2.2738(14)	2.456(3)	2.275(4)
C1–N1	1.323(2)	1.328(4)	1.343(6)
C1–N2	1.368(2)	1.342(5)	1.354(6)
C1–N3	1.350(2)	1.362(5)	1.348(6)
C12–N4	1.322(2)	1.329(5)	1.335(6)
C12–N5	1.374(2)	1.348(6)	1.350(6)
C12–N6	1.339(3)	1.365(6)	1.350(6)
Bond angles (°)			
O1–M–O2	158.35(6)	151.00(10)	158.03(15)
O3–M–O4	98.28(6)	96.69(12)	96.19(15)
N1–M–N4	84.91(5)	85.29(10)	86.81(14)
N1–M–O1	74.68(5)	72.08(10)	75.94(14)
N4–M–O2	75.24(6)	71.49(11)	75.02(14)
ρ^a	0.97	0.98	0.99

[a]Averaged value of both guanidine fragments and calculated as reported in the literature.[74]

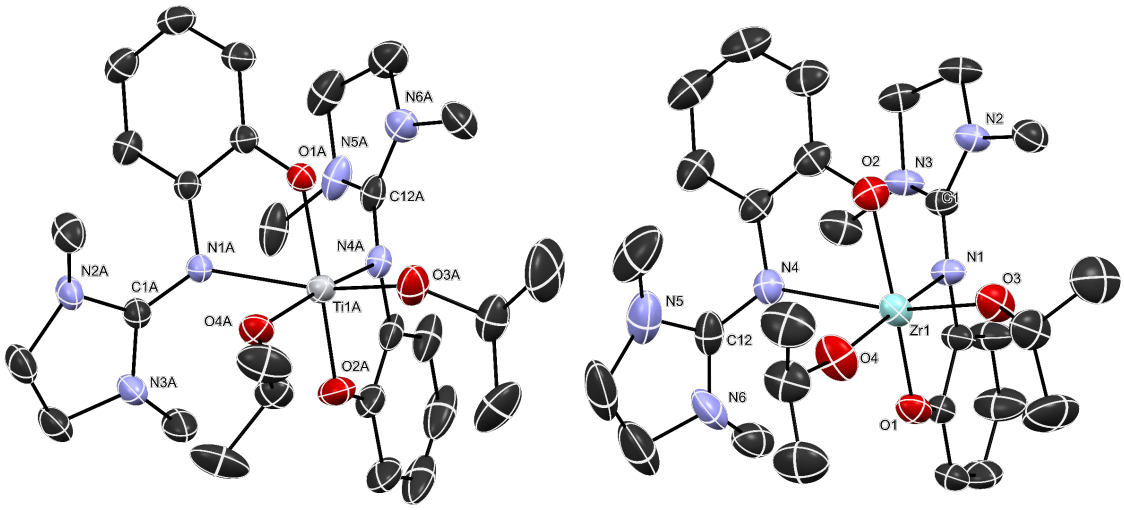

Ti(**L3a**)$_2$(O^{i}Pr)$_2$ Zr(**L3a**)$_2$(O^{i}Pr)$_2$

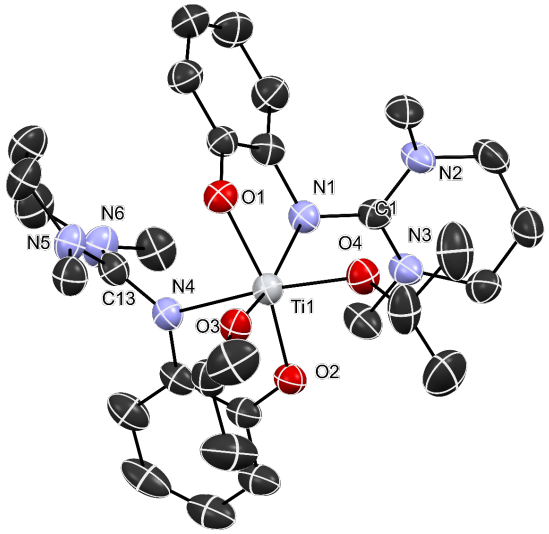

Ti(**L4a**)$_2$(O^{i}Pr)$_2$

Figure 2.2 Solid-state structures of Ti(**L3a**)$_2$(O^{i}Pr)$_2$, Zr(**L3a**)$_2$(O^{i}Pr)$_2$, and Ti(**L4a**)$_2$(O^{i}Pr)$_2$. Hydrogen atoms and solvent have been omitted for clarity. ORTEP drawn at 50% probability.

Analogous to the group 4 bis(imine–phenolate) complexes, five isomers (Figure *1.5*) are possible for the guanidine–phenolate system. Computational studies were performed using B3LYP-D3(BJ)/def2-SVP for geometry optimization and B3LYP-D3(BJ)/def2-TZVPP for single-point energy calculations for all possible isomers of Ti(**L3a**)$_2$(O^{i}Pr)$_2$, Zr(**L3a**)$_2$(O^{i}Pr)$_2$, and Ti(**L4a**)$_2$(O^{i}Pr)$_2$. DFT calculations align with the observed solid-state structures, with isomer **A**

predicted to be the most stable isomer by 1–28 kJ mol^{-1} compared to the cis isopropoxide isomers **B** and **C**, and by 35–70 kJ mol^{-1} for the trans isopropoxide isomers **D** and **E** (Table *2.2*).

Table 2.2 Calculated energies (kJ mol^{-1}) of the five diastereoisomers for the X-ray characterized bis(alkoxide) complexes Ti(**L3a**)$_2$(O^{i}Pr)$_2$, Zr(**L3a**)$_2$(O^{i}Pr)$_2$, and Ti(**L4a**)$_2$(O^{i}Pr)$_2$, relative to that of the most stable isomer **A**.

Complex	*cis*-(O^{i}Pr)$_2$		*trans*-(O^{i}Pr)$_2$	
	Isomer **B** (*cis*-N,N-*cis*-O,O)	Isomer **C** (*trans*-N,N-*cis*-O,O)	Isomer **D** (*cis*-N,N-*cis*-O,O)	Isomer **E** (*trans*-N,N-*trans*-O,O)
Ti(**L3a**)$_2$(O^{i}Pr)$_2$	5	15	46	50
Zr(**L3a**)$_2$(O^{i}Pr)$_2$	1	15	44	35
Ti(**L4a**)$_2$(O^{i}Pr)$_2$	28	27	70	62
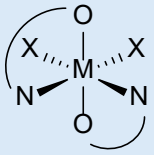 **A**	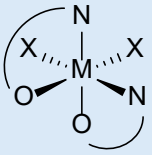 **B**	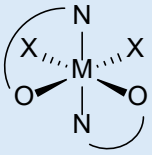 **C**	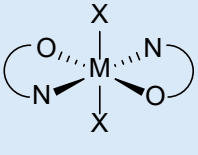 **D**	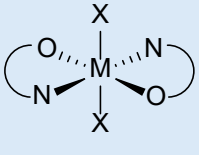 **E**
Most stable isomer				

Due to the large unfavorable energies associated with the trans isopropoxide isomers **D** and **E**, subsequent DFT calculations on complexes not characterized by X-ray diffraction were exclusively conducted on diastereomers **A–C** (Table *2.3*). The calculations indicate that isomer **A** is the most stable isomer. Isomer **C** for complexes Ti(**L1a**)$_2$(O^{i}Pr)$_2$ and Zr(**L1a**)$_2$(O^{i}Pr)$_2$ is less stable than isomer **A** by 45 and 28 kJ mol^{-1}, respectively. The substitution of methyl groups on the endocyclic nitrogen in M(**L1a**)$_2$(O^{i}Pr)$_2$ with a larger isopropyl substituent in M(**L2a**)$_2$(O^{i}Pr)$_2$ displayed an energy difference between the most stable isomer (isomer **A**) and **C** of 1 (Ti) and 17 kJ mol^{-1} (Zr). This indicates that isomer **C** is stabilized when there is greater steric demand, an effect more evident for Ti due to its smaller size. Conversely, Isomer **B** is destabilized for Zr, with a larger energy difference for Zr(**L2a**)$_2$(O^{i}Pr)$_2$ than Zr(**L1a**)$_2$(O^{i}Pr)$_2$ (41 kJ mol^{-1} vs 36 kJ mol^{-1}) relative to isomer **A**, whereas isomers **B** of Ti(**L1a**)$_2$(O^{i}Pr)$_2$ and Ti(**L2a**)$_2$(O^{i}Pr)$_2$ have a similar energy difference with respect to isomer **A**. In most instances, isomer **B** is the least stable diastereomer with notable exceptions for complexes Ti(**L1a**)$_2$(O^{i}Pr)$_2$, Ti(**L3a**)$_2$(O^{i}Pr)$_2$, and Zr(**L3a**)$_2$(O^{i}Pr)$_2$ which are 10–14 kJ mol^{-1} more stable than isomer **C**. The stabilization of isomer **B** might be attributed to the less sterically hindered guanidine moiety; isomer **B** is rarely observed in solution and in the solid state for the related imine–phenolate system, and the reasons for its stabilization are unclear.[10,75]

Table 2.3 Calculated energies (kJ mol^{-1}) of isomers **B** and **C** for bis(alkoxide) complexes not characterized by X-ray diffraction, relative to that of isomer **A**

Complex	Isomer **B** (*cis*-N,N-*cis*-O, O)	Isomer **C** (*trans*-N,N-*cis*-O,O)
Ti(**L1a**)$_2$(O^iPr)$_2$	35	45
Ti(**L1b**)$_2$(O^iPr)$_2$	43	39
Ti(**L2a**)$_2$(O^iPr)$_2$	34	1
Ti(**L3a**)$_2$(O^iPr)$_2$	5	15
Ti(**L4a**)$_2$(O^iPr)$_2$	28	27
Zr(**L1a**)$_2$(O^iPr)$_2$	36	28
Zr(**L1b**)$_2$(O^iPr)$_2$	38	25
Zr(**L2a**)$_2$(O^iPr)$_2$	41	17
Zr(**L3a**)$_2$(O^iPr)$_2$	1	15
Zr(**L4a**)$_2$(O^iPr)$_2$	33	25

2.2.4 Synthesis of Group 4 dichloride complexes

The titanium dichloride complexes Ti(**L1a**)$_2$Cl$_2$, Ti(**L1b**)$_2$Cl$_2$, and Ti(**L2a**)$_2$Cl$_2$ were prepared by reacting 2 equivalents of the guanidinium chloride salt **Lx**H·HCl with Ti(O^iPr)$_4$ in excellent yields (>90%) (Scheme *2.4*). ^{1}H NMR spectra of these complexes exhibit a single set of resonances for both coordinated ligands, indicating the presence of only one isomer. Furthermore, the spectra reveal magnetically-inequivalent protons for the alkyl substituents on the endocyclic nitrogen atoms. This is associated to a restricted rotation in the molecule about the C–N$_{exo}$ bond, generating different magnetic environments, once the ligand is attached to the metal center. The synthesis of these dichloride complexes was also achieved through the reaction of either the corresponding bis(isopropoxide) complexes (*vide supra*) with TMSCl or TiCl$_4$(THF)$_2$ with the sodium guanidine–phenolate salt (Scheme *2.4*), producing products that are indistinguishable spectroscopically. This shows that the formation of the predominant isomer is independent of the preparation method.

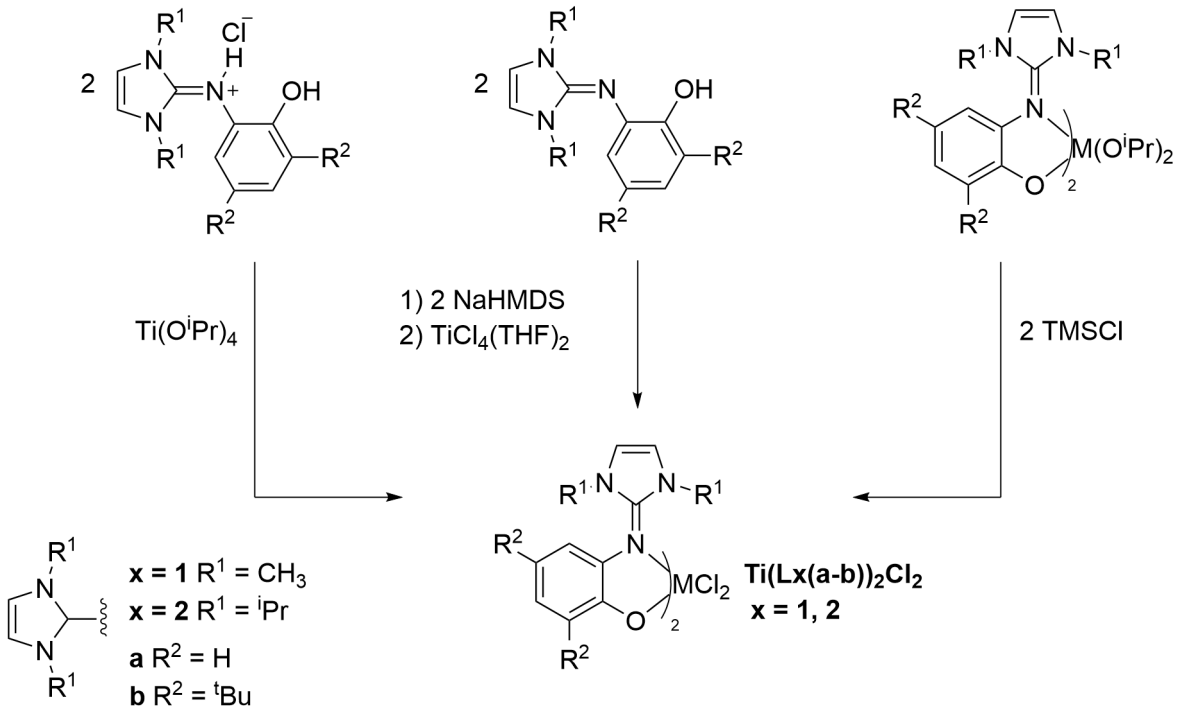

Scheme 2.4 Synthesis of bis(guanidine–phenolate) group 4 chloride complexes

A single crystal of Ti(**L2a**)$_2$Cl$_2$ was analyzed by X-ray diffraction analysis. The solid-state structure exhibits a distorted octahedral geometry, with a *trans*-N,N-*cis*-O,O (isomer **C**) ligand arrangement (Figure *2.3*, Table *2.4*). This observation contrasts with the *cis*-N,N-*trans*-O,O ligand arrangement (isomer **A**) observed for the isopropoxide complexes Ti(**L3a**)$_2$(O^{i}Pr)$_2$, Ti(**L4a**)$_2$(O^{i}Pr)$_2$, and Zr(**L3a**)$_2$(O^{i}Pr)$_2$ (Figure 2.2) and normally observed for related bis(imine–phenolate) titanium dichloride complexes. In the latter case, the *trans*-N,N-*cis*-O,O arrangement was limited to ligands with sterically demanding substituents on the nitrogen.[10,75] The guanidine–phenolate binds to Ti with an averaged bite angle of 76.94(6)°. The N1–M–N4 bond angle deviates from linearity, at 167.97(6)°. The Ti–Cl average bond length of 2.3833(6) Å is similar to analogous group 4 complexes of imine–phenolate ligands with the same stereo-arrangement.[76] A structural parameter (ρ) value of 1.0 indicates extensive electron delocalization over the guanidine moiety.

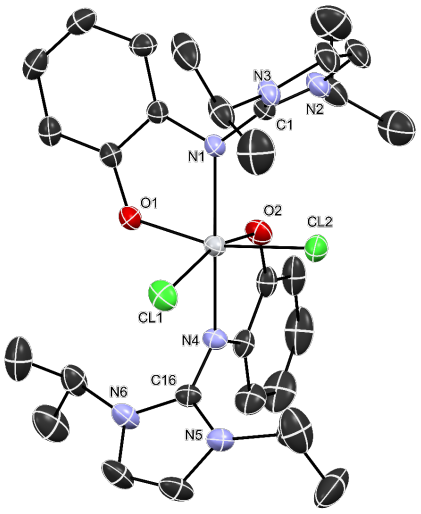

Figure 2.3 Solid-state structure of Ti(**L2a**)$_2$Cl$_2$. Hydrogen atoms have been omitted for clarity. ORTEP drawn at 50% probability.

Table 2.4 Selected bond distances [Å] and angles [°] of Ti(**L2a**)$_2$Cl$_2$

Selected bond lengths (Å)			
Ti–Cl1	2.3783(6)	Ti–Cl2	2.3883(6)
Ti–O1	1.9098(14)	Ti–O2	1.9277(14)
Ti–N1	2.0664(15)	Ti–N4	2.0666(14)
C1–N1	1.372(2)	C16–N4	1.369(2)
C1–N2	1.342(2)	C16–N5	1.343(2)
C1–N3	1.345(2)	C16–N6	1.345(2)
Selected bond angles (°)			
N1–M–Cl1	104.59(5)	N1–M–O1	77.43(6)
N1–M–N4	167.97(6)	N5–M–O2	76.45(6)
Cl1–M–Cl2	87.84(2)	O1–M–O2	94.38(6)
ρ[a]	1.00		

[a]Calculated as reported in the literature and averaged for both guanidine fragments.[74]

Interestingly, our earlier DFT calculations (*vide supra*) on the isopropoxide complexes predicted this arrangement (isomer **C**) to be the second most stable isomer. However, calculations on isomers **A**, **B** and **C** of the dichloride complexes Ti(**L1a**)$_2$Cl$_2$, Ti(**L1b**)$_2$Cl$_2$, and Ti(**L2a**)$_2$Cl$_2$ showed that isomer **C** is indeed predicted to be the most stable by 1–55 kJ mol^{-1} (Table *2.5*), in agreement with

the solid-state structure and further illustrating the important effect that sterics plays on dictating the preferred arrangement of the guanidine–phenolate (and imine–phenolate) ligands.

Table 2.5 Energies (kJ mol^{-1}) of isomers **A** and **B** for bis(guanidine–phenolate) titanium dichloride complexes, relative to that of isomer **C**.

Complex	Isomer **A** (*cis*-N,N-*trans*-O,O)	Isomer **B** (*cis*-N,N-*cis*-O,O)
Ti(**L1a**)$_2$Cl$_2$	1	36
Ti(**L1b**)$_2$Cl$_2$	6	21
Ti(**L2a**)$_2$Cl$_2$	18	55

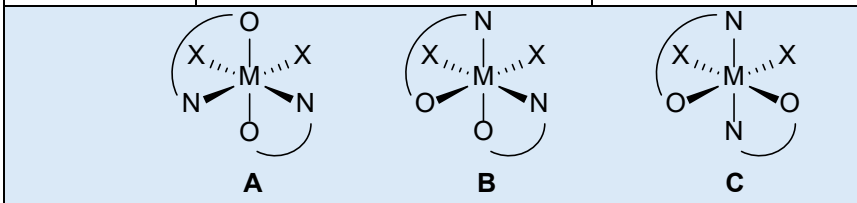

2.2.5 Polymerization studies

2.2.5.1 ROP of lactide with group 4 initiators

All complexes were investigated for their activity in the ROP of *rac*-lactide. Polymerization experiments were carried out without any solvent at 130 °C with a stoichiometric ratio of lactide to catalyst of 100:1, utilizing non-purified monomer. All group 4 bis(isopropoxide) complexes fully convert lactide to PLA within 6 h. The polymerization rate constants were obtained by monitoring the consumption of the monomer over time using ^{1}H NMR spectroscopy and calculated from the slope of the plot ln([lactide]$_0$/[lactide]t) vs time. On average, zirconium complexes exhibit an activity that is 28% greater than that of the corresponding titanium homologs, displaying k_{app} values of 1.17–1.82 × 10^{-4} s^{-1} and 1.39–3.21 × 10^{-4} s^{-1} (with an estimated error of 5% obtained by calculating the standard error on the slope and intercept from the regression line) for Ti and Zr complexes, respectively (Figure *2.4*). This aligns with results in other group 4 catalytic systems, and it is ascribed to a more favorable coordination of the monomer to the larger Zr metal, and to a more nucleophilic alkoxide ligand.[39] The rate constants of the group 4 catalysts are favorable when compared to those determined with Ti(O^{i}Pr)$_4$ (5.34 × 10^{-5} s^{-1}) and Zr(O^{i}Pr)$_4$·^{i}PrOH (2.79 × 10^{-5}

s^{-1}). However, the activities are approximately an order of magnitude lower than that observed for $Sn(Oct)_2$ (1.24×10^{-3} s^{-1}). The activity of titanium catalysts adheres to the following order Ti(**L1b**)$_2$(O^iPr)$_2$ > Ti(**L2a**)$_2$(O^iPr)$_2$ > Ti(**L3a**)$_2$(O^iPr)$_2$ > Ti(**L1a**)$_2$(O^iPr)$_2$ = Ti(**L4a**)$_2$(O^iPr)$_2$, whereas for zirconium complexes follow Zr(**L1b**)$_2$(O^iPr)$_2$ = Zr(**L2a**)$_2$(O^iPr)$_2$ > Zr(**L1a**)$_2$(O^iPr)$_2$ = Zr(**L3a**)$_2$(O^iPr)$_2$ > Zr(**L4a**)$_2$(O^iPr)$_2$. For both series, complexes containing **L1b** and **L2a** polymerized lactide faster; this might be associated with the ^{t}Bu and ^{i}Pr facilitating the migratory insertion of the alkoxide, relieving the steric congestion in the coordination sphere. An experiment with purified lactide was conducted with the most active catalyst Zr(**L2a**)$_2$(O^iPr)$_2$ under the same conditions, leading to a 20% increase in rate (entry 8 vs 9). This suggests the poisoning of the catalysts by impurities present in the unpurified lactide, such as lactic acid and water.

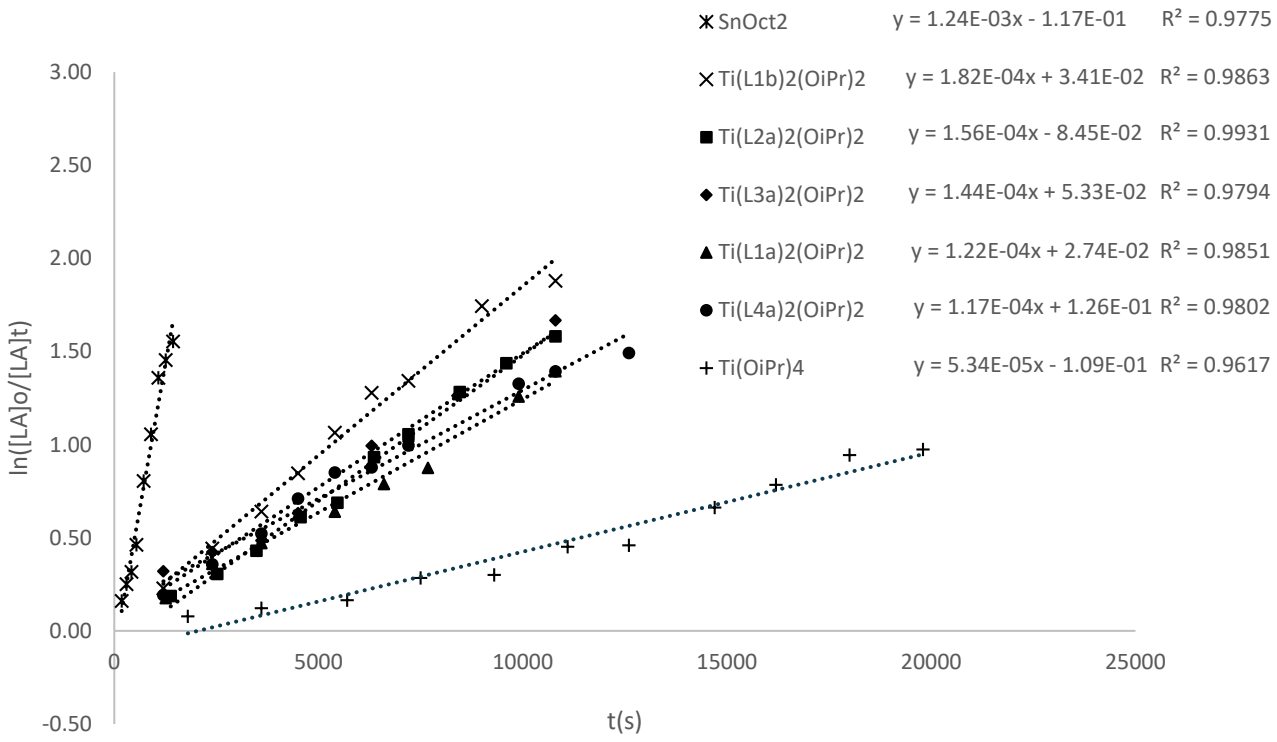

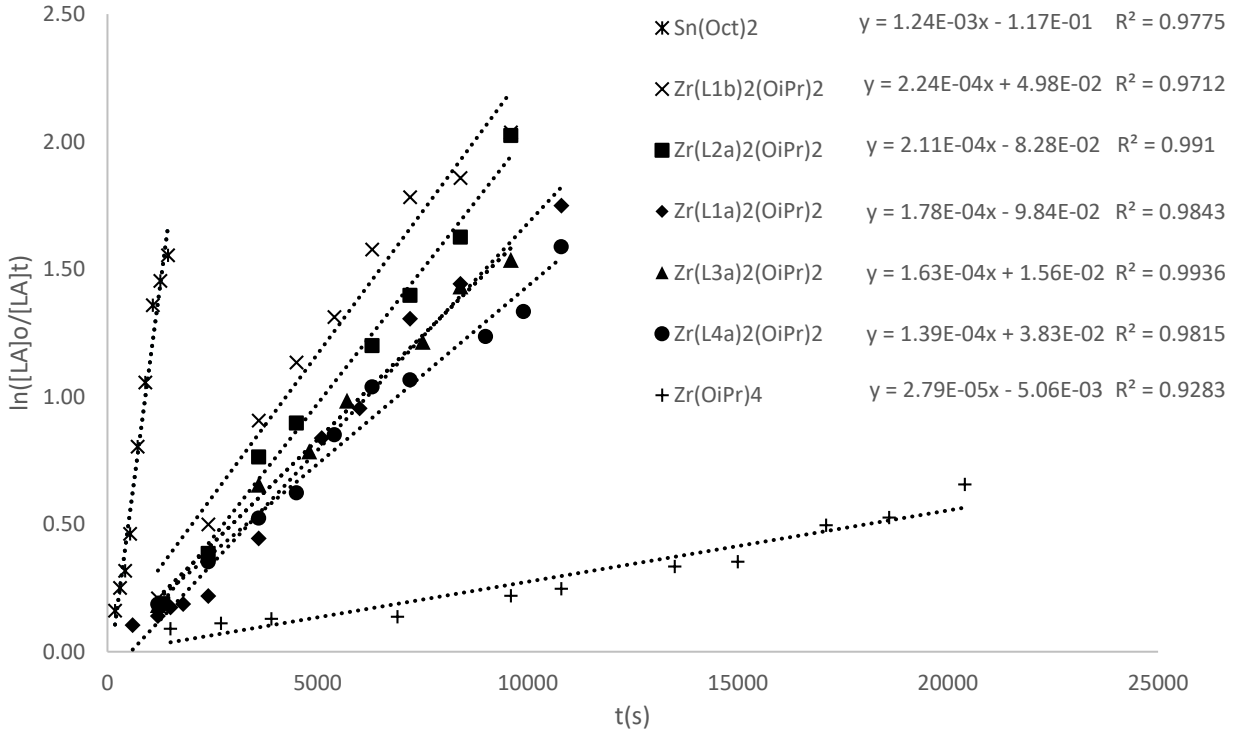

Figure 2.4 Kinetic plots for the polymerization of rac-lactide by $Sn(Oct)_2$, $Ti(O^iPr)_4$, Ti(**L1a**)$_2$(O^iPr)$_2$, Ti(**L1b**)$_2$(O^iPr)$_2$, Ti(**L2a**)$_2$(O^iPr)$_2$, Ti(**L3a**)$_2$(OiPr)$_2$, and Ti(**L4a**)$_2$(OiPr)$_2$ (top) and $Sn(Oct)_2$, $Zr(O^iPr)_4{\cdot}^iPrOH$, Zr(**L1a**)$_2$(O^iPr)$_2$, Zr(**L1b**)$_2$(O^iPr)$_2$, Zr(**L2a**)$_2$(O^iPr)$_2$, Zr(**L3b**)$_2$(O^iPr)$_2$, and Zr(**L4b**)$_2$(O^iPr)$_2$ (bottom).

The number-average molecular weight (M_n) of the polymers from the bis(guanidine–phenolate) group 4 complexes was determined by ^{1}H NMR end-group analysis and gel permeation chromatography (GPC) with values of 700–1800 Da and 1400–2700 Da, respectively. The weight-average molecular weight (M_w) was determined by diffusion-ordered spectroscopy (DOSY) and GPC with values of 1500–3000 Da, and 1600–4000 Da, respectively (Table *2.6*).[77,78] The values obtained are similar to those observed in the experiments with $Ti(O^iPr)_4$, $Zr(O^iPr)4{\cdot}^iPrOH$, and $Sn(Oct)_2$ with M_n ranging from 700—2000 (NMR) and 700—3300 (GPC) and M_w from 1500—3300 (DOSY) and 900—4700 (GPC). Interestingly, the results indicated that the choice of metal, whether Ti or Zr, did not have a significant impact on the polymers produced. The bis(guanidine–phenolate) complexes of **L3a** (entries 4 and 11, Table *2.6*) gave the polymers with the lowest molecular weights. Variation of the size in the endocyclic nitrogen from methyl to isopropyl results in an increase in polymer molecular weight for titanium (entry 1 vs 3, Table *2.6*). This change leads to the opposite effect with zirconium (entries 6 and 8, Table *2.6*). A similar trend is observed when the *tert*-butyl group was installed ortho to the phenolic oxygen with titanium generating polymers

with larger molecular weights (entry 1 vs 2, Table *2.6*) and a decrease with zirconium (entry 6 vs 7, Table *2.6*).

Table 2.6 Solvent-free polymerization of *rac*-lactide

entry[a]	Catalyst	k_{app} (10^{-4} s^{-1})[b]	M_n[c] (Da)	M_w[e] (Da)	$Đ$[f]	M_n[d] (Da)	M_w[d] (Da)	$Đ$[g]	P_r
1	Ti(**L1a**)$_2$(O^{i}Pr)$_2$	1.22	700	1600	2.3	1400	1900	1.4	0.63
2	Ti(**L1b**)$_2$(O^{i}Pr)$_2$	1.82	1400	2400	1.7	2700	4000	1.5	0.62
3	Ti(**L2a**)$_2$(O^{i}Pr)$_2$	1.56	1400	1900	1.4	2200	2900	1.3	0.56
4	Ti(**L3a**)$_2$(O^{i}Pr)$_2$	1.44	700	1500	2.1	1300	1600	1.2	0.62
5	Ti(**L4a**)$_2$(O^{i}Pr)$_2$	1.17	1000	1900	1.9	1600	2100	1.3	0.56
6	Zr(**L1a**)$_2$(O^{i}Pr)$_2$	1.75	1800	3000	1.6	2700	3500	1.3	0.56
7	Zr(**L1b**)$_2$(O^{i}Pr)$_2$	2.24	1100	2100	1.9	1700	2400	1.4	0.58
8	Zr(**L2a**)$_2$(O^{i}Pr)$_2$	2.11	1200	1900	1.6	1600	2100	1.3	0.58
9	Zr(**L2a**)$_2$(O^{i}Pr)$_2$[h]	2.54	1100	2400	2.2	1700	2300	1.4	0.58
10	Zr(**L2a**)$_2$(O^{i}Pr)$_2$[i]	3.21	1200	1900	1.6	1500	2100	1.4	0.58
11	Zr(**L3a**)$_2$(O^{i}Pr)$_2$	1.63	900	1700	1.8	1500	1900	1.3	0.62
12	Zr(**L4a**)$_2$(O^{i}Pr)$_2$	1.39	1500	2600	1.7	2300	2900	1.3	0.58
13	**L2a**H[j]	2.45	1400	3000	2.1	1700	2500	1.5	0.48
14	Sn(Oct)$_2$	12.4	2200	3300	1.5	3300	4700	1.4	0.50
15	Ti(O^{i}Pr)$_4$	0.53	700	1500	2.1	700	900	1.3	0.50
16	Zr(O^{i}Pr)$_4$·^{i}PrOH	0.28	700	1600	2.1	1000	1200	1.2	0.50

[a]All polymerization were carried out at 130 °C with a lactide-to-catalyst stoichiometric ratio of 100:1, with an M_n calculated value of 14,413 Da, assuming a living polymerization. [b]Kinetics were carried out at 130 °C with lactide/catalyst stoichiometric ratio of 100:1. [c]Determined by ^{1}H NMR end-group analysis assuming -O^{i}Pr as chain-end. [d]Determined by GPC in THF. [e] Determined by DOSY NMR in C_6D_6. [f]$Đ = M_{w\ DOSY} \div M_{n\ NMR}$. [g]$Đ = M_w \div M_n$ as determined by GPC. [h]r*ac*-Lactide recrystallized from toluene was employed. [i]2-propanol was employed as co-initiator 1:2 Cat:^{i}PrOH. [j]Lactide/catalyst stoichiometric ratio of 50:1 with an M_n calculated value of 7,206 Da, assuming a living polymerization.

PLA molecular weights were approximately 70% lower than anticipated based on the initial monomer-to-catalyst ratio, under the assumption of living polymerization where chain-transfer or termination reactions are absent and polymer chains grow continuously.[79] Molecular weights measured by ^{1}H NMR spectroscopy slowly increase with conversion and deviate from the

theoretical molecular weight, as shown in Figure 2.5, which is an indication of significant chain transfer and/or transesterification. Additionally, the use of purified lactide did not show an improvement in the molecular weight (entry 8 vs 9, Table *2.6*), suggesting that transesterification depends on the Lewis acidity of the metal center and/or the high temperature used. Although the group 4 systems did not polymerize lactide in a living fashion, the dispersity values (Đ) are considered satisfactory, ranging from 1.1 to 2.3.

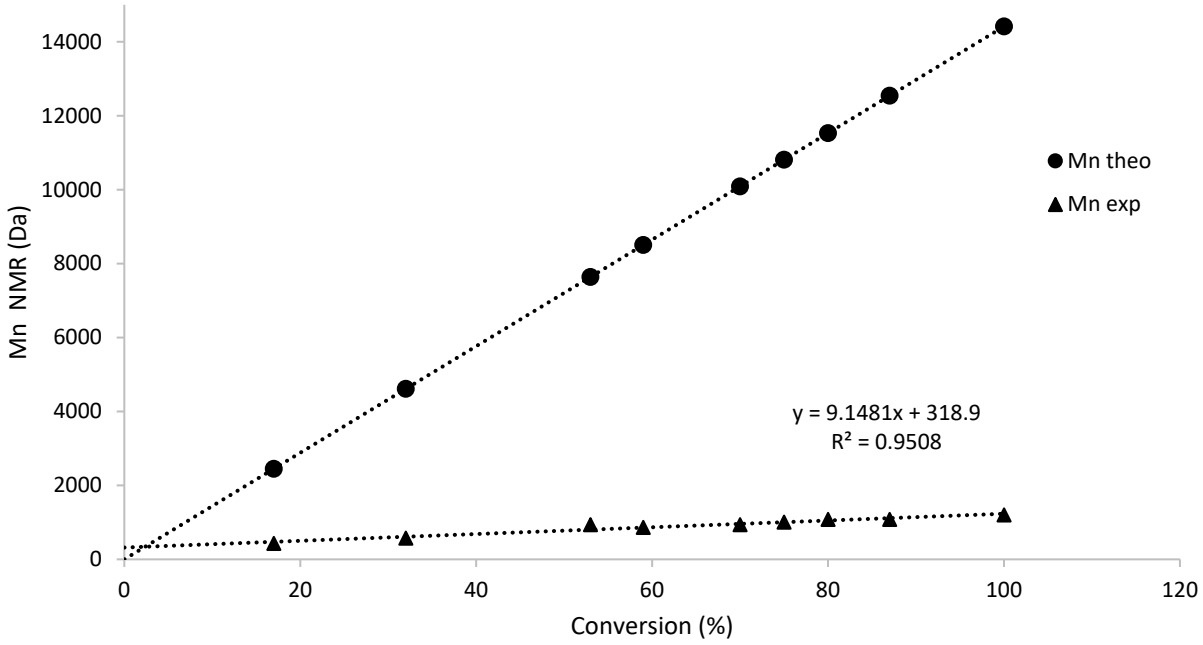

Figure 2.5 Graph of M_n, as determined by ^1H NMR spectroscopy, as a function of conversion. The triangles represent the M_n NMR of PLA generated by Zr(**L2a**)$_2$(O^{i}Pr)$_2$. *The circles represent the theoretical M_n calculated (M_n theoretical = ([Lactide]$_0$/[*Zr(**L2a**)$_2$(O^{i}Pr)$_2$*]$_0$)× 144.13 × conversion)*

The analysis of the ^{1}H and ^{13}C NMR spectra for all the synthesized polymers reveals the incorporation of an isopropyl group as a chain end, consistent with the polymerization proceeding via CIM and normally observed when group 4 alkoxides are employed.[39,80] The possibility of the competing AMM cannot be dismissed based on the lower-than-anticipated relative ratio of isopropyl to hydroxyl end groups observed. This finding is further corroborated by the enhanced rate when two equivalents of isopropanol are used (entry 10, Table *2.6*), which also increased the ratio of isopropyl to hydroxyl end groups. This result implies that nucleophilic impurities present in the monomer may also act as external initiators for the ROP of lactide.

The tacticity of the polymers was determined by homonuclear-decoupled $^{1}H\{^{1}H\}$ NMR spectroscopy, and all isolated polymers showed a heterotactic bias ($P_r = 0.56–0.62$).[81,82] The related imine–phenolate and benzoxazole–phenolate systems generated polymers with similar heterotactic biases. Notably, the influence of the ligand structure appeared to be negligible.[40,44]

The unexpectedly marginal impact of both metal and ligand structures on the catalysts' performance raised concern for the potential of the ligand itself acting as a catalyst after dissociation from the metal at elevated temperatures. Polymerization experiments were thus performed with guanidine–phenol ligand **L2a**H of the most active group 4 catalyst (entry 13, Table *2.6*), rate constants 1.6 and 1.2 times higher than the corresponding metal complexes Ti(**L2a**)$_2$(O^iPr)$_2$ and Zr(**L2a**)$_2$(O^iPr)$_2$, respectively, with comparable polymer molecular weights. However, **L2a**H does not impart any tacticity bias (P_r = 0.48). This observation supports the potential ligand dissociation, with free guanidine acting as a catalyst for the ROP of lactide, which has been reported for guanidines and cyclic esters.[83]

Thermostability studies were performed on complex Zr(**L2a**)$_2$(O^iPr)$_2$ to gain insight into the decomposition of the complex under the polymerization conditions used. A solution of the complex in toluene-d^8 with mesitylene as an internal standard was heated to 120 °C and monitored by ^{1}H NMR spectroscopy over 10 h. Complex Zr(**L2a**)$_2$(O^iPr)$_2$ did not present significant decomposition over the first 3 h, ascribed to the activation barrier of decomposition, which usually involves molecular rearrangement and bond breaking, then Zr(**L2a**)$_2$(O^iPr)$_2$ decomposed following first-order decay with a k value of $–5.38 \times 10^{–4}$ $s^{–1}$ an estimated half-life of 13 h (Figure 2.6). This provides evidence that ligands likely dissociate under reaction conditions and could thus participate in the ROP of lactide.

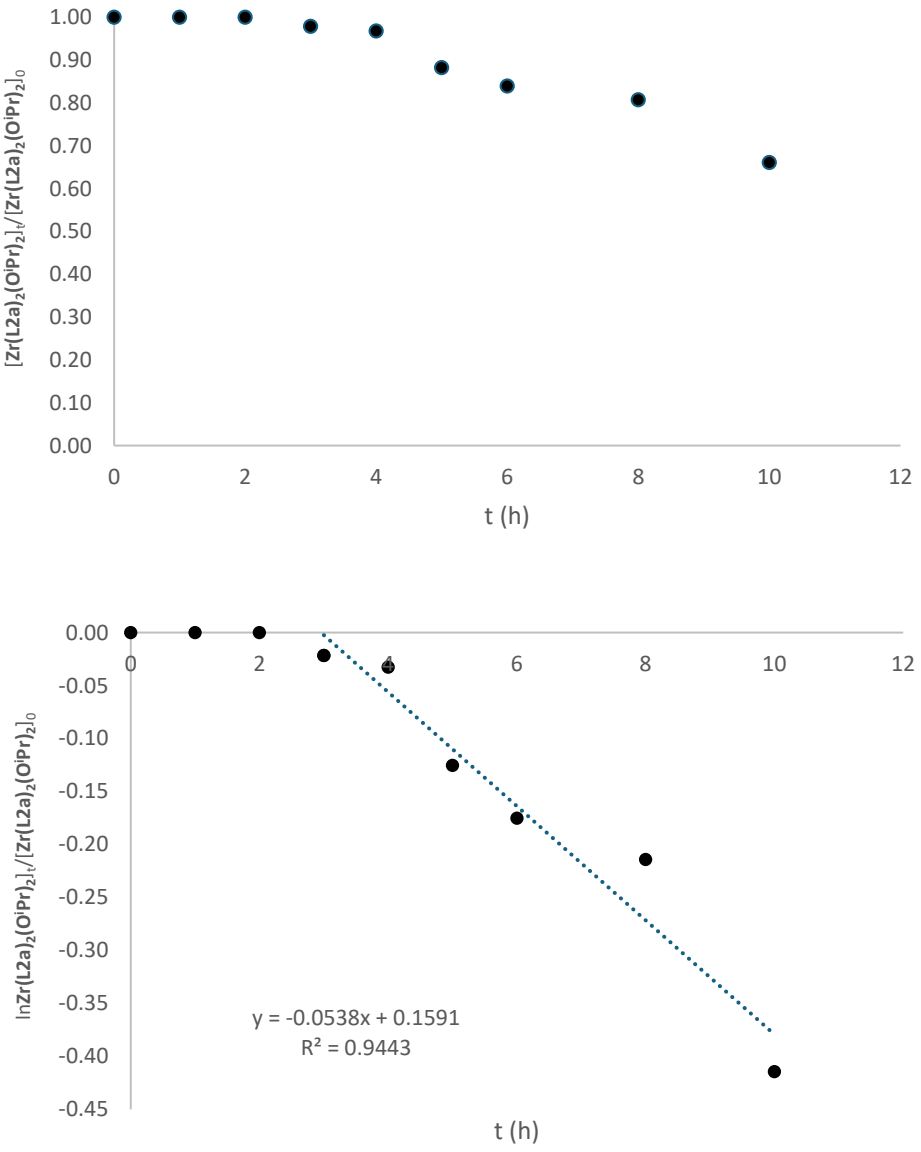

Figure 2.6 Thermostability study of Zr(**L2a**)$_2$(O^{i}Pr)$_2$ *performed in toluene at 120 °C.. [*Zr(**L2a**)$_2$(O^{i}Pr)$_2$*]$_t$/[*Zr(**L2a**)$_2$(O^{i}Pr)$_2$*]$_0$ vs time (top), ln([Zr2a]$_t$/[Zr2a]$_0$) vs time (bottom)*

MALDI-TOF mass spectrometry analysis was performed for the PLA generated by Ti(**L2a**)$_2$(O^{i}Pr)$_2$, Zr(**L2a**)$_2$(O^{i}Pr)$_2$, and **L2a**H (Figure *2.7*). The mass spectrum of all polymers showed a peak separation of m/z = 72, evidence of transesterification, consistent with the observed low molecular weights. Additionally, the spectra of polymers generated by Ti(**L2a**)$_2$(O^{i}Pr)$_2$ and Zr(**L2a**)$_2$(O^{i}Pr)$_2$ indicate the presence of both isopropyl and hydroxyl end-capped polymer chains, with no evidence of cyclic oligomers. The major signals in all spectra are the carboxylic acid and carboxylate end-capped polymers clustered with a sodium ion. Isopropyl end-capped polymer

chain fragments are not predominant, either due to hydrolysis of the polymer chains and/or water acting as an external nucleophile in the initiation step. Their presence suggests that these group 4 alkoxide complexes polymerize lactide via CIM, which is consistent with the NMR spectra obtained (*vide supra*). The mass spectrum analysis of PLA produced by **L2**H does not demonstrate the incorporation of the ligand into the polymer chain, and only hydroxyl end-capped polymer chains are present. This finding suggests that monomer activation occurs via hydrogen-bonding mechanism (Figure *2.8*), as observed for a metal-free guanidine-based catalyst.[83]

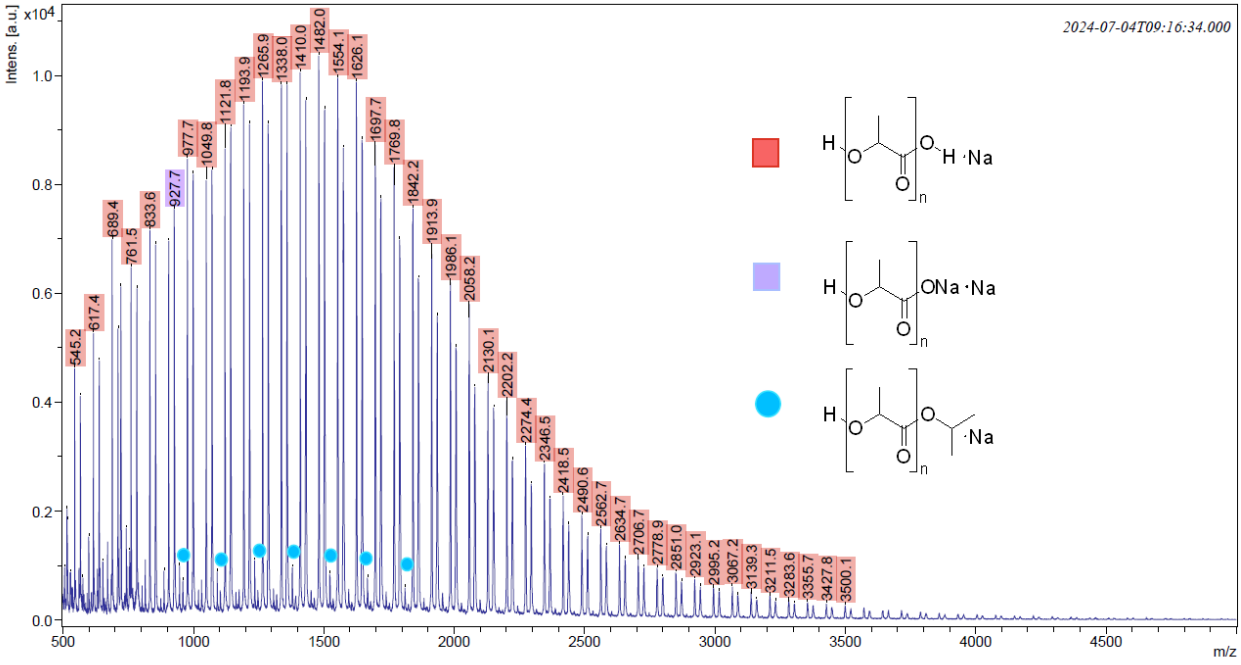

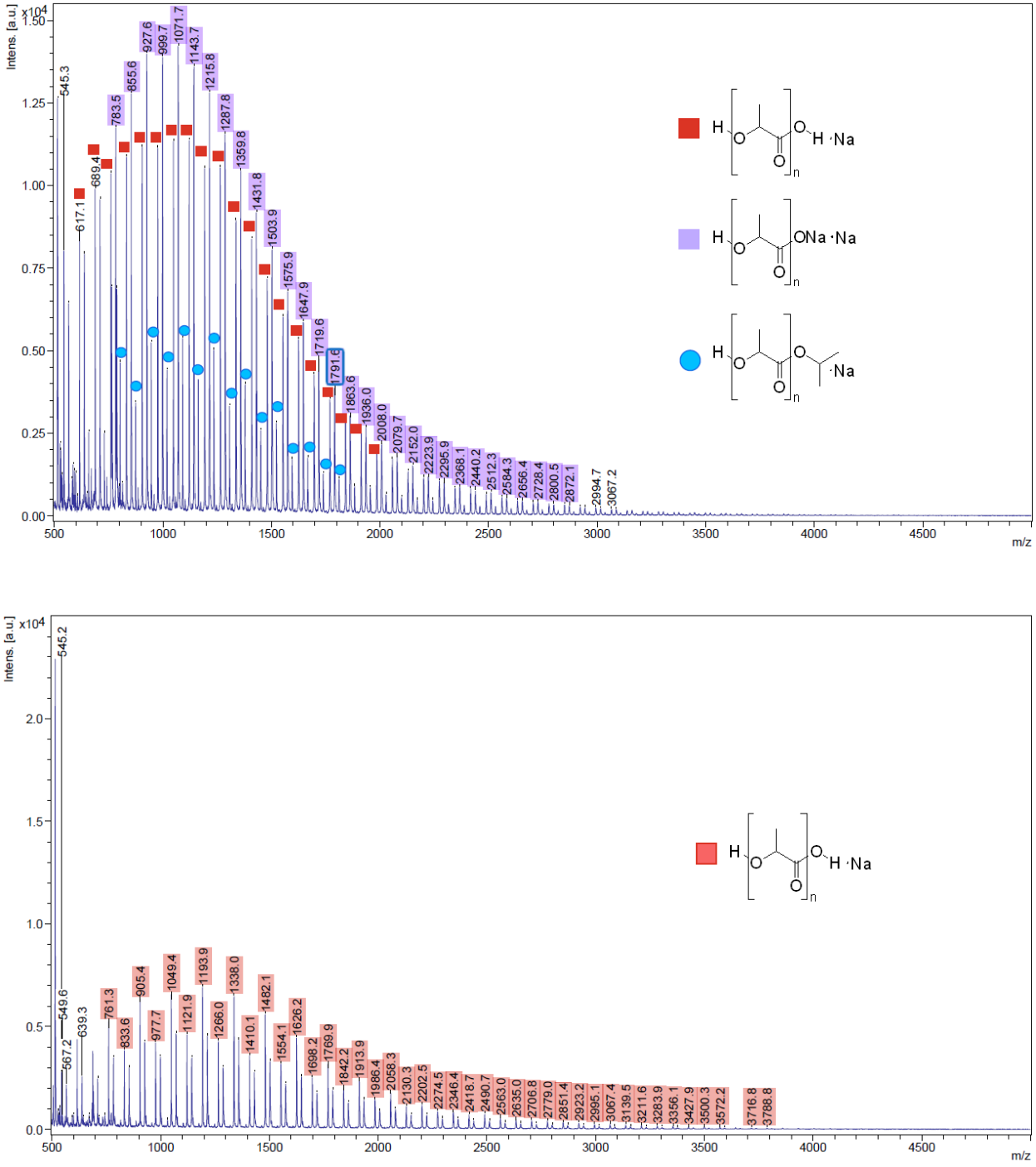

Figure 2.7 MALDI-TOF mass spectra of the polymers obtained using Ti(**L2a**)$_2$(O^{i}Pr)$_2$ (top), Zr(**L2a**)$_2$(O^{i}Pr)$_2$ (middle), and **L2a**H (bottom).

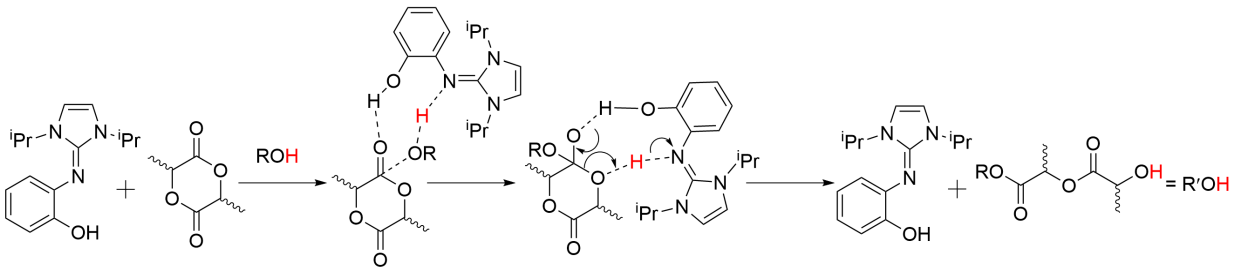

Figure 2.8 Activation of lactide by hydrogen bonding mechanism with **L2a**H

Lactide polymerizations were also performed with Ti(**L2a**)$_2$(O^{i}Pr)$_2$, Zr(**L2a**)$_2$(O^{i}Pr)$_2$, and **L2a**H at an increased lactide to catalysts ratio of 1000:1 at 130 °C (Table *2.7*). These conditions are closer to the industrial process and allow a better comparison versus the industrial standard Sn(Oct)$_2$. All catalysts displayed a decrease in the rate constant by approximately one order of magnitude with respect to experiments in Table *2.6*, as expected for the 10-fold increase in the lactide to catalysts ratio. Group 4 alkoxide complexes produced low-molecular-weight polymers, considering the lactide-to-catalyst ratio used, which might be associated with the increase of polar impurities due to the increase in the lactide-to-catalyst ratio, enhancing the susceptibility of the catalysts to poisoning and decomposition due to the temperature used, as previously showed in Figure 2.6.

Table 2.7 Solvent-free polymerization of rac-lactide in monomer to catalysts ratio 1000:1

entry[a]	Catalyst	k_{app} (10^{-5} s^{-1})	M_n[b] (Da)	M_w[b] (Da)	$Đ$[c]
1	Ti(**L2a**)$_2$(O^{i}Pr)$_2$	1.42	2600	3600	1.4
2	Zr(**L2a**)$_2$(O^{i}Pr)$_2$	2.03	2100	2900	1.4
3	**L2a**H[d]	0.92	2800	3900	1.4
4	Sn(Oct)$_2$	34.6	12000	21000	1.8

[a]All polymerizations were carried out at 130 °C to full conversion and a lactide-to-catalyst stoichiometric ratio of 1000:1, with Mn calculated values of 144,130 Da. [b]Determined by GPC in THF [c]$Đ = M_w \div M_n$ [d]Lactide:catalyst stoichiometric ratio of 500:1, with Mn calculated values of 72,065 Da.

2.2.5.2 Ethylene polymerization

Group 4 dichloride complexes Ti(**L1a**)$_2$Cl$_2$, Ti(**L1b**)$_2$Cl$_2$, and Ti(**L2a**)$_2$Cl$_2$ were evaluated for the polymerization of ethylene at room temperature with n-octyl-modified methylaluminoxane (MMAO-12) as cocatalysts. Catalysts Ti(**L1a**)$_2$Cl$_2$ and Ti(**L2a**)$_2$Cl$_2$ displayed comparable activities 1.1 and 0.8 $kg_{PE}\ mol_{Ti}^{-1}\ h^{-1}$ (over 1–3 h), respectively. Those productivities are two orders of magnitude lower than the benchmark catalysts Cp$_2$TiCl$_2$ (over 3 min). The addition of a ^{t}Bu group ortho position to the phenolic oxygen in Ti(**L1b**)$_2$Cl$_2$ did not have an impact on the

activity, and only traces of polymer were observed. This is in stark contrast with the 85-fold increase in activity reported for the FI catalyst (imine–phenolate)[10]. Fujita has indicated that the arrangement of the ^{t}Bu groups positioned above and below the reaction site (Cl–M–Cl), specifically in the cis-N,N-trans-O,O configuration (Isomer **A**, Figure 2.9), reduces the energy barrier for the olefin insertion and minimizes potential side reactions. The arrangement predicted by DFT for complex Ti(**L1b**)$_2$Cl$_2$ is trans-N,N-cis-O,O (Isomer **C**, Figure 2.9), placing the ^{t}Bu at the back of the reaction site. Group 4 imine–phenolate systems that presented this arrangement showed poor activity.[10,76] The poor activity observed in the bis(guanidine–phenolate) titanium catalysts might be ascribed to the presence of an undesirable diastereomer along with a less electrophilic metal center due to the strong electron-donating guanidine fragment.

Figure 2.9 Most stable isomer for the imine-phenolate and guanidine-phenolate systems

2.3 Conclusions

The bis(guanidine-phenolate) group 4 alkoxide complexes were evaluated for their efficacy in the ring-opening polymerization of *rac*-lactide under solvent-free conditions. The resultant polylactic acid (PLA) displayed molecular weights and dispersity values that are comparable to those achieved using the industry-standard Sn(Oct)$_2$ under identical experimental conditions. Notably, the guanidine-phenol proligands appear to significantly influence the polymerization rate, exhibiting performance similar to that of the corresponding metal complexes. Furthermore, PLA synthesized from these bis(alkoxide) complexes showed heterotactic bias in comparison to the proligand and other catalysts utilized in control experiments. The related dichloride titanium complexes exhibited limited activity in the polymerization of ethylene, even when employing the bulky tert-butyl phenolate derivative. The versatility of these guanidine–phenolate ligands, along with the potential for further tailoring of their electronic and steric properties, presents valuable opportunities to enhance the experimental framework and explore their application in additional catalytic transformations.

2.4 Experimental section

General considerations

All manipulations and materials were performed under a dry argon atmosphere, using Schlenk techniques or in a nitrogen-filled MBraun glovebox. $Ti(O^iPr)_4$, $Zr(O^iPr)_4 \cdot {}^iPrOH$, $TiCl_4(THF)_2$, $SnOct_2$, NaHMDS, and TMSCl were purchased from Sigma-Aldrich and used without further purification. Lactide was purchased from Thermo Fisher Scientific and used as received unless otherwise stated; if needed, the monomer was purified by one recrystallization from toluene. 2-Amino-4,6-di-*tert*-butylphenol,[84] 2-chloro-1-methylimidazole,[85] **3Cl**, **4Cl**,[86] and **L3a**H[87] were synthesized according to literature procedure. Deuterated solvents C_6D_6 and $CDCl_3$ were purchased from Sigma-Aldrich. C_6D_6 and $CDCl_3$ were dried over sodium and benzophenone, and over CaH_2, respectively. Both were degassed by freeze-pump-thaw cycles, vacuum transferred to dry ampules, and stored over molecular sieves prior to use. NMR spectra were recorded on a Bruker 400 MHz or Bruker UltraShield 300 MHz NMR spectrometer at room temperature. ^1H NMR chemical shifts are reported in ppm versus residual protons in deuterated solvents as follows: δ 7.27 $CDCl_3$ and δ 7.16 C_6D_6. $^{13}C\{^1H\}$ NMR chemical shifts are reported in ppm versus residual ^{13}C in the solvent: δ 77.16 $CDCl_3$ and δ 128.06 C_6D_6.

X-ray Crystallography

Diffraction data for ligands and complexes were collected on a Bruker APEX-II CCD diffractometer with a Mo Kα (λ = 0.71073 Å) radiation source. Crystals were selected under paratone oil and mounted under a stream of N_2 and kept at 173K during data collection. Structures were solved in Olex2[88] using direct methods and refined with SHELXL[89] refinement package using least-squares minimization.

Gel Permeation Chromatography

Number-average molecular weight (M_n), weight-average molecular weight (M_w) and dispersity (Đ; M_w/M_n) of samples were determined by gel permeation chromatography (GPC) using two PLgel miniMIX-B columns (4.6 mm x 250 mm) and two PLgel miniMIX-C columns (4.6 mm x 250 mm) from Agilent on elution with tetrahydrofuran (0.4 mL/min) at room temperature, equipped with an Agilent multi-detector suite composed of an Agilent G7801A refractive index detector, an Agilent G7803A dual-angle light scattering detector and an Agilent G7802A

viscometer. Columns were calibrated using seven polystyrene standards with a conventional approach (M_p = 482,000, 125,900, 66,600, 27,060, 9,310, 5,610, and 1,180 Da. Data were analyzed using the Agilent GPC software version A.02.01 software (Santa Clara, CA 95051, United States).

MALDI-TOF Mass spectrometry

MALDI-TOF data were obtained at the Advanced Instrumentation for Molecular Structure (AIMS) laboratory of the University of Toronto on a Bruker AutoFlex Speed MALDI-TOF mass spectrometer, with ionization using a 355 nm 3rd harmonic Nd YAG laser. The variable repetition was set to 2 kHz with a pulse energy ≥ 100 μJ. Samples were prepared in a dithranol THF matrix.

Computational details

The calculations were performed with the computational package Gaussian 09 on Shared Hierarchical Academic Research Computing Network (SHARCNET; www.sharcnet.ca) and made possible by Compute Canada (www.computecanada.ca). SHARCNET is a consortium of 19 colleges, universities and research institutes operating a network of high-performance computer clusters across Ontario. All geometry optimizations were performed using the B3LYP functional with the Def2SVP basis set,[90] and Grimme's empirical dispersion correction term with Becke–Johnson damping, D3(BJ), was applied.[91] Single-point energy calculations were performed on the structures optimized with the B3LYP-D3 (BJ)/Def2-TZVPP level of theory.

Synthesis of compound 1Cl

A Schlenk flask was charged with 2-chloro-1-methylimidazole (912 mg, 7.82 mmol, 1.0 equiv.) followed by the addition of 20 mL of DCM. CH_3I (750 mL,11.4 mmol, 1.5 equiv.) was added dropwise. The reaction mixture was stirred for 16 h at room temperature. Volatiles were removed *in vacuo* and the solids were washed with diethyl ether (2 × 10 mL). Volatiles were removed to give a tan solid (1.81 g, 7.02 mmol, 88%). ^{1}H NMR (400 MHz, $CDCl_3$): δ 7.97 (s, 2H, $N(CH)_2N$), 4.03 (s, 6H, N-CH_3). ^{13}C NMR (100 MHz, D_2O): δ 132.6 (s, C–Cl), 123.3 (s, $N(CH)_2N$), 35.6 (s, N-CH_3). Anal. Calcd for $C_5H_8ClIN_2$ (%): C, 23.23; H, 3.12; N, 10.84. Found (%): C, 23.45; H, 2.96; N, 10.54.

Synthesis of compound 2Cl

A round bottom flask was charged with 1,3-diisopropylimidazolium bromide (1.02 g, 4.37 mmol, 1 equiv.) followed by the addition of sodium *tert*-butoxide (0.049 g, 0.437 mmol, 0.1 equiv.) and sodium hydride (0.115 g, 4.80 mmol, 1.1 equiv.). Then, 15 mL of THF was added, and the solution stirred for 16 hours. The carbene 1,3-diisopropylimidazol-2-ylidene was extracted in THF. Subsequently, the THF solution was filtrated through Celite and slowly added to a solution containing C_2Cl_6 (1.13 g, 4.80 mmol, 1.1 equiv.) in THF at –40 °C. The reaction mixture was left to reach room temperature and stirred for 24 hours. The resulting solids were filtered and washed with THF (4 × 5 mL) and dried under vacuum to yield a tan solid (819 mg, 3.67mmol, 84%). ^{1}H NMR (400 MHz, $CDCl_3$): δ 8.38 (s, 2H, $N(CH)_2N$), 4.80 (sept, J = 6.7 Hz, 2H, C*H*Me$_2$), 1.64 (d, J = 6.7 Hz, 12H, CH*Me*$_2$).^{13}C (100 MHz, $CDCl_3$): δ 127.7 (s, C–Cl), 122.0 (s, $N(CH)_2N$), 53.5 (s, *C*HMe$_2$), 22.3 (s, CH*Me*$_2$). Anal. Calcd for $C_9H_{16}Cl_2N_2$ (%): C, 48.44; H, 7.23; N, 12.55. Found (%): C, 48.12; H,7.11; N, 12.66.

Synthesis of ligands

L1aH. A Schlenk flask was charged with 2-aminophenol (218 mg, 1.99 mmol, 1.0 equiv.) and triethylamine (0.50 mL, 4.10 mmol, 2.0 equiv.) with 20 mL of acetonitrile (MeCN). In a separate vial, compound **1Cl** (516 mg, 1.99 mmol, 1.0 equiv.) was dissolved in 10 mL of MeCN. The solution of **1** was added and the mixture stirred under reflux for 3 h. Thereafter KOH (226 mg, 4.10 mmol, 2.1 equiv.) in 3 mL of H_2O was then added and stirred for 15 min. Volatiles were removed under vacuum. The ligand was extracted with toluene (6 × 5 mL). The combined organic layers were dried over Na_2SO_4. Removal of the volatiles *in vacuo* gave a dark yellow solid (305 mg, 1.50 mmol, 75%). ^{1}H NMR (300 MHz, $CDCl_3$): δ 6.87–6.85 (m, 1H, Ar- CH), 6.63 –6.61 (m, 1H, Ar-CH), 6.26 (s, 2H, $N(CH)_2N$), 3.19 (s, 6H, NCH_3).^{13}C{^{1}H} NMR (75 MHz, $CDCl_3$) δ 149.4 (s, C=N), 149.1 (s, C-OH), 137.6 (s, C-N), 119.3 (s, CH-Ar), 119.1 (s, CH-Ar), 118.2 (s, CH-Ar), 114.6 (s, $N(CH)_2N$), 112.4 (s, CH-Ar), 33.9 (s, NCH_3). Anal. Calcd for $C_{11}H_{13}N_3O$ (%): C, 65.01; H, 6.45; N, 20.68. Found (%): C, 65.21; H, 6.06; N, 20.92.

L1aH·HCl. A round-bottom flask was charged with **L1a**H (150 mg, 0.738 mmol, 1 equiv.) and 10 mL of THF, followed by the addition of a solution of HCl in dioxane (0.25 mL, 1.00 mmol, 1.4 equiv.). The mixture was stirred for 30 min, thereafter, the volatiles were removed under vacuum. The tan solid was washed with diethyl ether, and dried under reduced pressure (172 mg, 0.721 mmol, 97%). ^{1}H NMR (300 MHz, D_2O): δ 6.90–6.87 (m, 1H, Ar- CH), 6.76–6.70 (m, 1H, Ar-CH),

6.16 (s, 2H, N(CH)$_2$N), 3.35 (s, 6H, NCH$_3$). Anal. Calcd for $C_{11}H_{14}ClN_3O$ (%): C, 55.12; H, 5.89; N, 17.53. Found (%): C, 55.48; H, 5.74; N, 17.30

L1bH. This compound was prepared by the same method as **L1a**H with 2-amino- 4,6-di-tert-butylphenol to give a green solid (205.5 mg, 0.553 mmol, 70%). ^{1}H NMR (300 MHz, $CDCl_3$): δ 6.74 (d, *J* = 3.0 Hz,1H, CH-Ar), 6.59 (d, *J* = 3.0 Hz,1H, CH-Ar), 6.22 (s, 2H, N(CH)$_2$N), 3.18 (s, 6H, NCH$_3$), 1.43 (s, 9H, C(CH$_3$)$_3$), 1.28 (s, 9H, C(CH$_3$)$_3$). ^{13}C{^{1}H} NMR (75MHz, $CDCl_3$) δ (s, C=N), 145.6 (s, C-OH), 139.7 (s, C-N), 136.6 (s, C-^{t}Bu), 132.4 (s, C-^{t}Bu), 114.3 (s, CH-Ar), 114.0 (s, N(CH)$_2$N), 113.8 (s, CH-Ar), 34.7 (s, *C*-(Me)$_3$, 34.3 (s, NCH$_3$), 33.9 (s, *C*-(Me)$_3$, 31.9 (s, C-(*Me*)$_3$), 29.8 (s, C-(*Me*)$_3$). Anal. Calcd for $C_{19}H_{29}N_3O$ (%): C, 72.34; H, 9.27; N, 13.32. Found (%): C, 72.73; H, 9.15; N, 12.99.

L1bH·HCl. This compound was prepared by the same method as **L1a**H·HCl, to give a tan solid (150 mg, 0.369 mmol, 97%). ^{1}H NMR (300 MHz, $CDCl_3$): δ 10.67 (s, 1H, NH) 7.15 (s, 1H, CH-Ar), 6.80 (s, 2H, N(CH)$_2$N), 6.58 (s,1H, CH-Ar) 3.51 (s, 6H, NCH$_3$), 1.41 (s, 9H, C(CH$_3$)$_3$), 1.24 (s, 9H, C(CH$_3$)$_3$). ^{13}C{^{1}H} NMR (75 MHz, $CDCl_3$) δ 147.4 (s, C=N), 143.9 (s, C-OH), 142.4 (s, C-N), 140.0 (s, C-^{t}Bu), 125.9 (s, C-^{t}Bu), 121.7 (s, CH-Ar), 118.5 (s, N(CH)$_2$N), 117.9 (s, CH-Ar), 35.5 (s, NCH$_3$), 34.3 (s, *C*-(Me)$_3$), 31.6 (s, C-(*Me*)$_3$), 29.8 (s, C-(*Me*)$_3$). Anal. Calcd for $C_{19}H_{30}ClN_3O$ (%): C, 64.85; H, 8.59; N, 11.94. Found (%): C, 64.70; H, 8.28; N, 11.75.

L2aH·HCl. A Schleck flask was charged with 2-aminophenol (300 mg, 1.99 mmol, 1.0 equiv.) and triethylamine (0.50 mL, 4.10 mmol, 2.0 equiv.) in 20 mL of MeCN. In a separated vial, compound **2Cl** (516 mg, 1.99 mmol, 1.0 equiv.) was dissolved in 10 mL of MeCN. The solution of **2Cl** was added and the mixture stirred under reflux for 6 h. Thereafter KOH (122 mg, 2.2 mmol, 1.1 equiv.) in 3 mL of H_2O was added and the solution stirred for 30 min. Volatiles were removed under vacuum. The product was extracted with THF (3 × 5 mL), then solvent was removed under vacuum to give a white solid (493,1.67 mmol, 84%). ^{1}H NMR (300 MHz, $CDCl_3$): δ 7.16–7.13 (m, 1H, Ar-CH), 7.03 (s, 2H, N(CH)$_2$N), 6.98–6.96 (m, 1H, Ar-CH), 6.77–6.72 (m, 1H, Ar-CH), 6.48–6.46 (m, 1H, Ar-CH), 4.71 (sept, *J* = 6.7 Hz, 2H, C*H*-Me$_2$), 1.40 (d, *J* = 6.7 Hz, 12H, CH-*Me*$_2$).^{13}C{^{1}H} NMR (75 MHz, $CDCl_3$) δ 149.0 (s, CH-Ar), 141.2 (s, C=N), 128.6 (s, C-OH), 125.4 (s, CH-Ar), 120.4 (s, CH-Ar), 119.9 (s, CH-Ar), 118.7 (s, C-N), 114.8 (s, N(CH)$_2$N), 50.1 (s, CH-^{i}Pr), 22.5 (s, CH-*Me*$_2$). Anal. Calcd for $C_{15}H_{22}ClN_3O$ (%): C, 60.91; H, 7.50; N, 14.21. Found (%): C, 61.29; H, 7.22, N, 14.13.

L2aH. A round-bottom flask was charged with **L2a**H·HCl (200 mg, 0.68 mmol, 1.0 equiv.) and 10 mL of MeCN, followed by the addition of KOH (40 mg, 0.70 mmol, 1.05 equiv.). The mixture was stirred for 30 min. Volatiles were removed under vacuum. The product was extracted with DCM (5 mL × 3) Solvent was removed under reduced pressure to yield a brown solid (150 mg, 0.57 mmol, 85%) ^{1}H NMR (300 MHz, CDCl3): δ 6.86 (m, 1H, Ar-CH), 6.67–6.59 (m, 3H, Ar-CH), 6.45 (s, 2H, N(CH)$_2$N), 4.44 (sept, *J* = 6.7 Hz, 2H, C*H*-Me$_2$), 1.23 (d, *J* = 6.7 Hz, 12H, CH-*Me*$_2$ 13C{1H} NMR (75.46 MHz, $CDCl_3$) δ 149.0 (s, C=N), 147.9 (s, C-OH), 138.8 (s, C-N), 119.4 (s, CH-Ar), 118.3 (s, CH-Ar), 116.0 (s, CH-Ar), 112.3 (s, CH-Ar), 110.0 (s, N(CH)2N), 46.3 (s, CH-^{i}Pr)., 22.0 (s, CH3-^{i}Pr). Anal. Calcd for $C_{15}H_{21}N_3O$ (%): C, 69.47; H, 8.16; N, 16.20. Found (%) C, 69.35; H, 8.10; N, 16.55.

L4aH·HCl. This compound was prepared by the same method as **L2a**H·HCl, to give a white solid (150 mg, 0.369 mmol, 97%). ^{1}H NMR (300 MHz, CDCl3): δ 9.86 (s, 1H, NH), 9.33 (s, 1H, OH), 7.23–7.21 (m,1H, CH-Ar) 6.99–6.97 (s, 1H, CH-Ar) 6.74–6.72 (s, 1H, CH-Ar), 3.30 (t, *J* = 6.0 Hz, 4H, NCH_2), 2.91 (s, 6H, NCH_3), 2.03 (q, *J* = 6.0 Hz, 4H, CH2).^{13}C{^{1}H} NMR (75 MHz, $CDCl_3$) δ 155.6 (s, C=N), 150.5 (s, C-OH), 126.9 (s, CH-Ar), 126.1 (s, C-N), 123.9 (s, CH-Ar), 120.4 (s, CH-Ar), 119.0 (s, CH-Ar) 48.6 (s, N-CH_3), 40.5 (N-CH_2), 22.4 ($CH_2CH_2CH_2$). Anal. Calcd for $C_{12}H_{18}ClN_3O$ (%): C, 56.36; H, 7.09; N, 16.43. Found (%) C, 56.61; H, 7.22; N, 16.58

L4aH This compound was prepared by the same method as **L2a**H**.** ^{1}H NMR (400 MHz, C_6D_6): δ 7.50 (s, 1H, OH), 7.28–7.27 (m,1H, CH-Ar) 6.99–6.97 (s, 3H, CH-Ar) 6.74–6.72 (s, 1H, CH-Ar), 2.44 (s, 6H, NCH_3), 2.41 (t, *J* = 6.0 Hz, 4H, NCH_2), 1.07 (q, *J* = 6.0 Hz, 4H, CH2). ^{13}C{^{1}H} NMR (100 MHz, $CDCl_3$) δ 155.7 (s, C=N), 150.5 (s, C-OH), 138.6 (s, C-N) 120.2 (s, CH-Ar), 119.4 (s, CH-Ar), 118.7 (s, CH-Ar), 113.1 (s, CH-Ar) 48.3 (s, N-CH_3), 39.0 (N-CH_2), 22.1 ($CH_2CH_2CH_2$) Anal. Calcd for $C_{12}H_{17}N_3O$ (%): C, 65.73; H, 7.81; N, 19.16. Found (%) C, 65.48; H, 7.63; N, 18.95.

Synthesis of complexes

Ti(**L1a**)$_2$(O^{i}Pr)$_2$ A solution of **L1a**H (105 mg, 0.517 mmol, 2.0 equiv.) in 5 mL of DCM was added to a solution of Ti(O^{i}Pr)$_4$ (73.8 mg, 0.261 mmol, 1.0 equiv.) in 5 mL of DCM. The reaction mixture was placed under reflux for 5 h. Thereafter, the solvent was removed under reduced pressure. The solid formed was washed with pentane to yield a yellow solid (125.9 mg, 0.220 mmol, 85 %). ^{1}H NMR (400 MHz, C_6D_6): δ 6.79–6.76 (m, 1H, Ar-CH), 6.63–6.61 (m, 2H, Ar-CH), 6.03–6.00 (m,

1H, Ar-CH), 5.49 (s, 2H, N(CH)$_2$N), 5.28 (sept, J = 6.0 Hz, 1H, OC*H*Me$_2$), 3.03 (s, 6H, NCH$_3$), 1.37 (d, J = 6.0 Hz, 6H, OCH*Me*$_2$). ^{13}C{^{1}H} NMR (100 MHz, C$_6$D$_6$) δ 160.7 (s, C=N), 153.2 (s, C-OH), 145.2 (s, C-N), 119.0 (s, CH-Ar), 116.7 (s, CH-Ar), 115.5 (s, N(CH)$_2$N), 113.9 (s, CH-Ar), 112.9 (s, CH-Ar), 75.6 (s, O*C*HMe$_3$), 34.3 (s, NCH$_3$), 26.5 (s, OCH-*Me*$_3$) δ Anal. Calcd for C$_{28}$H$_{38}$N$_6$O$_4$Ti (%): C, 58.95; H, 6.71; N, 14.73. Found (%) C, 59.30; H, 6.27; N, 15.22.

Ti(**L1b)**$_2$(O^{i}Pr)$_2$ A solution of **L1b**H (150 mg, 0.475 mmol, 2.0 equiv.) in 5 mL of toluene was added to a solution of Ti(O^{i}Pr)$_4$ (67.4 mg, 0.237 mmol, 1.0 equiv.) in 5 mL of toluene. The reaction mixture was placed under reflux for 5 h. Thereafter, the solvent was removed under reduced pressure. The solid formed was washed with pentane to yield a yellow solid (161 mg, 0.171 mmol, 86 %).^{1}H NMR (400 MHz, C$_6$D$_6$): δ 7.04 (d, J = 4.0 Hz , 1H, Ar-CH), 5.97 (d, J = 4.0 Hz, 1H, Ar-CH), 5.66–5.60 (s, 2H, N(CH)$_2$N), 5.46 (br, 1H, C*H*Me$_2$), 3.21 (s, 3H, NCH$_3$), 3.00 (s, 3H, NCH$_3$) 1.67 (s, 9H, C(CH$_3$)$_3$), 1.39 (s, 9H, C(CH$_3$)$_3$), 1.30 (d, J = 8.0 Hz, 6H, OCH*Me*$_2$). ^{13}C{^{1}H} NMR (100 MHz, C$_6$D$_6$) δ 157.2 (s, C=N), 153.8 (s, C-OH), 145.4 (s, C-N), 137.5 (s, *C*- C(CH$_3$)$_3$), 133.4 (s, *C*- C(CH$_3$)$_3$), 116.2 (s, N(CH)$_2$N), 113.0 (s, CH-Ar), 108.0 (s, CH-Ar), .6 (s, O*C*HMe$_3$), 35.3 (s, NCH$_3$), 34.3 (s, *C*(CH$_3$)$_3$), 32.4 (s, C(*C*H$_3$)$_3$), 30.2 (s, C(*C*H$_3$)$_3$), 28.1 (s, OCH-*Me*$_3$). Anal. Calcd for C$_{44}$H$_{70}$N$_6$O$_4$Ti (%): C, 66.48; H, 8.88; N, 10.57. Found (%) C, 66.61; H, 9.13; N, 10.85.

Ti(**L2a**)$_2$(O^{i}Pr)$_2$ This compound was prepared by the same method as Ti(**L1b**)$_2$(O^{i}Pr)$_2$ using **L2a**H to yield a yellow solid (133 mg, 0.19 mmol, 89%) .^{1}H NMR (300 MHz, C$_6$D$_6$) δ 7.00–6.96 (m,1H, Ar-CH), 6.82–6.79 (m, 1H, Ar-CH), 6.68–6.63 (m, 1H, Ar-CH), 6.07 (s, 1H, N(C*H*CH)N), 5.85–5.82 (m, 1H, Ar-CH) 5.25 (br, 2H, C*H*-Me$_2$), 4.97 (sept, 1H, J = 6.0 Hz, OC*H*-Me$_2$) 1.27 (d, J = 6.0 Hz, 6H, CH-*Me*$_2$), 1.09 (br, J = 6.0 Hz, 6H, OCH-*Me*$_2$), 0.95 (d, J = 6.0 Hz, 6H, CH-*Me*$_2$). ^{13}C{^{1}H} NMR (76 MHz, C$_6$D$_6$) δ 158.7 (s, C=N), 150.5 (s, C-O), 145.0 (s, C-N), 117.3 (s, CH-Ar) 112.9 (s, CH-Ar), 110.9 (s, CH-Ar), 110.3 (s, N(CH)2N) 108.5 (s, CH-Ar), 71.4 (s, O*C*H-Me$_2$), 45.9 (s, *C*H-Me$_2$), 25.0 (s, OCH-*Me*$_2$), 20.7 (s, CH-*Me*$_2$), 20.6 (s, CH$_3$- *Me*$_2$). Anal. Calcd for C$_{36}$H$_{54}$N$_6$O$_4$Ti (%): C, 63.33; H, 7.97; N, 12.31. Found (%) C, 63.56; H, 7.66; N, 12.60.

Ti(**L3a**)$_2$(O^{i}Pr)$_2$This compound was prepared by the same method as Ti(**L1b**)$_2$(O^{i}Pr)$_2$ using **L3a**H to yield a yellow solid (142 mg, 0.25 mmol, 95%) ^{1}H NMR (400 MHz, C$_6$D$_6$) 6.86–6.80 (m, 1H, Ar-CH), 6.57–6.54 (m, 1H, Ar-CH), 6.86–6.80 (m, 1H, Ar-CH), 5.32 (sept, 1H, J = 6.0 Hz, OC*H*-Me$_2$), 2.65 (s, 6H, N-CH$_3$), 2.54 (s, 4H, N-CH$_2$) 1.43 (d, J = 6.0 Hz, 6H, CH-*Me*$_2$). ^{13}C{^{1}H} NMR (100 MHz, C$_6$D$_6$) δ 162.1 (s, C=N), 161.3 (s, C-O), 145.2 (s, C-N), 119.7 (s, CH-Ar) 116.9 (s, CH-

Ar), 116.0 (s, CH-Ar), 113.6 (s, CH-Ar), 76.3 (s, O*C*H-Me$_2$), 48.4 (s, NCH$_3$), 40.4 (s, N-CH$_2$) 26.6 (s, OCH-*Me*$_2$) 22.3 (s, CH$_2$). Anal. Calcd for $C_{28}H_{42}N_6O_4Ti$ (%): C, 58.53; H, 7.37; N, 14.63. Found (%) C, 58.92; H, 7.23; N, 14.46.

Ti(**L4a**)$_2$(O^{i}Pr)$_2$ This compound was prepared by the same method as Ti(**L1b**)$_2$(O^{i}Pr)$_2$ using **L4a**H to yield a yellow solid (176 mg, 0.30 mmol, 88%). ^{1}H NMR (400 MHz, C_6D_6) δ 6.90–6.82 (m, 1H, Ar-CH), 6.80–6.72 (m, 2H, Ar-CH), 6.33–6.31 (m, 1H, Ar-CH), 5.37 (sept, 1H, *J* = 6.0 Hz, OC*H*-Me$_2$), 2.86 (s, 6H, N-CH$_3$), 2.59–2.52 (m, 2H, N-CH$_2$), 2.45–2.34 (m, 2H, N-CH$_2$), 1.48 (d, *J* = 6.0 Hz, 6H, CH-*Me*$_2$), 0.99–0.95 (m, 2H, CH$_2$). ^{13}C{^{1}H} (100 MHz, C_6D_6) δ 162.1 (s, C=N), 161.3 (s, C-O), 145.2 (s, C-N), 119.7 (s, CH-Ar) 116.9 (s, CH-Ar), 116.0 (s, CH-Ar), 113.6 (s, CH-Ar), 76.3 (s, O*C*H-Me$_2$), 48.4 (s, NCH$_3$), 40.4 (s, N-CH$_2$) 26.6 (s, OCH-*Me*$_2$), 22.3 (s, CH$_2$) Anal. Calcd for $C_{30}H_{46}N_6O_4Ti$ (%): C, 59.80; H, 7.69; N, 13.95. Found (%) C, 60.11; H, 7.44; N, 14.19.

Zr(**L1a**)$_2$(O^{i}Pr)$_2$ This compound was prepared by the same method as Ti(**L1a**)$_2$(O^{i}Pr)$_2$ using Zr(O^{i}Pr)$_4$·^{i}PrOH and **L1a**H to yield a green solid (144 mg, 0.24 mmol, 96%). ^{1}H NMR (400 MHz, C_6D_6): δ 6.80–6.77 (m, 1H, Ar-CH), 6.72–6.70 (m, 1H, Ar-CH), 6.60–6.56 (m, 1H, Ar-CH), 5.98–5.96 (m, 1H, Ar-CH), 5.51 (s, 2H, N(CH)$_2$N), 4.62 (sept, *J* = 8.0 Hz, 1H, OC*H*Me$_2$), 2.99 (s, 6H, NCH$_3$), 1.37 (d, *J* = 8.0 Hz, 6H, OCH*Me*$_2$). ^{13}C{^{1}H} NMR (100 MHz, C_6D_6) δ 159.6 (s, C=N), 153.14.88 (s, CH-Ar) 116.2 (s, CH-Ar), 115.6 (s, CH-Ar), 115.1 (s, N(CH)2N) 114.2 (s, CH-Ar), 70.3 (s, O*C*H-Me$_2$), 34.1 (s, NCH$_3$), 27.0 (s, OCH-*Me*$_2$). Anal. Calcd for $C_{28}H_{38}N_6O_4Zr$ (%): C, 54.78; H, 6.24; N, 13.69. Found (%) C, 55.14; H, 6.40; N, 13.92.

Zr(**L1b**)$_2$(O^{i}Pr)$_2$ This compound was prepared by the same method as Ti(**L1b**)$_2$(O^{i}Pr)$_2$ using Zr(O^{i}Pr)$_4$·^{i}PrOH and **L1b**H to yield a yellow solid (165 mg, 0.197 mmol, 92%). ^{1}H NMR (400 MHz, C_6D_6): δ 7.04 (d, *J* = 4.0 Hz , 1H, Ar-CH), 5.97 (d, *J* = 4.0 Hz, 1H, Ar-CH), 5.58 (s, 2H, N(CH)$_2$N), 4.68 (sept, *J* = 8.0 Hz 1H, C*H*Me$_2$), 3.06 (s, 6H, NCH$_3$), 1.70 (s, 9H, C(CH$_3$)$_3$), 1.41 (d, *J* = 8.0 Hz, 6H, OCH*Me*$_2$), 1.37 (s, 9H, C(CH$_3$)$_3$). ^{13}C{^{1}H} NMR (100 MHz, C_6D_6) δ 156.0 (s, C=N), 153.8 (s, C-OH), 145.0 (s, C-N), 136.8 (s, *C*- C(CH$_3$)$_3$), 133.4 (s, *C*- C(CH$_3$)$_3$), 116.0 (s, N(CH)$_2$N), 113.0 (s, CH-Ar), 108.0 (s, CH-Ar), 69.6 (s, O*C*HMe$_3$), 35.3 (s, NCH$_3$), 34.3 (s, *C*(CH$_3$)$_3$), 32.4 (s, C(*C*H$_3$)$_3$), 30.2 (s, C(*C*H$_3$)$_3$), 28.1 (s, OCH-*Me*$_3$). Anal. Calcd for $C_{44}H_{70}N_6O_4Zr$ (%): C, 63.04; H, 8.42; N, 10.03. Found (%) C, 63.22; H, 8.13; N, 9.88.

Zr(**L2a**)$_2$(O^{i}Pr)$_2$ This compound was prepared by the same method as **Ti2a** using Zr(O^{i}Pr)$_4$·^{i}PrOH and **L2a**H to yield a green solid (178 mg, 0.25, 89%). ^{1}H NMR (300 MHz, C_6D_6) δ 7.00–6.96

(m,1H, Ar-CH), 6.82–6.79 (m, 1H, Ar-CH), 6.68–6.63 (m, 1H, Ar-CH), 6.07 (s, 1H, N(C*H*CH)N), 5.85–5.82 (m, 1H, Ar-CH) 5.25 (br, 2H, C*H*-Me$_2$), 4.97 (sept, 1H, *J* = 6.0 Hz, OC*H*-Me$_2$) 1.27 (d, *J* = 6.0 Hz, 6H, CH-*Me$_2$*), 1.09 (br, *J* = 6.0 Hz, 6H, OCH-*Me$_2$*), 0.95 (d, *J* = 6.0 Hz, 6H, CH-*Me$_2$*). ^{13}C{^{1}H} NMR (76 MHz, C_6D_6) δ 159.8 (s, C=N), 152.2 (s, C-O), 146.7 (s, C-N), 119.3 (s, CH-Ar) 115.1 (s, CH-Ar), 114.7 (s, CH-Ar), 112.2 (s, N(CH)2N) 111.3 (s, CH-Ar), 69.3 (s, O*C*H-Me$_2$), 47.9 (s, *C*H-Me$_2$), 27.9 (s, OCH-*Me*$_2$), 23.0 (s, CH-*Me$_2$*), 22.3 (s, CH$_3$-^{i}Pr) Anal. Calcd for $C_{36}H_{54}N_6O_4Zr$ (%): C, 59.55; H, 7.50; N, 11.57. Found (%) C, 59.26; H, 7.45; N, 11.88

Zr(**L3a**)$_2$(O^{i}Pr)$_2$ This compound was prepared by the same method as **Ti2a** using Zr(O^{i}Pr)$_4$·^{i}PrOH and **L3a**H to yield a green solid (140 mg, 0.23 mmol, 93%). ^{1}H NMR (400 MHz, C_6D_6) δ 6.83–6.80 (m, 1H, Ar-CH), 6.70–6.67 (m, 1H, Ar-CH), 6.54–6.51 (m, 1H, Ar-CH), 4.68 (sept, 1H, *J* = 8.0 Hz, OC*H*-Me$_2$), 2.62 (s, 6H, N-CH$_3$), 2.49 (s, 4H, N-CH$_2$) 1.46 (d, *J* = 8.0 Hz, 6H, CH-*Me$_2$*). ^{13}C{^{1}H} NMR (100 MHz, C_6D_6) δ 165.9 (s, C=N), 160.2 (s, C-O), 142.7 (s, C-N), 121.3 (s, CH-Ar) 118.4 (s, CH-Ar), 116.3 (s, CH-Ar), 115.8 (s, CH-Ar), 71.0 (s, O*C*H-Me$_2$), 47.8 (s, NCH$_3$), 35.6 (s, N-CH$_2$) 27.7 (s, OCH-*Me*$_2$). Anal. Calcd for $C_{28}H_{42}N_6O_4Zr$ (%): C, 54.43; H, 6.85; N, 13.60. Found (%) C,54.78; H, 6.95; N, 13.76.

Zr(**L4a**)$_2$(O^{i}Pr)$_2$ This compound was prepared by the same method as Ti(**L2a**)$_2$(O^{i}Pr)$_2$ using Zr(O^{i}Pr)$_4$·^{i}PrOH and **L4a**H to yield a green solid (173 mg 0.28 mmol , 93%) ^{1}H NMR (400 MHz, C_6D_6) δ 6.90–6.88 (m, 1H, Ar-CH), 6.73–6.70 (m, 1H, Ar-CH), 6.30–6.28 (m, 1H, Ar-CH), 4.72 (sept, 1H, *J* = 8.0 Hz, OC*H*-Me$_2$), 2.83 (s, 6H, N-CH$_3$), 2.62–2.54 (m, 2H, N-CH$_2$), 2.42–2.35 (m, 2H, N-CH$_2$), 1.51 (d, *J* = 8.0 Hz, 6H, CH-*Me$_2$*), 1.13–1.07 (m, 1H, CH$_2$), 1.03–0.98 (m, 1H, CH$_2$). ^{13}C{^{1}H} (100 MHz, C_6D_6) δ 162.5 (s, C=N), 160.1 (s, C-O), 144.1 (s, C-N), 120.2 (s, CH-Ar) 116.3 (s, CH-Ar), 116.2 (s, CH-Ar), 115.8 (s, CH-Ar), 70.6 (s, O*C*H-Me$_2$), 48.3 (s, NCH$_3$), 40.1 (s, N-CH$_2$) 27.9 (s, OCH-*Me*$_2$), 22.2 (s, CH$_2$). Anal. Calcd for $C_{30}H_{46}N_6O_4Zr$ (%): C, 55.78; H, 7.18; N, 13.01. Found (%) EA C, 55.55; H, 7.03; N, 12.76.

Ti(**L1a**)$_2$Cl$_2$ A solution of **L1a**H·HCl (150 mg, 0.62 mmol, 2.0 equiv.) in 5 mL of DCM was added to a solution of Ti(O^{i}Pr)$_4$ (88.8 mg, 0.31 mmol, 1.0 equiv.) in 5 mL of DCM. After 6 h the solvent was removed under reduced pressure. The solid was washed with pentane, solvent was removed under vacuum to yield a red solid (154 mg, 0.29 mmol, 95%). ^{1}H NMR (400 MHz, $CDCl_3$): δ 6.89 (s, 2H, N(CH)$_2$N), 6.69–6.65 (m, 1H, Ar-CH), 6.58–6.55 (m, 1H, Ar- CH), 6.45–6.44 (m, 1H, Ar-CH), 5.69–5.67 (m, 1H, Ar-CH), 3.88 (s, 3H, NCH$_3$), 3.72 (s, 3H, NCH$_3$). ^{13}C{^{1}H} NMR (100

MHz, $CDCl_3$) δ 157.5 (s, C=N), 152.7 (s, C-OH), 144.4 (s, C-N), 120.3 (s, CH-Ar), 120.0(s, CH-Ar), 118.1 (s, N(CH)2N), 112.0 (s, CH-Ar), 109.2 (s, CH-Ar), 34.9 (s, NCH3), 34.7 (s, NCH3). Anal. Calcd for $C_{22}H_{24}Cl_2N_6O_2Ti$ (%): C, 50.50; H, 4.62; N, 16.06. Found (%) C, 50.95; H, 5.01; N, 15.63.

Ti(**L1b**)$_2$Cl$_2$ This compound was prepared by the same method as Ti(**L1a**)$_2$Cl$_2$ using **L1b**H·HCl to yield a red solid (92.2 mg, 0.12 mmol, 92%). ^{1}H NMR (300 MHz, C_6D_6) δ 6.90 (d, *J* = 3.0 Hz 1H, N(C*H*CH)N), 6.87 (d, *J* = 3.0 Hz 1H, N(C*H*CH)N) 6.70 (d, *J* = 3.0 Hz,1H, CH-Ar), 5.47 (d, *J* = 3.0 Hz,1H, CH-Ar), 3.80 (s, 1H, NCH3), 3.75 3.80 (s, 1H, NCH3), 1.36 (s, 9, C(CH$_3$)$_3$), 1.20 (s, 9, C(CH$_3$)). ^{13}C{^{1}H} (76 MHz, $CDCl_3$) δ 153.9 (s, C=N), 153.4 (s, C-OH), 145.1 (s, C-N), 141.9 (s, CH-Ar), 131.6 (s, CH-Ar), 117.9 (s, N(CH)$_2$N), 117.6 (s, N(CH)$_2$N), 114.0 (s, CH-Ar), 104.9 (s, CH-Ar), 35.1 (s, NCH$_3$), 34.7 (s, NCH$_3$), 34.6 (s, *C*(CH$_3$)$_3$), 34.3 (s, *C*(CH$_3$)$_3$), 32.0 (s, C(*C*H$_3$)$_3$), 30.0 (s, C(*C*H$_3$)$_3$). Anal. Calcd for $C_{38}H_{56}Cl_2N_6O_2Ti$ (%): C, 61.05; H, 7.55; N, 11.24. Found (%) C, 61.33; H, 7.40; N, 11.49.

Ti(**L2a**)$_2$Cl$_2$ This compound was prepared by the same method as Ti(**L1a**)$_2$Cl$_2$ using **L2a**H·HCl to yield a red solid (92.4 mg, 0.107 mmol, 90%).^{1}H NMR (400 MHz, $CDCl_3$): δ 7.00 (s, 2H, N(CH)$_2$N), 6.65–6.61 (m, 1H, CH-Ar), 6.53–6.49 (m, 1H, CH-Ar), 6.41–6.39 (m, 1H, CH-Ar), 5.63–5.61 (m, 1H, CH-Ar), 5.32 (sept, *J* = 6.0 Hz, 1H, C*H*-Me$_2$), 4.96 (sept, *J* = 6.0 Hz, 1H, C*H*-Me$_2$),1.63 (d, *J* = 6.0 Hz, 3H, CH-*Me*2), 1.51 (d, *J* = 6.0 Hz, 1H, CH-*Me*$_2$), 1.36 (d, *J* = 6.0 Hz, 1H, CH-*Me*$_2$), 1.31 (d, *J* = 6.0 Hz, 1H, CH-*Me*2). ^{13}C{^{1}H} (100 MHz, $CDCl_3$) δ 157.8 (s, C=N), 150.2 (s, C-OH), 146.0 (s, C-N), 119.9 (s, CH-Ar), 119.6 (s, CH-Ar), 114.1 (s, N(CH)$_2$N), 114.0 (s, N(CH)$_2$N), 111.7 (s, CH-Ar), 109.0 (s, CH-Ar), 49.0 (s, *C*H-Me$_2$), 48.7 (s, *C*H-Me$_2$), 24.2 (s, CH-*Me*$_2$), 23.3 (s, CH-*Me*$_2$), 23.2 (s, CH-*Me*$_2$), 23.2 (s, CH-*Me*$_2$), 22.2 (s, CH-*Me*$_2$). Anal. Calcd for $C_{30}H_{40}Cl_2N_6O_2Ti$ (%): C, 56.70; H, 6.35; N, 13.23. Found (%) C, 56.85; H, 6.62; N, 13.44.

General Procedure for the Polymerization of *rac*-lactide

Unless otherwise specified, all polymerizations (group 4 guanidine–phenolate catalysts, group 4 precursors, free-ligand, and Sn(Oct)$_2$) were performed using *rac*-lactide (99%). In a typical experiment, a flask was charged with 60 μmol of catalyst and 6.0 mmol of *rac*-lactide under inert conditions. The mixture was submerged in an oil bath at 130 °C and stirred until full conversion was achieved (as confirmed by ^{1}H NMR). The polymerization was cooled down to room

temperature and terminated by the addition of 10 mL of wet $CHCl_3$. Volatiles were removed under vacuum at 50 °C for several hours. The remaining material was analyzed without further purification. Kinetic studies of solvent-free polymerization were performed under the same conditions with a [Monomer]:[Cat] ratio of 100:1. Aliquots were removed from the reaction mixture at different times to monitor the monomer conversion by ^1H NMR spectroscopy. Molecular weight averages were determined by GPC, and by end-chain analysis (M_n) and by diffusion ordered ^1H NMR spectroscopy (DOSY; M_w).

General Procedure for the Polymerization of ethylene

All polymerization experiments were performed under 1 atm of ethylene and at 25 °C in a 100-mL Schlenk flask charged with a stir bar. A Schlenk flask was charged with 40 mL of toluene and degassed by two freeze-pump-thaw cycles. The solution was saturated with ethylene for 10 min under vigorous stirring, then treated with 4 mL (220 equiv.) of methylaluminoxane solution 7 wt% in toluene (MMAO-12). The solution was left stirring for another 15 min, at which point the polymerization was initiated by the addition of a 2 mL solution of the precatalyst (40 mmol) in DCM to the flask. The reaction was quenched by the addition of 10 mL of a 1:1 solution of MeOH and concentrated HCl. The polymer was collected by filtration, washed with water and MeOH, and dried for several hours at 60 °C under vacuum.

Chapter 3 Zinc complexes of guanidine– and amidine–phenolate ligands for the ring-opening polymerization of lactide

3.1 Introduction

As outlined in Chapter 2, metal-based catalysts bearing guanidines have emerged as excellent candidates in the polymerization of cyclic esters. This includes the nontoxic and biocompatible metal Zn. Numerous zinc complexes have incorporated nitrogen-donor ligands, including β-diiminate,[46,92] imine–phenolate,[48,49,93–97] amine–phenolate,[47,98,99] and amidine–phenolate[100,101] systems, which exhibited good catalytic activity in the ROP of cyclic esters. Nevertheless, the effectiveness of these initiators in producing PLA under industrial conditions, characterized by high temperatures while utilizing non-purified monomer, remains limited.

This chapter describes the synthesis and characterization of Zn complexes bearing the guanidine scaffold, which exhibited the best performance in the group 4 bis(alkoxide) catalysts. The steric effect and electronics in the phenolic oxygen were also studied by using different aminophenol building blocks. Finally, two additional N-donor fragments were investigated: an acylated guanidine and an unexplored CAAC-based amidine. These experiments allow a better understanding of the criteria to enhance the performance of Zn-based catalysts for the ROP of lactide or other cyclic esters.

3.2 Results and Discussion

3.2.1 Synthesis of guanidine– and amidine phenol proligands

Guanidine– and amidine– phenols (**L*x*H**) were synthesized through the reaction of ***x***Cl with an aminophenol as illustrated in Scheme *3.1*. The ^{1}H NMR spectra of **L2**[**a–d**]H exhibited magnetically-equivalent isopropyl substituents. This result suggests significant single bond character for the formal C=N_{exo} double bond, which can be ascribed to π-electron delocalization over the guanidine functional group. In contrast, the ^{1}H NMR spectrum of the reaction product of 2-aminophenol with the diacylated **5Cl** salt presented inequivalent isopropyl groups, indicating greater C=N_{exo} double bond character due to electron-withdrawing acyl groups.[54] Interestingly, the ^{1}H-^{13}C HMBC spectrum of this product indicates that both the phenolic and the isopropyl methine

protons correlate to one quaternary carbon, suggesting the formation of the spiro compound **L5a'**H. The addition of a bulky group, *ortho* to the phenol, to increase the steric repulsion and mitigate the cyclization was explored with **L5b**H. Unfortunately, the addition of a bulky group did not have an impact on preventing the cyclization, and a similar behavior to **L5a'**H was observed. This was corroborated by the solid-state structure obtained for **L5a'**H (vide infra). The ^{1}H NMR spectrum of the amidine–phenol ligand **L6a**H supports the proposed structure, showing two different sets of isopropyl groups. This was attributed to the restricted rotation about the N–2,6-diisopropylphenyl (N–Dipp) bond, which is caused by the adjacent methyl groups.

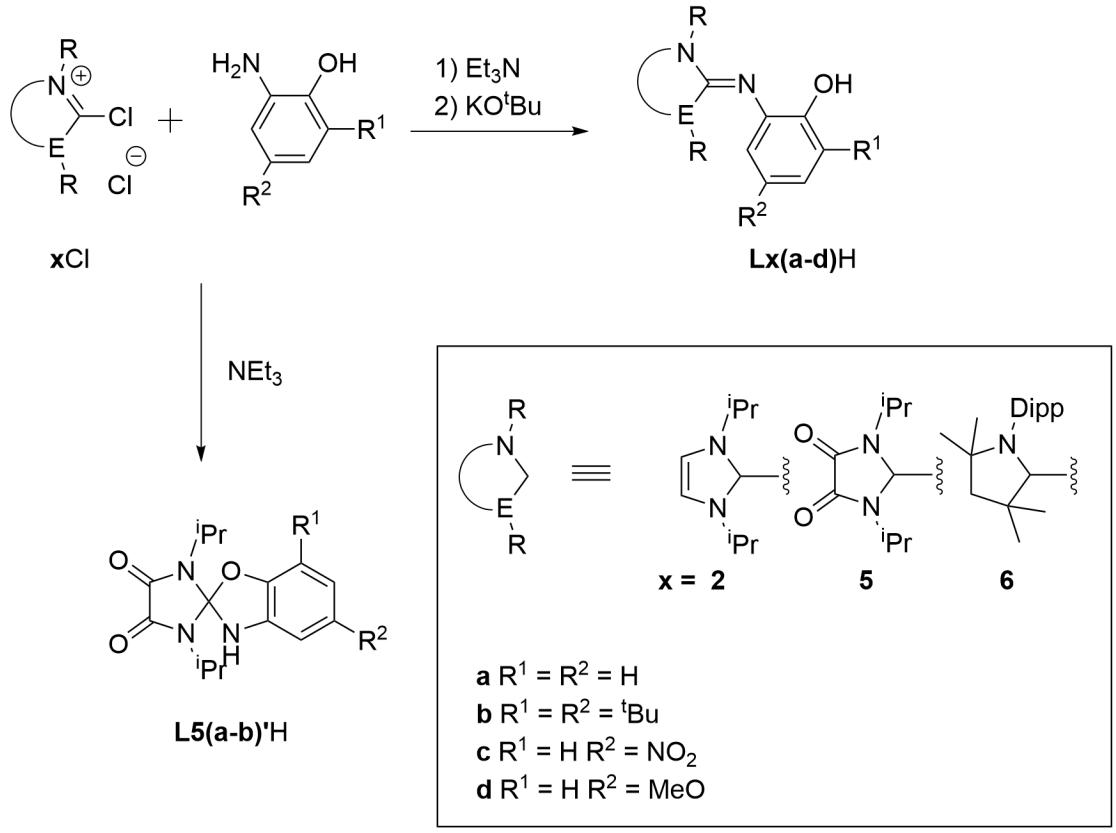

Scheme 3.1 Synthesis of guanidine– and amidine– phenol ligands.

Suitable crystals for X-ray diffraction analysis were obtained from **L5a'**H, **L5b'**H, and **L6a**H by slow evaporation of solutions in THF for the acylated guanidine compounds and hexane for the amidine–phenol ligand (Table *3.1*). The solid-state structure confirmed the formation of the spiro compounds **L5a'**H and **L5b'**H, facilitated by the increased electrophilicity of the guanidine functional group (Figure *3.1*), which aligns with the previously discussed NMR spectra. The N2–C1 and N3–C1 bonds in **L5a'**H and **L5b'**H are longer (~1.449(5) and ~1.454 (3) Å, respectively)

than that of the N1–C1 bond (1.428(5) Å and 1422(3)). This indicates significant delocalization of electron density towards the acyl groups. Additionally, the shorter N2–C2 and N3–C3 bond lengths compared to nonacylated derivatives (~1.345(5) vs (~1.390(5) Å) and longer C2–O2 and C3–O3 bond lengths (~1.225(5) Å) than N-acyl amides (~1.218(1) Å) supports this observation.[102] The bond lengths O1–C1 in **L5a'**H and **L5b'**H are statistically equivalent, indicating that the ^{t}Bu group does not have an impact on weakening the aforementioned bond.

The N1–C1 formal double bond in **L6a**H (1.287(2) Å) is shorter than both the N2–C1 bond (1.362(2) Å) and the corresponding N=C double bond observed in guanidines bearing alkyl groups on the endocyclic nitrogen, indicative of less π-electron delocalization in the amidine and a lower partial negative charge on its exocyclic nitrogen.[50] The N2–C1 (1.362(2) Å) formal single bond in **L6a**H is expectedly slightly longer than the N2–C2 (1.341(5) Å) and N3–C3 (1.349(5) Å) bonds in **L5a'**H and N2–C2 (1.334(4) Å) and N3–C3 (1.350(4) Å in **L5b'**H, due to electron delocalization towards the acyl group. N1A and H1 distance of 2.290 Å in **L6a**H indicates a strong intramolecular H-bond. The planes formed by the phenol and Dipp rings are approximately orthogonal (82.05° and 85.45°, respectively) to the amidine functional group, similar to that reported in other non-cyclic amidine–phenol ligands.[100,101]

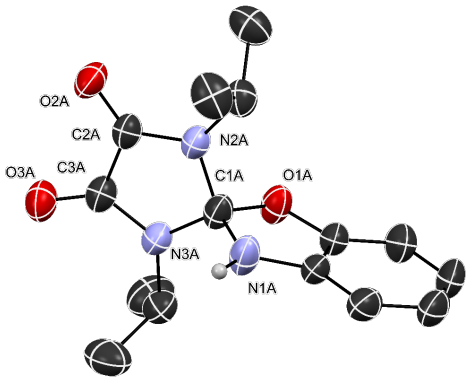

L5a′H

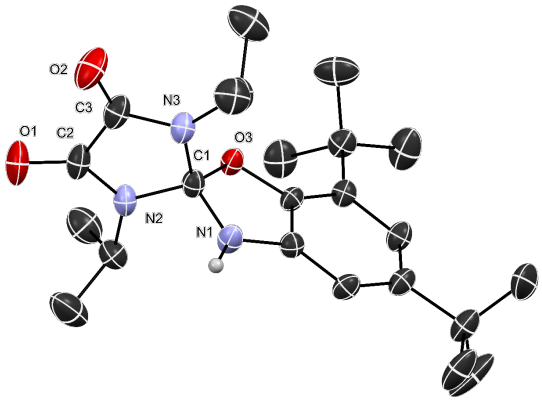

L5b′H

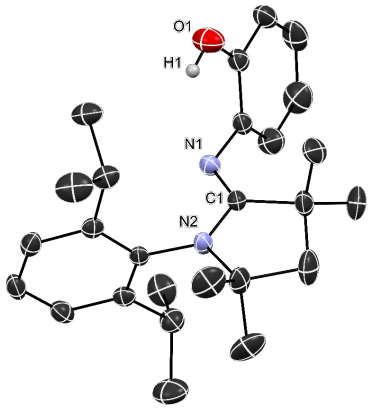

L6aH

Figure 3.1 Solid-state structures of **L5a'**H (top, left), **L5b'**H (top, right), and **L6a**H (bottom). For clarity, only the NH (**L5a'**H and **L5b'**H) and OH (**L6a**H) protons, located in the Fourier map, are included. Solvent molecules have been omitted for clarity. ORTEP drawn at 50% probability. Only one of the independent molecules in the unit cell is drawn for **L5a'**H

Table 3.1 Selected bond distances and angles for ligands of **L5′a**H, **L5′b**H, and **L6a**H

L5′aH[a]		**L5′b**H[a]	**L6a**H	
Bond lengths (Å)				
N1–C1	1.428(5)	1.422(3)	N1–C1	1.287(2)
N2–C1	1.453(5)	1.456(3)	N2–C1	1.362(2)
N3–C1	1.444(5)	1.453(3)		
N2–C2	1.341(5)	1.334(4)		
N3–C3	1.349(5)	1.350(4)		
O2–C2	1.226(5)	1.210(4)		
O3–C3	1.223(5)	1.221(4)		
O1–C1	1.435(4)	1.439(3)		
Bond angles (°)				
N1–C1–N2	114.7(3)	114.0(2)	N1–C1–N2	120.3(2)
N1–C1–N3	115.1(3)	114.8(2)	N1–C1–C4	131.2(2)
N2–C1–N3	103.2(3)	103.0(3)	N2–C1–C4	108.6(1)
O1–C1–N3	110.0(3)	110.9(2)		
O1–C1–N2	109.3(3)	109.6(2)		
O1–C1–N1	104.6(3)	104.6(2)		

[a]Averaged bond lengths and angles of independent molecules in the unit cell.

3.2.2 Synthesis of Zn complexes

Zn[**L2a–d**]$_2$ complexes were synthesized in excellent yields (>88%) through the addition of two equivalents of **L*x***H to $ZnEt_2$. Complex Zn[**L5a**]$_2$ was prepared by reacting the potassium salt of the spiro compound **L5a'**H with $ZnCl_2$ at 66 °C in THF (Scheme *3.2*). Coordination of two ligands to the metal results in restricted rotation about the formal C=N_{exo} double bond, leading to inequivalent resonances in the ^{1}H NMR spectra for the isopropyl groups in **L2a** and **L5a**. The preparation and isolation of the amidine–phenolate Zn[**L6a**]$_2$ complex was not possible. However, the heteroleptic Zn[**L6a**]Et was successfully prepared in good yield by reacting one equivalent of **L6a**H with $ZnEt_2$. The related Zn[**L2a**]Et and Zn[**L2b**]Et were similarly prepared. All three ethyl complexes displayed broad resonances in the ^{1}H NMR spectra, which is likely attributable to a

dynamic equilibrium between monomeric and dimeric structures, as reported in other alkyl zinc complexes.[103]

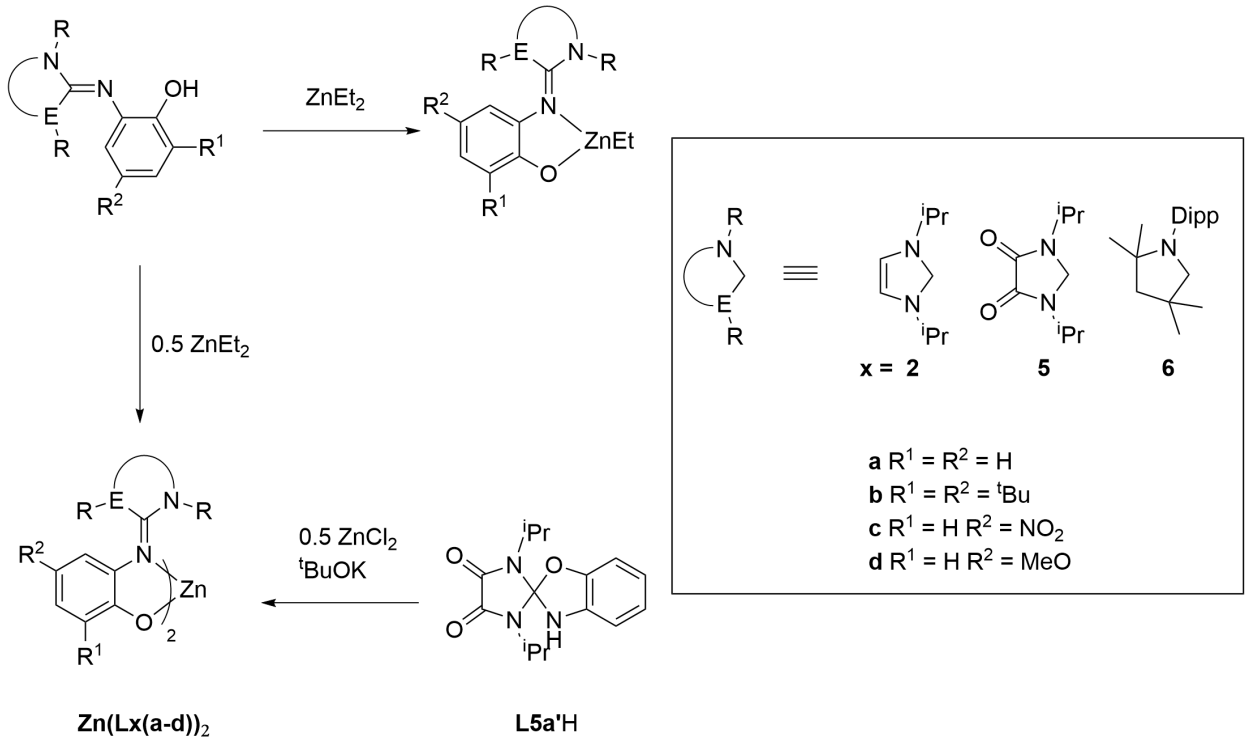

Scheme 3.2 Synthesis of guanidine– and amidine– phenolate Zn complexes

The structure of Zn[**L2a**]$_2$ was determined by single-crystal X-ray diffraction analysis (Figure *3.2* and Table *3.2*). The guanidine–phenolate ligands chelate to the metal with an average bite angle of 85.70° and a τ_4 value of 0.78, indicating a distorted tetrahedral geometry.[104] Notably, the Zn–N and Zn–O bond lengths are comparable, despite nitrogen being formally neutral and oxygen negatively charged, evidence of the excellent σ-donating properties of the guanidine fragment. Similar Zn–N bond lengths are reported in Zn complexes with a neutral bidentate guanidine donor.[54,105] Furthermore, a structural parameter (ρ) value of 0.98 indicates extensive electron delocalization over the guanidine moiety. This is further reflected by an angle of 60.0° between the best planes formed by the imidazole and phenol rings, a result facilitated by the significant single bond character of the C=N_{exo} bond.

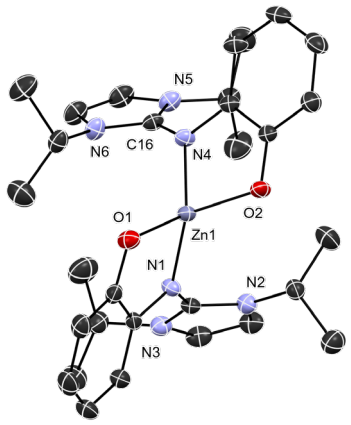

Figure 3.2 Solid-state structure of Zn[**L2a**]$_2$. Hydrogen atoms have been omitted for clarity. ORTEP drawn at 50% probability.

Table 3.2 Selected bond lengths and angles for complex Zn[**L2a**]$_2$

Selected bond lengths (Å)			
Zn1–N1	2.002(11)	Zn1–N4	1.949(11)
Zn1–O1	1.938(10)	Zn1–O2	1.943(10)
N1–C1	1.336(17)	N4–C16	1.337(17)
N2–C1	1.360(18)	N5–C16	1.359(17)
N3–C1	1.394(18)	N6–C16	1.358(17)
Selected bond angles (°)			
N1–Zn–O1	85.73(4)	N4–Zn–O2	85.67(4)
N1–Zn–O2	125.59(5)	N4–Zn–O1	124.19(5)
O1–Zn–O2	117.40(5)	N1–Zn–N4	122.82(5)
N1–Zn–O1	85.73(4)	N4–Zn–O2	85.67(4)

A solution in THF of an attempted synthesis of Zn[**L5a**]$_2$ gave crystals suitable for X-ray analysis. The structures obtained were inconsistent with the expected product (Figure 3.3). Subsequent analysis of the ^{1}H NMR spectrum showed two species containing an isopropyl fragment, consistent with the structures observed in the solid state (Figure S71). This showed evidence of the acylated moiety being susceptible to hydrolysis, leading to an N-isopropyl oxamate (NIPOx) and 2-methylamino-benzoxazole (BONHMe) species (Figure *3.4*).

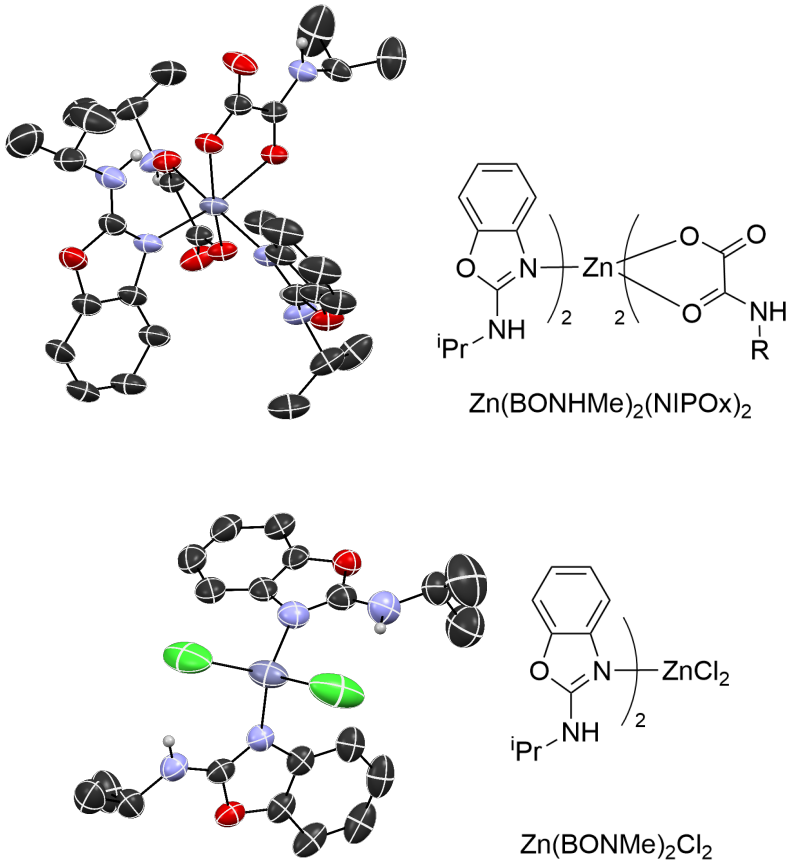

Figure 3.3. Solid-state structures of Zn complexes bearing the hydrolyzed ligand **L5a'**. For clarity, only the NH protons, located using riding model, are included. ORTEP drawn at 50% probability (left). ChemDraw representations of Zn complexes bearing the hydrolyzed ligand **L5a'** (right).

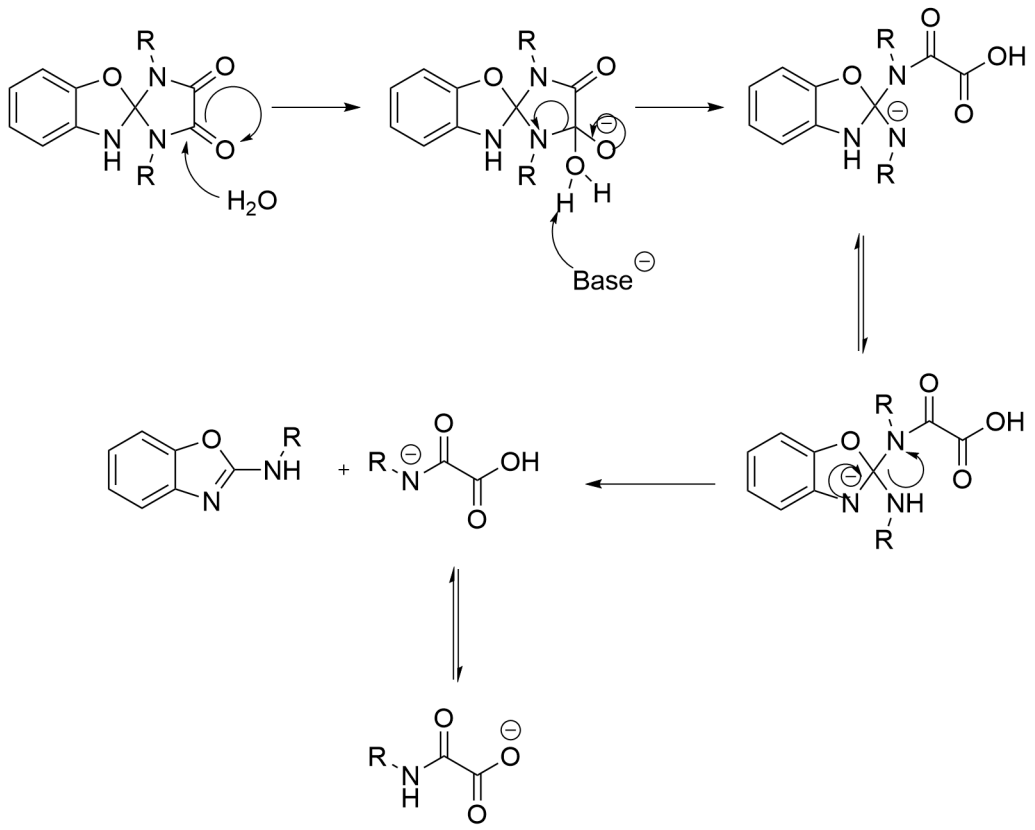

Figure 3.4 Proposed mechanism for the hydrolysis of **L5a'**H

3.2.3 Ring-opening polymerization of rac-lactide

All zinc complexes were evaluated for their ability to polymerize *rac*-lactide under solvent-free conditions at 130 °C using a monomer-to-catalyst stoichiometric ratio of 100:1 with or without benzyl alcohol (BnOH) as co-initiator. The rate constants (k_{app}) for the Zn catalysts were measured by monitoring the monomer consumption over time by ^{1}H NMR spectroscopy and ranged from 0.71–4.37 × 10^{-4} s^{-1} (Figure *3.5*), with Zn[**L2a**]$_2$ being the most active and approximately a third as active as Sn(Oct)$_2$ (12.4–15.1 × 10^{-4} s^{-1}). The addition of BnOH to Zn[**L2a**]$_2$ did not have an impact on the activity of the catalyst. The zero-order dependence on the co-initiator suggests coordination of the monomer to the metal center as the rate-determining step and no influence of the dormant alcohol in the propagation step.

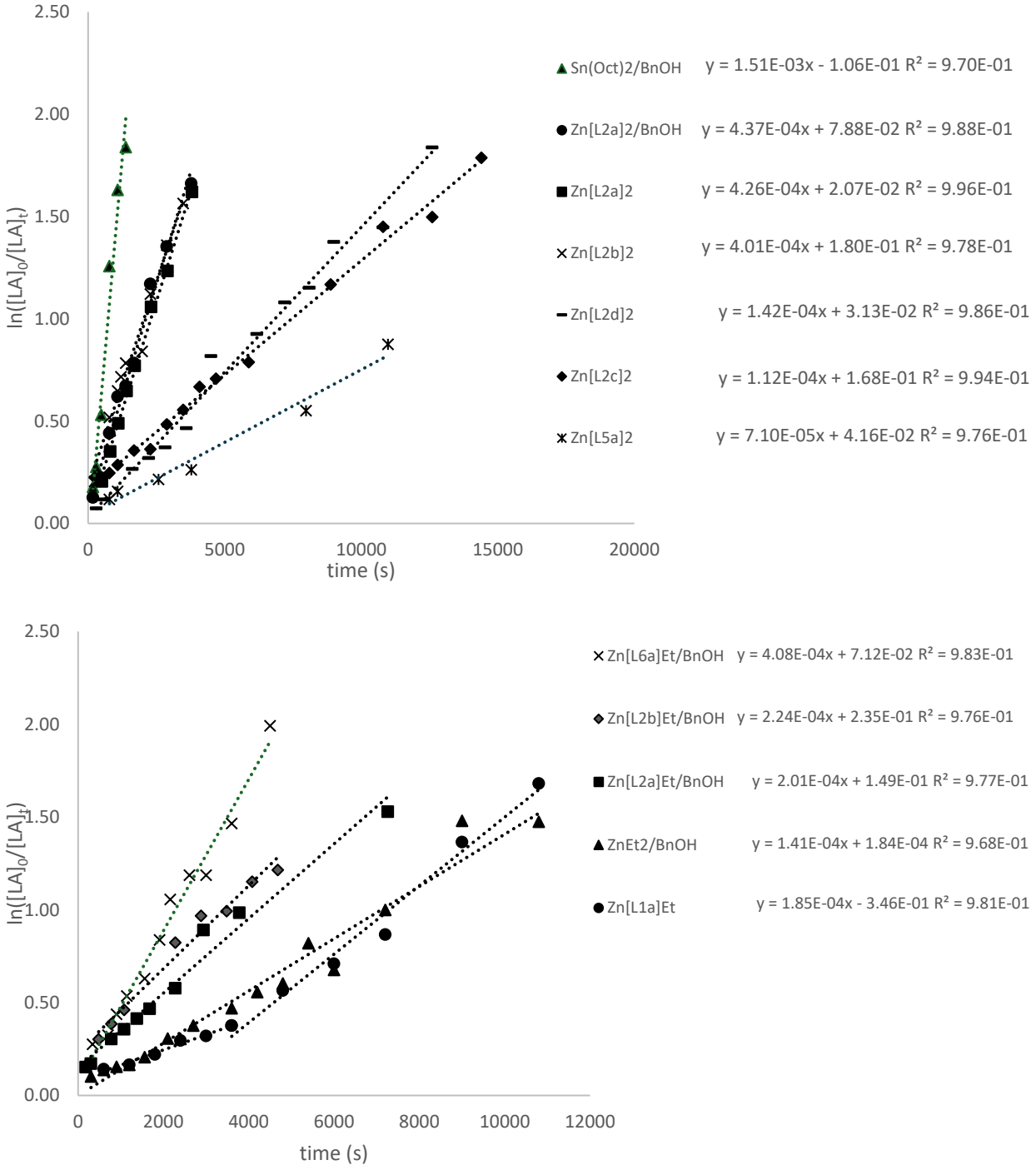

Figure 3.5 Kinetic plots for the polymerization of *rac*-lactide by Sn(Oct)2, Zn[**Lx**]$_2$ (top) and ZnEt$_2$, Zn[**Lx**]Et (bottom)

The activity of Zn[**L2b**]$_2$, containing a bulkier *tert*-butyl group, is comparable to that of the parent complex Zn[**L2a**]$_2$. Surprisingly, installing either an electron-withdrawing nitro group or an electron-donating methoxy group on the phenoxide ring, as in **L2c**H and **L2d**H, respectively,

results in a significant reduction in the polymerization activity, with an approximately 75% decrease in polymerization activity relative to that observed with Zn[**L2a**]$_2$. The zinc complex of the diacylated guanidine ligand (Zn[**L2**]$_2$) showed the lowest activity among all catalysts tested. This outcome highlights the significance of tuning the electronics of the ligand through a thoughtful modular design. While an electron-poor ligand has the potential to enhance the Lewis acidity of the metal and thus increase its activity, it might also increase the catalyst´s vulnerability to poisoning by polar impurities and possibly even dissociation of the ligand itself. Conversely, an electron-rich ligand might help mitigate the risk of poisoning and ligand dissociation, albeit at the expense of less effective monomer activation.

The heteroleptic Zn[**L6a**]Et complex catalyzed the ring-opening polymerization of lactide in the presence of benzyl alcohol at a rate constant of 4.08×10^{-4} s^{-1}, which is twice as fast as the one displayed for the complex Zn[**L2a**]Et (2.01×10^{-4} s^{-1}). Similarly to the homoleptic complexes, the *tert*-butyl derivative Zn[**L2b**]Et showed a comparable activity to that observed in Zn[**L2a**]Et. An experiment in the absence of benzyl alcohol was performed with Zn[**L2a**]Et, where an induction period of about 1 h was observed, followed by a polymerization rate constant of (1.85×10^{-4} s^{-1}), indicative of benzyl alcohol having a beneficial impact in the initiation step. The homoleptic complexes Zn[**L2a**]$_2$ and Zn[**L2b**]$_2$ demonstrated an activity that is double that of the corresponding ethyl complexes. Consequently, Zn[**L6a**]$_2$ could in theory be the most active catalyst, with an estimated rate of 8×10^{-4} s^{-1}, if successfully prepared and isolated. This offers future opportunities to enhance the performance of these zinc catalysts.

The observed 50% decrease in activity of Zn[**L2a**]Et compared to Zn[**L2a**]$_2$ is possibly due to the disproportionation of in situ generated Zn[**L2a**]OBn into 0.5 equivalent Zn[**L2a**]$_2$ (and 0.5 equivalent Zn(OBn)$_2$). This behavior has also been reported in analogous zinc complexes of imine–phenolate ligands[49] and guanidine–ethenolate ligands.[106] The disproportionation was confirmed by the addition of one equivalent of benzyl alcohol to Zn[**L2a**]Et and the immediate quantitative formation of a product that is spectroscopically identical to Zn[**L2a**]$_2$ and Zn(OBn)$_2$. Furthermore, disproportionation was also observed with the *tert*-butyl substituted Zn**[L2b**]Et analogue. To assess the role of Zn(OBn)$_2$ in catalytic activity, a polymerization was conducted with ZnEt$_2$ and two equivalents of benzyl alcohol (to generate Zn(OBn)$_2$ in situ). This experiment displayed a rate

constant of 1.41 × 10^{-4} s^{-1}, suggesting its possible participation as an active species in polymerizations with Zn[**L*x***]Et, and BnOH as co-initiator.

The performance of the guanidine– and amidine–phenols (**L*x***H) themselves as catalysts for the ROP of *rac*-lactide was also investigated. The monomer-to-catalyst ratio was chosen to allow for a direct comparison to the homoleptic zinc complexes, assuming complete dissociation of the ligands in Zn[**L*x***]$_2$ and Zn[**L*x***]Et complexes under reaction conditions. Thus, a lactide-to-**L*x***H ratio of 50:1 was used for **L2a**H, **L2b**H, **L2c**H, **L2d**H and **L2a**H, and 100:1 for **L6a**H. Proligands **L2a**H, **L2b**H, and **L2a**H catalyzed the reaction with rate constants approximately half that those observed for their corresponding homoleptic complexes (Figure 3.6), suggesting that dissociation of the ligand in the homoleptic zinc complex occurs. Nevertheless, the ligands themselves could still catalyze the polymerization of lactide, possibly via a hydrogen bonding mechanism. [83]

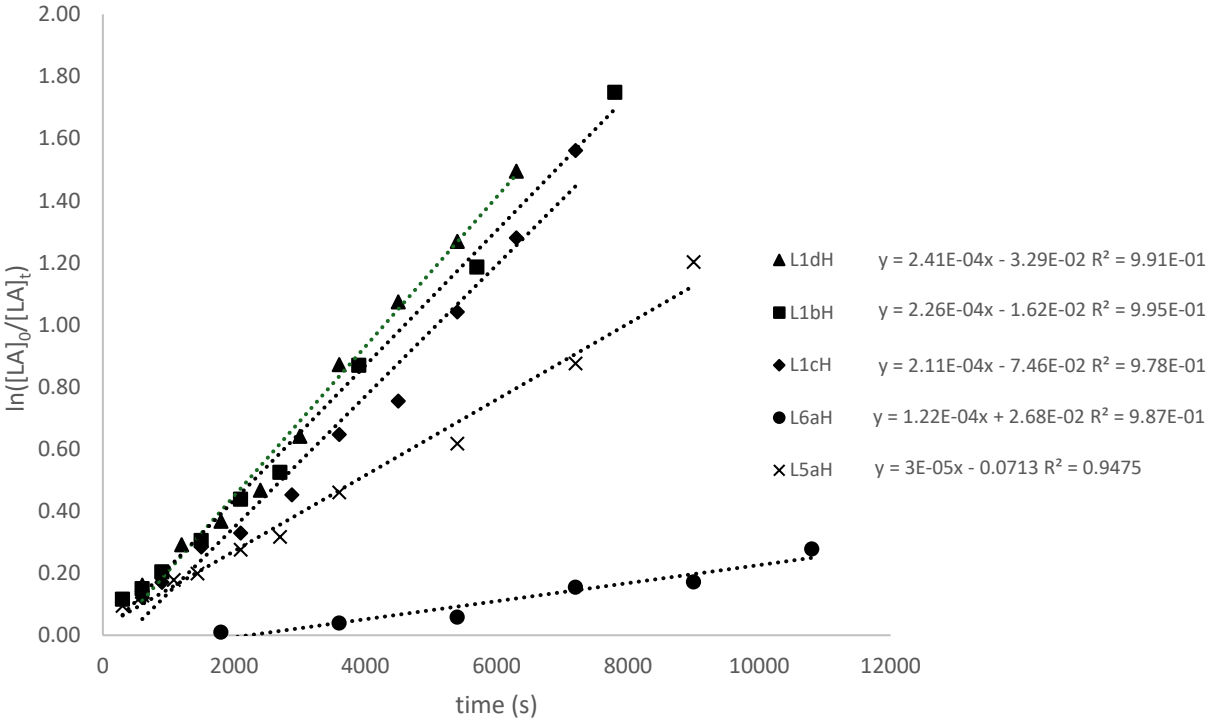

*Figure 3.6 Kinetic plots for the polymerization of rac-lactide by guanidine–phenol proligands (**Lx**H)*

The activity of **L2c**H itself is 1.9 times faster than that observed with the corresponding zinc complex, further supporting that the strong electron-withdrawing nitro group enhances the poisoning of the metal center by polar impurities, lowering the activity. Although the electron-donating methoxy group in **L2d** should mitigate dissociation from the metal, the activity of **L2d**H

in fact showcased a 1.7-fold increase in activity compared to the corresponding bischelate zinc complex. The lower activity observed with the complex must then be associated with either a slower coordination of the monomer and/or poorer activation due to a less electrophilic Zn center. Interestingly, the cyclic (alkyl)(amino)imine-based system again stands out, with **L6a**H being now 3 times slower than Zn[**L6a**]Et. This further demonstrates the uniqueness of these CAAI-based complexes, with a more tightly bound amidine–phenolate ligand and yet a more activating zinc center. Regardless, data from the experiments clearly further demonstrate that these proligands do have the ability to polymerize lactide under reaction conditions.

The number-average (M_n) and weight-average molecular weight (M_w) of the polymers generated by the zinc complexes and the phenols **L*x***H, in the absence of BnOH, were measured by NMR spectroscopy (600–2200 Da and 1200–4300 Da, respectively) and gel permeation chromatography (400–3300 Da and 700–4900 Da, respectively).[77,78] These molecular weights are comparable to those obtained using $Sn(Oct)_2$ and lower than predicted based on the 100:1 monomer-to-initiator ratio, indicating chain transfer and/or transesterification and further supported by dispersity values (Đ) ranging from 1.2 to 2.3 (Table *3.3*).

Table 3.3 Solvent-free polymerization of rac-lactide by Zn complexes

Entry[a]	Catalyst	[LA]:[Cat]:[BnOH]	k_{app}[b] (10^{-4} s^{-1})	M_n[c] (Da)	M_w[d] (Da)	Đ[e]	M_n[f] (Da)	M_w[f] (Da)	Đ[g]	P_r
1	Zn[**L2a**]$_2$	100:1:0	4.26	2200	3200	1.5	1800	2500	1.4	0.58
2	Zn[**L2a**]$_2$	100:1:1	4.37	1600	2800	1.7	1400	2100	1.5	0.58
3	Zn[**L2a**]Et	100:1:1	2.01	2100	3100	1.5	1700	2600	1.6	0.55
4	Zn[**L2a**]Et	100:1:0	1.85	1700	2800	1.6	2000	3000	1.5	0.54
5	Zn[**L2b**]$_2$	100:1:0	4.01	2000	4300	2.2	3200	4900	1.5	0.54
6	Zn[**L2b**]Et	100:1:1	2.24	1700	2700	1.5	1100	1600	1.4	0.54
7	Zn[**L2c**]$_2$	100:1:0	1.11	600	1200	2.1	400	700	1.8	0.47
8	Zn[**L2d**]$_2$	100:1:0	1.41	1600	2000	1.2	3000	3800	1.3	0.52
9	Zn[**L5a**]$_2$	100:1:0	0.71	1100	2500	2.3	800	1200	1.5	0.54
10	Zn[**L6a**]Et	100:1:1	4.08	2200	3800	1.7	2700	3700	1.4	0.62
11	**L2a**H[h]	50:1:0	2.45	1400	3000	2.1	1700	2500	1.5	0.48
12	**L2b**H	50:1:0	2.26	1100	1800	1.6	1700	2000	1.2	0.50
13	**L2c**H	50:1:0	2.11	1300	1600	1.2	1900	2700	1.4	0.50
14	**L2d**H	50:1:0	2.41	900	1600	1.8	1100	1600	1.4	0.51
15	**L5a′**H	50:1:0	0.30	1200	2000	1.6	1300	1900	1.5	0.50
16	**L6a**H	100:1:0	1.22	800	1000	1.2	1000	1300	1.3	0.49

17	$ZnEt_2$	200:1:2	1.41	800	1000	1.2	1200	1500	1.3	0.56
18	$Sn(Oct)_2$	100:1:1	15.1	2200	4300	1.8	2100	3100	1.5	0.68
19	$Sn(Oct)_2$[h]	100:1:0	12.4	2200	3300	1.5	3300	4700	1.4	0.68

[a] All polymerizations were carried out at 130 °C, with M_n calculated values of 28,826, 14,413, and 7206 Da for [LA]:[Cat] of 200:1, 100:1, and 50:1, respectively, assuming a living polymerization. [b] Determined from the slope of the plots of ln $([LA]_o/[LA]_t$ vs. time, with an average standard error of 5%. [c] Determined by ^1H NMR end-group analysis with –OH as chain-end. [d] Determined by DOSY NMR in C_6D_6. [e] $Đ = M_{w\ DOSY} \div M_{n\ NMR}$. [f] Determined by GPC in THF. [g] $Đ = M_w \div M_n$ as determined by GPC. [h] From chapter 2.

Addition of BnOH to the reaction mixture, expectedly, further decreased the molecular weight of the polymer, with incorporation of BnO as a chain end, supported by both ^1H NMR spectroscopy and MALDI-TOF mass spectrometry. The latter also showed hydroxyl end-capped polymers, suggesting reaction of water with the ester group in the lactide monomer (as initiator) or in the polymer itself (as chain-transfer agent). This also suggests that the Zn[**L*x***]$_2$ catalysts operate through an activated monomer mechanism, as reported for another homoleptic Zn-based catalyst. Interestingly, peaks associated with Zn[**L*x***]$_2$ complexed cyclic polymers were observed, indicating the presence of back-biting reactions. The data did not provide evidence of incorporation of the guanidine–phenolate ligand in the polymer, which rules out its role as initiator (Figure 3.7).

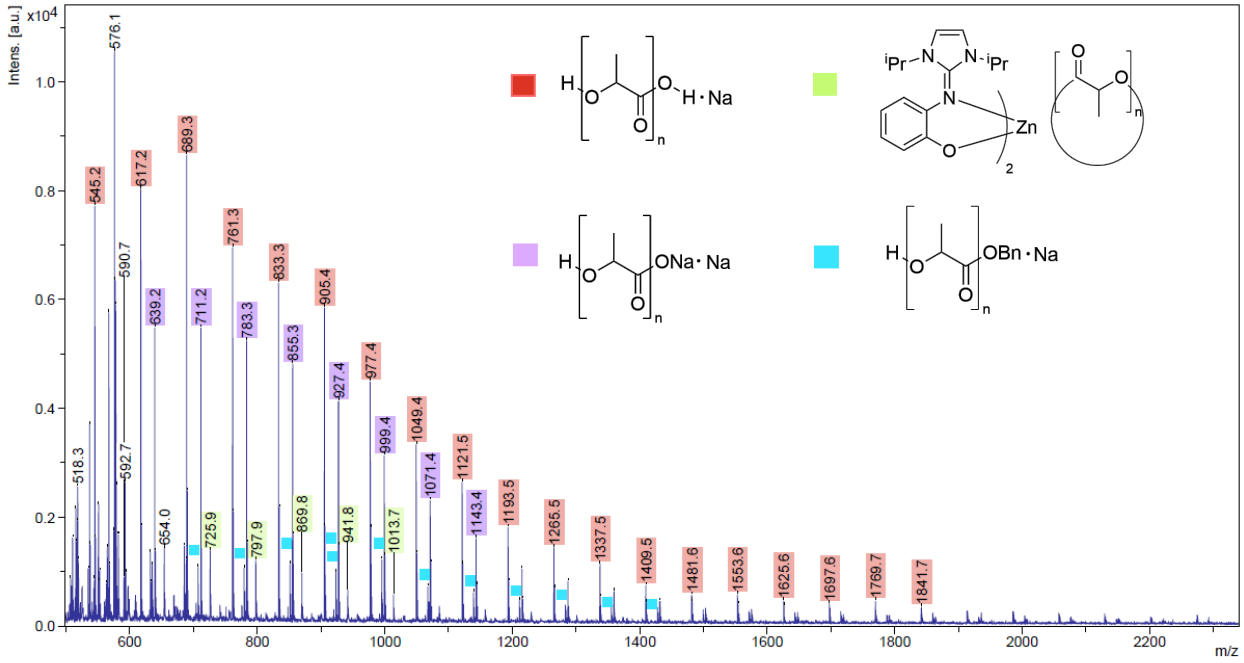

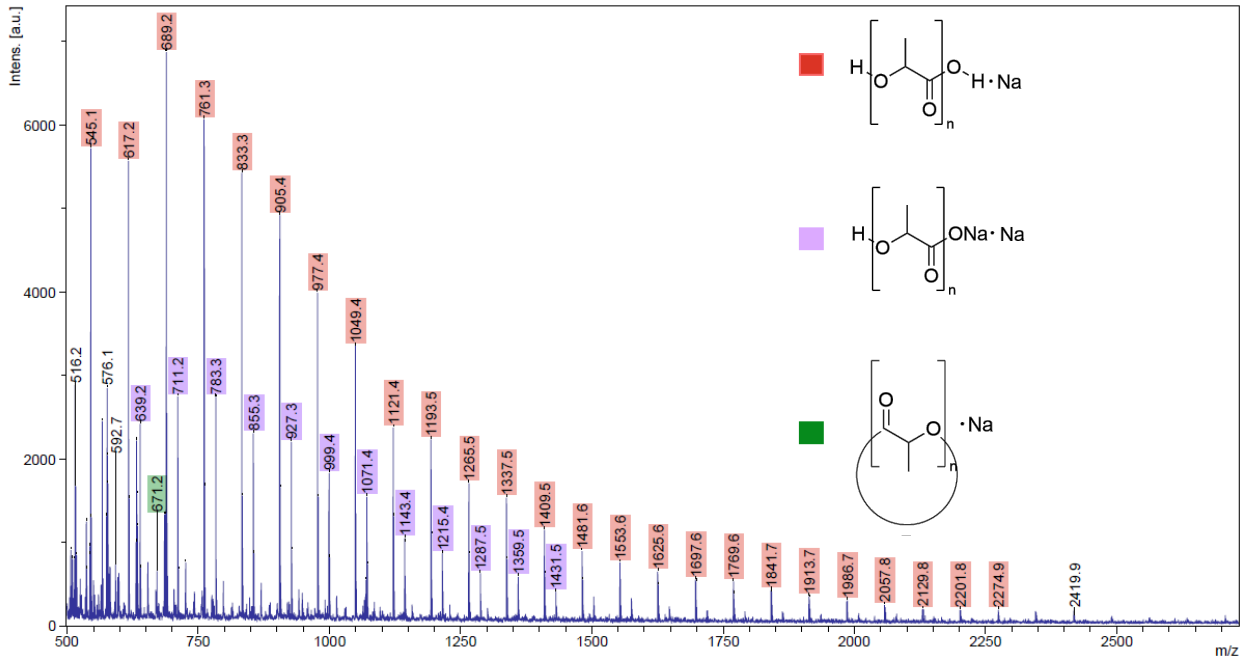

*Figure 3.7 MALDI-TOF mass spectra of the polymers obtained using Zn[**L2a**]$_2$/BnOH (top) and Zn[**L2a**]$_2$ (bottom)*

Polymerization with zinc complex Zn[**L2b**]$_2$ of the *tert*-butyl substituted ligand gave polymers with larger weight-average molecular weights (entry 5, Table *3.3*). Conversely, a decrease in the molecular weights was observed when an electron-withdrawing nitro group was present (entry 7, Table *3.3*). A similar effect was observed in PLA obtained from the zinc complex Zn[**L2a**]$_2$ of the diacylated ligand (entry 9, Table *3.3*), with molecular weights lower than those generated by Zn[**L2a**]$_2$ (entry 1, Table *3.3*). Again, the amidine **L6a**-based ethyl zinc complex stood out (entry 9, Table *3.3*), producing PLA with larger molecular weights than the guanidine–phenolate **L2a**-based analog (entry 3, Table *3.3*). The phenol with the least donating capability (**L2c**H, entry 13, Table *3.3*) generated larger polymers than its corresponding Zn[**L*x***]$_2$ complex. In contrast, **L2d**H (entry 14, Table *3.3*) with a more nucleophilic oxygen and **L6a**H (entry 16, Table *3.3*) with a stronger N-donor both gave polymers with lower molecular weights than their corresponding bischelate zinc complex.

The tacticity of polymers was determined by homonuclear-decoupled ^{1}H NMR spectroscopy. PLA from all Zn catalysts showed a slight heterotactic bias with P_r values from 0.52 to 0.62, with the exception of Zn[**L2c**]$_2$ (P_r = 0.47). In contrast, all proligands gave mainly atactic PLA (P_r = 0.48–0.51). The poor tacticity control of the Zn-based catalysts might be further evidence of the ligands themselves catalyzing the polymerization. The presumably lower binding constant for the electron-

poor **L2c** and thus its more favorable dissociation might explain the poorer stereoselectivity observed with Zn[**L2c**]$_2$.

The most active catalyst Zn**[L2a]**$_2$ was further explored at a higher lactide:catalyst ratio of 1000:1 and a higher temperature (150 °C), using both purified and non-purified *L*-lactide. The purity of the monomer had no effect on the activity of the catalyst. In contrast, Sn(Oct)$_2$ is much more sensitive to the purity of the monomer, with an approximately two-fold enhancement in activity observed with purified lactide. The k_{app} values for Zn[**L2a**]$_2$ and Sn(Oct)$_2$ decreased by approximately five- and two-fold, respectively, relative to those obtained at 130 °C with a lactide-to-catalyst ratio of 100:1. The rate decrease for Sn(Oct)$_2$ is consistent with the change in lactide-to-catalyst ratio, assuming no temperature effect. In contrast, Zn[**L2a**]$_2$ showed a lower k_{app} than expected, possibly due to enhanced ligand dissociation at the higher temperature.

The k_{app} values (entries 1 and 2, Table 3.4) of Zn[**L2a**]$_2$ are five times lower than those reported by Herres-Pawlis for the related Zn Schiff base complexes under those experimental conditions. The increased monomer-to-catalyst ratio had no marked effect on the molecular weight of the polymers obtained from Zn[**L2a**]$_2$. This is in contrast with the polymers obtained with Sn(Oct)$_2$, which showed a large increase in molecular weights, consistent with the 10-fold increase in monomer-to-catalyst ratio. The low molecular weight polymers obtained from Zn[**L2a**]$_2$ support enhanced ligand dissociation at these elevated temperatures, resulting in the deactivation of the catalyst and promoting chain scission, as observed in a common cyclic guanidine, although incorporation of the guanidine was not observed in the polymer chain, probably due to a fast hydrolysis after quench.[107] Interestingly, the P_r of the PLA generated by Zn[**L2a**]$_2$ displayed an averaged value of 0.37. Since P_r refers to the probability of forming a racemic diad, in the absence of D-Lactide the resultant polymer is expected to be purely isotactic (PLLA and $P_r = 0$). This result proves that epimerization was occurring and associated with free ligand performing a base-catalyzed epimerization as previously reported in the literature (Figure 3.8).

Table 3.4 Solvent-free polymerization of L-lactide[a]

Entry	Catalyst	k_{app}[b] (10^{-4} s^{-1})	M_n[c] (Da)	M_w[d] (Da)	Đ[e]	M_n[f] (Da)	M_w[f] (Da)	Đ[g]	P_r
1	Zn[**L2a**]$_2$	0.88	2000	2800	1.4	2300	3600	1.6	0.38
2	Zn[**L2a**]$_2$[h]	0.84	2200	2900	1.3	3800	5500	1.4	0.36
3	Sn(Oct)$_2$	5.72	3800	8700	2.3	25,000	55,000	2.2	0
4	Sn(Oct)$_2$[h]	9.88	3900	13000	3.3	36,000	79,000	2.2	0

[a] All polymerizations were carried out at 150 °C and a lactide-to-catalyst ratio of 1000:1 using unpurified *L*-lactide unless otherwise specified, with Mn calculated values of 144,130 Da, assuming a living polymerization .[b] An average standard error of 5% was calculated for the rate constants. [c] Determined by ^{1}H NMR end-group analysis with –OH as chain-end. [d] Determined by DOSY NMR in C_6D_6. [e] Đ = $M_{w\ DOSY} \div M_{n\ NMR}$. [f] Determined by GPC in $CHCl_3$. [g] Đ = $M_w \div M_n$ as determined by GPC. [h] *L*-lactide recrystallized from toluene was employed

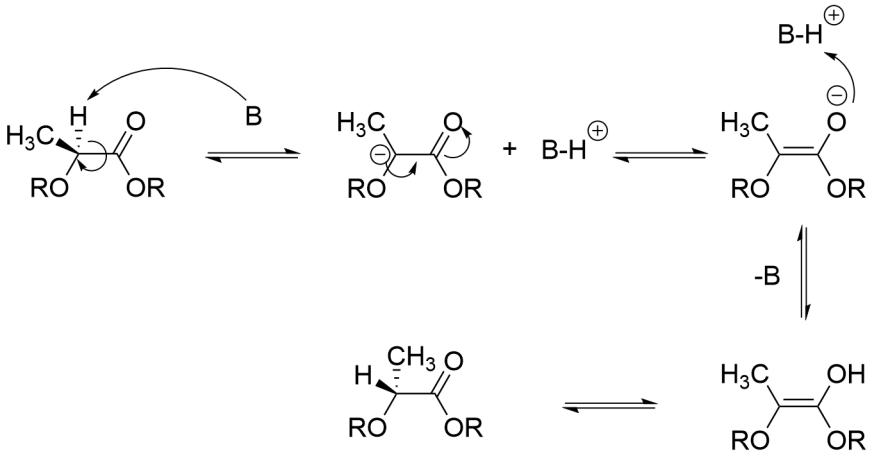

Figure 3.8 Base (B)-catalyzed epimerization. Adapted from the literature.[107]

Polycaprolactone (PCL) (Figure 3.9) is another biodegradable polymer of interest due to its mechanical properties and capability to form homogeneous blends with other polymers such as polycarbonates, nitrocellulose, and poly(vinyl chloride). The physical properties of PCL are dependent on the molecular weight of the polymer, with applications in drug delivery systems, medical devices, and microelectronics.[108] Similarly to PLA production, the most often used catalyst for the ROP of ε-caprolactone is Sn(Oct)$_2$ presenting the same drawbacks as PLA, catalyzing transesterification at high temperatures and thus decreasing in molecular weight.

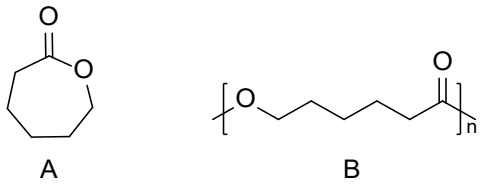

Figure 3.9 A) ε-caprolactone and B) polycaprolactone

Homopolymerization of ε-caprolactone was achieved with catalyst Zn[**L2a**]$_2$, albeit with a rate constant 60 times lower than the industrial standard Sn(Oct)$_2$ (Table 3.5). Additionally**,** the apparent rate constant, k_{app}, exhibited a value 33 times lower than that for the ring-opening polymerization of PLA for Zn[**L2a**]$_2$ and 1.5 times lower for Sn(Oct)$_2$. The differences in the activity between monomers can be related to the lactide having two carbonyls capable of coordinating to the metal center. In addition to this, the ROP of caprolactone leads to the formation of a primary alkoxide that is expected to have a stronger interaction with the metal center than the more sterically hindered secondary alkoxide generated by the ROP of lactide, thus leading to a slower propagation rate. The molecular weights determined by end-group analysis and DOSY NMR also showed larger polymer chains for the industrial standard Sn(Oct)$_2$. However, the molecular weights obtained were lower than the theoretical 11,414 Da, likely due to transesterification. Moreover, the number-average degree of polymerization (DP) for PCL (DP = 31 for Zn[**L2a**]$_2$, and 56 for Sn(Oct)$_2$) was greater than that observed for PLA (DP = 15 for both Zn[**L2a**]$_2$, and Sn(Oct)$_2$). This can be attributed to a higher quantity of ester groups in the PLA chain compared to the PCL, making the former more susceptible to transesterification reactions. However, the purity of the monomer might also play an important role; a purer caprolactone than *rac*-lactide might lead to less transesterification.

Table 3.5 Solvent-free polymerization of ε-caprolactone

Entry[a]	Catalyst	k_{app}[b] (10^{-4} s^{-1})	M_n[c] (Da)	M_w[d] (Da)	Đ[e]
1	Zn[**L2a**]$_2$	0.13	3500	3900	1.1
2	Sn(Oct)$_2$	8.12	6400	9200	1.4

[a]All polymerizations were carried out at 130 °C and a ε-caprolactone-to-catalyst ratio of 100:1 using unpurified a ε-caprolactone, with M_n calculated values of 11,414 Da assuming a living polymerization. [b]An average standard error of 5% was calculated for the rate constants. [c] Determined by ^{1}H NMR end-group analysis with –OH as chain-end. [d] Determined by DOSY NMR in C_6D_6. [e] Đ = $M_{w\ DOSY} \div M_{n\ NMR}$

3.3 Conclusions

The guanidine– and amidine–phenolate Zn complexes are active for the ROP of *rac*-lactide under solventless conditions and produced polymers with molecular weights comparable to the industrial standard $Sn(Oct)_2$ under most conditions studied, but underperformed under more demanding conditions (150 °C and 1000:1 lactide-to-catalyst ratio). Homoleptic complexes $Zn[\mathbf{L}\boldsymbol{x}]_2$ were approximately twice as active as the corresponding heteroleptic complexes Zn[**L*x***]Et, shown to undergo disproportionation to form 0.5 equivalent of $Zn[\mathbf{L}\boldsymbol{x}]_2$ and 0.5 equivalent of $Zn(OBn)_2$. The electronic nature of the ligand has a profound effect on the activity of the catalyst, with electron-rich systems poorly activating the monomer and electron-poor ones leading to both ligand dissociation and possibly enhanced poisoning of the more electrophilic metal. The guanidine– and amidine– phenols (**L*x***H) themselves proved to be effective catalysts, demonstrating that dissociated proligands cannot be ruled out as active species under the studied reaction conditions, especially for the guanidine–phenolate system. Interestingly, the amidine–phenolate-based system (**L6a**) stands out amongst the other systems for both the activity of the catalyst and the molecular weight of the polymer and is thus being further studied. Polymers generated from Zn complexes showed a heterotactic bias except for $Zn[\mathbf{L2c}]_2$, which gave atactic PLA, consistent with dissociation of the ligand from the metal under reaction conditions; all **L*x***H gave atactic PLA. This new class of ligands and the corresponding Zn complexes are much less sensitive to impurities found in the monomer feed than $Sn(Oct)_2$ and thus offer great potential, with future work aimed at further exploiting amidine–phenolates as spectator ligands for the ROP of lactide.

3.4 Experimental section

General considerations

All manipulations and materials were performed under a dry argon atmosphere, using Schlenk techniques or in a nitrogen-filled MBraun glovebox. *Rac*-lactide was purchased from Thermo Fisher Scientific and used without further purification. L-lactide and ε-caprolactone were purchased from Sigma Aldrich and used as received unless otherwise stated; if needed, L-lactide and *rac*-lactide were purified by one recrystallization from toluene. NMR spectra were recorded on a Bruker 400 MHz or Bruker UltraShield 300 MHz NMR spectrometer at room temperature. ^{1}H NMR chemical shifts are reported in ppm versus residual protons in deuterated solvents as follows: δ 7.27 $CDCl_3$, δ 7.16 C_6D_6, and δ 3.31 MeOD. $^{13}C\{^{1}H\}$ NMR chemical shifts are reported in ppm versus residual ^{13}C in the solvent: δ 77.16 $CDCl_3$, δ 128.06 C_6D_6, and δ 49.0 MeOD.

X-ray Crystallography

Diffraction data for ligands and complexes were collected on a Bruker APEX-II CCD diffractometer with a Mo Kα (λ = 0.71073 Å) radiation source. Crystals were selected under paratone oil and mounted under a stream of N_2 and kept at 173K during data collection. Structures were solved in Olex2[88] using direct methods and refined with SHELXL[89] refinement package using least-squares minimization.

Gel Permeation Chromatography

Number-average molecular weight (M_n), weight-average molecular weight (M_w) and dispersity (Đ; M_w/M_n) of samples were determined by gel permeation chromatography (GPC) using two PLgel miniMIX-B columns (4.6 mm x 250 mm) and two PLgel miniMIX-C columns (4.6 mm x 250 mm) from Agilent on elution with tetrahydrofuran (0.4 mL/min) at room temperature, equipped with an Agilent multi-detector suite composed of an Agilent G7801A refractive index detector, an Agilent G7803A dual-angle light scattering detector and an Agilent G7802A viscometer. Columns were calibrated using seven polystyrene standards with a conventional approach (Mp = 482,000, 125,900, 66,600, 27,060, 9,310, 5,610, and 1,180 Da). Data were analyzed using the Agilent GPC software version A.02.01 software (Santa Clara, CA 95051, United States).

MALDI-TOF Mass spectrometry

MALDI-TOF data were obtained at the AIMS laboratory of University of Toronto on a Bruker AutoFlex Speed MALDI-TOF instrument. The laser used for ionization was a 355 nm 3rd harmonic Nd YAG laser. The variable repetition was set to 2 kHz, the pulse energy ≥ 100 μJ. Samples were prepared in a dithranol THF matrix.

General procedure for the synthesis L2bH, L2cH and L2dH. A Schlenk flask was charged with the proper 2-aminophenol derivative (approximately 1.08 mmol, 1.0 equiv.) and triethylamine (2.0 equiv.) with 10 mL of DCM. A solution of compound **2Cl** (1.0 equiv.) in 10 mL of DCM was added, and the mixture was stirred for 16 h at room temperature (with the exception of **L2b**H, where MeCN was used, and the mixture was stirred under reflux for 3 days). The solvent was removed under vacuum, and 5 mL of EtOH was added, followed by the addition of KO^{t}Bu (2.0 equiv.) in 10 mL of EtOH. The mixture was stirred at room temperature for 1 h. Thereafter, volatiles were removed *in vacuo*, and the product was extracted with DCM (3 × 10 mL). The combined fractions were dried *in vacuo*. **L2b**H, 208 mg, 0.56 mmol, 77%. ^{1}H NMR (400 MHz, $CDCl_3$): δ 6.72 (d, *J* = 4.0 Hz, 1H, CH-Ar), 6.64 (d, *J* = 4.0 Hz, 1H, CH-Ar), 6.41 (d, 2H, $N(CH)_2N$), 4.47 (sept, *J* = 8.0 Hz, 2H, C*H*Me$_2$) 1.44 (s, 9H, $C(Me)_3$), 1.27 (s, 9H, $C(Me)_3$), 1.22 (d, *J* = 8.0 Hz, 12H, CH*Me*$_2$). ^{13}C{^{1}H} NMR (100 MHz, $CDCl_3$) δ 146.9 (s, C=N), 145.3 (s, C-OH), 139.9 (s, C-N), 136.8 (s, C-^{t}Bu), 132.7 (s, C-^{t}Bu), 113.7 (s, CH-Ar), 112.1 (s, CH-Ar), 109.7 (s, $N(CH)_2N$), 45.9 (s, *C*HMe$_2$), 34.8 (s, *C*-$(Me)_3$), 34.5 (s, *C*-$(Me)_3$), 32.0 (s, C-(*Me*)$_3$), 29.8 (s, C-(*Me*)$_3$) 21.9 (s, CH*Me*$_2$). Anal. Calcd for $C_{23}H_{37}N_3O$ (%): C, 74.35; H, 10.04; N, 11.31. Found (%): C, 74.12; H, 9.88; N, 11.60.

L2cH, 276 mg, 0.91 mmol, 81%. ^{1}H NMR (400 MHz, CD_3OD): δ 7.79 (dd, *J* = 8.0, 4.0 Hz, 1H, CH-Ar), 7.40 (d, *J* = 4.0 Hz, 1H, CH-Ar), 7.39 (s, 2H, $N(CH)_2N$), 6.42 (d, *J* = 8.0 Hz, 1H, CH-Ar) 4.51 (sept, *J* = 8.0 Hz, 2H, C*H*Me$_2$) 1.40 (d, *J* = 8.0 Hz, 12H, CH*Me*$_2$). ^{13}C{^{1}H} NMR (100 MHz, $CDCl_3$) δ 171.2 (s, C–NO_2), 143.0 (s, C=N), 134.8 (s, C-OH), 133.3 (s, C-N), 124.0 (s, CH-Ar), 118.3 (s, CH-Ar), 115.9 (s, $N(CH)_2N$), 113.2 (s, CH-Ar), 50.3 (s, *C*HMe$_2$), 22.3 (s, CH*Me*$_2$). Anal. Calcd for $C_{15}H_{20}N_4O_2$ (%): C, 59.20; H, 6.62; N, 18.41. Found (%): C, 58.92; H, 6.57; N, 18.20.

L2dH**,** 151 mg, 0.522 mmol, 83%. ^{1}H NMR (400 MHz, $CDCl_3$): δ 7.77 (d, *J* = 8.0 Hz, 1H, CH-Ar), 6.49 (s, 2H, $N(CH)_2N$), 6.23–6.18 (m, 3H, CH-Ar), 4.48 (sept, *J* = 8.0 Hz, 2H, C*H*Me$_2$) 3.70 (s, 3H, OCH_3), 1.26 (d, *J* = 8.0 Hz, 12H, CH*Me*$_2$). ^{13}C{^{1}H} NMR (100 MHz, $CDCl_3$) δ 153.3 (s,

C-OCH_3) 147.8 (s, C=N), 143.4 (s, C-OH), 139.2 (s, C-N), 111.7 (s, CH-Ar), 110.2 (s, $N(CH)_2N$), 102.9 (s, CH-Ar), 102.1 (s, CH-Ar), 55.9 (s, C-O*Me*) 46.4 (s, *C*HMe_2), 21.9 (s, CH*Me*$_2$). Anal. Calcd for $C_{15}H_{20}N_4O_2$ (%): C, 59.20; H, 6.62; N, 18.41. Found (%): C, 58.92; H, 6.57; N, 18.20.

L5a′H. A 20-mL vial was charged with 2-aminophenol (132 mg, 1.21 mmol, 1.0 equiv.) and triethylamine (0.50 mL, 3.6 mmol, 3.0 equiv.) in 5 mL of THF. A solution of **2Cl** (310 mg, 1.22 mmol, 1.0 equiv.) in 10 mL of THF was added, and the mixture was stirred for 16 h at room temperature. The THF soluble fraction was filtered, and the solvent was removed under reduced pressure. Solids were washed with pentane and dried under vacuum to yield a pale-yellow solid (242 mg, 0.82 mmol, 66%). ^{1}H NMR (400 MHz, $CDCl_3$): δ 6.90–6.95 (m, 2H, CH-Ar), 6.85–6.81 (m, 2H, CH-Ar) 4.98 (s, 1H, NH), 3.59 (sept, *J* = 8.0 Hz, 2H, C*H*Me_2) 1.43 (d, *J* = 8.0 Hz, 12H, CH*Me*$_2$). 1.41 (d, *J* = 8.0 Hz, 12H, CH*Me*$_2$). ^{13}C{^{1}H} NMR (100 MHz, $CDCl_3$) δ 156.8 (s, C=O), 146.6 (s, C-O), 134.6 (s, C-N), 122.5 (s, C-Ar), 119.2 (s, C-Ar), 113.2 (s, CH-Ar), 108.2 (s, CH-Ar), 108.2 (s, N-C-N), 45.6 (s, *C*HMe2), 20.1 (s, CH*Me*2). Anal. Calcd for $C_{15}H_{19}N_3O_3$ (%): C, 62.27; H, 6.62; N, 14.52. Found (%): C, 62.21; H, 6.77; N, 14.77.

L6aH. A 20-mL vial was charged with 2-aminophenol (81.6 mg, 0.748 mmol, 1.0 equiv.) and triethylamine (0.30 mL, 2.1 mmol, 2.8 equiv.) in 5 mL of DCM. A solution of **3Cl** (263 mg, 0.738 mmol, 1 equiv.) in 10 mL of DCM was added and the mixture was stirred for 16 h at room temperature. The solvent was removed under vacuum and the product extracted with diethyl ether. Volatiles were removed under reduced pressure and solids washed with cold hexane and dried to yield an orange solid (260 mg, 0.66 mmol, 88%). ^{1}H NMR (400 MHz, $CDCl_3$): δ 7.34–7.30 (m,1H, Ar-CH), 7.24–7.22 (m, 2H, Ar-CH), 6.82–6.78 (m, 2H, Ar-CH), 6.70–6.69 (m, 2H, Ar-CH), 3.16 (sept, *J* = 7.0 Hz, 2H, C*H*Me_2), 2.09 (s, 2H, CH_2), 1.35 (d, *J* = 7.0 Hz, 6H, CH*Me*$_2$), 1.32 (s, 6H, CH_3), 1.27 (d, *J* = 7.0 Hz, 6H, CH*Me*$_2$), 1.26 (s, 6H, CH_3). ^{13}C{^{1}H} NMR (100 MHz, $CDCl_3$) δ 169.3 (s, C=N), 148.6 (s, *C*-^{i}Pr), 148.1 (s, C-N-Dipp), 137.4 (s, C-OH), 132.2 (s, C-N), 128.4 (s, CH-Dipp) 124.2 (s, CH-Dipp), 122.5 (s, CH-Ar), 122.4 (s, CH-Ar), 119.3 (s, CH-Ar), 113.5 (s, CH-Ar), 62.0 (s, *C*-$(Me)_2$), 54.9 (s, *C*-$(Me)_2$), 43.0 (s, CH_2), 29.6 (s, *C*H$(Me)_2$), 29.2 (s, *C*-$(Me)_2$), 29.0 (s, *C*-$(Me)_2$), 26.8 (s, CH(*Me*)$_2$), 23.3 (s, CH(*Me*)$_2$). Anal. Calcd for $C_{26}H_{36}N_2O$ (%): C, 79.55; H, 9.24; N, 7.14. Found (%): C, 79.29; H, 8.89; N, 7.01.

General procedure for the synthesis of Zn[L2a]Et, Zn[L2b]Et and Zn[L6a]Et. A solution of **L*x*H** (approximately 0.49 mmol) 1.0 equiv.) in DCM (10 mL) was added to a solution of $ZnEt_2$

(1.0 M in *n*-hexane, 1.0 equiv.) in DCM (5 mL). The mixture was stirred for 6 h at room temperature. Thereafter, the solvent was removed under reduced pressure. The solid was washed with pentane to yield a tan solid. Zn[**L2a**]Et. 335 mg, 0.957 mmol, 82%. ^{1}H NMR (400 MHz, $CDCl_3$) δ 6.78–6.69 (br,1H, Ar-CH), 6.72 (s, 1H, N(CH)$_2$N) 6.60–6.54 (br, 1H, Ar-CH), 6.46–6.40 (m, 1H, Ar-CH), 6.32–6.27 (m, 1H, Ar-CH) 4.67–4.56 (br, 2H, C*H*-Me$_2$), 1.33–1.32 (br, 6H, CH-*Me*$_2$), 1.25 (d, *J* = 8.0 Hz, 6H, CH-*Me*$_2$), 0.95–0.86 (br, 3H, CH$_2$*Me*), 0.0 – –0.15 (br, 2H, CH$_2$*Me*). ^{13}C{^{1}H} NMR (100 MHz, $CDCl_3$) δ 156.8 (s, C=N), 150.3 (s, C-O), 118.9 (s, CH-Ar), 117.4 (s, C-N), 117.4 (s, CH-Ar), 115.6 (s, CH-Ar), 112.9 (s, CH-Ar), 111.8 (s, N(CH)$_2$N), 47.4 (s, C*H*Me$_2$) 22.7 (s, CH*Me*$_2$), 22.1 (s, CH*Me*$_2$), 13.1 (s, CH$_2$*C*H$_3$), 1.9 (*C*H$_2$CH$_3$). Anal. Calcd for $C_{17}H_{25}N_3OZn$ (%): C, 57.88; H, 7.14; N, 11.91. Found (%): C, 58.10; H, 7.34; N, 12.16.

Zn[**L2b**]Et. 157 mg, 0.337 mmol, 79%. ^{1}H NMR (400 MHz, $CDCl_3$): δ 6.72 (d, *J* = 4.0 Hz, 1H, CH-Ar), 6.64 (d, *J* = 4.0 Hz, 1H, CH-Ar), 6.41 (s, 2H, N(CH)$_2$N), 4.47 (sept, *J* = 8.0 Hz, 2H, C*H*Me$_2$) 1.44 (s, 9H, C(Me)$_3$), 1.27 (s, 9H, C(Me)$_3$), 1.22 (d, *J* = 8.0 Hz, 12H, CH*Me*$_2$). ^{13}C{^{1}H} NMR (100 MHz, $CDCl_3$) δ 150.4 (s, C=N), 149.9 (s, C-OH), 142.1 (s, C-N), 139.2 (s, C-^{t}Bu), 136.7 (s, C-^{t}Bu), 115.6 (s, CH-Ar), 112.9 (s, N(CH)$_2$N), 109.3 (s, CH-Ar), 48.6 (s, *C*HMe$_2$), 48.2 (s, *C*HMe$_2$), 35.4 (s, *C*-(Me)$_3$), 34.3 (s, *C*-(Me)$_3$), 31.9 (s, C-(*Me*)$_3$), 31.4 (s, C-(*Me*)$_3$), 21.0 (s, CH*Me*$_2$), 21.9 (s, CH*Me*$_2$), 20.9 (CH$_2$*Me*) .Anal. Calcd for $C_{25}H_{41}N_3OZn$ (%): C, 64.57; H, 8.89; N, 9.04. Found (%): C, 64.84; H, 9.10; N, 9.31.

Zn[**L6a**]Et. (86 mg, 0.17 mmol, 85%) ^{1}H NMR (400 MHz, $CDCl_3$): δ 7.45–7.43 (br,1H, Ar-CH), 7.36–7.34 (br, 2H, Ar-CH), 6.93–6.91 (br, 2H, Ar-CH), 6.74 (br, 1H, Ar-CH), 6.37 (br, 1H, Ar-CH) 3.05 (br, 2H, C*H*Me$_2$), 2.19 (s, 2H, CH$_2$), 1.49 (s, 6H, CH$_3$) 1.33–1.30 (br,18H, CH*Me*$_2$, CH$_3$). ^{13}C{^{1}H} NMR (100 MHz, $CDCl_3$) δ 169.3 (s, C=N), 148.1 (s, *C*-^{i}Pr), 135.0 (s, C-N-Dipp), 130.8 (s, C-OH), 129.2 (s, C-N), 128.4 (s, CH-Dipp) 127.0 (s, CH-Dipp), 126.7 (s, CH-Ar), 122.5 (s, CH-Ar), 117.0 (s, CH-Ar), 111.9 (s, CH-Ar), 65.2 (s, *C*-(Me)$_2$), 56.9 (s, *C*-(Me)$_2$), 44.2 (s, CH$_2$), 30.7 (s, *C*H(Me)$_2$), 29.2 (s, *C*-(Me)$_2$), 28.7 (s, *C*-(Me)$_2$), 26.9 (s, CH(*Me*)$_2$), 24.2 (s, CH(*Me*)$_2$), 11.8 (Zn-CH$_2$*C*H$_3$), –1.6 (Zn-*C*H$_2$CH$_3$). Anal. Calcd for $C_{28}H_{40}N_2OZn$ C, 69.20; H, 8.30; N, 5.76. Found (%): C, 69.47; H, 8.07; N, 6.02.

General procedure for the synthesis of Zn(L2[a–d])$_2$. ZnEt$_2$ (1.0 M in *n*-hexane, 1.0 equiv.) was added to a solution of **L2**[**a–d**]H (approximately 0.58 mmol), 2.0 equiv.) in DCM (x mL). The reaction mixture was stirred for 6 h at room temperature. The solvent was decanted, and the solids

formed were washed with pentane. The product was dried under reduced pressure to yield a solid. Zn[**L2a**]$_2$. 253 mg, 0.436 mmol, 87%. ^{1}H NMR (400 MHz, CD_3OD) δ 7.12 (s, 2H, N(CH)$_2$N), 6.69 (dd, *J* = 8.0, 2.0 Hz, 1H, CH-Ar) 6.56 (td, *J* = 8.0, 2.0 Hz, 1H, CH-Ar) 6.35 (td, *J* = 8.0, 2.0 Hz, 1H, CH-Ar) 6.29 (dd, *J* = 8.0, 2.0 Hz, 1H, CH-Ar) 4.58 (sept, *J* = 8.0, 7.0 Hz, 2H, C*H*-Me$_2$) 1.33 (d, *J* = 7.0 Hz, 6H, CH-*Me*$_2$) 0.97 (d, *J* = 7.0 Hz, 6H, CH-*Me*$_2$). ^{13}C{^{1}H} NMR (100 MHz, CD_3OD) δ 157.6 (s, C=N), 150.0 (s, C-O), 140.7 (s, C-N), 121.0 (s, CH-Ar), 116.3 (s, CH-Ar), 115.9 (s, CH-Ar), 114.3 (s, N(CH)$_2$N) 113.6 (s, CH-Ar) 23.0 (s, CH*Me*$_2$), 21.8 (s, CH*Me*$_2$). Anal. Calcd for $C_{30}H_{40}N_6O_2Zn$ (%): C, 61.90; H, 6.93; N, 14.44. Found (%): C, 62.15; H, 7.11; N, 14.18. Zn[**L2b**]$_2$.177 mg, 0.219 mmol, 88%. ^{1}H NMR (400 MHz, $CDCl_3$) δ 6.76 (s, 1H, CH-Ar), 6.60 (s, 2H, N(CH)$_2$N), 6.33 (s, 1H, CH-Ar), 4.87 (br, 2H, C*H*Me$_2$), 1.46 (s, 9H, C(Me)$_3$), 1.30 (d, *J* = 6.0 Hz, 6H, CH*Me*$_2$), 1.24 (s, 9H, C(Me)$_3$), 0.91 (d, *J* = 6.0 Hz, 12H, CH*Me*$_2$). ^{13}C{^{1}H} NMR (100 MHz, $CDCl_3$) δ 155.1 (s, C=N), 149.3 (s, C-OH), 137.1 (s, C-N), 133.5 (s, C-^{t}Bu), 131.6 (s, C-^{t}Bu), 113.6 (s, CH-Ar), 110.5 (s, N(CH)$_2$N), 107.1 (s, CH-Ar) 46.2 (s, *C*HMe$_2$), 34.4 (s, *C*-(Me)$_3$), 33.2 (s, *C*-(Me)$_3$), 32.0 (s, C-(*Me*)$_3$), 21.8 (s, C-(*Me*)$_3$) 21.3 (s, CH*Me*$_2$). Anal. Calcd for $C_{46}H_{72}N_6O_2Zn$ (%): C, 68.51; H, 9.00; N, 10.42. Found (%): 68.44; H, 8.79; N, 10.17. Zn[**L2c**]$_2$. 167 mg, 0.248 mmol, 95%. ^{1}H NMR (400 MHz, CD_3OD) δ 7.61 (dd, *J* = 9.0, 3.0 Hz, 1H, CH-Ar),7.38 (s, 2H, N(CH)$_2$N), 6.81 (d, *J* = 3.0 Hz, 1H, CH-Ar) 6.41 (d, *J* = 9.0 Hz, 1H, CH-Ar), 4.42 (sept, *J* = 7.0 Hz, 2H, C*H*-Me$_2$) 1.34 (d, *J* = 7.0 Hz, 6H, CH-*Me*$_2$) 1.27 (d, *J* = 7.0 Hz, 6H, CH-*Me*$_2$). ^{13}C{^{1}H} NMR (100 MHz, CD_3OD) δ 168.0 (s, C–NO_2), 133.6 (s, C=N), 132.0 (s, C-OH), 122.6 (s, C-N), 116.9 (s, N(CH)$_2$N), 114.4 (s, CH-Ar), 114.4 (s, CH-Ar), 111.9 (s, CH-Ar), 20.9 (s, CH*Me*$_2$). Anal. Calcd for $C_{30}H_{38}N_8O_2Zn$ (%): C, 53.62; H, 5.70; N, 16.67. Found (%): C, 53.90;H, 5.55; N, 16.38.

Zn[**L2d**]$_2$. 166 mg, 0.258 mmol, 92%. ^{1}H NMR (400 MHz, $CDCl_3$) δ 7.34 (d, *J* = 3.0 Hz, 1H, CH-Ar), 6.87 (d, *J* = 3.0 Hz, 1H, N(C*H*CH)N), 6.80 (d, *J* = 3.0 Hz, 1H, N(CHC*H*)N), 6.01 (dd, *J* = 9.0, 3.0 Hz, 1H, CH-Ar), 5.29 (d, *J* = 3.0 Hz, 1H, CH-Ar), 4.95 (sept, *J* = 8.0 Hz, 1H, C*H*Me$_2$), 4.05 (sept, *J* = 8.0 Hz, 1H, C*H*Me$_2$), 3.58 (s, 3H, OCH_3), 1.49 (d, *J* = 7.0 Hz, 3H, CH-*Me*$_2$), 1.30 (d, *J* = 7.0 Hz, 3H, CH-*Me*$_2$), 1.19 (d, *J* = 7.0 Hz, 3H, CH-*Me*$_2$), 0.86 (d, *J* = 7.0 Hz, 3H, CH-*Me*$_2$). ^{13}C{^{1}H} NMR (100 MHz, $CDCl_3$) δ 154.0 (s, *C*-OCH_3) 149.5 (s, C=N), 148.7 (s, C-O), 139.7 (s, C-N), 114.3 (s, CH-Ar), 111.9 (s, N(CH)$_2$N), 103.6 (s, CH-Ar), 101.7 (s, CH-Ar), 56.3 (s, C-O*Me*) 47.7 (s, *C*HMe$_2$), 22.4 (s, CH*Me*$_2$), 22.1 (s, CH*Me*$_2$). Anal. Calcd for $C_{32}H_{44}N_6O_2Zn$ (%): C, 59.86; H, 6.91; N, 13.09. Found (%): C, 59.59; H, 7.15; N, 12.84.

Zn[L5a]$_2$. A solution of **L5a′**H (136 mg, 0.470 mmol, 2.0 equiv.) in 15 mL of THF was added to a Schlenk flask containing a solution of $ZnCl_2$ (32.4 mg, 0.240 mmol, 1.0 equiv.) and KO^{t}Bu (54.2 mg, 0.483 mg, 2.0 equiv.) in THF. The mixture was left stirring under reflux; after 24 h, volatiles were removed under reduced pressure. The product was dissolved in MeCN and filtered; thereafter, the solvent was removed under vacuum to yield a white solid (120 mg, 0.186 mmol, 77%). ^{1}H NMR (400 MHz, CD_3OD): δ 7.36 (d, *J* = 8.0 Hz , 1H, CH-Ar), 7.30 (d, *J* = 8.0 Hz , 1H, CH-Ar), 7.15 (t, *J* = 8.0 Hz , 1H, CH-Ar), 7.04 (t, *J* = 8.0 Hz , 1H, CH-Ar), 4.00 (sept, *J* = 6.0 Hz, 2H, C*H*Me$_2$) 1.32 (d, *J* = 6.0 Hz, 12H, CH*Me*$_2$). 1.21 (d, *J* = 6.0 Hz, 12H, CH*Me*$_2$). ^{13}C{^{1}H} NMR (100 MHz, $CDCl_3$) Anal. Calcd for $C_{30}H_{36}N_6O_6Zn$ (%): C, 56.12; H, 5.65; N, 13.09. Found (%): C, 56.37; H, 5.80; N, 13.25

General procedure for the polymerization of *rac*-lactide.

Unless otherwise specified, all polymerizations were performed using *rac*-lactide (99%). In a typical experiment, a flask was charged with 50 μmol of catalyst and 5.0 mmol of *rac*-lactide under inert conditions. The mixture was submerged in an oil bath at 130 °C and stirred. Aliquots were sampled using a syringe of the crude material at different times to monitor the monomer conversion by ^{1}H NMR spectroscopy ($CDCl_3$). Polymerization was left to reach full conversion within the appropriate time.. The polymerization was cooled down to room temperature and terminated by the addition of 10 mL of wet $CHCl_3$. Volatiles were removed under vacuum at 50 °C for several hours. The remaining material was analyzed without further purification. Aliquots were removed from the reaction mixture at different times to monitor the monomer conversion by ^{1}H NMR spectroscopy. Molecular weight averages were determined by GPC, by end-chain analysis (M_n), and by diffusion ordered ^{1}H NMR spectroscopy (DOSY; M_w).

General procedure for the polymerization of L-lactide.

Unless otherwise specified, all polymerizations were performed using L-lactide (98%). In a typical experiment, a flask was charged with 14 μmol of catalyst and 14 mmol of L-lactide under inert conditions. The mixture was submerged in an oil bath at 150 °C and stirred. Aliquots were sampled using a syringe of the crude material at different times to monitor the monomer conversion by ^{1}H NMR spectroscopy ($CDCl_3$). Polymerization was left to reach full conversion within the appropriate time. The polymerization was cooled down to room temperature and terminated by the addition of 20 mL of wet $CHCl_3$. Volatiles were removed under vacuum at 50 °C for several hours.

The remaining material was analyzed without further purification. Aliquots were removed from the reaction mixture at different times to monitor the monomer conversion by ^{1}H NMR spectroscopy. Molecular weight averages were determined by GPC, by end-chain analysis (M_n), and by diffusion ordered ^{1}H NMR spectroscopy (DOSY; M_w).

General procedure for the polymerization of ε-caprolactone

All polymerizations were performed using ε-caprolactone (97%). In a typical experiment, in a glovebox, a flask was charged with 50 μmol of catalyst and 5.0 mmol of ε-caprolactone. The mixture was submerged in an oil bath at 130 °C and stirred. Aliquots were sampled using a syringe of the crude material at different times to monitor the monomer conversion by ^{1}H NMR spectroscopy ($CDCl_3$). Polymerization was left to reach full conversion within the appropriate time. The polymerization was cooled down to room temperature and terminated by the addition of 10 mL of wet $CHCl_3$. Volatiles were removed under vacuum at 50°C for several hours. The polymer was analyzed without further purification.

Chapter 4 Conclusions and future work

4.1 Conclusions

This work focused on the application of guanidine- and amidine-based ligands to develop robust catalysts capable of mediating catalytic processes, including the polymerization of ethylene and cyclic esters. As detailed in chapters 2 and 3, the guanidine and amidine scaffolds offer valuable opportunities to modify and tune the electronics and steric properties of the ligands. This led to the synthesis of a first generation of group 4 and Zn catalysts, which demonstrate potential for further improvement.

Chapter 2 presented the synthesis of Ti(IV) and Zr(IV) complexes containing a guanidine–phenolate ligand. The spatial arrangement of these complexes was examined by X-ray when possible and DFT. The study demonstrated that bis(alkoxide) metal complexes with a *cis*-N,N-*trans*-O,O ligand arrangement to be the most stable arrangement, whereas bis(guanidine–phenolate) titanium dichloride complexes favored the *trans*-N,N-*cis*-O,O disposition.

The catalytic activity of the bis(alkoxide) complexes for the ring-opening polymerization of lactide under solvent-free conditions was investigated. The zirconium complexes performed better than the titanium analogs. In addition, the Zr complex of L**2a**, based on the imidazole backbone and isopropyl substituent on the endocyclic nitrogen, presented the fastest rate of polymerization among all experimental catalysts. The small differences between the activities led us to investigate the probable dissociation of the ligand and its participation in the polymerization process. Interestingly, the free guanidine–phenol polymerized lactide faster than its corresponding metal complexes. The ability of the bis(guanidine–phenolate) titanium dichloride complexes to polymerize ethylene was also explored. Unfortunately, the catalytic activities of these complexes were significantly lower than those observed for benchmark experiments with Cp_2MCl_2.

Insights gained from Chapter 2 allowed us to focus on ligands containing the guanidine fragment x = **2** for their coordination to Zn and subsequent application for the ROP of cyclic esters. In addition to this, the steric and electronic effects of the phenolic oxygen were explored, and two other neutral fragments were investigated, leading to acylated guanidine and cyclic amidine ligands. All Zn complexes were active for the ROP polymerization of lactide under solvent-free conditions. The homoleptic Zn complex with the guanidine–phenolate ligand **L2a** performed

better among all catalysts. The addition of a bulky group in the phenolate fragment in **L2b** gave larger molecular weight polymers with no significant impact on the rate of polymerization, whereas the modification of the electronics of the phenolic oxygen (as in the methoxy and nitro-derivatives **L2c** and **L2d**, respectively) had a negative impact on the performance of the catalysts. The amidine–phenolate system (**L6a**) stood out as the best initiator, among the heteroleptic Zn[**Lx**]Et catalysts, with a performance comparable to the best homoleptic complex. As in chapter 2, polymerization studies demonstrated that the free ligands could also polymerize lactide, giving comparable results to those obtained with the corresponding Zn complexes, proving that participation of the free ligand in the latter cannot be ruled out.

4.2 Future work

4.2.1 Further investigation for the group 4 guanidine–phenolate systems

As highlighted in chapters 2 and 3, the most common impurities in non-purified lactide are water and lactic acid. Group 4 bis(alkoxide) complexes have been treated with water to form oxo-bridged dinuclear or multinuclear metal complexes.[44,45,109] Moreover, these types of complexes have proved to be active for the ROP of lactide, a dinuclear Zr benzoxazole–phenolate-based system presented high activity and generated isotactic-biased PLA.[45] Therefore, the synthesis of the oxo-bridged Ti and Zr complexes bearing guanidine–phenolate ligands can be accomplished by the controlled hydrolysis of the group 4 bis(isopropoxide) complexes presented in chapter 2 (Scheme 4.1). The performance of producing PLA using oxo-bridged complexes can be tested under the same conditions as their bis(isopropoxide) precursors (T > 130 °C, solventless), allowing for a better understanding of the possible participation and reactivity of other species that can be formed due to impurities present in the monomer feed.

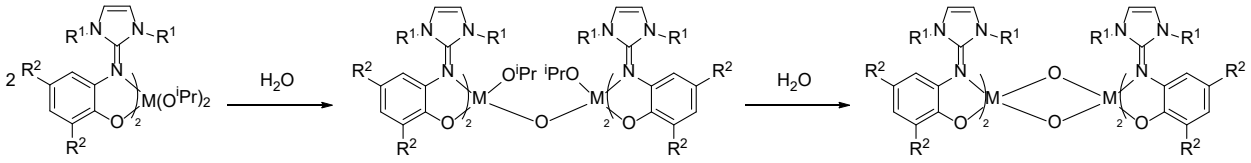

Scheme 4.1 Synthesis of oxo-bridged dinuclear group 4 complexes

The impurities present in lactide can also promote the dissociation of the ligand. This might generate a metal species that can act as an activating agent of the carbonyl group in the lactide, making it more susceptible to nucleophiles, such as the free guanidine–phenol ligand. Further

experiments can explore the reactivity of the free ligand in the presence of a group 4 metal precursor with low activity towards the polymerization of lactide, such as $TiCl_4$.[110] The results of this experiment will give a better insight into whether the $P_r > 0.5$ observed in the PLA produced for the group 4 guanidine–phenolate catalyst was due to the catalyst itself or a combination of a metal species present with the free ligand performing the polymerization.

4.2.1 Explore cyclic(alkyl)(amino)imine (CAAC) Zn-based catalyst

As part of Chapter 3, a cyclic(alkyl)(amino)imine (CAAC) moiety and the corresponding Zn-based catalyst, which stood out among all the initiators, were studied. The activity of these species could be further explored by modifying the steric of the quaternary carbon of the former carbenoid carbon (Figure 4.1). Steric effects proved to have an important role in the control of the stereochemistry of a polymer, influencing how the monomer incorporates into the growing polymer chain. Modifications in the CAAC fragment are not limited to the steric effects; incorporation of stereogenic centers in the ligand framework has also proven to have an effect on the tacticity of the polymer. Future work might also include the addition of stereogenic centers (Figure 4.1), as these modifications remain unexplored in the context of ROP of cyclic esters. The synthesis of these novel CAAC-based systems can be approached as shown in Scheme 4.2, where the selected CAAC precursors have been reported and isolated.[111–113] The corresponding zinc complexes can be easily obtained by the protonolysis of $ZnEt_2$ to obtain either the ZnEtL or ZnL_2. These catalysts can be examined for the ROP of lactide under industrial relevant conditions (T > 130 °C and solventless) to fill the gap in the reactivity of Zn-based systems containing a cyclic amidine fragment.

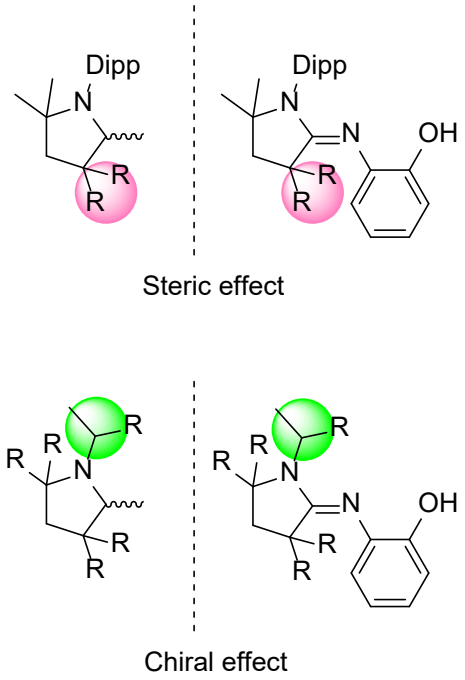

Figure 4.1 Proposed ligand modifications in the CAAC moiety for future ligand design: steric effect (pink), addition of a chiral center (green)

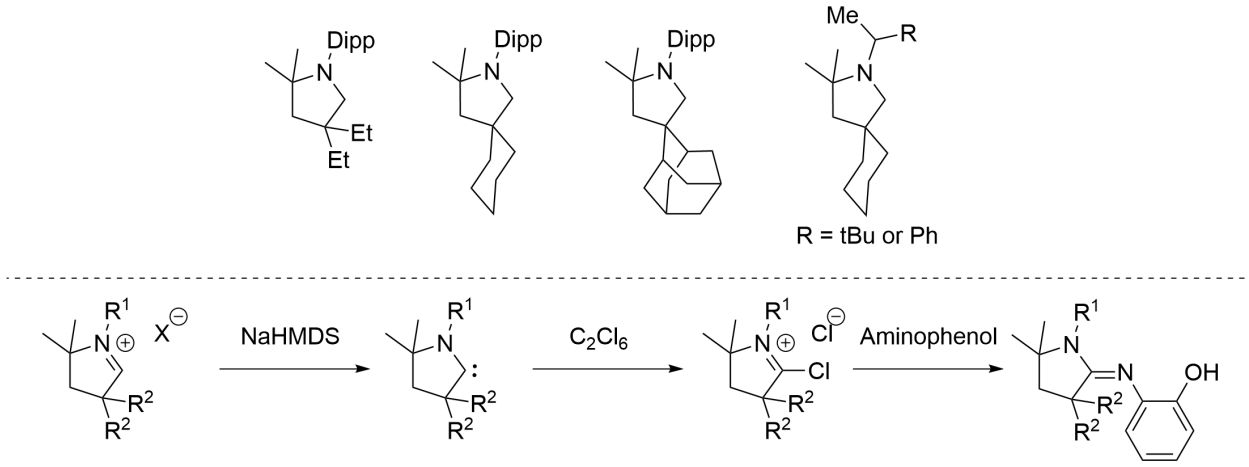

Scheme 4.2 Synthesis of plausible amidine–phenol ligands to be used for the ROP of cyclic esters

4.2.2 Depolymerization of polylactic acid

Nowadays, zinc complexes are still being explored for the ROP of cyclic esters. However, they have also proven to be effective in catalyzing the depolymerization of PLA and PET by alcoholysis. In this context, polyesters have great potential in a circular economy framework due to their biodegradability and recycling capacity. However, recycling methods that incorporate the principles of Green Chemistry are still being developed. In the literature, N-donor ligands,

including guanidines, have been developed for this purpose (Scheme 4.3).[114–116] This opens a new field where complexes containing guanidines and amidines scaffolds can be tested for their ability to catalyze alcoholysis of polyesters.

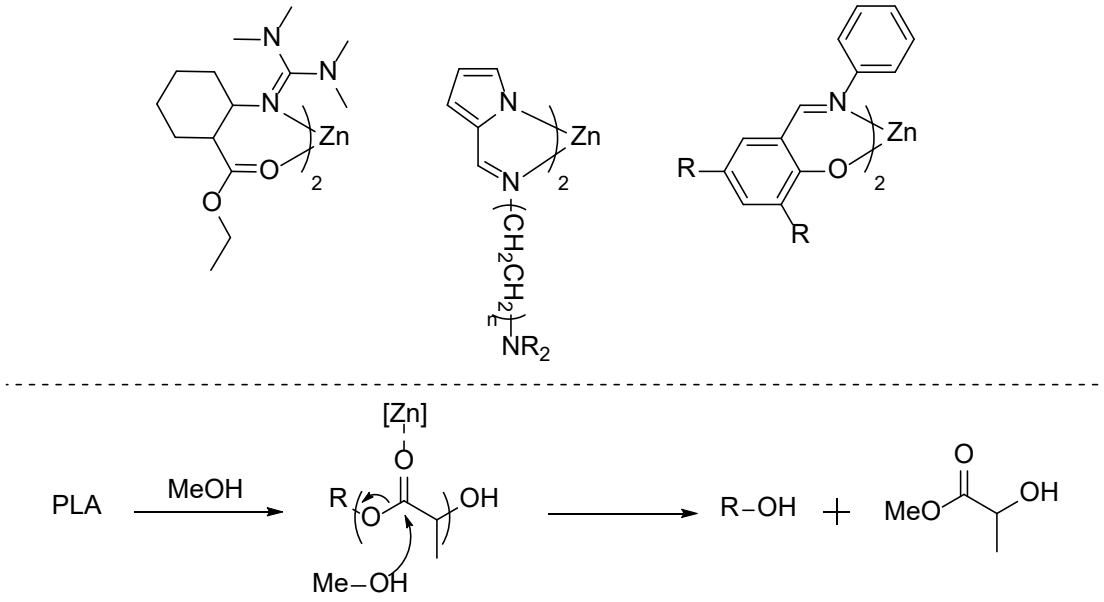

Scheme 4.3 Guanidine-based, imino-pyrrol, and imine-phenolate Zn systems used in the depolymerization of PLA (top) and Zn-mediated degradation of PLA via transesterification with MeOH (adapted from literature)

Chapters 2 and 3 demonstrated that proligand could not be ruled out as an initiator of ring-opening polymerization of lactide. However, the use of organocatalysts is not limited to the polymerization of lactide, triazabicyclodecene (TBD), a guanidine-based organocatalyst, has been used in the catalytic depolymerization of PLA using a wide variety of primary alcohols.[117] More recently, Enthaler´s group investigated the depolymerization of PLA using 4-dimethylaminopyridine (DMAP) in the presence of MeOH, additionally PLA commodities were effectively converted to methyl lactate.[118] This offers an opportunity to examine the ability of guanidine–phenol systems for the depolymerization of PLA in the presence of methanol, guanidine–phenol can be suitable to catalyze the aforementioned process via a dual-activation mechanism as proposed for TBD.[117]

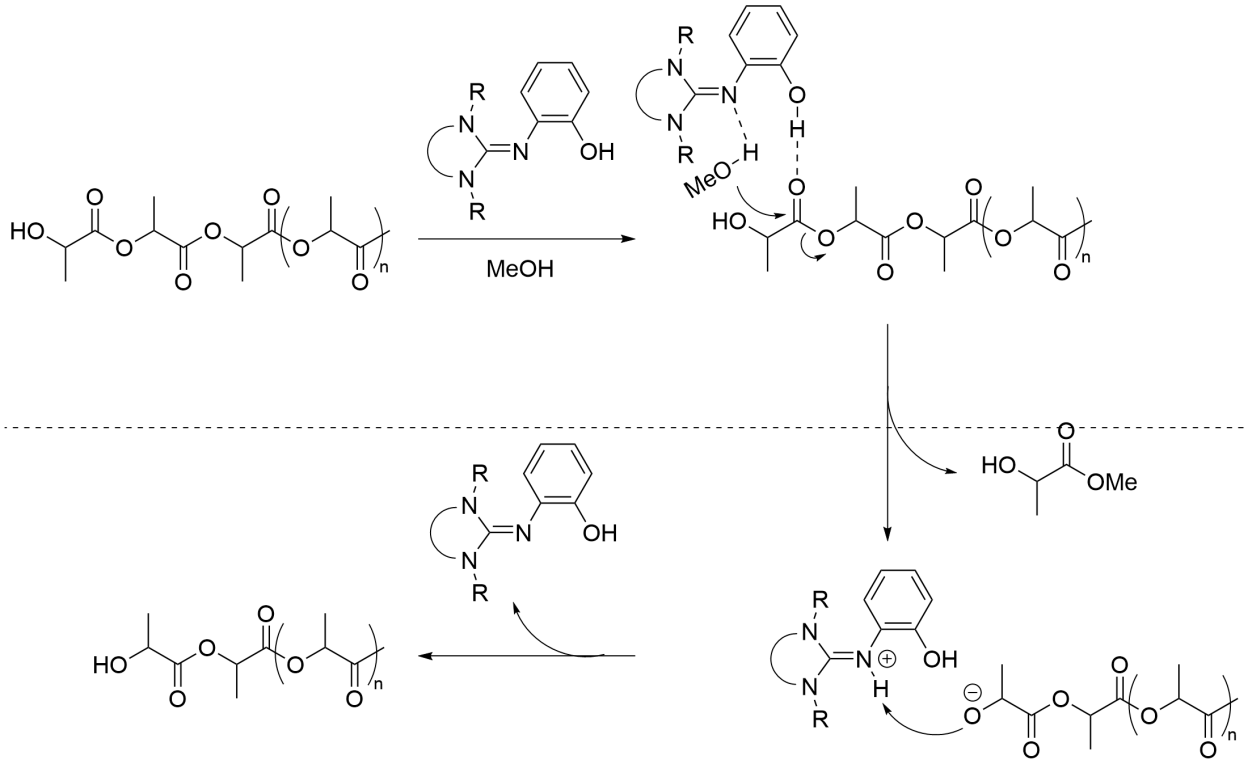

Scheme 4.4 Dual-activation mechanism of depolymerization of PLA via methanolysis using a guanidine–phenol catalyst.

Chapter 5 References

(1) Stürzel, M.; Mihan, S.; Mülhaupt, R. From Multisite Polymerization Catalysis to Sustainable Materials and All-Polyolefin Composites. *Chem. Rev.* **2016**, *116* (3), 1398–1433. https://doi.org/10.1021/acs.chemrev.5b00310.

(2) Chum, P. S.; Swogger, K. W. Olefin Polymer Technologies—History and Recent Progress at The Dow Chemical Company. *Prog. Polym. Sci.* **2008**, *33* (8), 797–819. https://doi.org/10.1016/j.progpolymsci.2008.05.003.

(3) Keyes, A.; Basbug Alhan, H. E.; Ordonez, E.; Ha, U.; Beezer, D. B.; Dau, H.; Liu, Y.; Tsogtgerel, E.; Jones, G. R.; Harth, E. Olefins and Vinyl Polar Monomers: Bridging the Gap for Next Generation Materials. *Angew Chem Int Ed* **2019**, *58* (36), 12370–12391. https://doi.org/10.1002/anie.201900650.

(4) Jubinville, D.; Esmizadeh, E.; Saikrishnan, S.; Tzoganakis, C.; Mekonnen, T. A Comprehensive Review of Global Production and Recycling Methods of Polyolefin (PO) Based Products and Their Post-Recycling Applications. *Sustainable Materials and Technologies* **2020**, *25*, e00188. https://doi.org/10.1016/j.susmat.2020.e00188.

(5) Eisch, J. J. Fifty Years of Ziegler–Natta Polymerization: From Serendipity to Science. A Personal Account. *Organometallics* **2012**, *31* (14), 4917–4932. https://doi.org/10.1021/om300349x.

(6) Fisch, A. G. Ziegler-Natta Catalysts. In *Kirk-Othmer Encyclopedia of Chemical Technology*; Kirk-Othmer, Ed.; Wiley, 2019; pp 1–22. https://doi.org/10.1002/0471238961.2609050703050303.a01.pub2.

(7) Kaminsky, W. The Discovery of Metallocene Catalysts and Their Present State of the Art. *J. Polym. Sci. A Polym. Chem.* **2004**, *42* (16), 3911–3921. https://doi.org/10.1002/pola.20292.

(8) Izmer, V. V.; Lebedev, A. Y.; Kononovich, D. S.; Borisov, I. S.; Kulyabin, P. S.; Goryunov, G. P.; Uborsky, D. V.; Canich, J. A. M.; Voskoboynikov, A. Z. *Ansa*- Metallocenes Bearing 4-(*N* -Azolyl)-2-Methylindenyl and Related Ligands: Development of Highly Isoselective Catalysts for Propene Polymerization at Higher Temperatures. *Organometallics* **2019**, *38* (24), 4645–4657. https://doi.org/10.1021/acs.organomet.9b00648.

(9) Wang, B. Ansa-Metallocene Polymerization Catalysts: Effects of the Bridges on the Catalytic Activities. *Coordination Chemistry Reviews* **2006**, *250* (1–2), 242–258. https://doi.org/10.1016/j.ccr.2005.05.012.

(10) Makio, H.; Terao, H.; Iwashita, A.; Fujita, T. FI Catalysts for Olefin Polymerization—A Comprehensive Treatment. *Chem. Rev.* **2011**, *111* (3), 2363–2449. https://doi.org/10.1021/cr100294r.

(11) Furuyama, R.; Saito, J.; Ishii, S.; Mitani, M.; Matsui, S.; Tohi, Y.; Makio, H.; Matsukawa, N.; Tanaka, H.; Fujita, T. Ethylene and Propylene Polymerization Behavior of a Series of Bis(Phenoxy–Imine)Titanium Complexes. *Journal of Molecular Catalysis A: Chemical* **2003**, *200* (1–2), 31–42. https://doi.org/10.1016/S1381-1169(03)00096-7.

(12) Norrby, P.-O. Organotransition Metal Chemistry: From Bonding to Catalysis. John Hartwig. *ChemCatChem* **2010**, *2* (7), 872–872. https://doi.org/10.1002/cctc.201000172.

(13) Pang, X.; Zhuang, X.; Tang, Z.; Chen, X. Polylactic Acid (PLA): Research, Development and Industrialization. *Biotechnology Journal* **2010**, *5* (11), 1125–1136. https://doi.org/10.1002/biot.201000135.

(14) Narancic, T.; Cerrone, F.; Beagan, N.; O'Connor, K. E. Recent Advances in Bioplastics: Application and Biodegradation. *Polymers* **2020**, *12* (4), 920. https://doi.org/10.3390/polym12040920.

(15) Taib, N.-A. A. B.; Rahman, M. R.; Huda, D.; Kuok, K. K.; Hamdan, S.; Bakri, M. K. B.; Julaihi, M. R. M. B.; Khan, A. A Review on Poly Lactic Acid (PLA) as a Biodegradable Polymer. *Polym. Bull.* **2023**, *80* (2), 1179–1213. https://doi.org/10.1007/s00289-022-04160-y.

(16) Castro-Aguirre, E.; Iñiguez-Franco, F.; Samsudin, H.; Fang, X.; Auras, R. Poly(Lactic Acid)—Mass Production, Processing, Industrial Applications, and End of Life. *Advanced Drug Delivery Reviews* **2016**, *107*, 333–366. https://doi.org/10.1016/j.addr.2016.03.010.
(17) Auras, R.; Singh, S.; Singh, J. Performance Evaluation of PLA against Existing PET and PS Containers. *Journal of Testing and Evaluation* **2006**, *34* (6), 530–536. https://doi.org/10.1520/JTE100041.
(18) Royal Society of Chemistry. *Poly(Lactic Acid) Science and Technology: Processing, Properties, Additives and Applications*; Jiménez, A., Peltzer, M., Ruseckaite, R., Eds.; The Royal Society of Chemistry, 2014. https://doi.org/10.1039/9781782624806.
(19) Kricheldorf, H. R.; Weidner, S. M. Syntheses of Polylactides by Means of Tin Catalysts. *Polym. Chem.* **2022**, *13* (12), 1618–1647. https://doi.org/10.1039/D2PY00092J.
(20) Kricheldorf, H. R.; Berl, M.; Scharnagl, N. Poly(Lactones). 9. Polymerization Mechanism of Metal Alkoxide Initiated Polymerizations of Lactide and Various Lactones. *Macromolecules* **1988**, *21* (2), 286–293. https://doi.org/10.1021/ma00180a002.
(21) Dubois, P.; Jacobs, C.; Jerome, R.; Teyssie, P. Macromolecular Engineering of Polylactones and Polylactides. 4. Mechanism and Kinetics of Lactide Homopolymerization by Aluminum Isopropoxide. *Macromolecules* **1991**, *24* (9), 2266–2270. https://doi.org/10.1021/ma00009a022.
(22) Von Schenck, H.; Ryner, M.; Albertsson, A.-C.; Svensson, M. Ring-Opening Polymerization of Lactones and Lactides with Sn(IV) and Al(III) Initiators. *Macromolecules* **2002**, *35* (5), 1556–1562. https://doi.org/10.1021/ma011653i.
(23) Rao, W.; Cai, C.; Tang, J.; Wei, Y.; Gao, C.; Yu, L.; Ding, J. Coordination Insertion Mechanism of Ring-Opening Polymerization of Lactide Catalyzed by Stannous Octoate†. *Chinese Journal of Chemistry* **2021**, *39* (7), 1965–1974. https://doi.org/10.1002/cjoc.202000519.
(24) Okamoto, Y. Cationic Ring-Opening Polymerization of Lactones in the Presence of Alcohol. *Makromolekulare Chemie. Macromolecular Symposia* **1991**, *42–43* (1), 117–133. https://doi.org/10.1002/masy.19910420109.
(25) Penczek, S.; Pretula, J. Activated Monomer Mechanism (AMM) in Cationic Ring-Opening Polymerization. The Origin of the AMM and Further Development in Polymerization of Cyclic Esters. *ACS Macro Lett.* **2021**, *10* (11), 1377–1397. https://doi.org/10.1021/acsmacrolett.1c00509.
(26) D'Auria, I.; Tedesco, C.; Mazzeo, M.; Pellecchia, C. New Homoleptic Bis(Pyrrolylpyridiylimino) Mg(II) and Zn(II) Complexes as Catalysts for the Ring Opening Polymerization of Cyclic Esters via an "Activated Monomer" Mechanism. *Dalton Trans.* **2017**, *46* (36), 12217–12225. https://doi.org/10.1039/C7DT02445B.
(27) Hoskins, J. N.; Grayson, S. M. Cyclic Polyesters: Synthetic Approaches and Potential Applications. *Polym. Chem.* **2011**, *2* (2), 289–299. https://doi.org/10.1039/C0PY00102C.
(28) Bonnet, F.; Stoffelbach, F.; Fontaine, G.; Bourbigot, S. Continuous Cyclo-Polymerisation of L -Lactide by Reactive Extrusion Using Atoxic Metal-Based Catalysts: Easy Access to Well-Defined Polylactide Macrocycles. *RSC Adv.* **2015**, *5* (40), 31303–31310. https://doi.org/10.1039/C4RA16634E.
(29) Kricheldorf, H. R. Cyclic Polymers: Synthetic Strategies and Physical Properties. *J. Polym. Sci. A Polym. Chem.* **2010**, *48* (2), 251–284. https://doi.org/10.1002/pola.23755.
(30) Dechy-Cabaret, O.; Martin-Vaca, B.; Bourissou, D. Controlled Ring-Opening Polymerization of Lactide and Glycolide. *Chem. Rev.* **2004**, *104* (12), 6147–6176. https://doi.org/10.1021/cr040002s.
(31) Albertsson, A.-C.; Varma, I. K. Recent Developments in Ring Opening Polymerization of Lactones for Biomedical Applications. *Biomacromolecules* **2003**, *4* (6), 1466–1486. https://doi.org/10.1021/bm034247a.
(32) Punyodom, W.; Meepowpan, P.; Girdthep, S.; Limwanich, W. Influence of Tin(II), Aluminum(III) and Titanium(IV) Catalysts on the Transesterification of Poly(L-Lactic Acid). *Polym. Bull.* **2022**, *79* (12), 11409–11429. https://doi.org/10.1007/s00289-021-04005-0.

(33) Lipik, V. T.; Widjaja, L. K.; Liow, S. S.; Abadie, M. J. M.; Venkatraman, S. S. Effects of Transesterification and Degradation on Properties and Structure of Polycaprolactone–Polylactide Copolymers. *Polymer Degradation and Stability* **2010**, *95* (12), 2596–2602. https://doi.org/10.1016/j.polymdegradstab.2010.07.027.
(34) Tsuji, H. Poly(Lactide) Stereocomplexes: Formation, Structure, Properties, Degradation, and Applications. *Macromolecular Bioscience* **2005**, *5* (7), 569–597. https://doi.org/10.1002/mabi.200500062.
(35) Chile, L.-E.; Mehrkhodavandi, P.; Hatzikiriakos, S. G. A Comparison of the Rheological and Mechanical Properties of Isotactic, Syndiotactic, and Heterotactic Poly(Lactide). *Macromolecules* **2016**, *49* (3), 909–919. https://doi.org/10.1021/acs.macromol.5b02568.
(36) Tsuji, H.; Arakawa, Y. Synthesis, Properties, and Crystallization of the Alternating Stereocopolymer Poly(L -Lactic Acid- *Alt* - D -Lactic Acid) [Syndiotactic Poly(Lactic Acid)] and Its Blend with Isotactic Poly(Lactic Acid). *Polym. Chem.* **2018**, *9* (18), 2446–2457. https://doi.org/10.1039/C8PY00391B.
(37) Fortun, S.; Daneshmand, P.; Schaper, F. Isotactic *rac* -Lactide Polymerization with Copper Complexes: The Influence of Complex Nuclearity. *Angew. Chem.* **2015**, *127* (46), 13873–13876. https://doi.org/10.1002/ange.201505674.
(38) Domenek, S.; Fernandes-Nassar, S.; Ducruet, V. Rheology, Mechanical Properties, and Barrier Properties of Poly(Lactic Acid). In *Synthesis, Structure and Properties of Poly(lactic acid)*; Di Lorenzo, M. L., Androsch, R., Eds.; Springer International Publishing: Cham, 2018; pp 303–341. https://doi.org/10.1007/12_2016_17.
(39) Sauer, A.; Kapelski, A.; Fliedel, C.; Dagorne, S.; Kol, M.; Okuda, J. Structurally Well-Defined Group 4 Metal Complexes as Initiators for the Ring-Opening Polymerization of Lactide Monomers. *Dalton Trans.* **2013**, *42* (25), 9007–9023. https://doi.org/10.1039/c3dt00010a.
(40) Chmura, A. J.; Cousins, D. M.; Davidson, M. G.; Jones, M. D.; Lunn, M. D.; Mahon, M. F. Robust Chiral Zirconium Alkoxide Initiators for the Room-Temperature Stereoselective Ring-Opening Polymerisation of Rac-Lactide. *Dalton Trans.* **2008**, No. 11, 1437–1443. https://doi.org/10.1039/b716304e.
(41) Kumar Saha, T.; Rajashekhar, B.; Chakraborty, D. Alkoxides of Group 4 Metals Containing the Bis(Imino)Phenoxide Ligand: Synthesis, Structural Characterization and Polymerization Studies. *RSC Adv.* **2012**, *2* (1), 307–318. https://doi.org/10.1039/C1RA00543J.
(42) Saha, T. K.; Mandal, M.; Chakraborty, D.; Ramkumar, V. Imino Phenoxide Complexes of Group 4 Metals: Synthesis, Structural Characterization and Polymerization Studies. *New J. Chem.* **2013**, *37* (4), 949. https://doi.org/10.1039/c3nj40916c.
(43) Chmura, A. J.; Davidson, M. G.; Jones, M. D.; Lunn, M. D.; Mahon, M. F.; Johnson, A. F.; Khunkamchoo, P.; Roberts, S. L.; Wong, S. S. F. Group 4 Complexes with Aminebisphenolate Ligands and Their Application for the Ring Opening Polymerization of Cyclic Esters. *Macromolecules* **2006**, *39* (21), 7250–7257. https://doi.org/10.1021/ma061028j.
(44) Pappuru, S.; Ramkumar, V.; Chakraborty, D. Benzoxazole Phenoxide Ligand Supported Group IV Catalysts and Their Application for the Ring-opening Polymerization of *Rac* -lactide and *ε* -caprolactone. *Polym. Adv. Technol.* **2021**, *32* (9), 3392–3401. https://doi.org/10.1002/pat.5349.
(45) Pappuru, S.; Chakraborty, D.; Vijaya Sundar, J.; Roymuhury, S. K.; Ramkumar, V.; Subramanian, V.; Chand, D. K. Group 4 Complexes of Salicylbenzoxazole Ligands as Effective Catalysts for the Ring-Opening Polymerization of Lactides, Epoxides and Copolymerization of ε-Caprolactone with L-Lactide. *Polymer* **2016**, *102*, 231–247. https://doi.org/10.1016/j.polymer.2016.08.007.
(46) Chamberlain, B. M.; Cheng, M.; Moore, D. R.; Ovitt, T. M.; Lobkovsky, E. B.; Coates, G. W. Polymerization of Lactide with Zinc and Magnesium β-Diiminate Complexes: Stereocontrol and Mechanism. *J. Am. Chem. Soc.* **2001**, *123* (14), 3229–3238. https://doi.org/10.1021/ja003851f.

(47) Williams, C. K.; Breyfogle, L. E.; Choi, S. K.; Nam, W.; Young, V. G.; Hillmyer, M. A.; Tolman, W. B. A Highly Active Zinc Catalyst for the Controlled Polymerization of Lactide. *J. Am. Chem. Soc.* **2003**, *125* (37), 11350–11359. https://doi.org/10.1021/ja0359512.
(48) Fuchs, M.; Schmitz, S.; Schäfer, P. M.; Secker, T.; Metz, A.; Ksiazkiewicz, A. N.; Pich, A.; Kögerler, P.; Monakhov, K. Yu.; Herres-Pawlis, S. Mononuclear Zinc(II) Schiff Base Complexes as Catalysts for the Ring-Opening Polymerization of Lactide. *Eur. Polym. J.* **2020**, *122*, 109302. https://doi.org/10.1016/j.eurpolymj.2019.109302.
(49) Li, M.; Behzadi, S.; Chen, M.; Pang, W.; Wang, F.; Tan, C. Phenoxyimine Ligands Bearing Nitrogen-Containing Second Coordination Spheres for Zinc Catalyzed Stereoselective Ring-Opening Polymerization of *Rac* -Lactide. *Organometallics* **2019**, *38* (2), 461–468. https://doi.org/10.1021/acs.organomet.8b00788.
(50) Tamm, M.; Petrovic, D.; Randoll, S.; Beer, S.; Bannenberg, T.; Jones, P. G.; Grunenberg, J. Structural and Theoretical Investigation of 2-Iminoimidazolines ? Carbene Analogues of Iminophosphoranes. *Org. Biomol. Chem.* **2007**, *5* (3), 523. https://doi.org/10.1039/b615418b.
(51) Hopkinson, M. N.; Richter, C.; Schedler, M.; Glorius, F. An Overview of N-Heterocyclic Carbenes. *Nature* **2014**, *510* (7506), 485–496. https://doi.org/10.1038/nature13384.
(52) Larocque, T. G.; Dastgir, S.; Lavoie, G. G. Coordination and Reactivity Study of Titanium and Zirconium Complexes of the First Imidazol-2-Imine Ethenolate Ligand. *Organometallics* **2013**, *32* (15), 4314–4320. https://doi.org/10.1021/om4004708.
(53) Schäfer, P. M.; Fuchs, M.; Ohligschläger, A.; Rittinghaus, R.; McKeown, P.; Akin, E.; Schmidt, M.; Hoffmann, A.; Liauw, M. A.; Jones, M. D.; Herres-Pawlis, S. Highly Active N,O Zinc Guanidine Catalysts for the Ring-Opening Polymerization of Lactide. *ChemSusChem* **2017**, *10* (18), 3547–3556. https://doi.org/10.1002/cssc.201701237.
(54) Khan, B. S.; Flores-Romero, V.; LeBlanc, J.; Lavoie, G. G. Lactide Polymerization Using Zinc Dichloride Complexes Containing a Neutral Bidentate Ligand with a Diacylated Cyclic Guanidine. *Organometallics* **2022**, *41* (19), 2668–2677. https://doi.org/10.1021/acs.organomet.2c00254.
(55) D'Auria, I.; Ferrara, V.; Tedesco, C.; Kretschmer, W.; Kempe, R.; Pellecchia, C. Guanidinate Zn(II) Complexes as Efficient Catalysts for Lactide Homo- and Copolymerization under Industrially Relevant Conditions. *ACS Appl. Polym. Mater.* **2021**, *3* (8), 4035–4043. https://doi.org/10.1021/acsapm.1c00552.
(56) Soleilhavoup, M.; Bertrand, G. Cyclic (Alkyl)(Amino)Carbenes (CAACs): Stable Carbenes on the Rise. *Acc. Chem. Res.* **2015**, *48* (2), 256–266. https://doi.org/10.1021/ar5003494.
(57) Ma, W.; Zhang, J.-X.; Lin, Z.; Tilley, T. D.; Ye, Q. Synthesis, Structure and DFT Calculations of Mononuclear Cyclic (Alkyl)(Amino) Carbene Supported Titanium(II) Complexes. *Dalton Trans.* **2019**, *48* (40), 14962–14965. https://doi.org/10.1039/C9DT03342D.
(58) Horrer, G.; Krummenacher, I.; Mann, S.; Braunschweig, H.; Radius, U. *N* -Heterocyclic Carbene and Cyclic (Alkyl)(Amino)Carbene Complexes of Vanadium(III) and Vanadium(V). *Dalton Trans.* **2022**, *51* (29), 11054–11071. https://doi.org/10.1039/D2DT01250B.
(59) Luz, C.; Glok, E.; Horrer, G.; Radius, U. N-Heterocyclic Carbene and Cyclic (Alkyl)(Amino)Carbene Complexes of Molybdenum(IV) and Tungsten(IV). *Dalton Trans.* **2022**, *51* (47), 18337–18352. https://doi.org/10.1039/D2DT03409C.
(60) Morvan, J.; Mauduit, M.; Bertrand, G.; Jazzar, R. Cyclic (Alkyl)(Amino)Carbenes (CAACs) in Ruthenium Olefin Metathesis. *ACS Catal.* **2021**, *11* (3), 1714–1748. https://doi.org/10.1021/acscatal.0c05508.
(61) Tran, B. L.; Fulton, J. L.; Linehan, J. C.; Balasubramanian, M.; Lercher, J. A.; Bullock, R. M. Operando XAFS Studies on Rh(CAAC)-Catalyzed Arene Hydrogenation. *ACS Catal.* **2019**, *9* (5), 4106–4114. https://doi.org/10.1021/acscatal.8b04929.

(62) Paul, U. S. D.; Radius, U. Synthesis and Reactivity of Cyclic (Alkyl)(Amino)Carbene Stabilized Nickel Carbonyl Complexes. *Organometallics* **2017**, *36* (7), 1398–1407. https://doi.org/10.1021/acs.organomet.7b00109.
(63) Marigo, N.; Morgenstern, B.; Biffis, A.; Munz, D. (CAAC)Pd(Py) Catalysts Disproportionate to $Pd(CAAC)_2$. *Organometallics* **2023**, *42* (13), 1567–1572. https://doi.org/10.1021/acs.organomet.3c00150.
(64) Proetto, M. T.; Alexander, K.; Melaimi, M.; Bertrand, G.; Gianneschi, N. C. Cyclic (Alkyl)(Amino)Carbene (CAAC) Gold(I) Complexes as Chemotherapeutic Agents. *Chemistry A European J* **2021**, *27* (11), 3772–3778. https://doi.org/10.1002/chem.202004317.
(65) Melaimi, M.; Jazzar, R.; Soleilhavoup, M.; Bertrand, G. Cyclic (Alkyl)(Amino)Carbenes (CAACs): Recent Developments. *Angew Chem Int Ed* **2017**, *56* (34), 10046–10068. https://doi.org/10.1002/anie.201702148.
(66) Goettel, J. T.; Gao, H.; Dotzauer, S.; Braunschweig, H. ^{Me} CAAC=N$^-$: A Cyclic (Alkyl)(Amino)Carbene Imino Ligand. *Chem. – Eur. J.* **2020**, *26* (5), 1136–1143. https://doi.org/10.1002/chem.201904715.
(67) Huynh, S.; Arrowsmith, M.; Meier, L.; Dietz, M.; Härterich, M.; Michel, M.; Gärtner, A.; Braunschweig, H. Cyclic Alkyl(Amino)Iminates (CAAIs) as Strong 2σ,4π-Electron Donor Ligands for the Stabilisation of Boranes and Diboranes(4): A Synthetic and Computational Study. *Dalton Trans.* **2023**, *52* (12), 3869–3876. https://doi.org/10.1039/D3DT00298E.
(68) Li, M.; Cai, Z.; Eisen, M. S. Neutral Nickel(II) Complexes Bearing Aryloxide Imidazolin-2-Imine Ligands for Efficient Copolymerization of Norbornene and Polar Monomers. *Organometallics* **2018**, *37* (24), 4753–4762. https://doi.org/10.1021/acs.organomet.8b00752.
(69) Li, M.; Eisen, M. S.; Cai, Z. Robust Cobalt Catalysts with N,N-Bidentate Aldimine Imidazolidine-2-Imine/Guanidine Ancillary Ligand for Isoprene Polymerization. *Journal of Catalysis* **2024**, *435*, 115581. https://doi.org/10.1016/j.jcat.2024.115581.
(70) Liu, N.; Liu, B.; Cui, D. Alkaline Earth Metal Complexes Stabilized by Amidine and Guanidine Ligands: Synthesis, Structure and Their Catalytic Activity towards Polymerization of *Rac* -Lactide. *Dalton Trans.* **2018**, *47* (36), 12623–12632. https://doi.org/10.1039/C8DT01434E.
(71) Kessler, H.; Leibfritz, D. Nachweis Innermolekularer Beweglichkeit Durch NMR-Spektroskopie, XVIII1) Vergleich Der Inversionsgeschwindigkeiten Am Doppelt Gebundenen Stickstoff Bei Guanidinen Und Imidazolidiniminen. *Justus Liebigs Annalen der Chemie* **1970**, *737* (1), 53–60. https://doi.org/10.1002/jlac.19707370106.
(72) Back, O.; Henry-Ellinger, M.; Martin, C. D.; Martin, D.; Bertrand, G. ^{31} P NMR Chemical Shifts of Carbene–Phosphinidene Adducts as an Indicator of the π-Accepting Properties of Carbenes. *Angew Chem Int Ed* **2013**, *52* (10), 2939–2943. https://doi.org/10.1002/anie.201209109.
(73) Johnson, A. L.; Davidson, M. G.; Lunn, M. D.; Mahon, M. F. Synthesis, Isolation and Structural Investigation of Schiff-Base Alkoxytitanium Complexes: Steric Limitations of Ligand Coordination. *Eur. J. Inorg. Chem.* **2006**, No. 15, 3088–3098. https://doi.org/10.1002/ejic.200600113.
(74) Börner, J.; Flörke, U.; Huber, K.; Döring, A.; Kuckling, D.; Herres-Pawlis, S. Lactide Polymerisation with Air-Stable and Highly Active Zinc Complexes with Guanidine–Pyridine Hybrid Ligands. *Chemistry – A European Journal* **2009**, *15* (10), 2362–2376. https://doi.org/10.1002/chem.200802128.
(75) Flisak, Z. Theoretical Study of Isomerism in Phenoxyimine-Based Precursors of Coordinative Olefin Polymerization Catalysts. *J. Mol. Catal. A: Chem.* **2010**, *316* (1–2), 83–89. https://doi.org/10.1016/j.molcata.2009.10.003.
(76) Strauch, J.; Warren, T. H.; Erker, G.; Fröhlich, R.; Saarenketo, P. Formation and Structural Properties of Salicylaldiminato Complexes of Zirconium and Titanium. *Inorg. Chim. Acta* **2000**, *300–302*, 810–821. https://doi.org/10.1016/S0020-1693(99)00573-3.

(77) Espartero, J. L.; Rashkov, I.; Li, S. M.; Manolova, N.; Vert, M. NMR Analysis of Low Molecular Weight Poly(Lactic Acid)s. *Macromolecules* **1996**, *29* (10), 3535–3539. https://doi.org/10.1021/ma950529u.
(78) Lewinski, P.; Sosnowski, S.; Kazmierski, S.; Penczek, S. L -Lactide Polymerization Studied by ^{1}H NMR with Diffusion-Ordered Spectroscopy (DOSY): A "One NMR Tube Experiment" Providing Data on Monomer Conversion, Polymer Structure, M_n and M_w. *Polym. Chem.* **2015**, *6* (24), 4353–4357. https://doi.org/10.1039/C5PY00455A.
(79) Grubbs, R. B.; Grubbs, R. H. *50th Anniversary Perspective* : Living Polymerization—Emphasizing the *Molecule* in *Macromolecules*. *Macromolecules* **2017**, *50* (18), 6979–6997. https://doi.org/10.1021/acs.macromol.7b01440.
(80) Le Roux, E. Recent Advances on Tailor-Made Titanium Catalysts for Biopolymer Synthesis. *Coordination Chemistry Reviews* **2016**, *306*, 65–85. https://doi.org/10.1016/j.ccr.2015.06.006.
(81) Chisholm, M. H.; Iyer, S. S.; McCollum, D. G.; Pagel, M.; Werner-Zwanziger, U. Microstructure of Poly(Lactide). Phase-Sensitive HETCOR Spectra of Poly(*Meso* -Lactide), Poly(*r Ac* -Lactide), and Atactic Poly(Lactide). *Macromolecules* **1999**, *32* (4), 963–973. https://doi.org/10.1021/ma9806864.
(82) Zell, M. T.; Padden, B. E.; Paterick, A. J.; Thakur, K. A. M.; Kean, R. T.; Hillmyer, M. A.; Munson, E. J. Unambiguous Determination of the ^{13}C and ^{1}H NMR Stereosequence Assignments of Polylactide Using High-Resolution Solution NMR Spectroscopy. *Macromolecules* **2002**, *35* (20), 7700–7707. https://doi.org/10.1021/ma0204148.
(83) Chuma, A.; Horn, H. W.; Swope, W. C.; Pratt, R. C.; Zhang, L.; Lohmeijer, B. G. G.; Wade, C. G.; Waymouth, R. M.; Hedrick, J. L.; Rice, J. E. The Reaction Mechanism for the Organocatalytic Ring-Opening Polymerization of L -Lactide Using a Guanidine-Based Catalyst: Hydrogen-Bonded or Covalently Bound? *J. Am. Chem. Soc.* **2008**, *130* (21), 6749–6754. https://doi.org/10.1021/ja0764411.
(84) Baltrun, M.; Watt, F. A.; Schoch, R.; Wölper, C.; Neuba, A. G.; Hohloch, S. A New Bis-Phenolate Mesoionic Carbene Ligand for Early Transition Metal Chemistry. *Dalton Trans.* **2019**, *48* (39), 14611–14625. https://doi.org/10.1039/C9DT03099A.
(85) Bellina, F.; Lessi, M.; Marianetti, G.; Panattoni, A. Highly Regioselective C-5 Alkynylation of Imidazoles by One-Pot Sequential Bromination and Sonogashira Cross Coupling. *Tetrahedron Lett.* **2015**, *56* (25), 3855–3857. https://doi.org/10.1016/j.tetlet.2015.04.094.
(86) Maronna, A.; Hübner, O.; Enders, M.; Kaifer, E.; Himmel, H.-J. Bisguanidines with Biphenyl, Binaphthyl, and Bipyridyl Cores: Proton-Sponge Properties and Coordination Chemistry. *Chemistry – A European Journal* **2013**, *19* (27), 8958–8977. https://doi.org/10.1002/chem.201204294.
(87) Li, M.; Shu, X.; Cai, Z.; Eisen, M. S. Synthesis, Structures, and Norbornene Polymerization Behavior of Neutral Nickel(II) and Palladium(II) Complexes Bearing Aryloxide Imidazolidin-2-Imine Ligands. *Organometallics* **2018**, *37* (7), 1172–1180. https://doi.org/10.1021/acs.organomet.8b00059.
(88) Dolomanov, O. V.; Bourhis, L. J.; Gildea, R. J.; Howard, J. A. K.; Puschmann, H. OLEX2: A Complete Structure Solution, Refinement and Analysis Program. *J. Appl. Cryst.* **2009**, No. 42, 339–341.
(89) Sheldrick, G. M. Crystal Structure Refinement with *SHELXL*. *Acta Crystallogr., Sect. C: Struct. Chem.* **2015**, *71* (1), 3–8. https://doi.org/10.1107/S2053229614024218.
(90) Frisch, M. J.; Trucks, G. W.; Schlegel, H. B.; Scuseria, G. E.; Robb, M. A.; Cheeseman, J. R.; Scalmani, G.; Barone, V.; Petersson, G. A.; Nakatsuji, H.; Li, X.; Caricato, M.; Marenich, A.; Bloino, J.; Janesko, B. G.; Gomperts, R.; Mennucci, B.; Hratchian, H. P.; Ortiz, J. V.; Izmaylov, A. F.; Sonnenberg, J. L.; Williams-Young, D.; Ding, F.; Lipparini, F.; Egidi, F.; Goings, J.; Peng, B.; Petrone, A.; Henderson, T.; Ranasinghe, D.; Zakrzewski, V. G.; Gao, J.; Rega, N.; Zheng, G.; Liang, W.; Hada, M.; Ehara, M.; Toyota, K.; Fukuda, R.; Hasegawa, J.; Ishida, M.; Nakajima, T.; Honda, Y.; Kitao, O.; Nakai, H.; Vreven, T.; Throssell, K.; Montgomery, JrJ. A.; Peralta, J. E.; Ogliaro, F.; Bearpark, M.; Heyd, J. J.; Brothers, E.; Kudin, K. N.; Staroverov, V. N.; Keith, T.; Kobayashi, R.; Normand, J.; Raghavachari, K.; Rendell, A.;

Burant, J. C.; Iyengar, S. S.; Tomasi, J.; Cossi, M.; Millam, J. M.; Klene, M.; Adamo, C.; Cammi, R.; Ochterski, J. W.; Martin, R. L.; Morokuma, K.; Farkas, O.; Foresman, J. B.; Fox, D. J. Gaussian 16, Revision C.01, 2016.

(91) Grimme, S.; Antony, J.; Ehrlich, S.; Krieg, H. A Consistent and Accurate *Ab Initio* Parametrization of Density Functional Dispersion Correction (DFT-D) for the 94 Elements H-Pu. *J. Chem. Phys.* **2010**, *132* (15), 154104–154122. https://doi.org/10.1063/1.3382344.

(92) Wheaton, C. A.; Hayes, P. G.; Ireland, B. J. Complexes of Mg, Ca and Zn as Homogeneous Catalysts for Lactide Polymerization. *Dalton Trans.* **2009**, No. 25, 4832–4846. https://doi.org/10.1039/b819107g.

(93) Jones, M. D.; Davidson, M. G.; Keir, C. G.; Hughes, L. M.; Mahon, M. F.; Apperley, D. C. Zinc(II) Homogeneous and Heterogeneous Species and Their Application for the Ring-Opening Polymerisation of Rac-Lactide. *Eur. J. Inorg. Chem.* **2009**, *2009* (5), 635–642. https://doi.org/10.1002/ejic.200801049.

(94) Nuñez-Dallos, N.; Posada, A. F.; Hurtado, J. Coumarin Salen-Based Zinc Complex for Solvent-Free Ring Opening Polymerization of ε-Caprolactone. *Tetrahedron Lett.* **2017**, *58* (10), 977–980. https://doi.org/10.1016/j.tetlet.2017.01.088.

(95) McKeown, P.; McCormick, S. N.; Mahon, M. F.; Jones, M. D. Highly Active Mg(II) and Zn(II) Complexes for the Ring Opening Polymerisation of Lactide. *Polym. Chem.* **2018**, *9* (44), 5339–5347. https://doi.org/10.1039/C8PY01369A.

(96) Munzeiwa, W. A.; Nyamori, V. O.; Omondi, B. N,O-Amino-Phenolate Mg(II) and Zn(II) Schiff Base Complexes: Synthesis and Application in Ring-Opening Polymerization of ε-Caprolactone and Lactides. *Inorganica Chimica Acta* **2019**, *487*, 264–274. https://doi.org/10.1016/j.ica.2018.12.028.

(97) Hsieh, Y.-L.; Benchaphanthawee, W.; Teng, H.-H.; Huang, N.; Yang, J.-H.; Sun, J.-R.; Lee, G.-H.; Kungwan, N.; Peng, C.-H. Ring-Opening Polymerization of Cyclic Esters Mediated by Zinc Complexes Coordinated with Benzotriazo-Based Imino-Phenoxy Ligands. *Polymer* **2023**, *267*, 125687. https://doi.org/10.1016/j.polymer.2023.125687.

(98) Kan, C.; Hu, J.; Huang, Y.; Wang, H.; Ma, H. Highly Isoselective and Active Zinc Catalysts for *Rac* -Lactide Polymerization: Effect of Pendant Groups of Aminophenolate Ligands. *Macromolecules* **2017**, *50* (20), 7911–7919. https://doi.org/10.1021/acs.macromol.7b01420.

(99) Pongpanit, T.; Saeteaw, T.; Chumsaeng, P.; Chasing, P.; Phomphrai, K. Highly Active Homoleptic Zinc and Magnesium Complexes Supported by Constrained Reduced Schiff Base Ligands for the Ring-Opening Polymerization of Lactide. *Inorg. Chem.* **2021**, *60* (22), 17114–17122. https://doi.org/10.1021/acs.inorgchem.1c02382.

(100) Vaillant-Coindard, V.; Théron, B.; Printz, G.; Chotard, F.; Balan, C.; Rousselin, Y.; Richard, P.; Tolbatov, I.; Fleurat-Lessard, P.; Bodio, E.; Malacea-Kabbara, R.; Bayardon, J.; Dagorne, S.; Le Gendre, P. Phenoxy-Amidine Ligands: Toward Lactic Acid-Tolerant Catalysts for Lactide Ring-Opening Polymerization. *Organometallics* **2022**, *41* (21), 2920–2932. https://doi.org/10.1021/acs.organomet.2c00343.

(101) Théron, B.; Vaillant-Coindard, V.; Balan, C.; Rousselin, Y.; Bayardon, J.; Malacea-Kabbara, R.; Le Gendre, P. Al and Zn Phenoxy-Amidine Complexes for Lactide ROP Catalysis. *Dalton Trans.* **2023**, *52* (23), 7854–7868. https://doi.org/10.1039/D3DT01216F.

(102) Rahman, Md. M.; Pyle, D. J.; Bisz, E.; Dziuk, B.; Ejsmont, K.; Lalancette, R.; Wang, Q.; Chen, H.; Szostak, R.; Szostak, M. Evaluation of Cyclic Amides as Activating Groups in N–C Bond Cross-Coupling: Discovery of N-Acyl-δ-Valerolactams as Effective Twisted Amide Precursors for Cross-Coupling Reactions. *J. Org. Chem.* **2021**, *86* (15), 10455–10466. https://doi.org/10.1021/acs.joc.1c01110.

(103) Bai, J.; Xiao, X.; Zhang, Y.; Chao, J.; Chen, X. β-Pyridylenolate Zinc Catalysts for the Ring-Opening Homo- and Copolymerization of ε-Caprolactone and Lactides. *Dalton Trans.* **2017**, *46* (30), 9846–9858. https://doi.org/10.1039/C7DT01877K.
(104) Yang, L.; Powell, D. R.; Houser, R. P. Structural Variation in Copper(I) Complexes with Pyridylmethylamide Ligands: Structural Analysis with a New Four-Coordinate Geometry Index, τ_4. *Dalton Trans.* **2007**, No. 9, 955–964. https://doi.org/10.1039/B617136B.
(105) Hermann, A.; Becker, T.; Schäfer, M. A.; Hoffmann, A.; Herres-Pawlis, S. Effective Ligand Design: Zinc Complexes with Guanidine Hydroquinoline Ligands for Fast Lactide Polymerization and Chemical Recycling. *ChemSusChem* **2022**, *15* (18), e202201075. https://doi.org/10.1002/cssc.202201075.
(106) Campos-Rivera, Lya; LeBlanc, Jesse; Flores-Romero, Victor; Lavoie, Gino. Unpublished Results. *Unpublished results*.
(107) Meimoun, J.; Favrelle-Huret, A.; Bria, M.; Merle, N.; Stoclet, G.; De Winter, J.; Mincheva, R.; Raquez, J.-M.; Zinck, P. Epimerization and Chain Scission of Polylactides in the Presence of an Organic Base, TBD. *Polymer Degradation and Stability* **2020**, *181*, 109188. https://doi.org/10.1016/j.polymdegradstab.2020.109188.
(108) Labet, M.; Thielemans, W. Synthesis of Polycaprolactone: A Review. *Chem. Soc. Rev.* **2009**, *38* (12), 3484. https://doi.org/10.1039/b820162p.
(109) Jenkins, D. T.; Fazekas, E.; Patterson, S. B. H.; Rosair, G. M.; Vilela, F.; McIntosh, R. D. Polymetallic Group 4 Complexes: Catalysts for the Ring Opening Polymerisation of Rac-Lactide. *Catalysts* **2021**, *11* (5). https://doi.org/10.3390/catal11050551.
(110) Kim, Y.; Jnaneshwara, G. K.; Verkade, J. G. Titanium Alkoxides as Initiators for the Controlled Polymerization of Lactide. *Inorg. Chem.* **2003**, *42* (5), 1437–1447. https://doi.org/10.1021/ic026139n.
(111) Jazzar, R.; Dewhurst, R. D.; Bourg, J.; Donnadieu, B.; Canac, Y.; Bertrand, G. Intramolecular "Hydroiminiumation" of Alkenes: Application to the Synthesis of Conjugate Acids of Cyclic Alkyl Amino Carbenes (CAACs). *Angew Chem Int Ed* **2007**, *46* (16), 2899–2902. https://doi.org/10.1002/anie.200605083.
(112) Madron Du Vigné, A.; Cramer, N. Chiral Cyclic Alkyl Amino Carbene (CAAC) Transition-Metal Complexes: Synthesis, Structural Analysis, and Evaluation in Asymmetric Catalysis. *Organometallics* **2022**, *41* (19), 2731–2741. https://doi.org/10.1021/acs.organomet.2c00351.
(113) Zhou, L.; Zhang, D.; Hu, J.; Wu, Y.; Geng, J.; Hu, X. Thermal Dehydrogenation and Hydrolysis of BH_3NH_3 Catalyzed by Cyclic (Alkyl)(Amino)Carbene Iridium Complexes under Mild Conditions. *Organometallics* **2021**, *40* (15), 2643–2650. https://doi.org/10.1021/acs.organomet.1c00302.
(114) Fuchs, M.; Schäfer, P. M.; Wagner, W.; Krumm, I.; Walbeck, M.; Dietrich, R.; Hoffmann, A.; Herres-Pawlis, S. A Multitool for Circular Economy: Fast Ring-Opening Polymerization and Chemical Recycling of (Bio)Polyesters Using a Single Aliphatic Guanidine Carboxy Zinc Catalyst. *ChemSusChem* **2023**, *16* (12), e202300192. https://doi.org/10.1002/cssc.202300192.
(115) Stewart, J. A.; Powell, L. T. W.; Cullen, M. J.; Kociok-Köhn, G.; Davidson, M. G.; Jones, M. D. Imino-Pyrrole Zn(II) Complexes for the Rapid and Selective Chemical Recycling of Commodity Polymers. *Angewandte Chemie International Edition* **2025**, *n/a* (n/a), e202502845. https://doi.org/10.1002/anie.202502845.
(116) Payne, J.; McKeown, P.; Jones, M. D. A Circular Economy Approach to Plastic Waste. *Polym. Degrad. Stab.* **2019**, *165*, 170–181. https://doi.org/10.1016/j.polymdegradstab.2019.05.014.
(117) Leibfarth, F. A.; Moreno, N.; Hawker, A. P.; Shand, J. D. Transforming Polylactide into Value-Added Materials. *Journal of Polymer Science Part A: Polymer Chemistry* **2012**, *50* (23), 4814–4822. https://doi.org/10.1002/pola.26303.

(118) Alberti, C.; Damps, N.; Meißner, R. R. R.; Enthaler, S. Depolymerization of End-of-Life Poly(Lactide) via 4-Dimethylaminopyridine-Catalyzed Methanolysis. *ChemistrySelect* **2019**, *4* (23), 6845–6848. https://doi.org/10.1002/slct.201901316.

Chapter 6 Appendix

TABLE OF CONTENTS APPENDIX

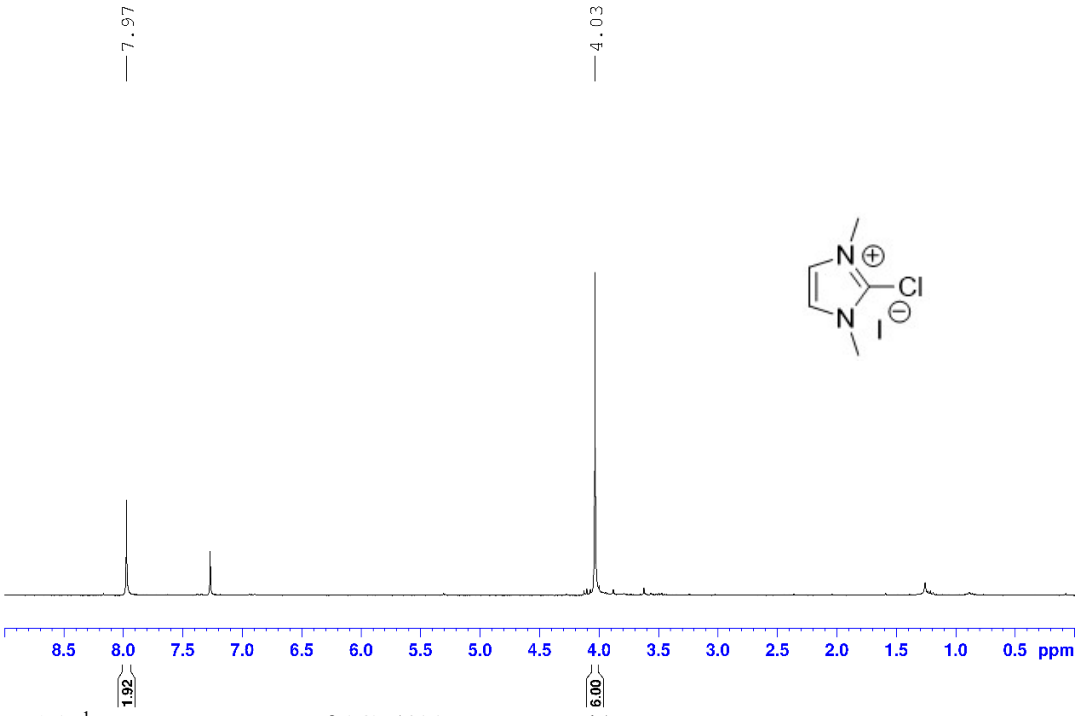

Figure A1. ^{1}H NMR spectrum of **1Cl** (400 MHz, $CDCl_3$)

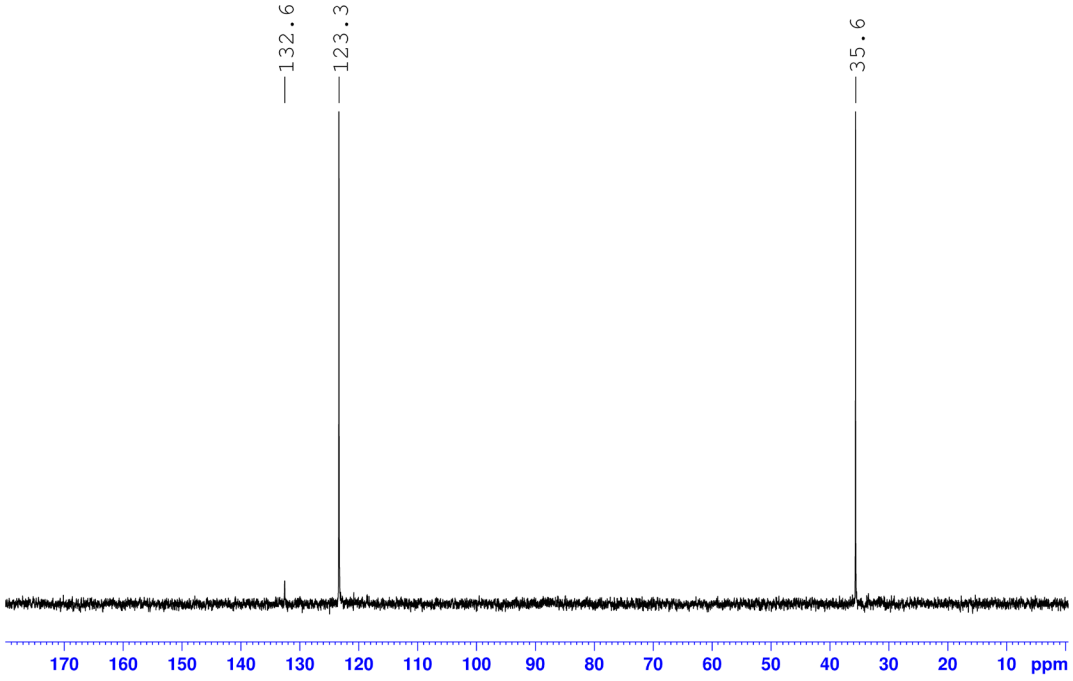

Figure A2. $^{13}C\{^{1}H\}$ NMR spectrum of **1Cl** (100 MHz, D_2O)

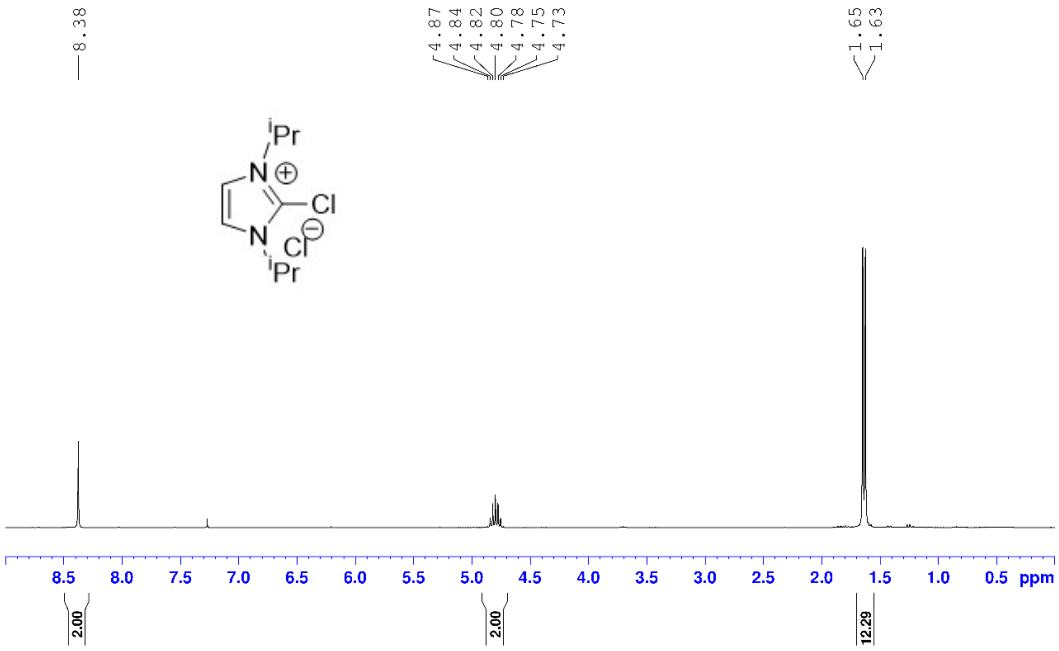

Figure A3. ^{1}H NMR spectrum of **2Cl** (300 MHz, $CDCl_3$)

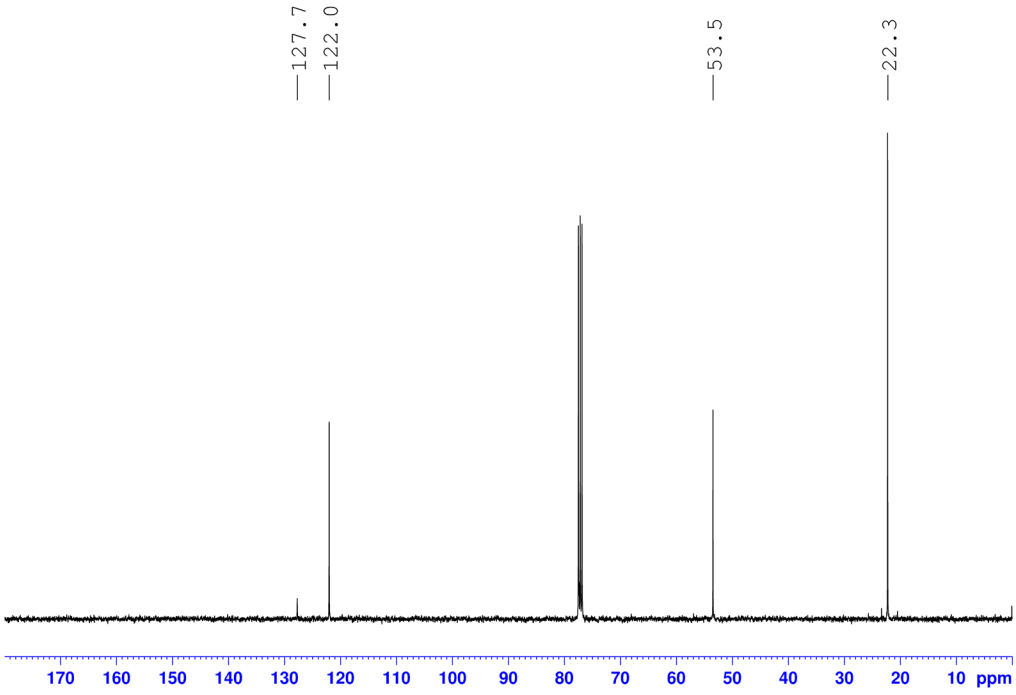

Figure A4. $^{13}C\{^{1}H\}$ NMR spectrum of **2Cl** (100 MHz, $CDCl_3$)

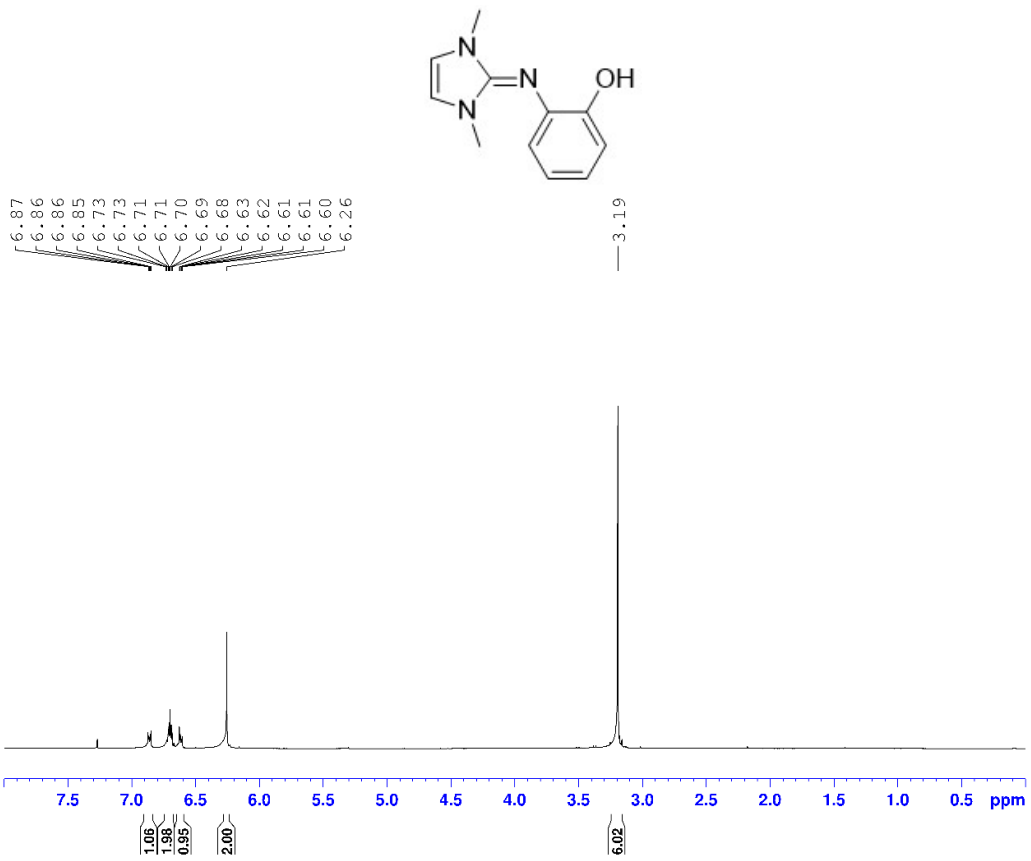

Figure A5. ^{1}H NMR spectrum of **L1a**H (300 MHz, $CDCl_3$)

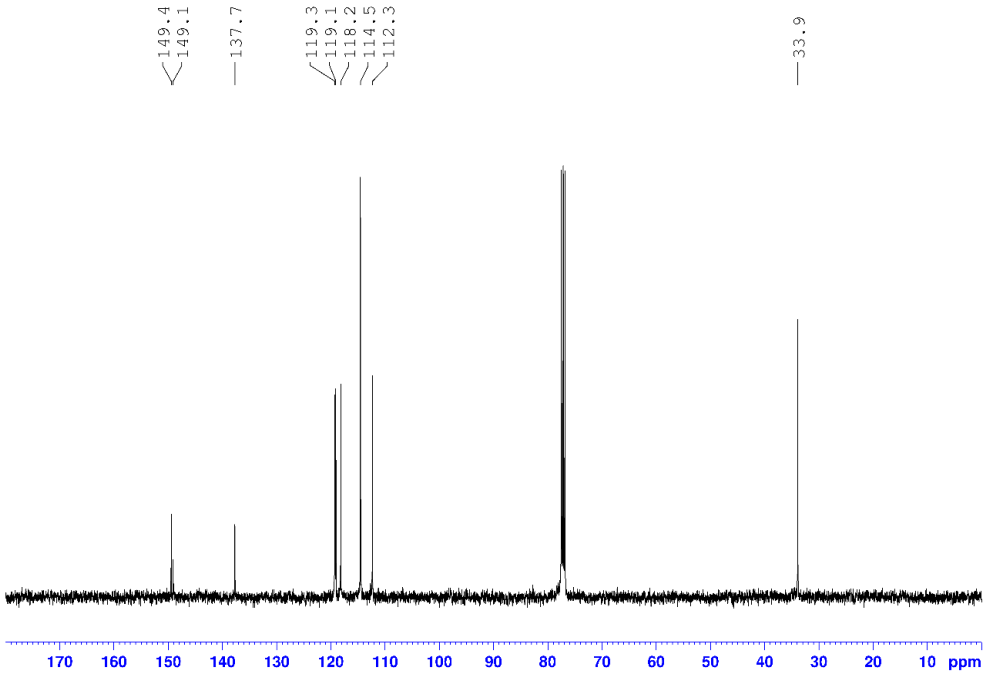

Figure A6. $^{13}C\{^{1}H\}$ NMR spectrum of **L1a**H (75 MHz, $CDCl_3$)

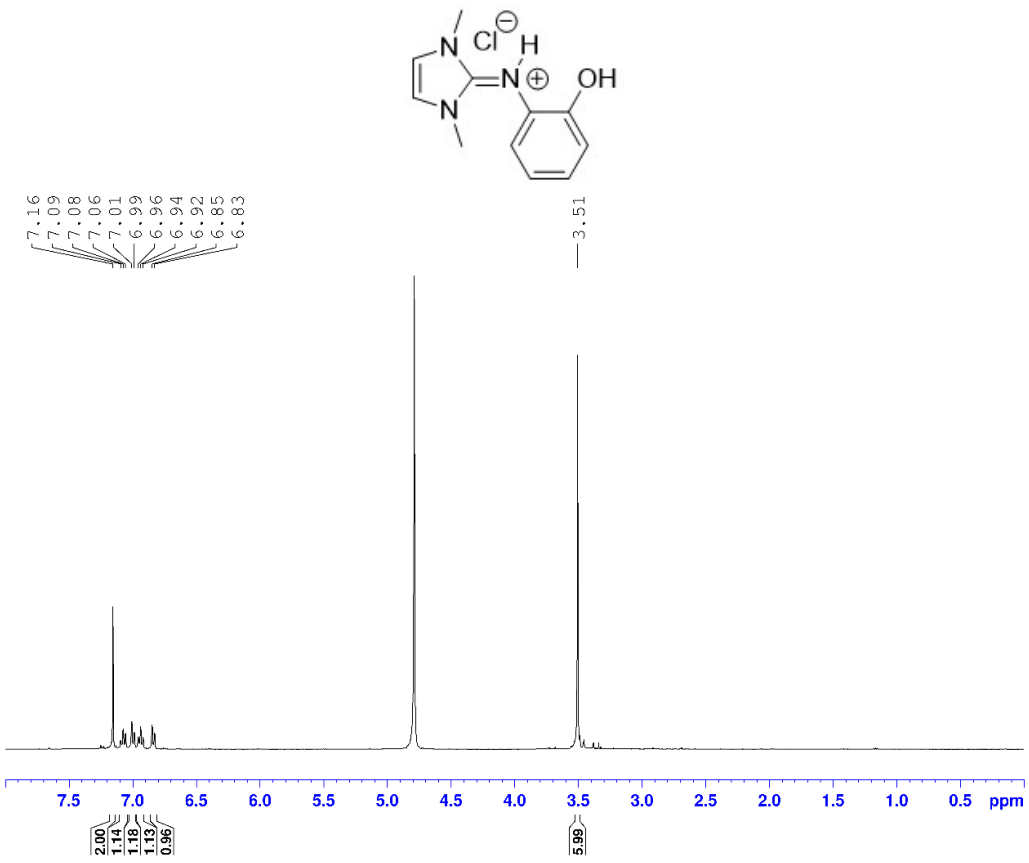

Figure A7. ^{1}H NMR spectrum of **L1a**H·HCl (400 MHz, D2O)

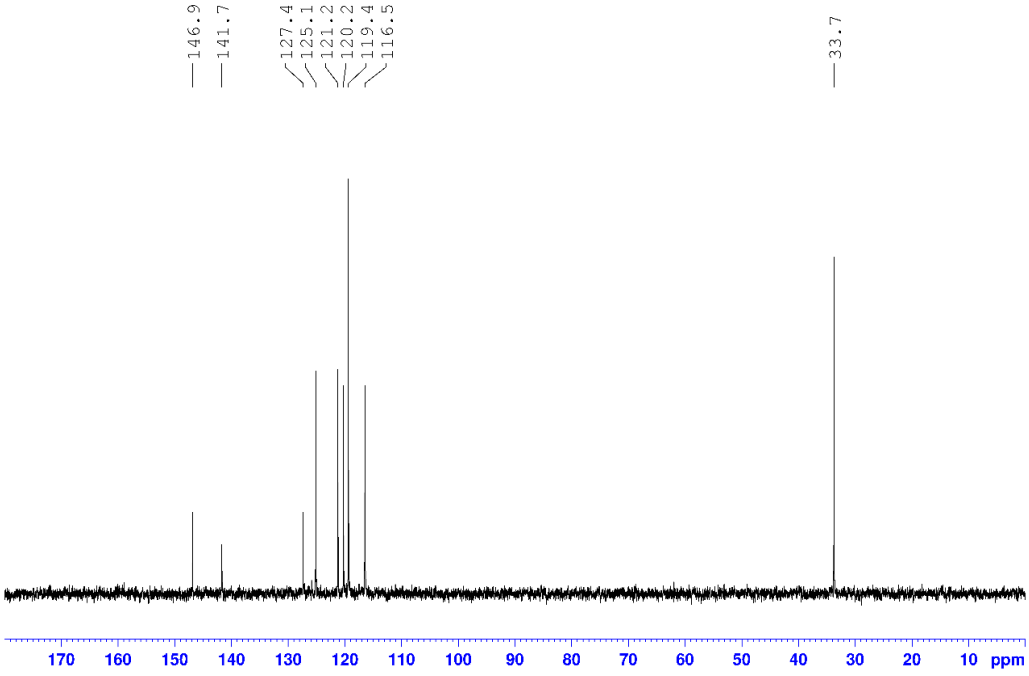

Figure A8. ^{13}C{^{1}H} NMR spectrum of **L1a**H·HCl (100 MHz, D_2O)

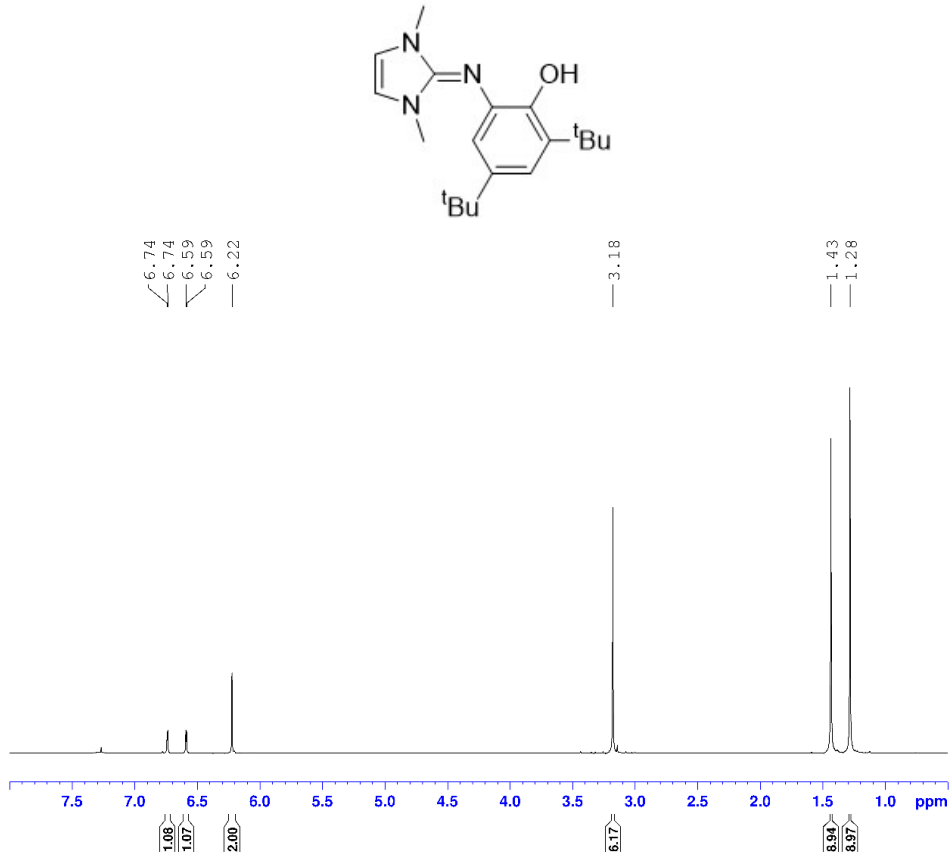

Figure A9. ^{1}H NMR spectrum of **L1b**H (400 MHz, $CDCl_3$)

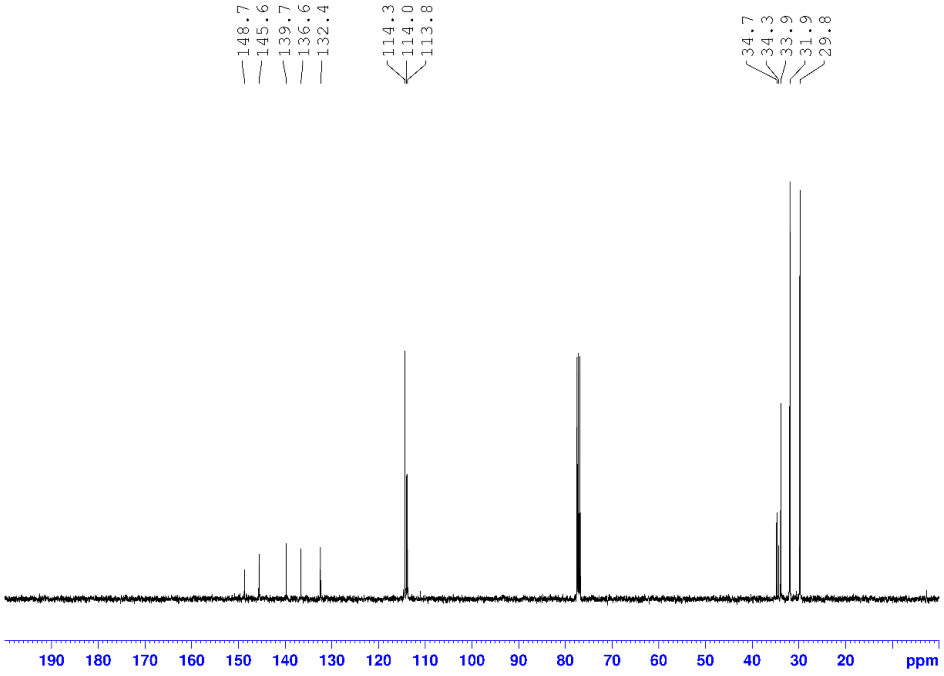

Figure A10. ^{13}C{^{1}H} NMR spectrum of **L1b**H (75 MHz, $CDCl_3$)

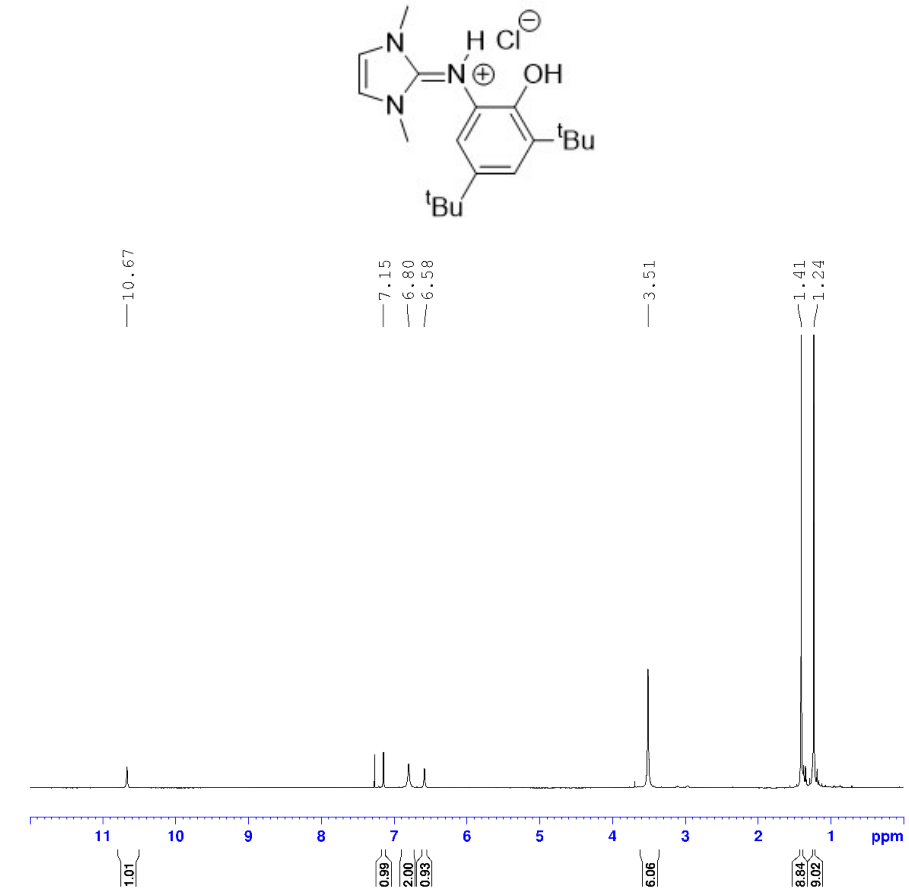

Figure A11. ^{1}H NMR spectrum of **L1b**H·HCl (400 MHz, $CDCl_3$)

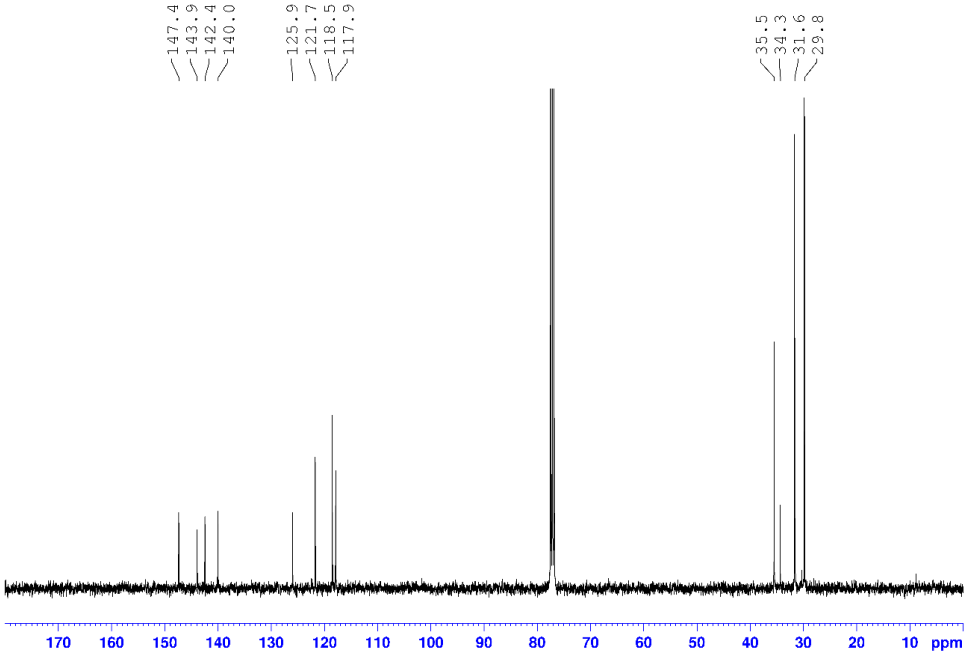

Figure A12. ^{13}C NMR spectrum of **L1b**H·HCl (100 MHz, $CDCl_3$)

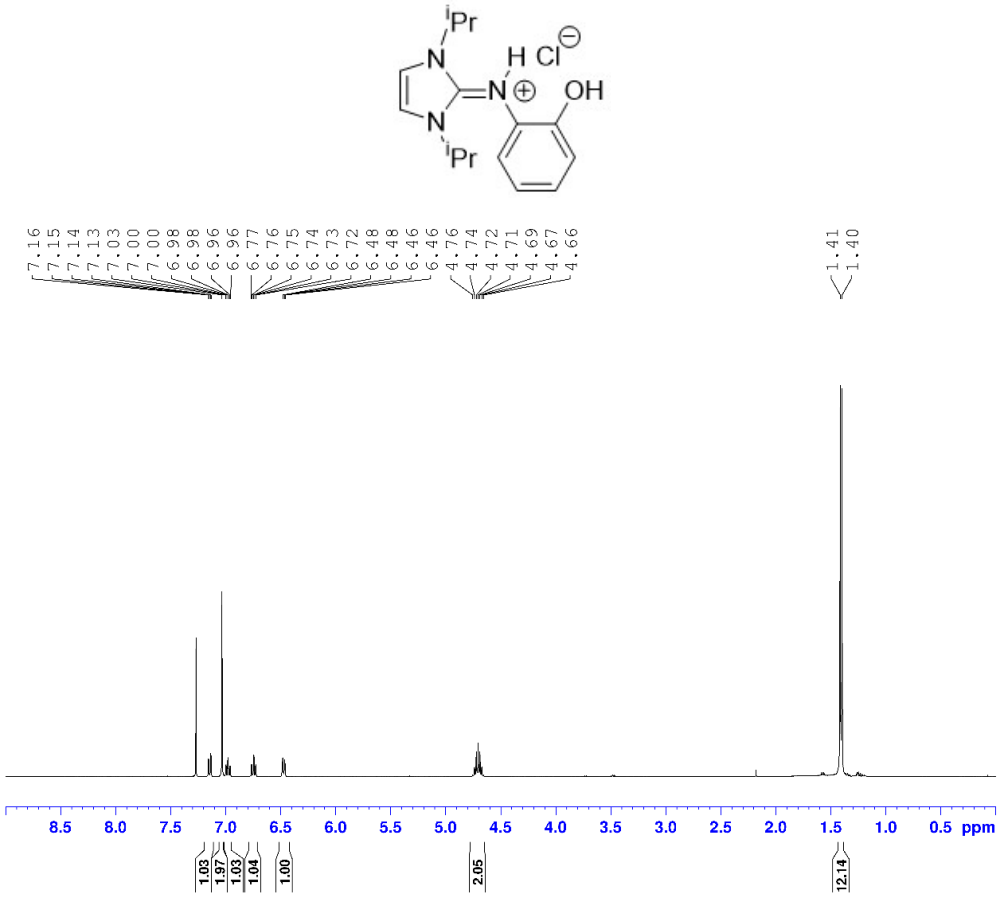

Figure A13. ^{1}H NMR spectrum of **L2a**H·HCl (300 MHz, $CDCl_3$)

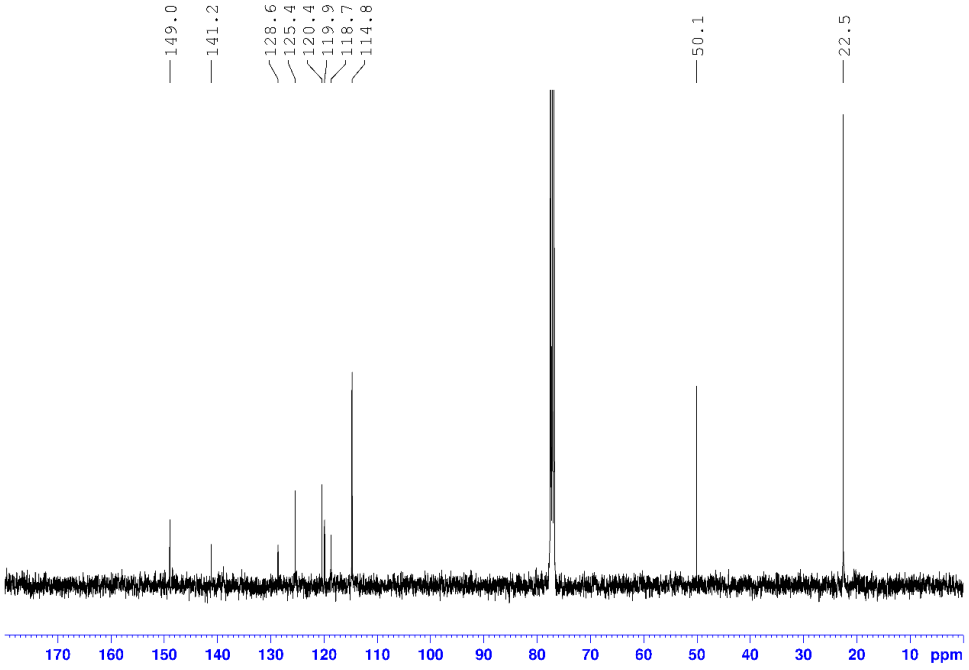

Figure A14. ^{13}C{^{1}H} NMR spectrum of **L2a**H·HCl (75 MHz, $CDCl_3$)

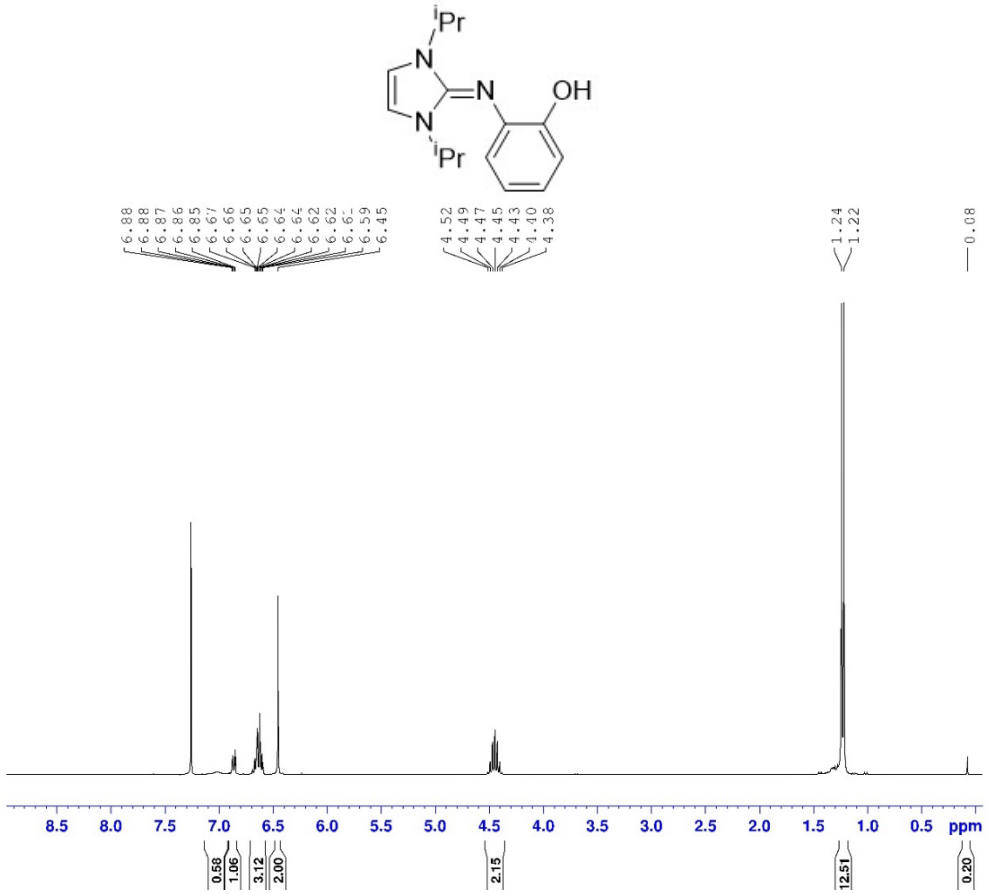

Figure A15. ^{1}H NMR spectrum of **L2a**H (300 MHz, $CDCl_3$)

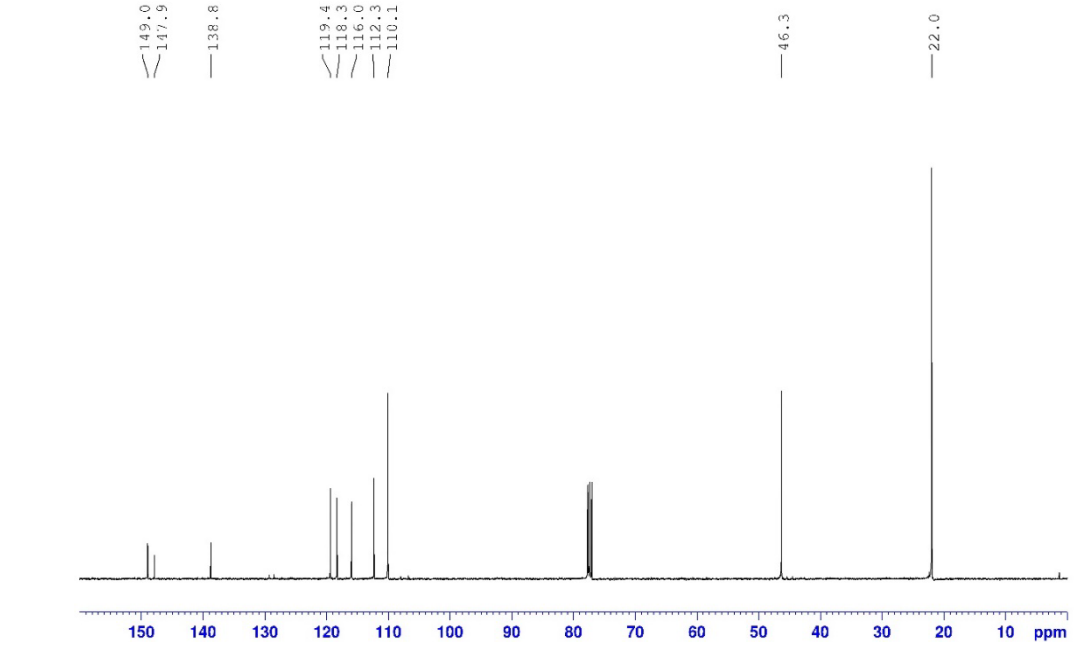

Figure A16. $^{13}C\{^{1}H\}$ NMR spectrum of **L2a**H (75 MHz, $CDCl_3$)

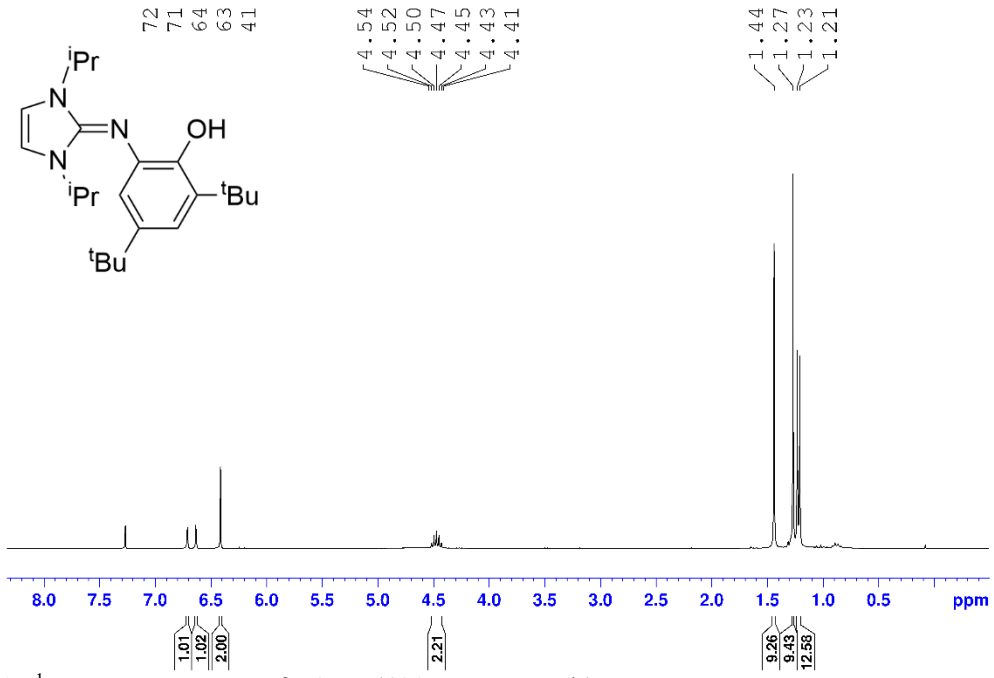

Figure A17 ^{1}H NMR spectrum of **L2b**H (400 MHz, $CDCl_3$)

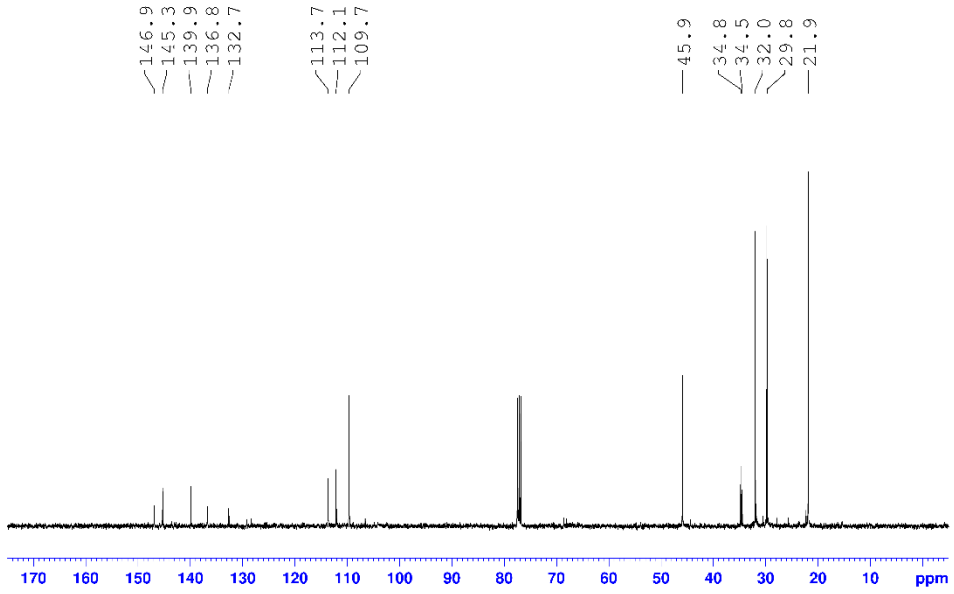

Figure A18 ^{13}C{^{1}H} NMR spectrum of **L2b**H (100 MHz, $CDCl_3$)

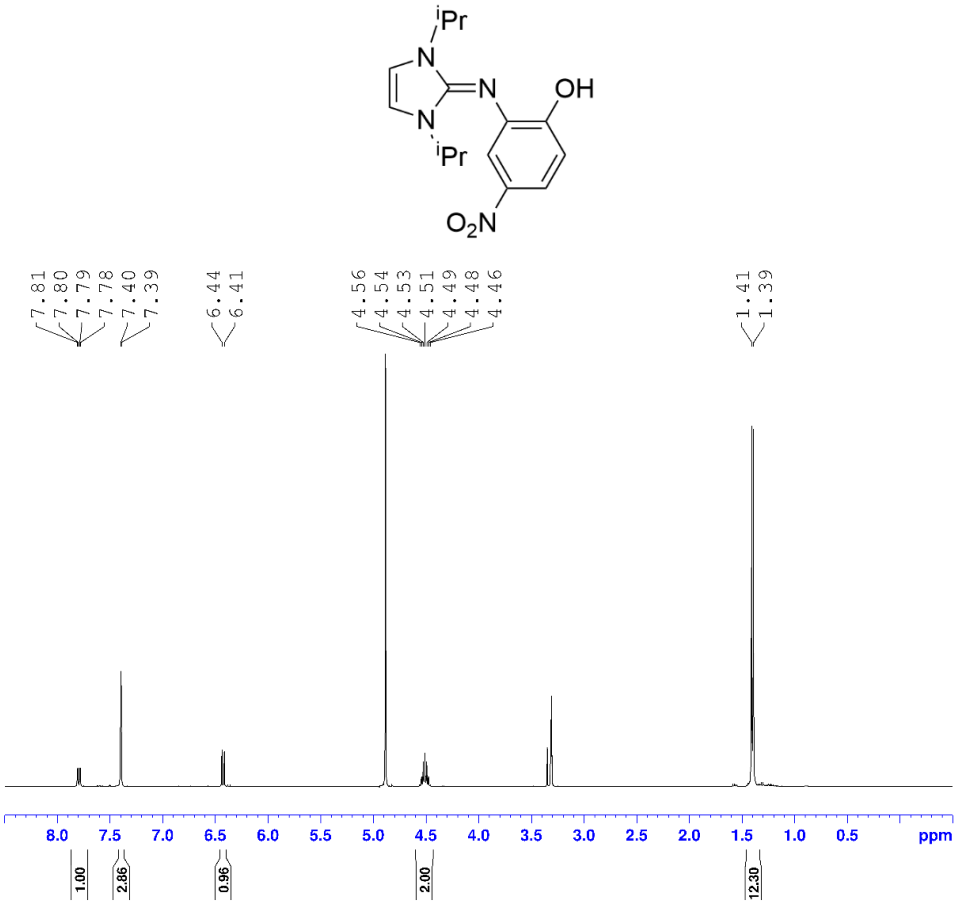

Figure A19 ^{1}H NMR spectrum of **L2c**H (400 MHz, CD_3OD)

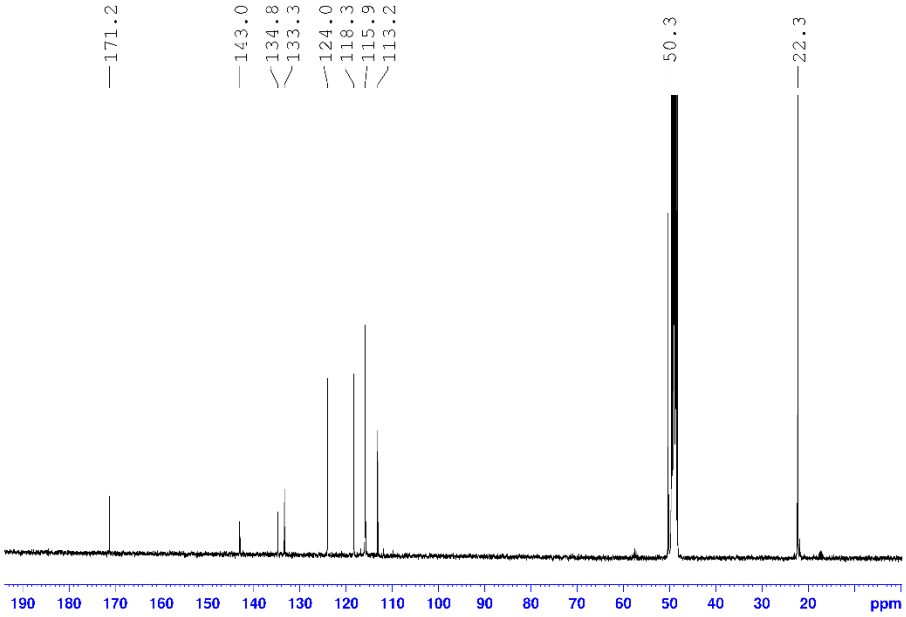

Figure A20 $^{13}C\{^{1}H\}$ NMR spectrum of **L2c**H (100 MHz, CD_3OD)

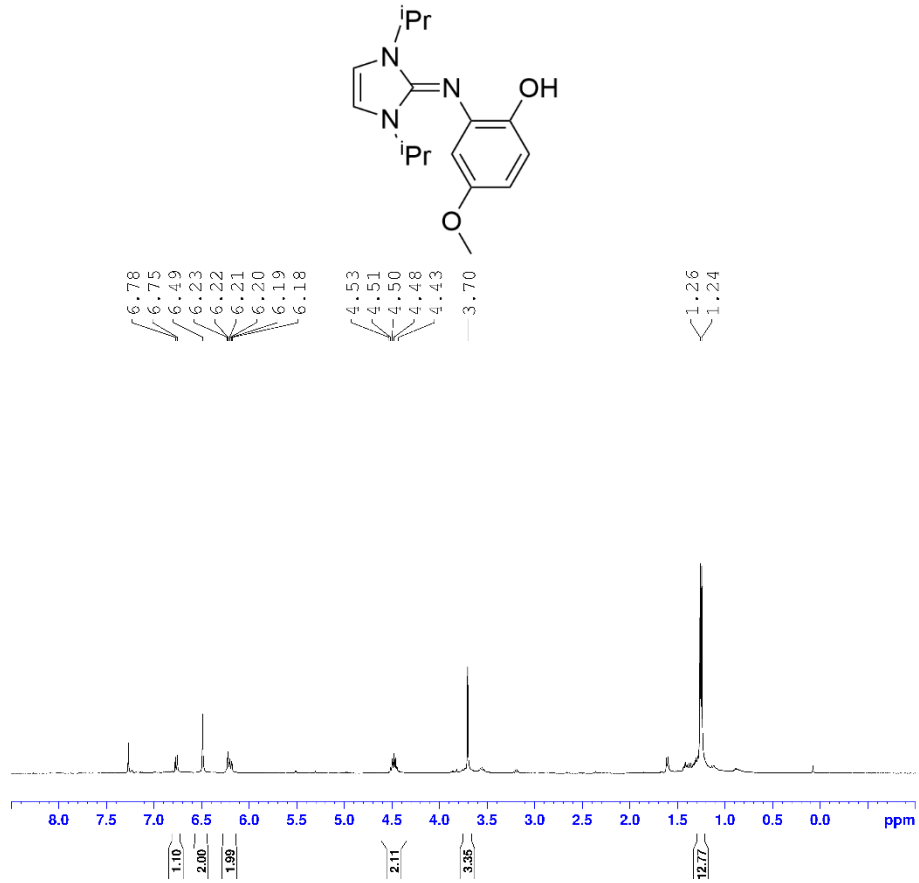

Figure A21 ^{1}H NMR spectrum of **L2d**H (400 MHz, $CDCl_3$)

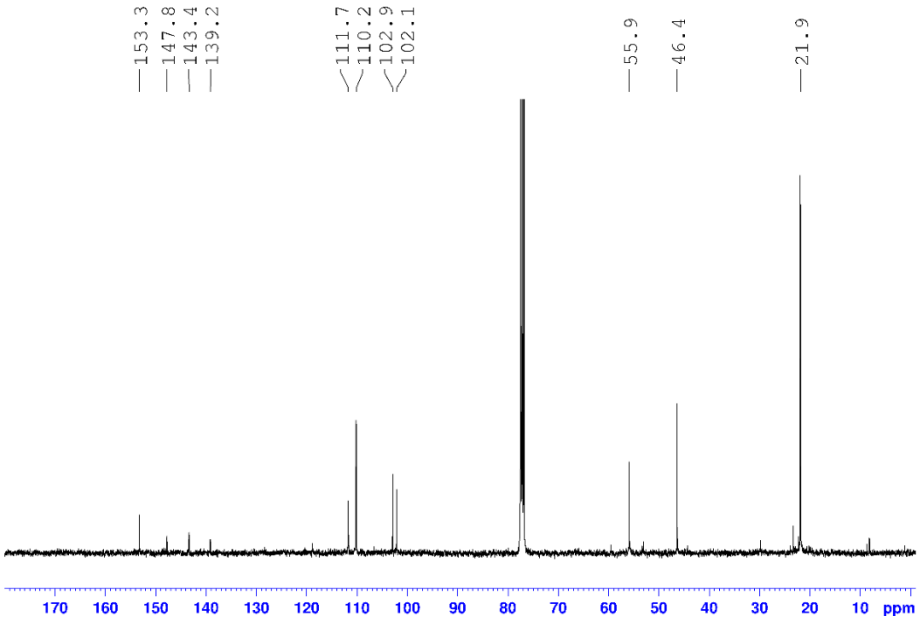

Figure A22 ^{13}C{^{1}H} NMR spectrum of **L2d**H (100 MHz, $CDCl_3$)

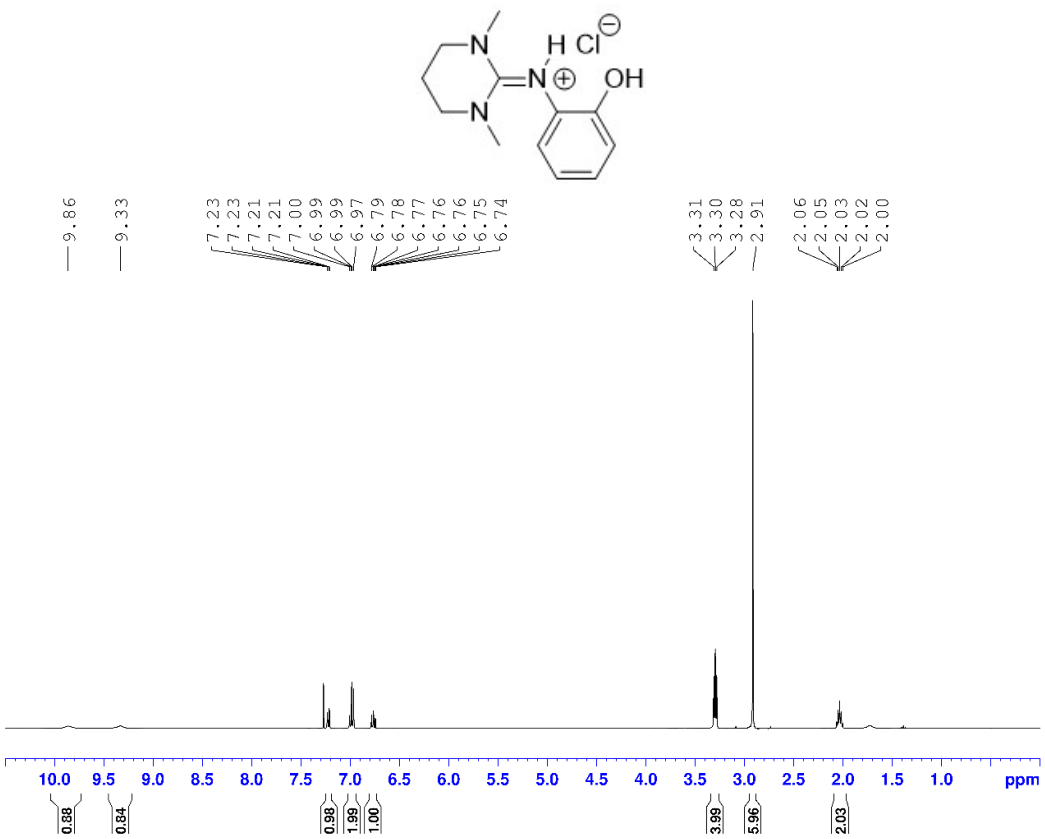

Figure A23. ^{1}H NMR spectrum of **L4a**H·HCl (400 MHz, $CDCl_3$)

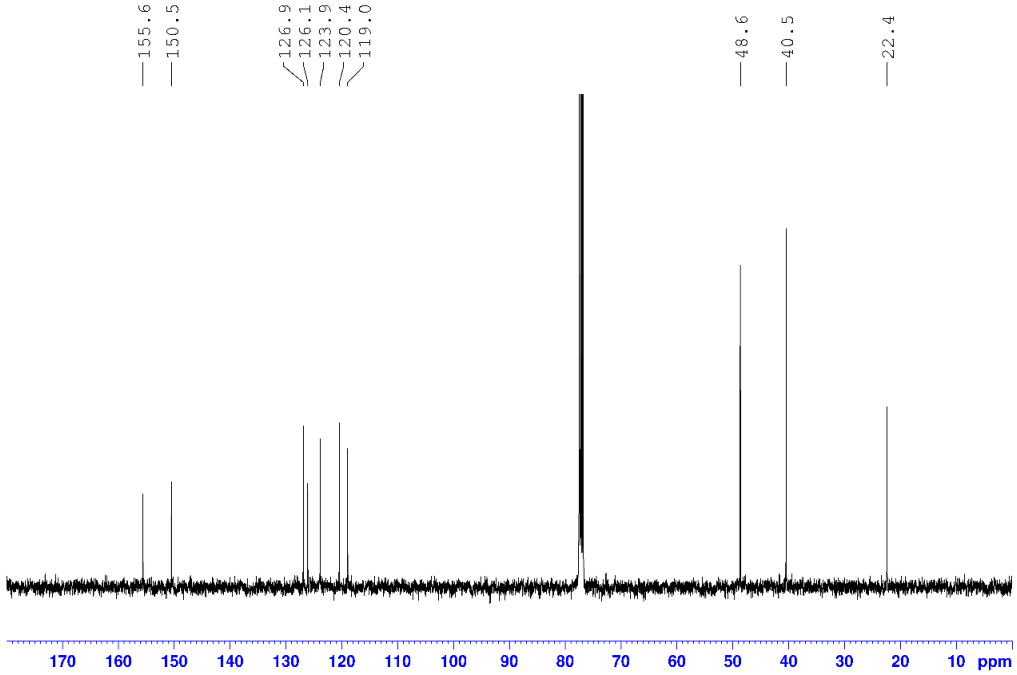

Figure A24. ^{13}C{^{1}H} NMR spectrum of **L4a**H·HCl (100 MHz, $CDCl_3$)

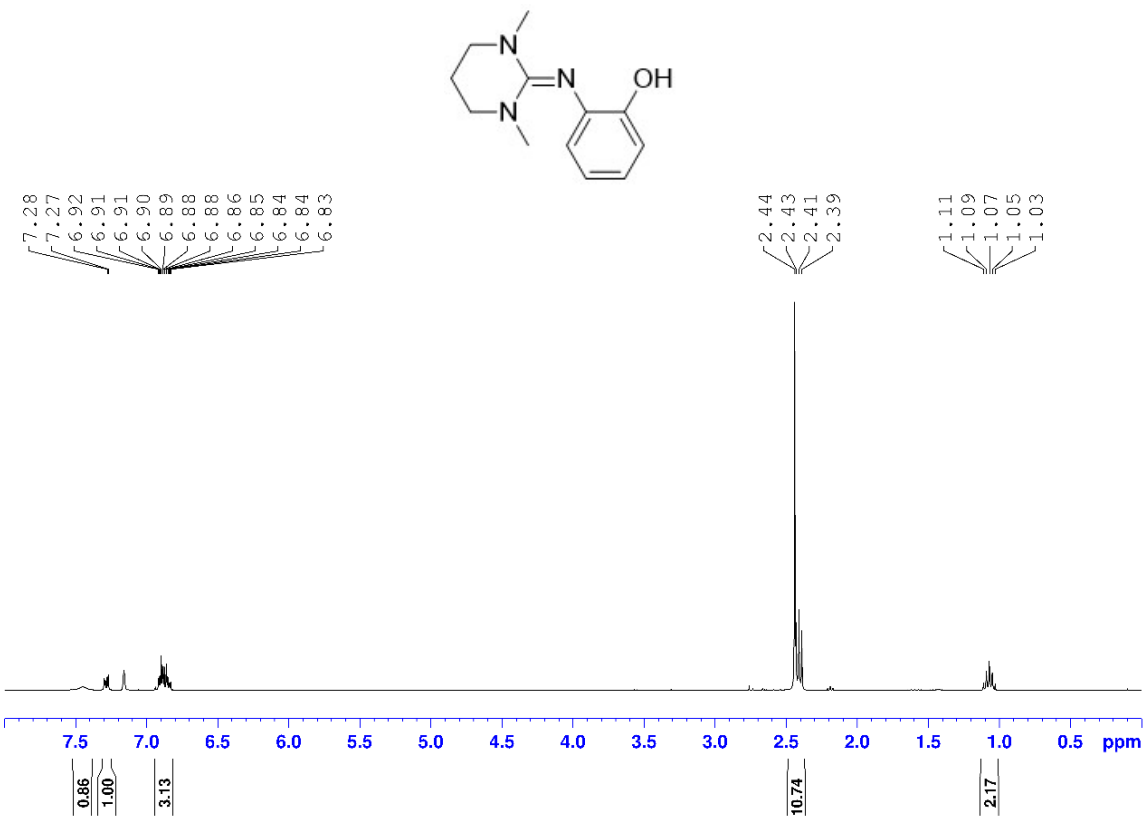

Figure A25. 1H NMR spectrum of **L4a**H (400 MHz, C6D6)

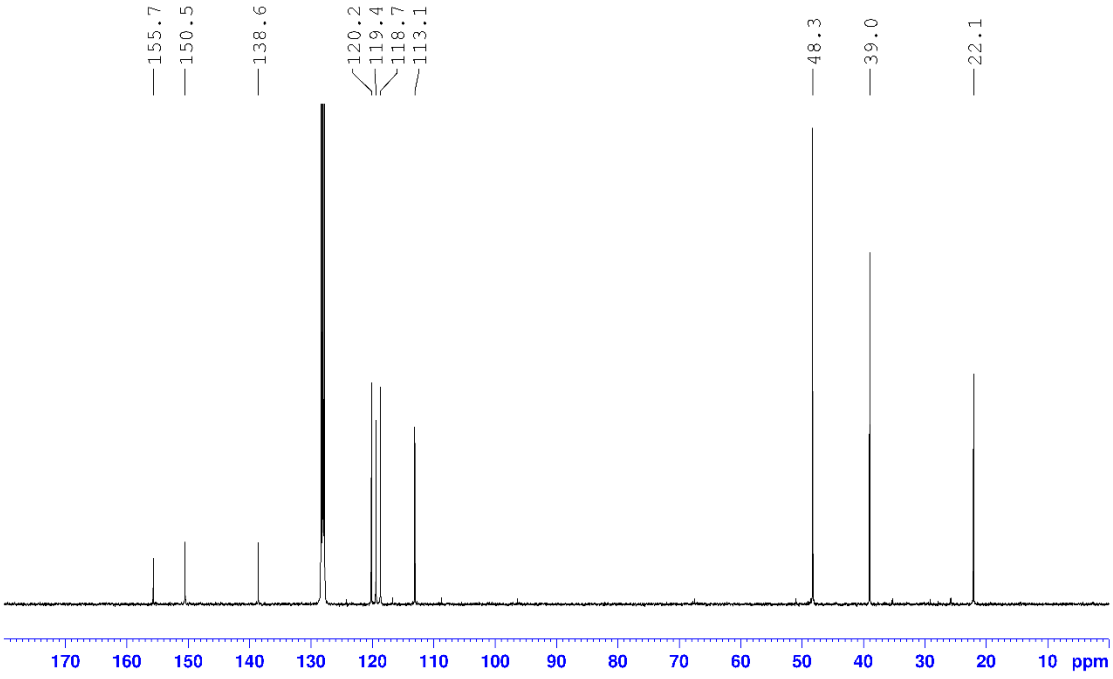

Figure A26. $^{13}C\{^{1}H\}$ NMR spectrum of **L4a**H (100 MHz, C_6D_6)

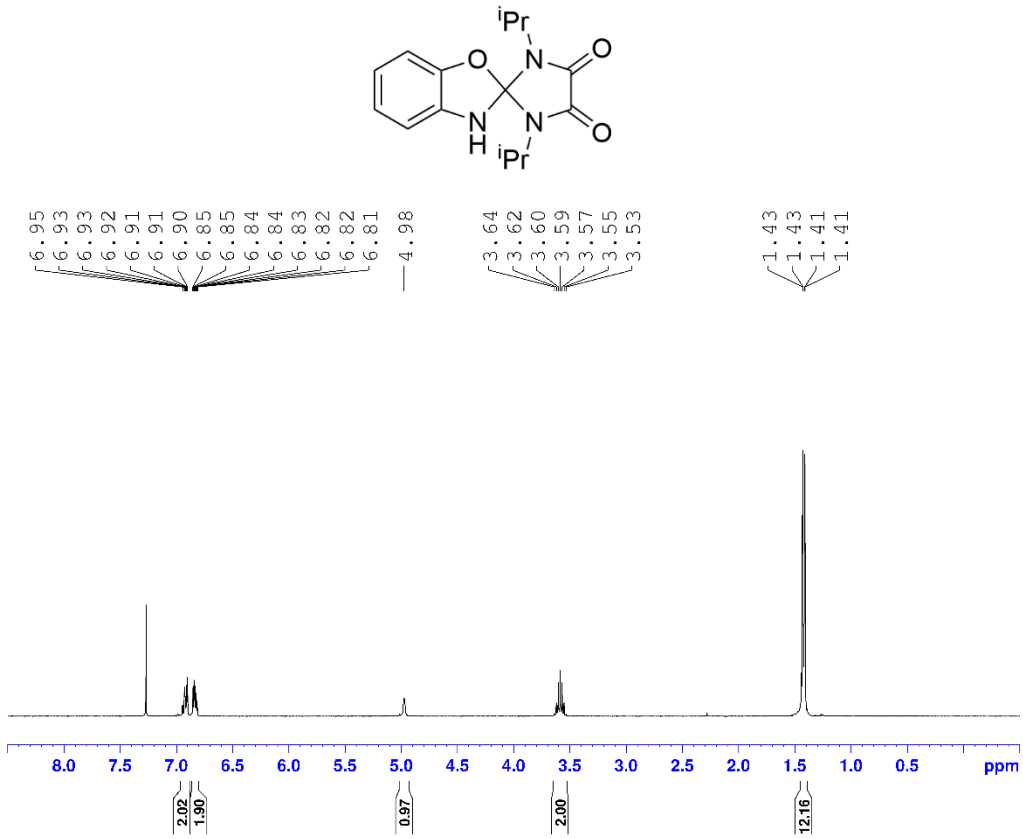

Figure A27 ^{1}H NMR spectrum of **L5a′**H (400 MHz, $CDCl_3$)

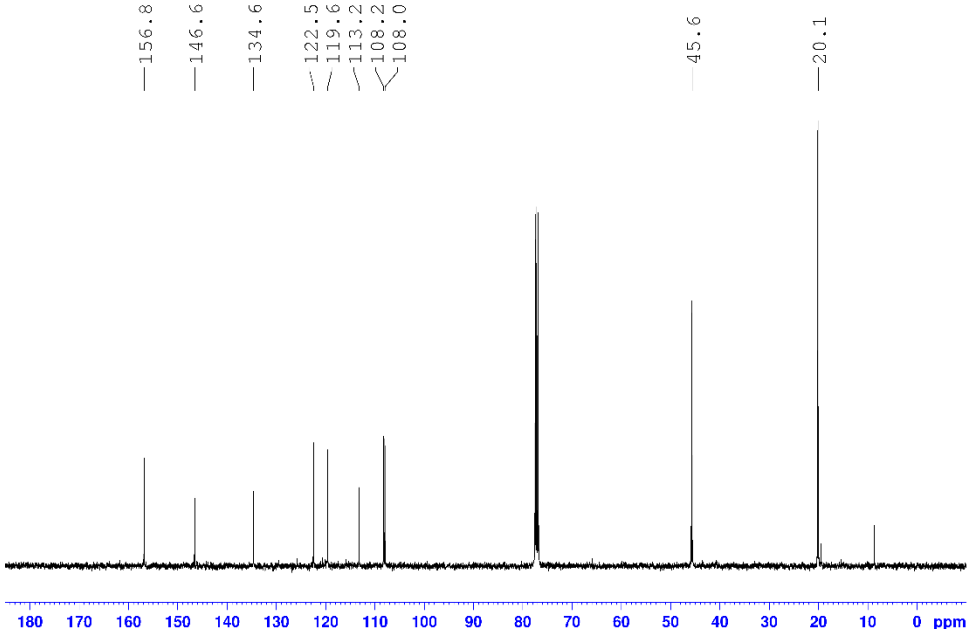

Figure A28 $^{13}C\{^{1}H\}$ NMR spectrum of **L5a′**H (100 MHz, $CDCl_3$)

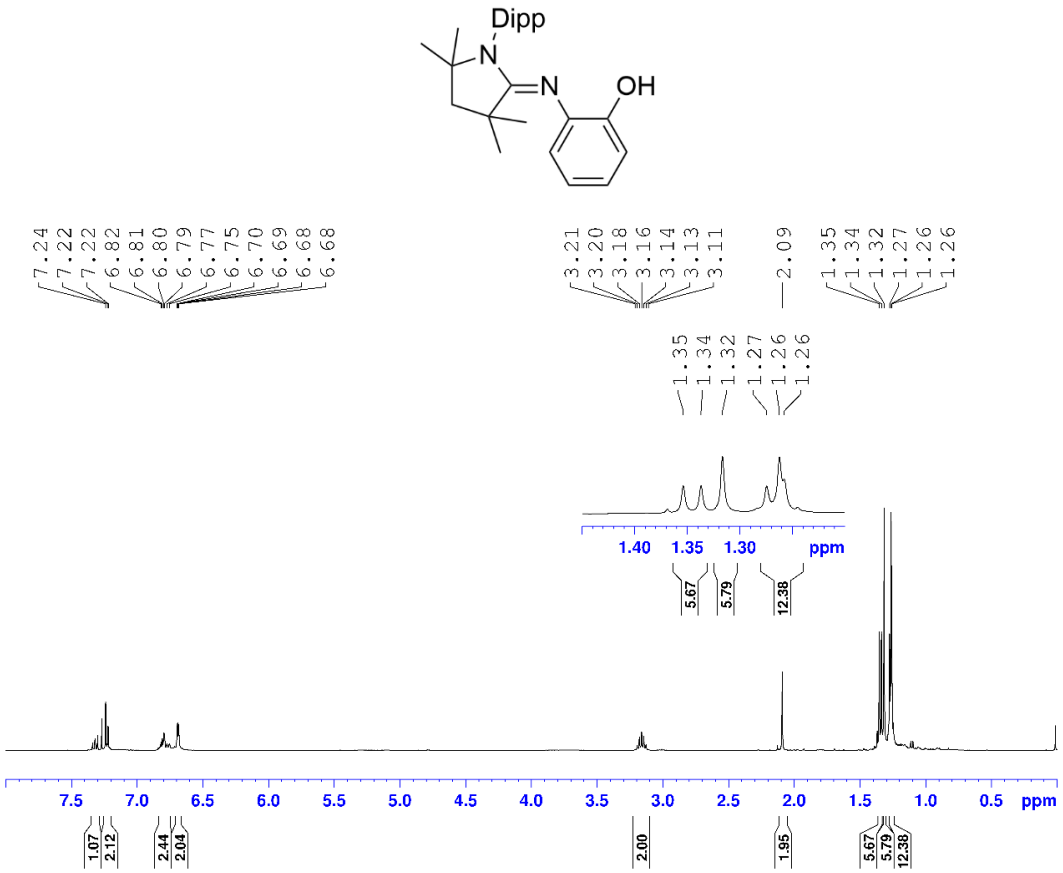

Figure A29 ^{1}H NMR spectrum of **L6a**H (400 MHz, $CDCl_3$)

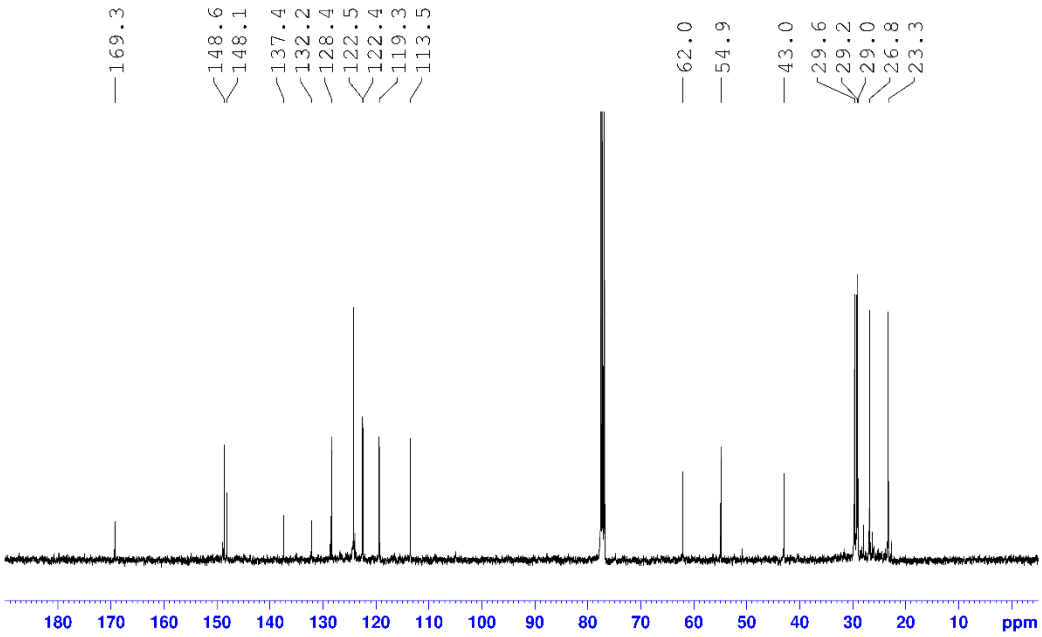

Figure A30 $^{13}C\{^{1}H\}$ NMR spectrum of **L6a**H (100 MHz, $CDCl_3$)

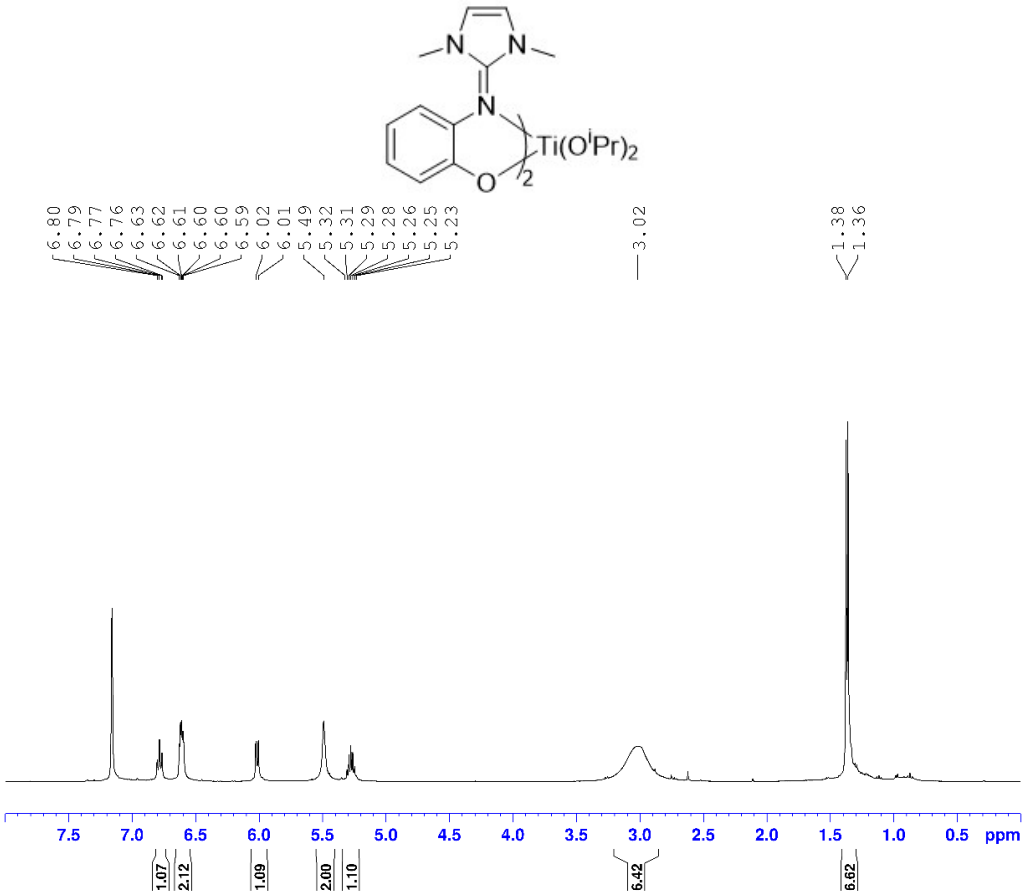

Figure A31. ^{1}H NMR spectrum of Ti(**L1a**)$_2$(O^{i}Pr)$_2$ (400 MHz, C_6D_6)

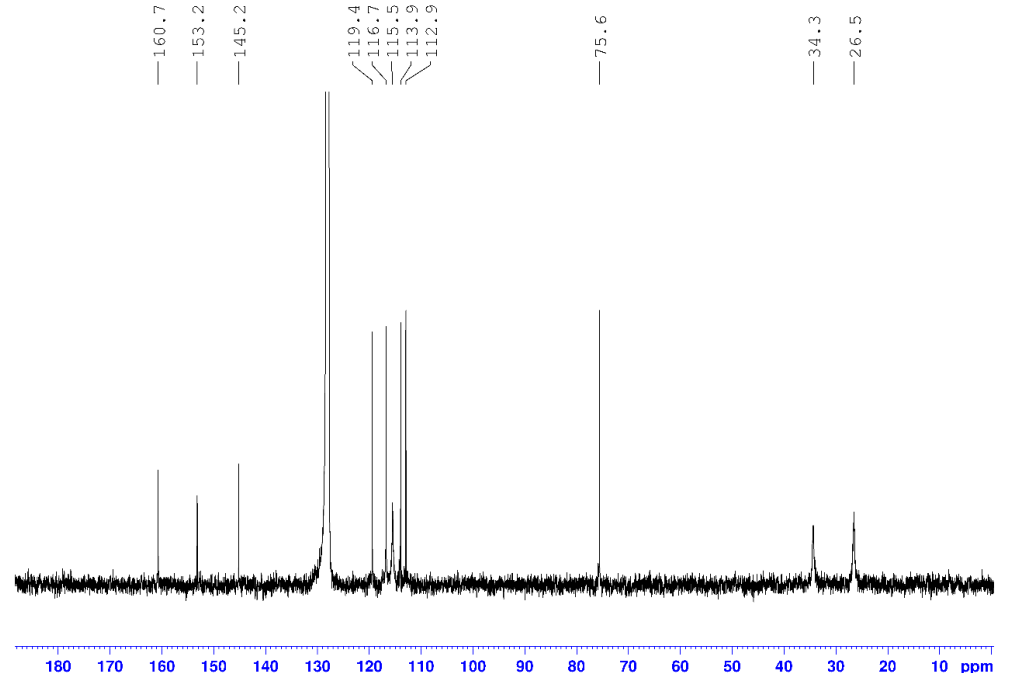

Figure A32.^{13}C{^{1}H} NMR spectrum of Ti(**L1a**)$_2$(O^{i}Pr)$_2$ (100 MHz, C_6D_6)

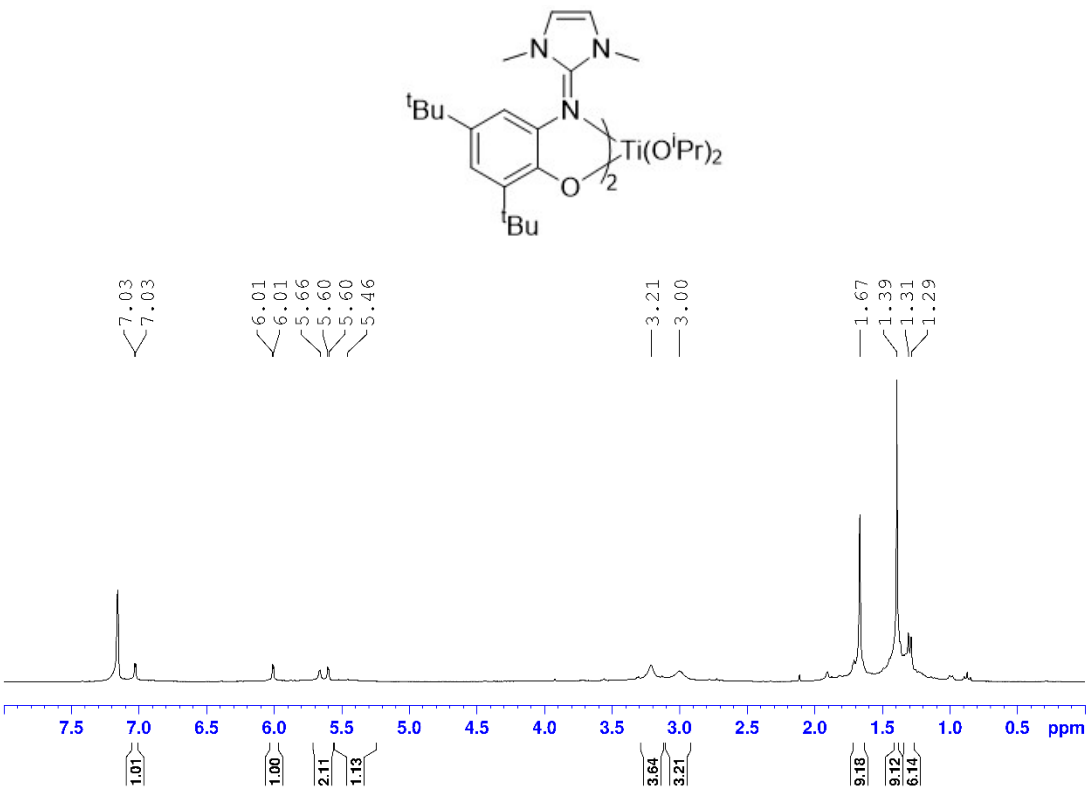

Figure A33 1H NMR spectrum of Ti(**L1b**)$_2$(O^{i}Pr)$_2$ (400 MHz, C_6D_6)

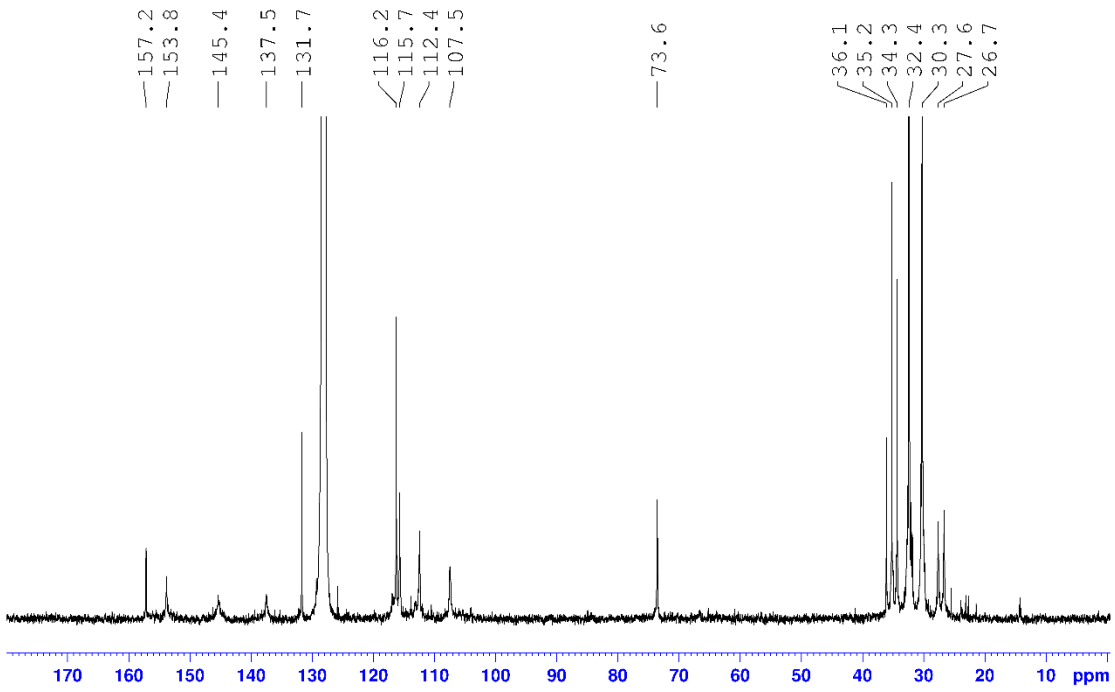

Figure A34.$^{13}C\{^1H\}$ NMR spectrum of Ti(**L1b**)$_2$(O^{i}Pr)$_2$ (100 MHz, C_6D_6)

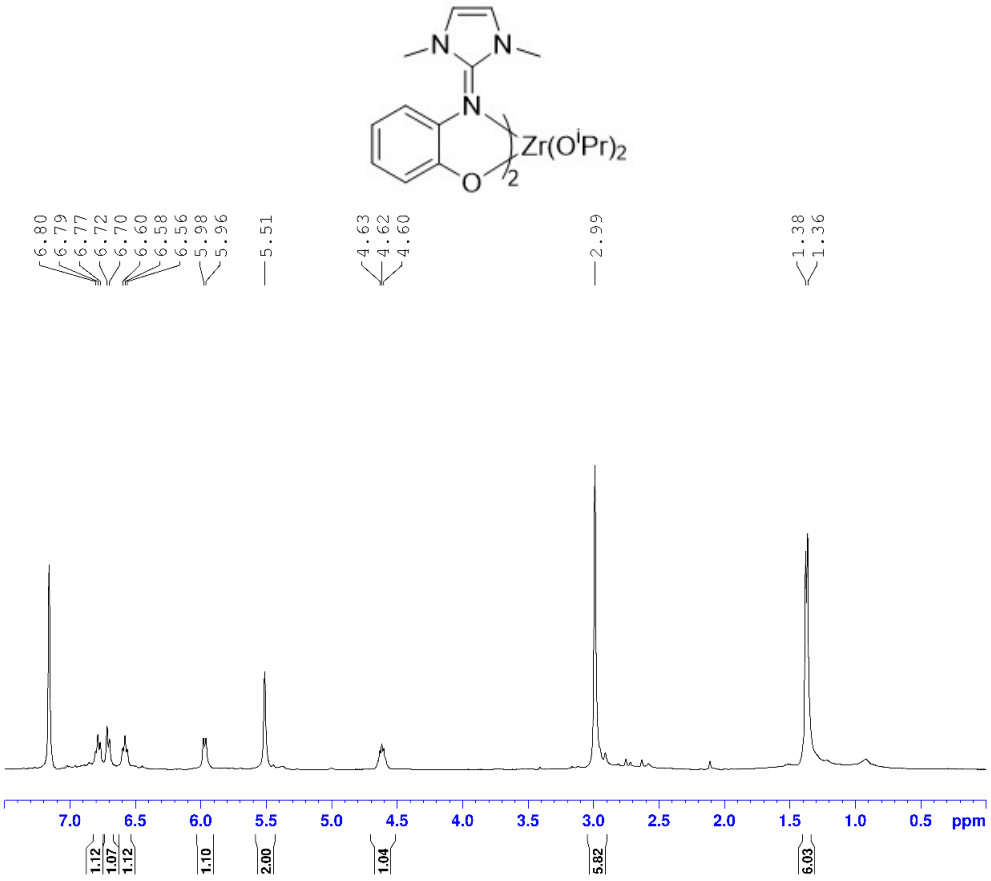

Figure A35.^{1}H NMR spectrum of Zr(**L1a**)$_2$(O^{i}Pr)$_2$ (400 MHz, C_6D_6)

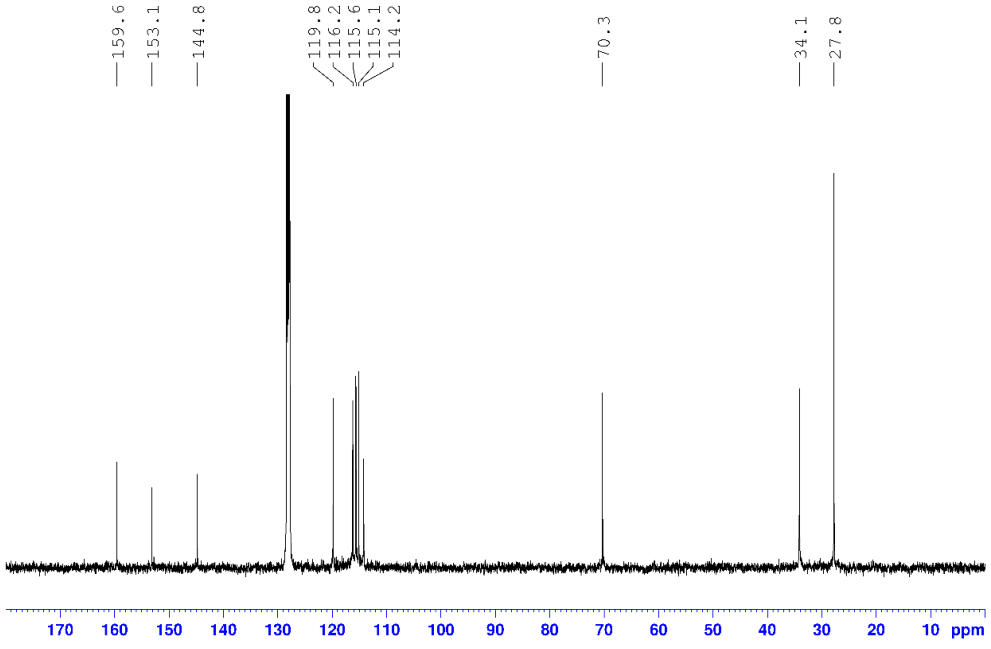

Figure A36.^{13}C{^{1}H} NMR spectrum of Zr(**L1a**)$_2$(O^{i}Pr)$_2$ (100 MHz, C_6D_6)

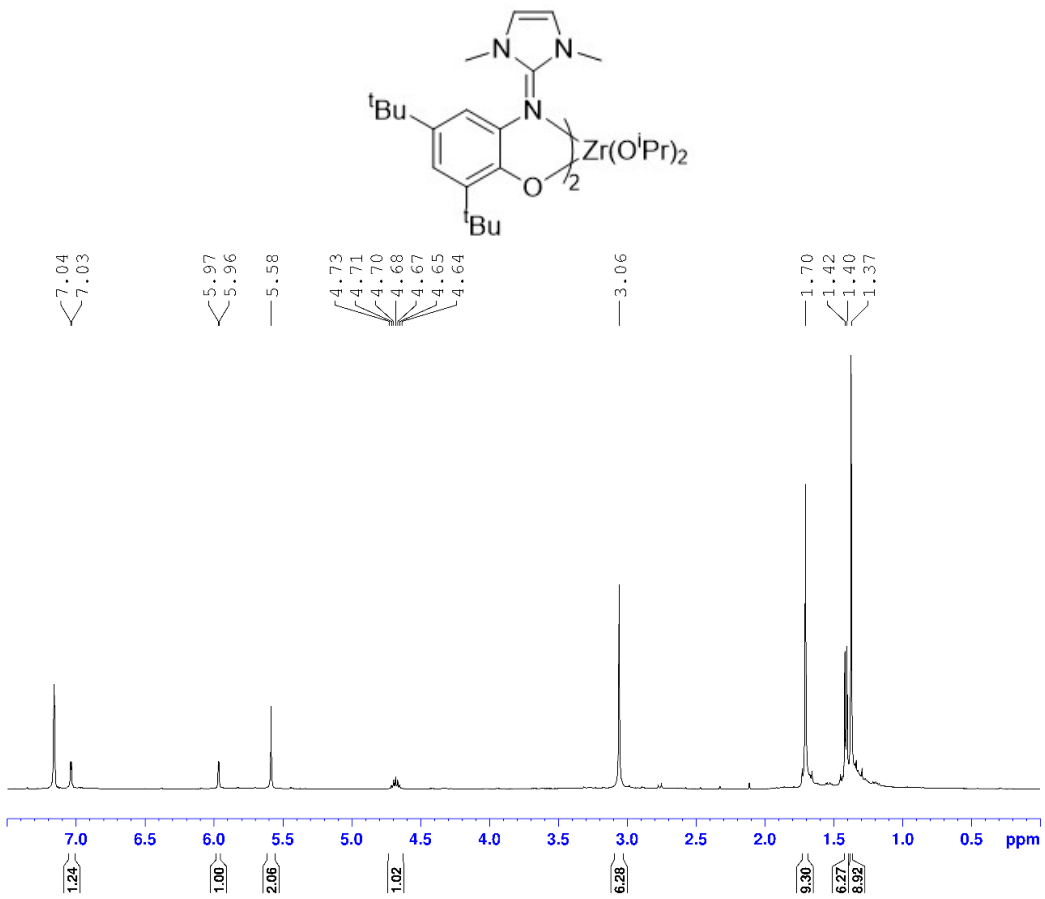

Figure A37.[1]H NMR spectrum of Zr(**L1b**)$_2$(O^{i}Pr)$_2$(400 MHz, C_6D_6)

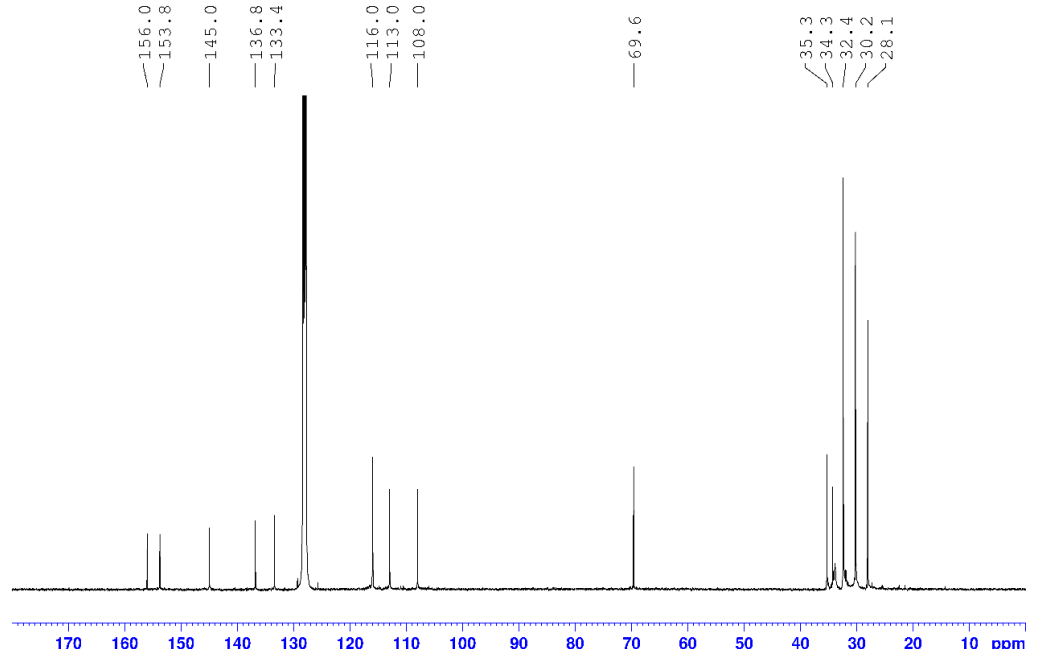

Figure A38.[13]C{[1]H} NMR spectrum of Zr(**L1b**)$_2$(O^{i}Pr)$_2$(100 MHz, C_6D_6)

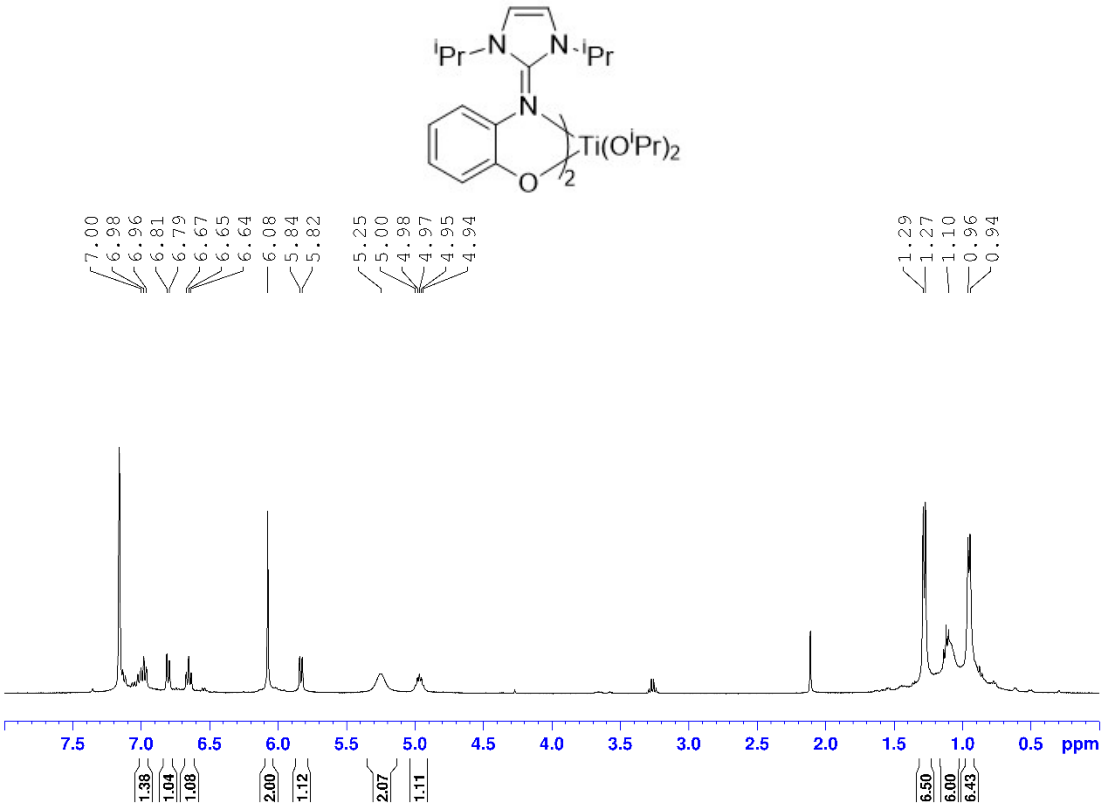

Figure A39.[1]H NMR spectrum of Ti(**L2a**)$_2$(O^{i}Pr)$_2$ (400 MHz, C_6D_6)

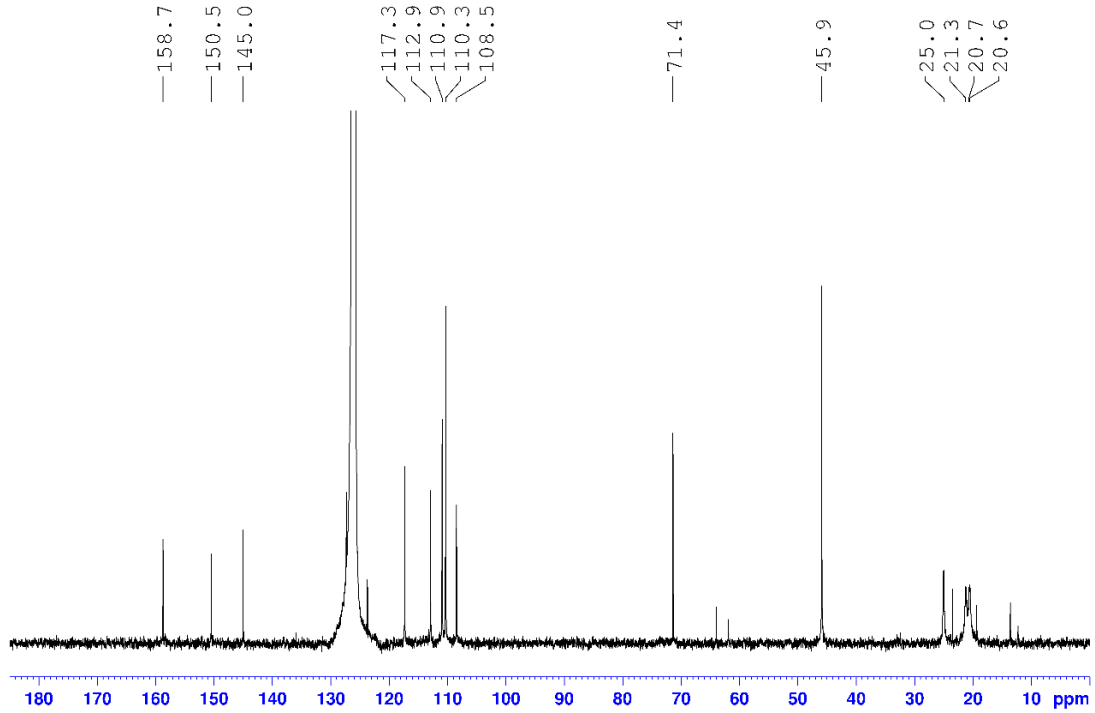

Figure A40.[13]C{[1]H} NMR spectrum of Ti(**L2a**)$_2$(O^{i}Pr)$_2$ (75 MHz, $CDCl_3$)

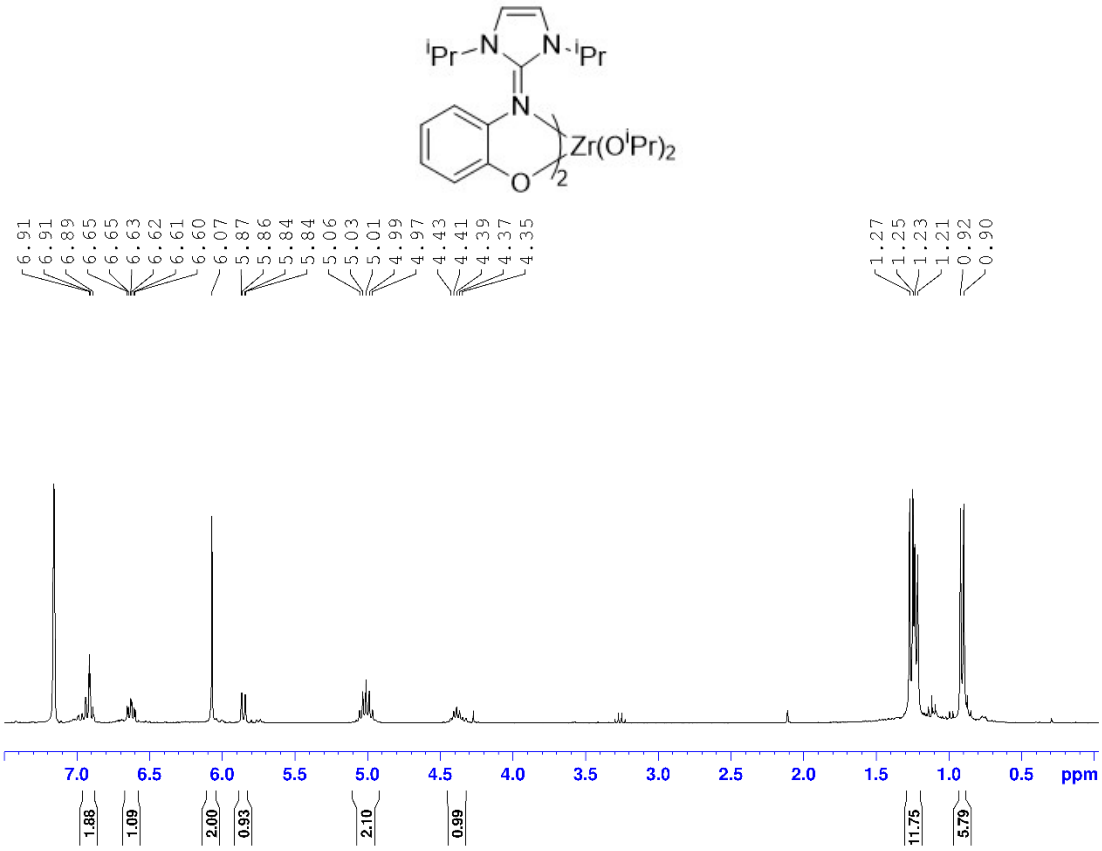

Figure A41.[1]H NMR spectrum of Zr(**L2a**)$_2$(O^{i}Pr)$_2$ (300 MHz, C_6D_6)

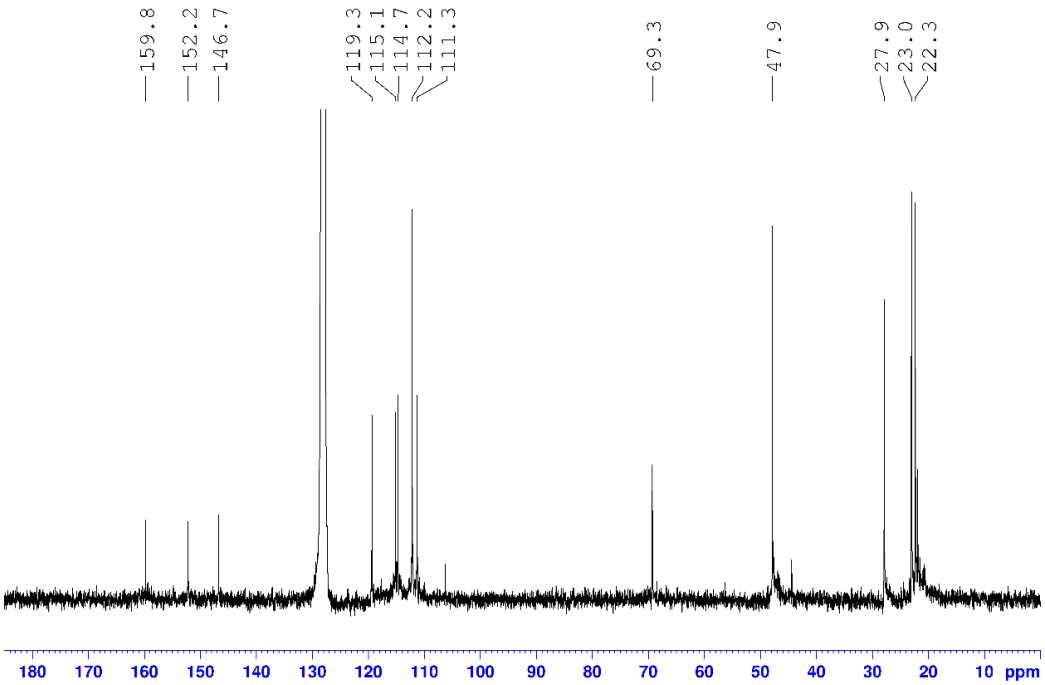

Figure A42.[13]C{[1]H} NMR spectrum of Zr(**L2a**)$_2$(O^{i}Pr)$_2$ (75 MHz, C_6D_6)

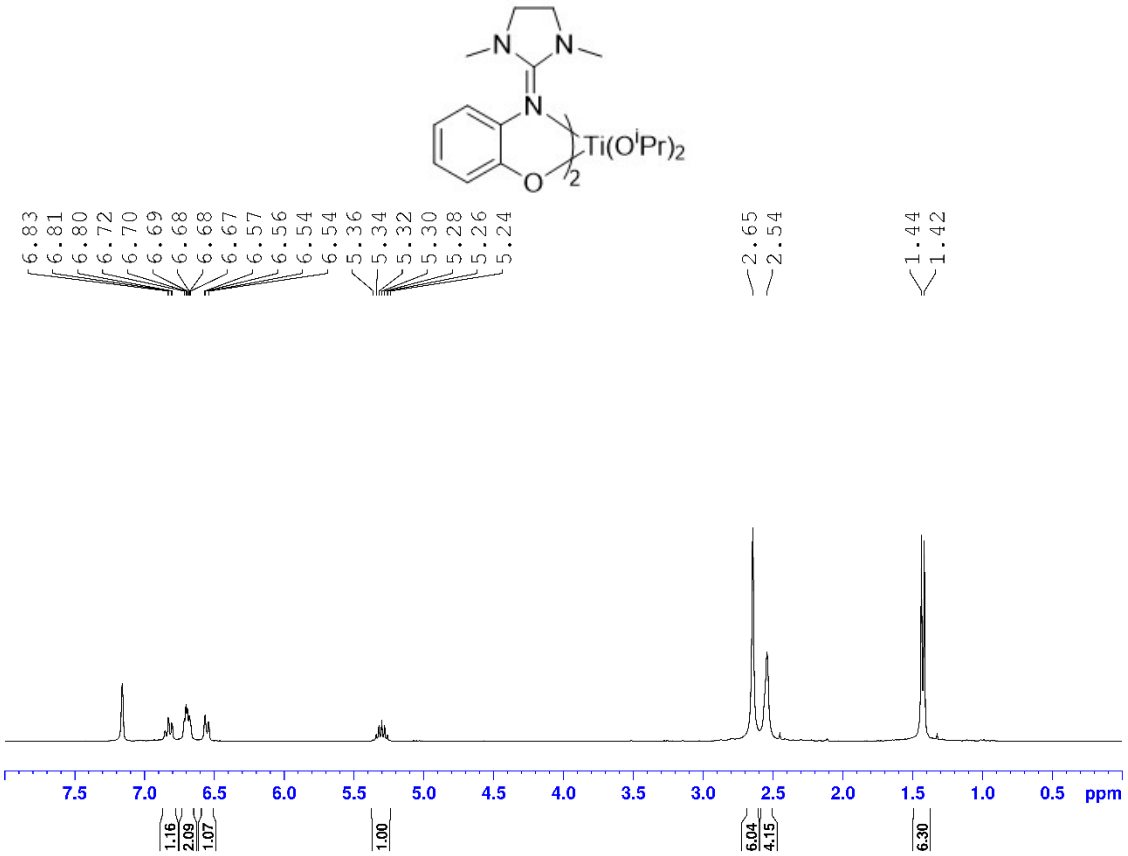

Figure A43.[1]H NMR spectrum of Ti(**L3a**)$_2$(O^{i}Pr)$_2$ (300 MHz, C_6D_6)

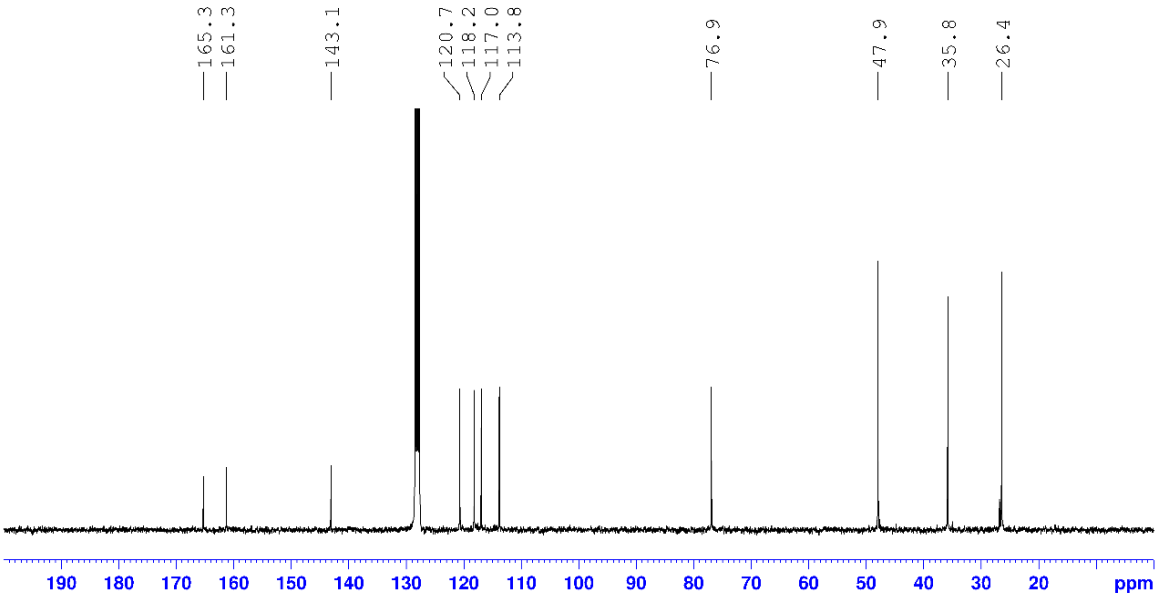

Figure A44.[13]C{[1]H} NMR spectrum of Ti(**L3a**)$_2$(O^{i}Pr)$_2$ (75 MHz, C_6D_6)

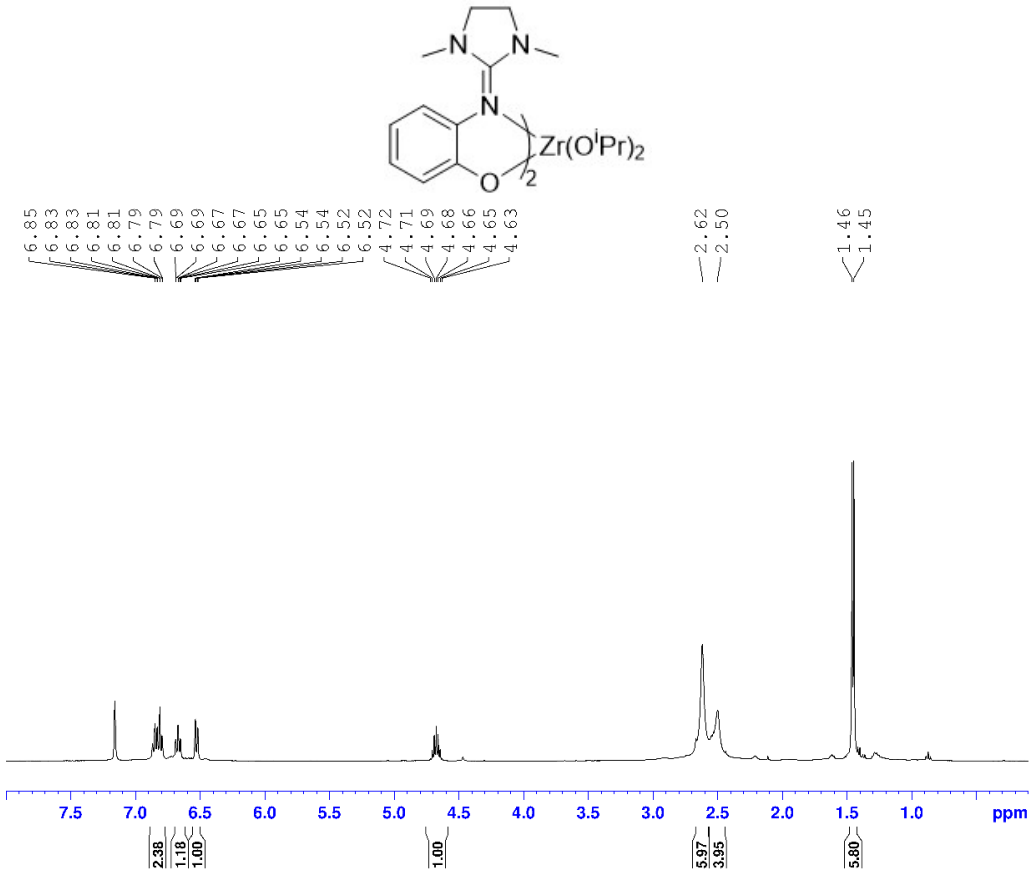

Figure A45.[1]H NMR spectrum of Zr(**L3a**)$_2$(O^{i}Pr)$_2$ (400 MHz, C_6D_6)

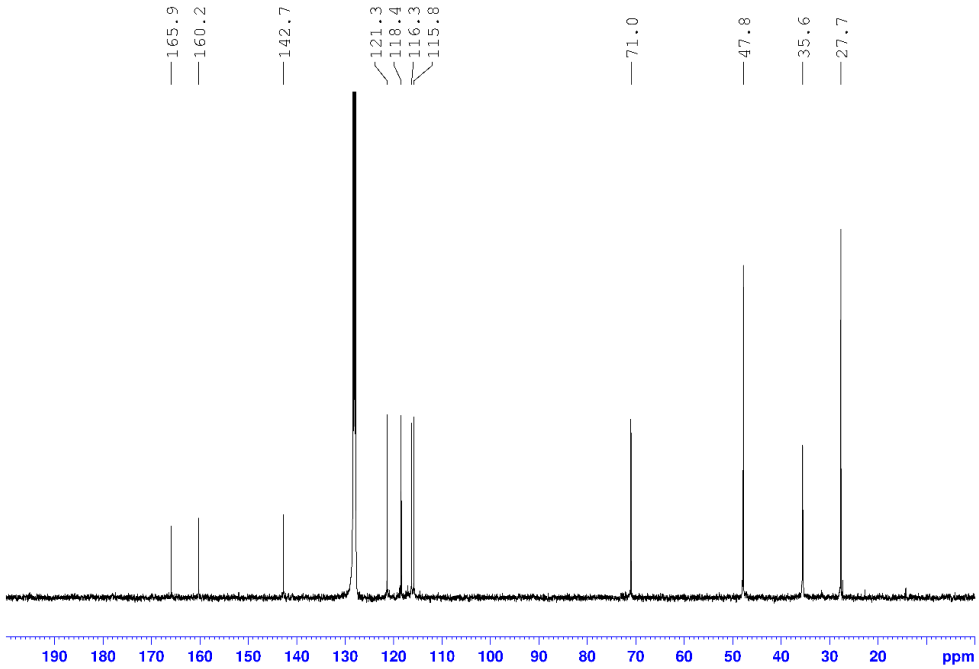

Figure A46.[13]C{[1]H} NMR spectrum of Zr(**L3a**)$_2$(O^{i}Pr)$_2$ (100 MHz, C_6D_6)

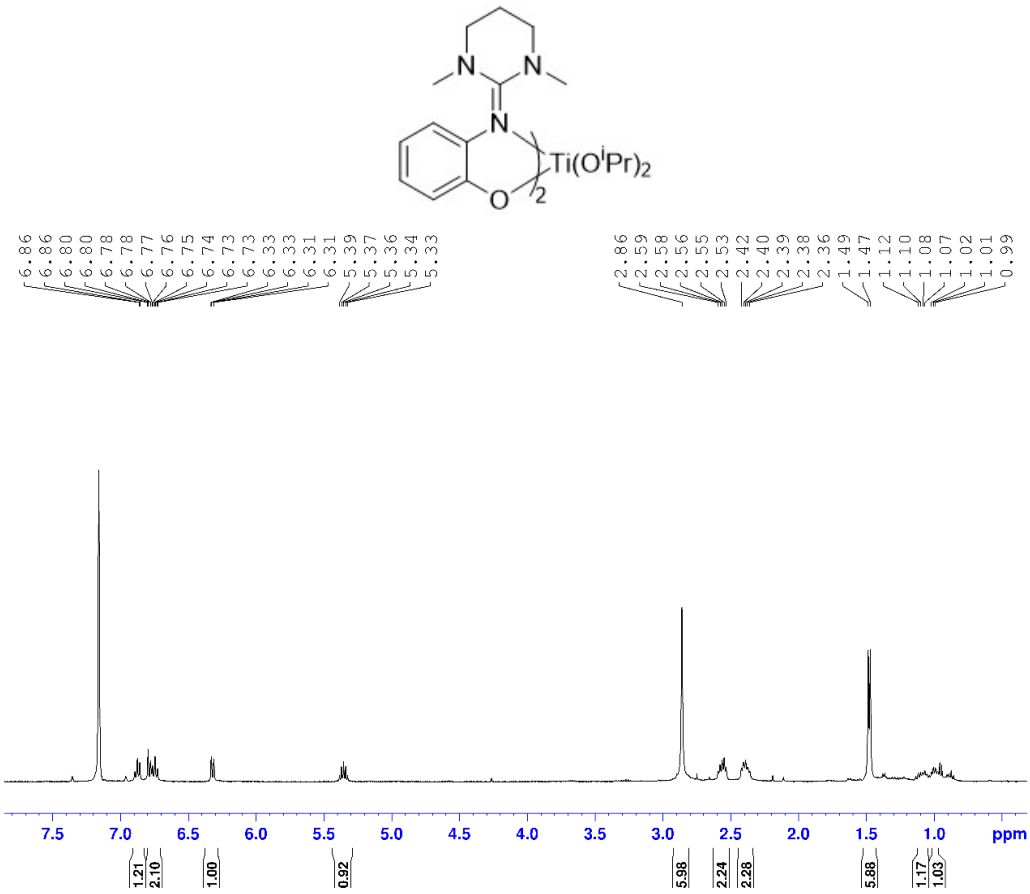

Figure A47.[1]H NMR spectrum of Ti(**L4a**)$_2$(O^{i}Pr)$_2$ (300 MHz, C_6D_6)

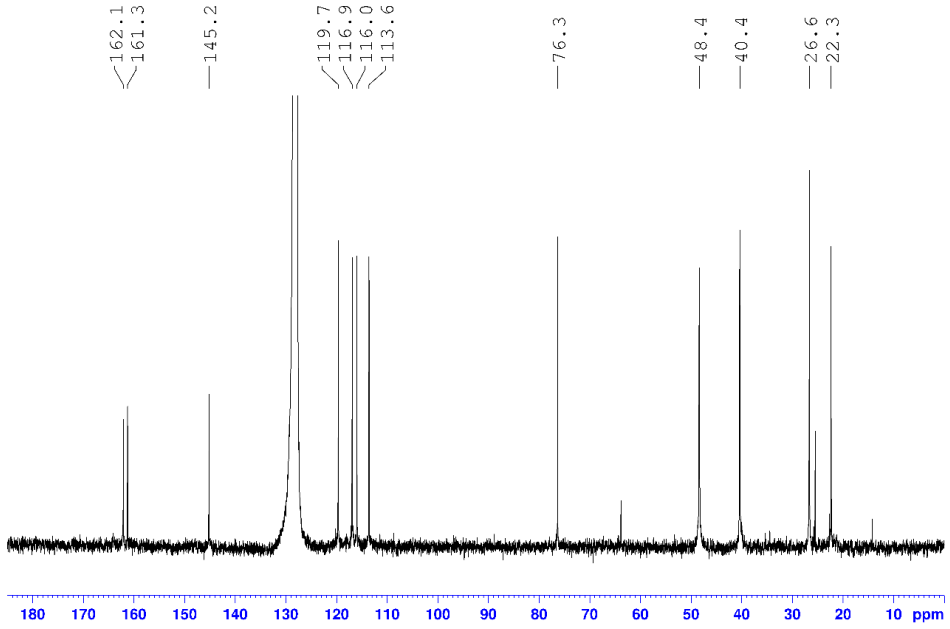

Figure A48.[13]C{[1]H} NMR spectrum of Ti(**L4a**)$_2$(OiPr)$_2$ (75 MHz, C_6D_6)

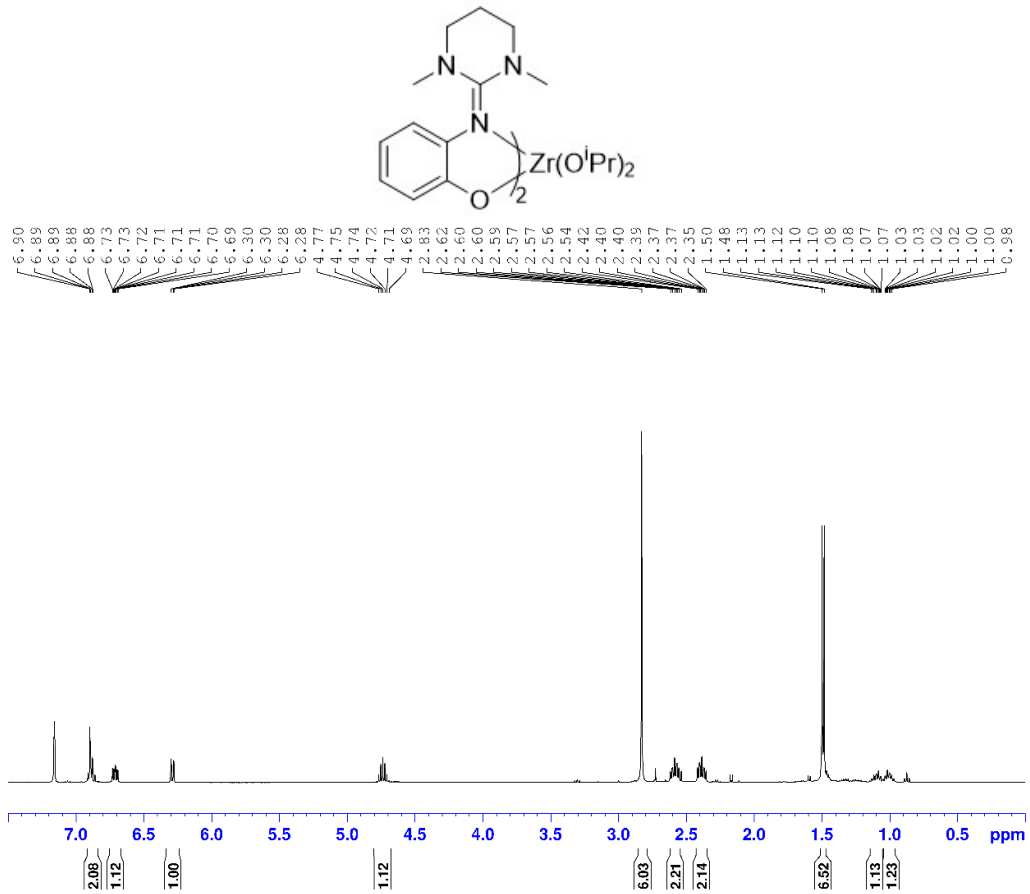

Figure A49.[1]H NMR spectrum of Zr(**L4a**)$_2$(O^{i}Pr)$_2$ (400 MHz, C_6D_6)

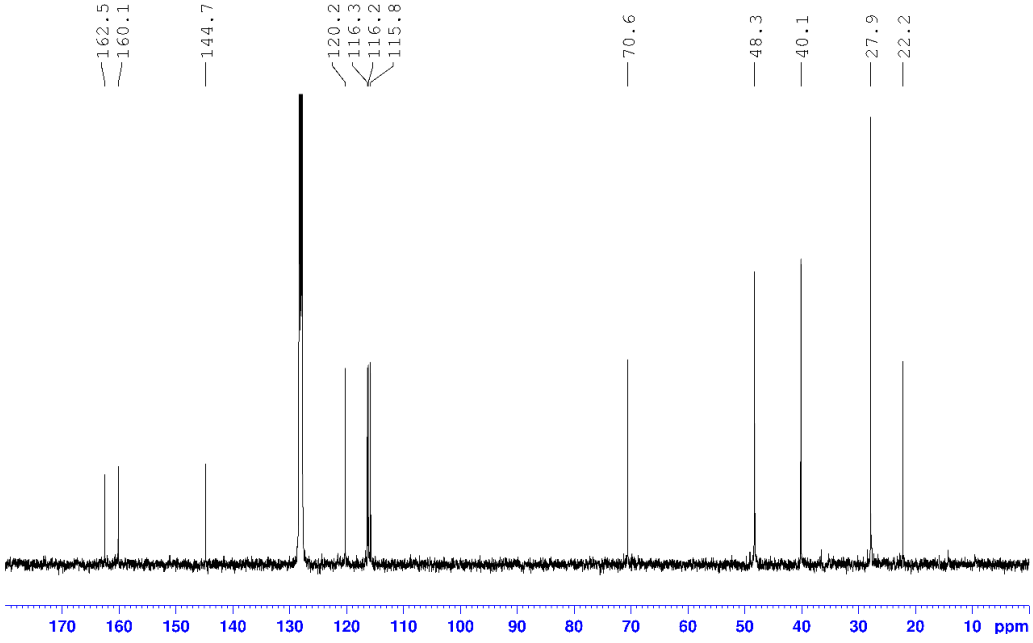

Figure A50.[13]C{[1]H} NMR spectrum of Zr(**L4a**)$_2$(O^{i}Pr)$_2$ (100 MHz, C_6D_6)

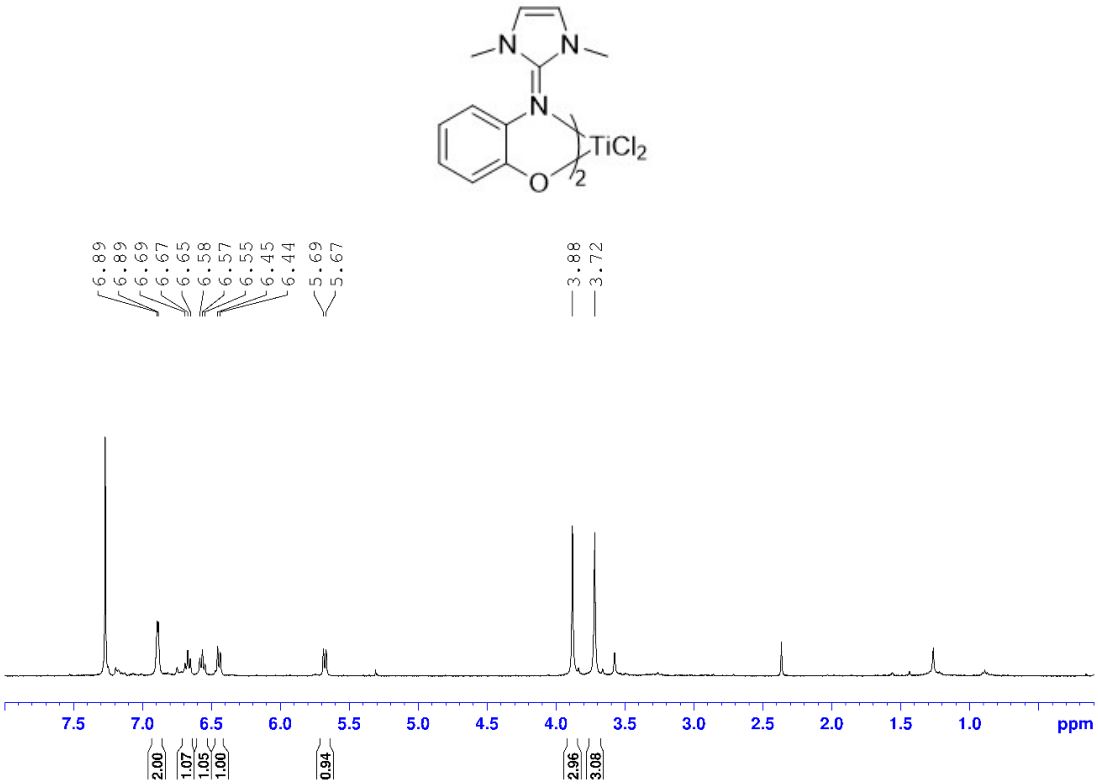

Figure A51.[1]H NMR spectrum of Ti(**L1a**)$_2$Cl$_2$ (400 MHz, C_6D_6)

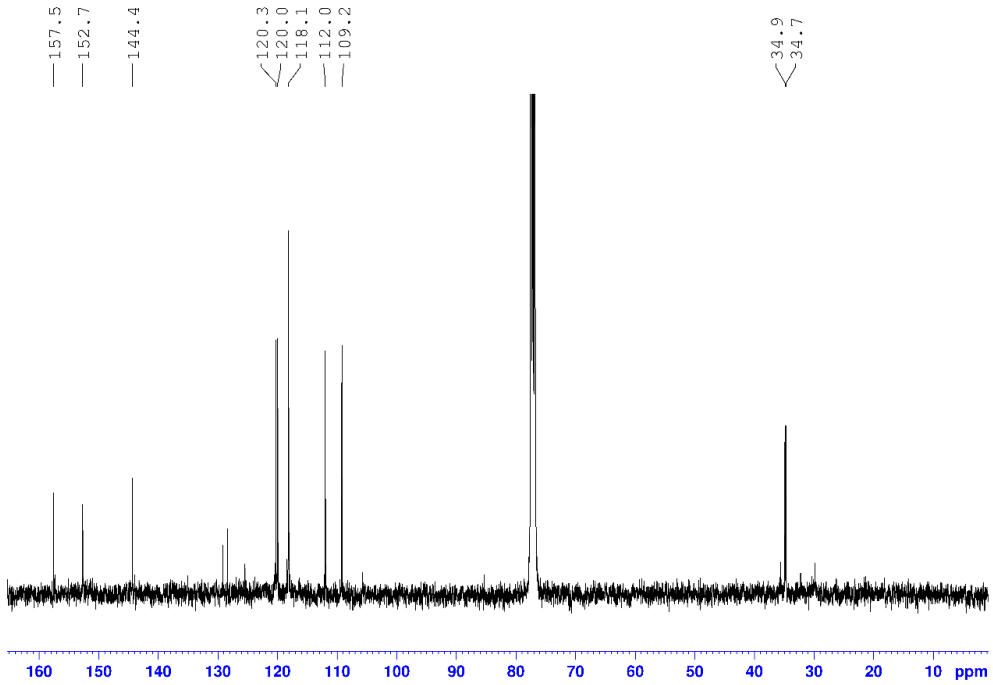

Figure A52.[13]C{[1]H} NMR spectrum of Ti(**L1a**)$_2$Cl$_2$ (100 MHz, C_6D_6)

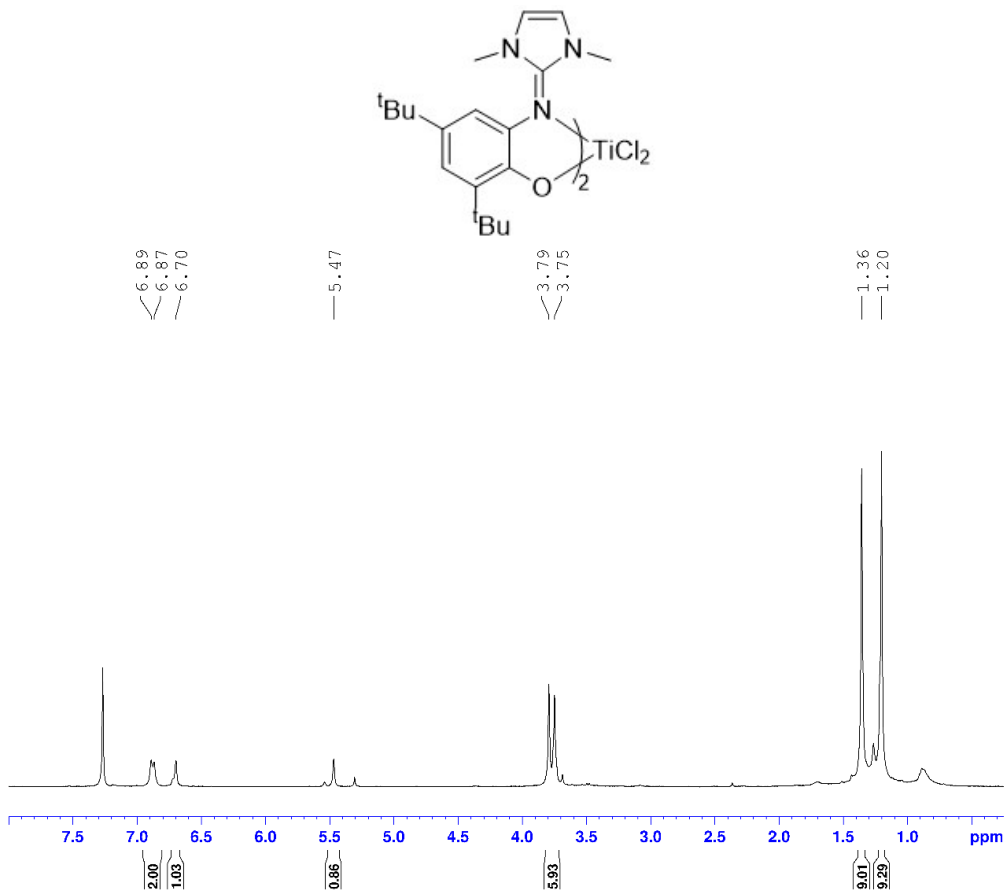

Figure A53.1H NMR spectrum of Ti(**L1b**)$_2$Cl$_2$(400 MHz, CDCl3)

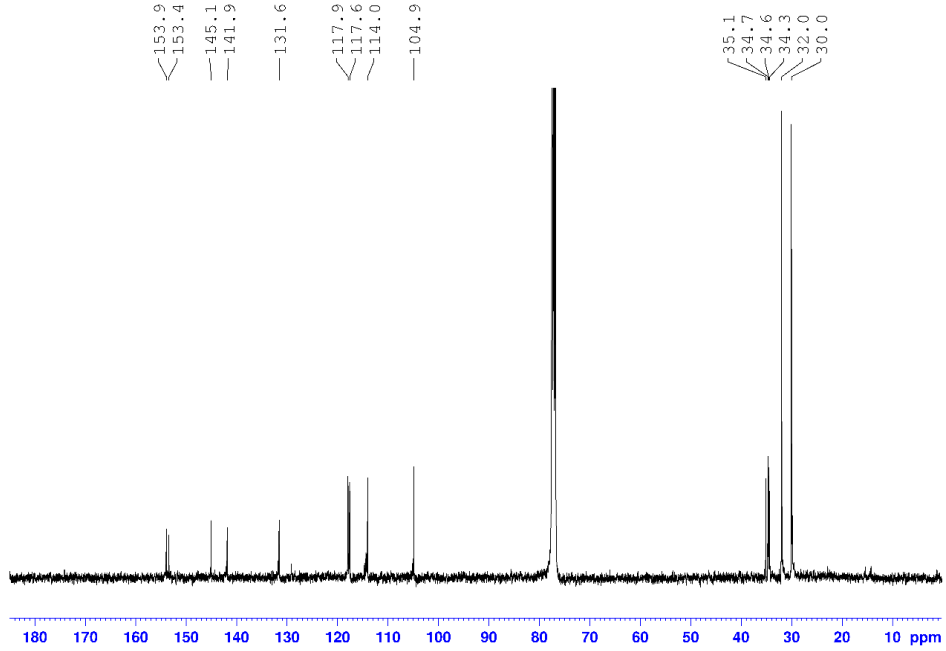

Figure A54.^{13}C{^{1}H} NMR spectrum of Ti(**L1b**)$_2$Cl$_2$(100 MHz, C_6D_6)

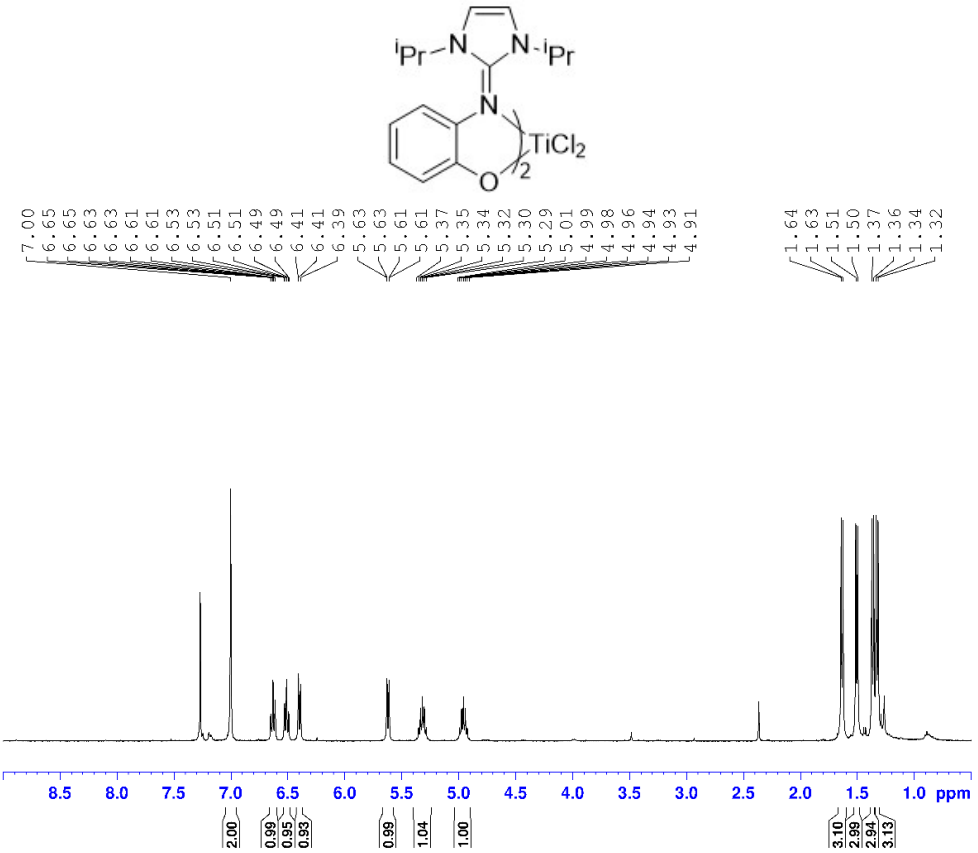

Figure A55.[1]H NMR spectrum of Ti(**L2a**)$_2$Cl$_2$ (400 MHz, CDCl3)

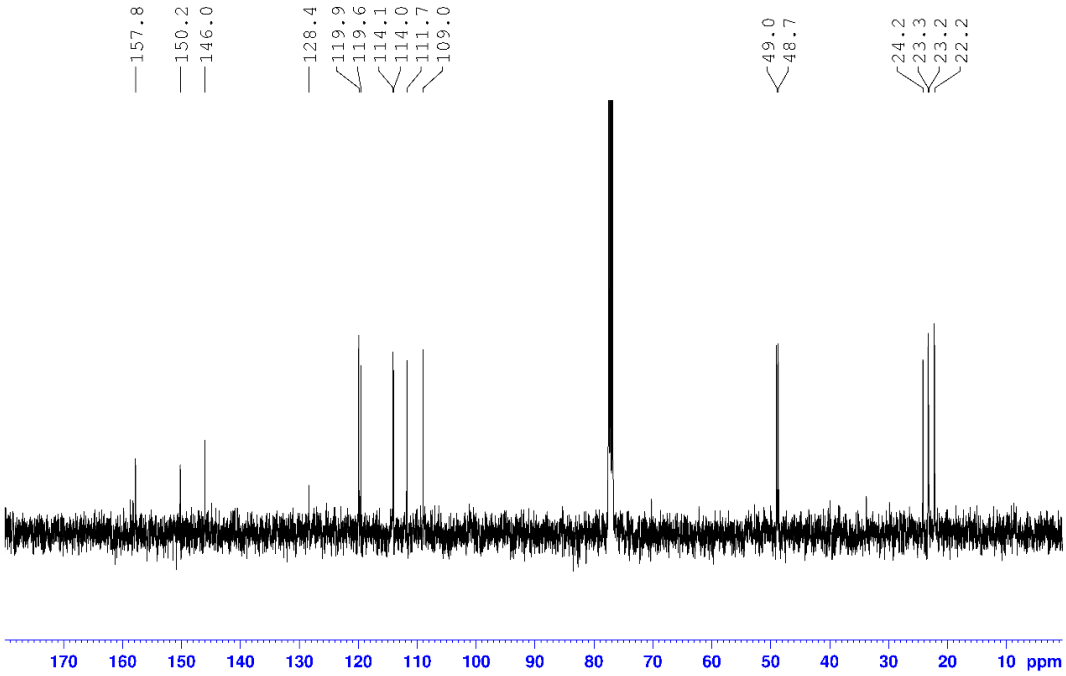

Figure A56.[13]C{[1]H} NMR spectrum of Ti(**L2a**)$_2$Cl$_2$ (100 MHz, CDCl$_3$)

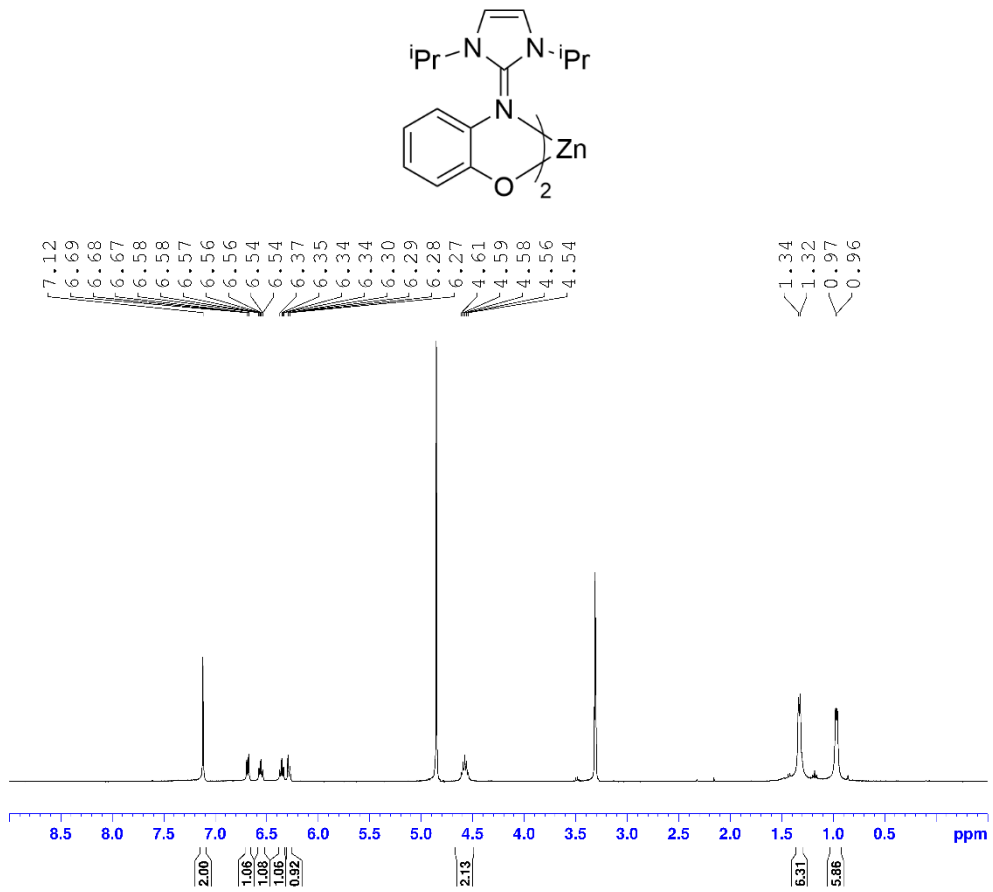

Figure A57 ^{1}H NMR spectrum of **Zn[L2a]$_2$** (400 MHz, CD_3OD)

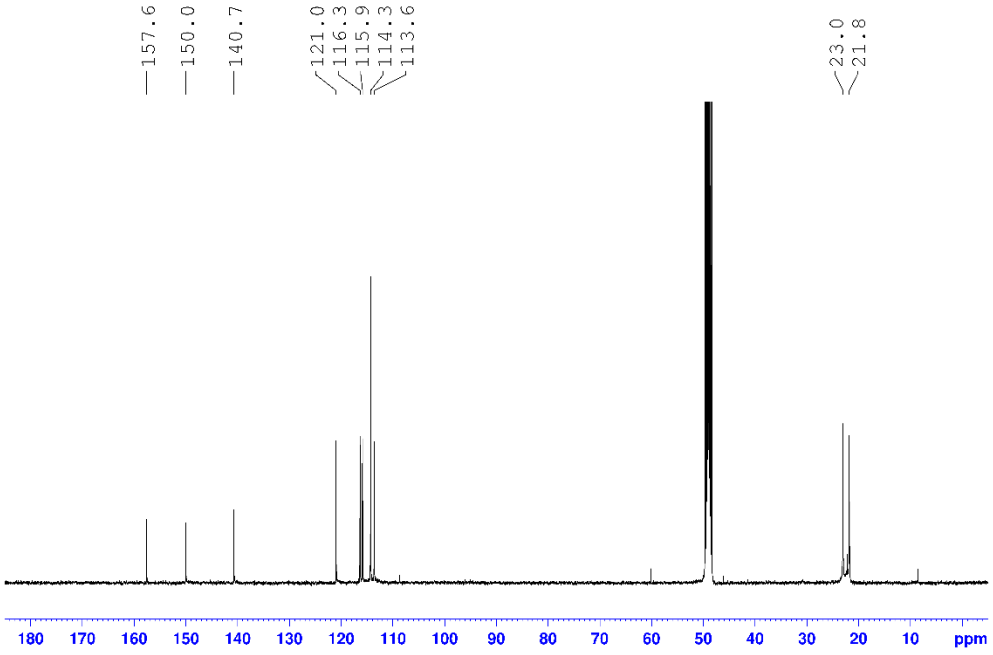

Figure A58 $^{13}C\{^{1}H\}$ NMR spectrum of **Zn[L2a]$_2$** (100 MHz, CD_3OD)

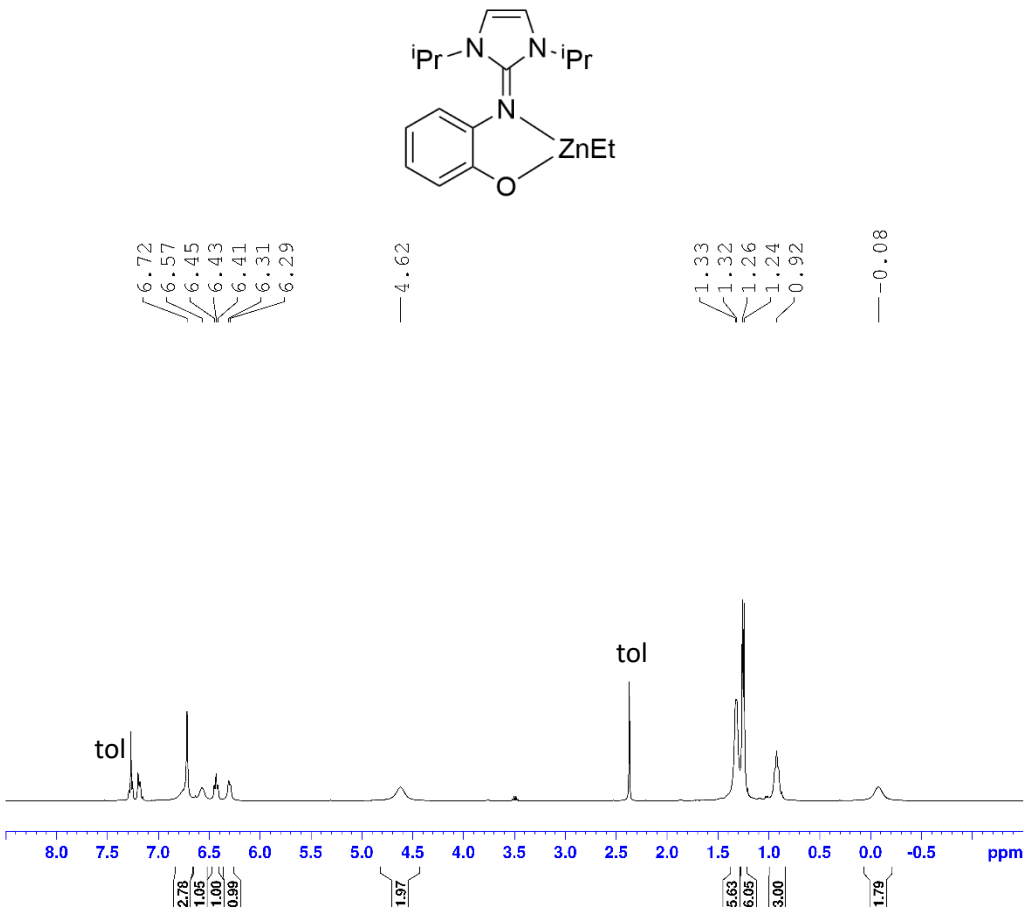

Figure A59 ^{1}H NMR spectrum of Zn[**L2a**]Et (400 MHz, $CDCl_3$)

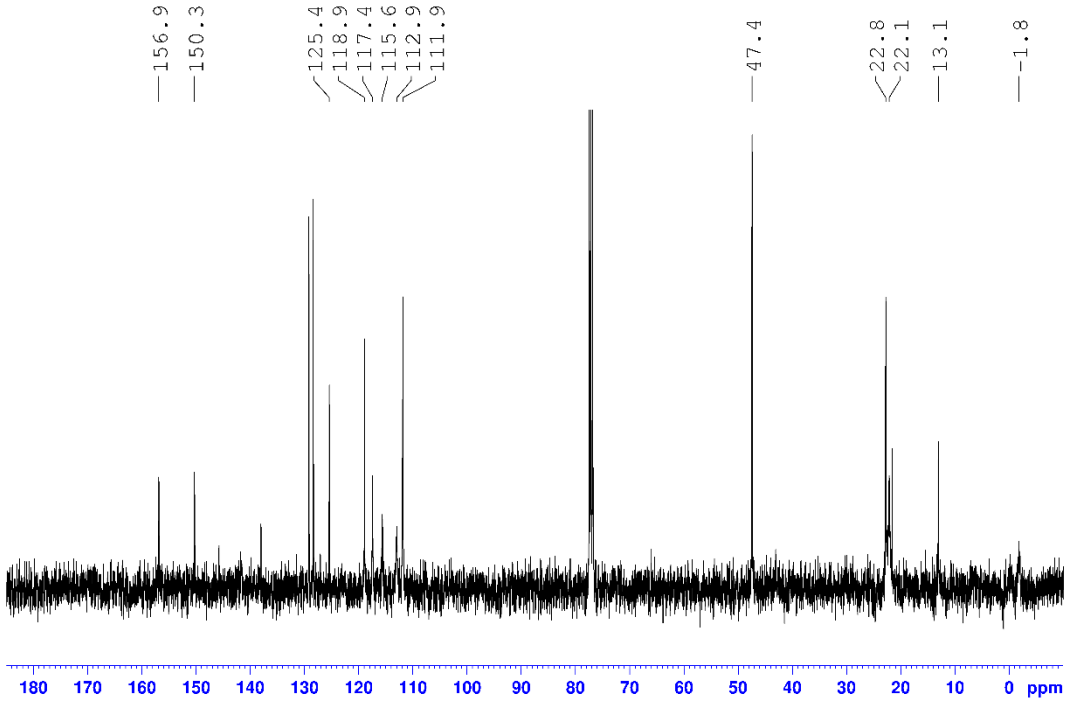

Figure A60 ^{13}C{1H} NMR spectrum of Zn[**L2a**]Et (100 MHz, $CDCl_3$)

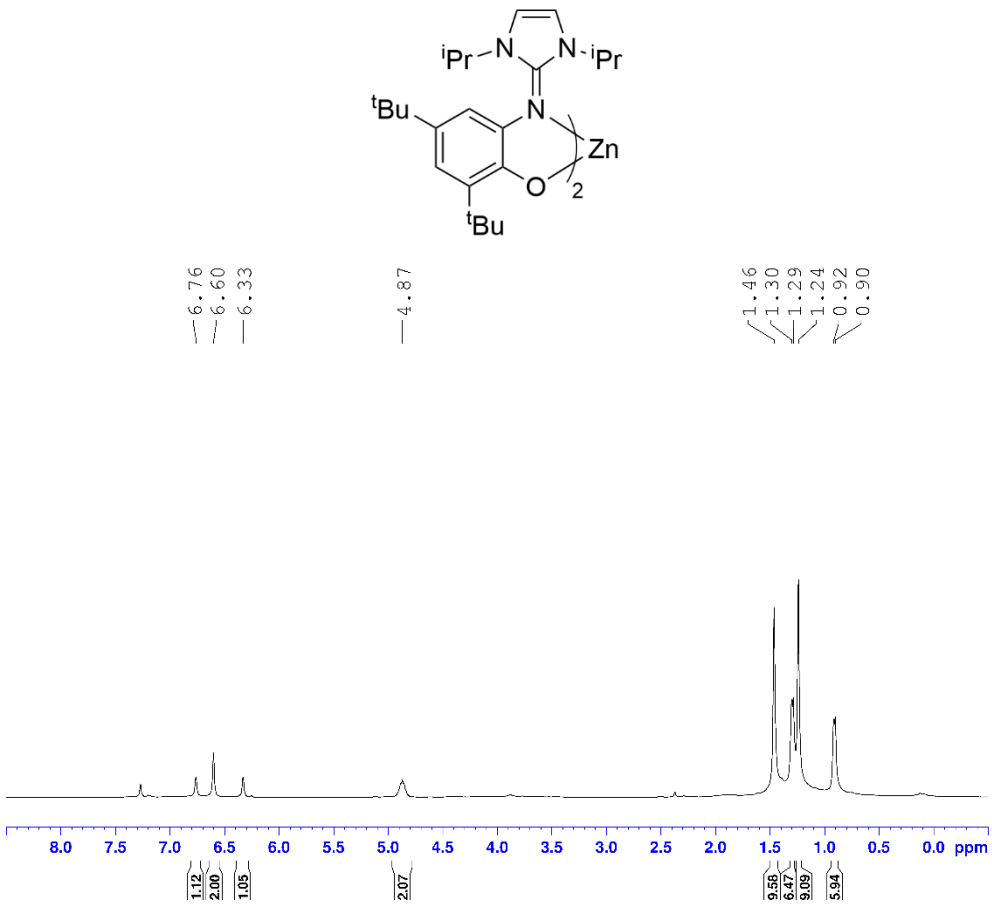

Figure A61 ^{1}H NMR spectrum of Zn[**L2b**]$_2$ (400 MHz, $CDCl_3$)

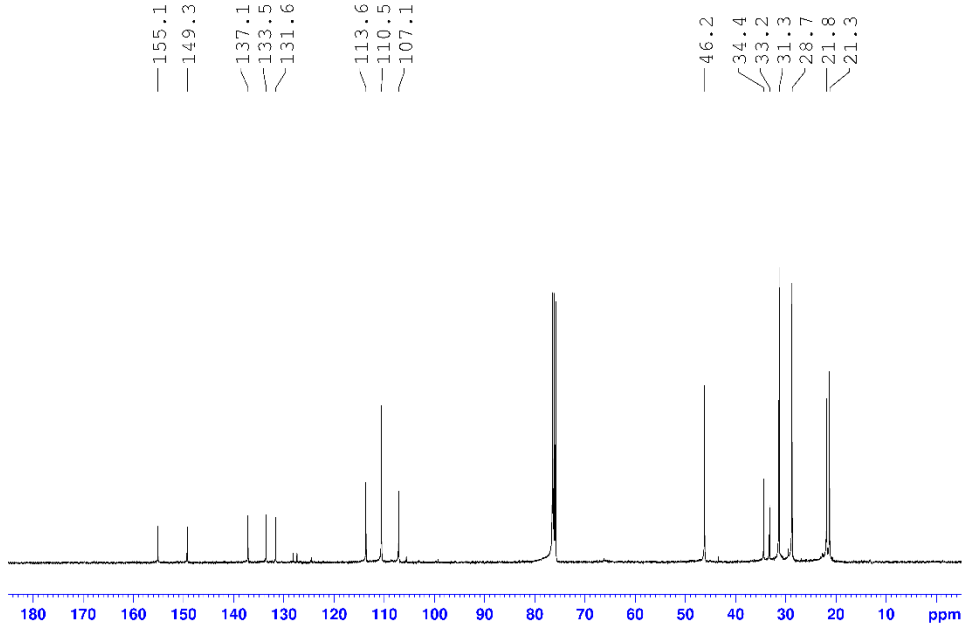

Figure A62 ^{13}C{^{1}H} NMR spectrum of Zn[**L2b**]$_2$ (100 MHz, $CDCl_3$)

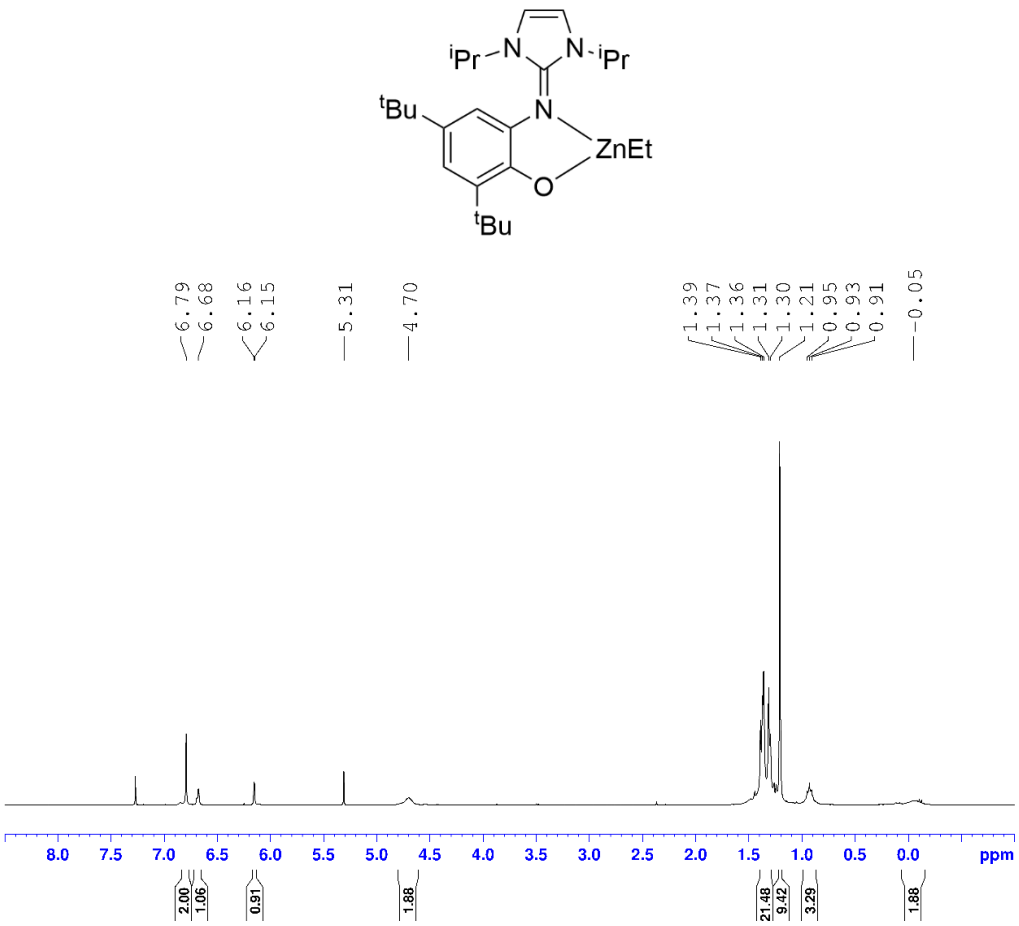

Figure A63 ^{1}H NMR spectrum of Zn[**L2b**]Et (400 MHz, $CDCl_3$)

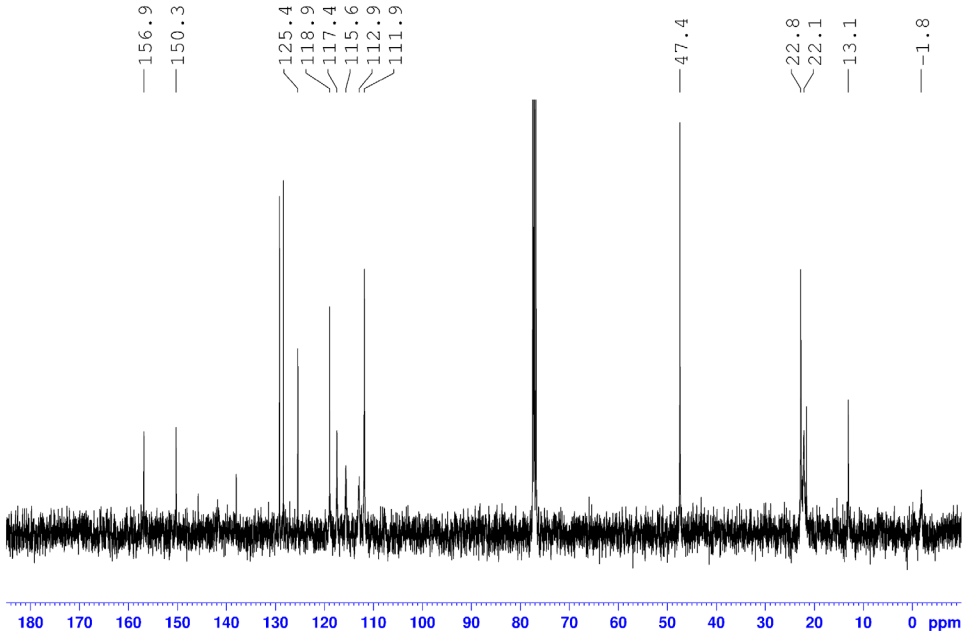

Figure A64 $^{13}C\{^{1}H\}$ NMR spectrum of Zn[**L2b**]Et (100 MHz, $CDCl_3$)

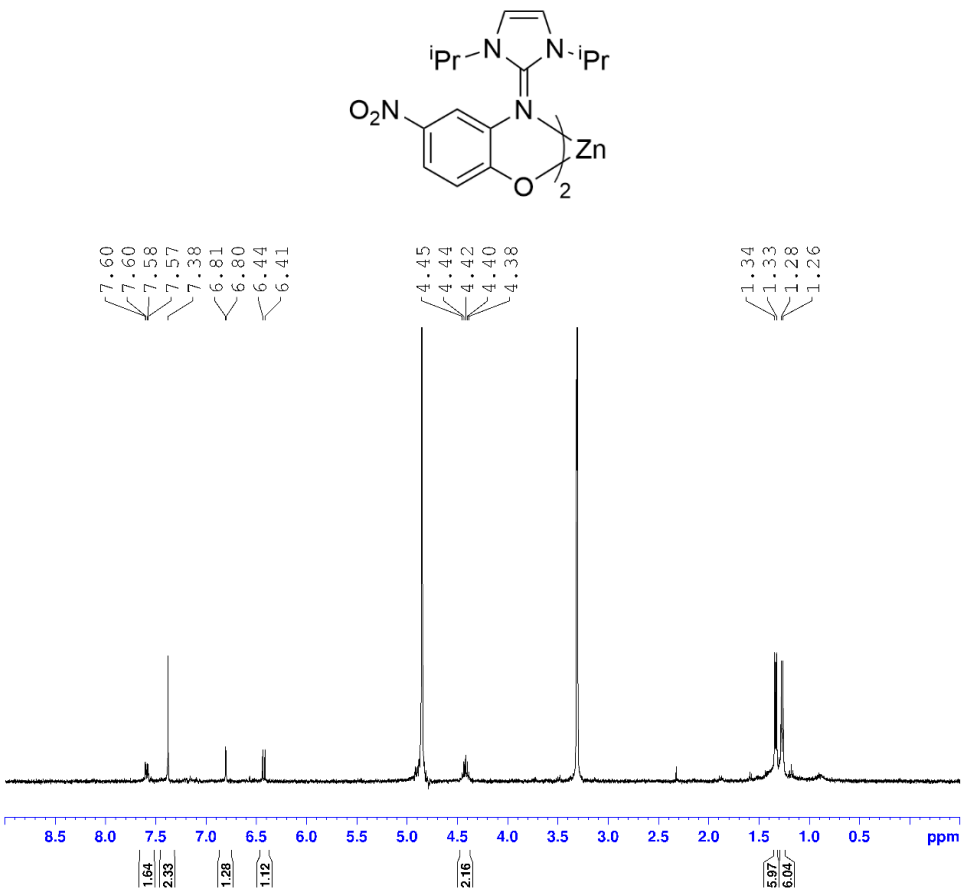

Figure A65 ^{1}H NMR spectrum of Zn[**L2c**]$_2$ (400 MHz, CD_3OD)

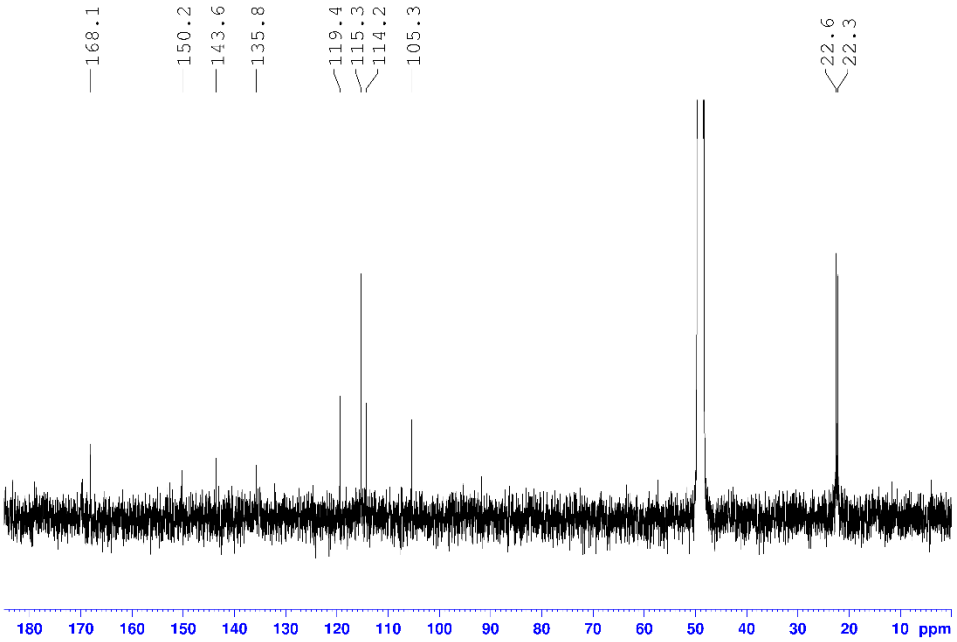

Figure A66 ^{13}C{^{1}H} NMR spectrum of Zn[**L2c**]$_2$ (100 MHz, CD_3OD)

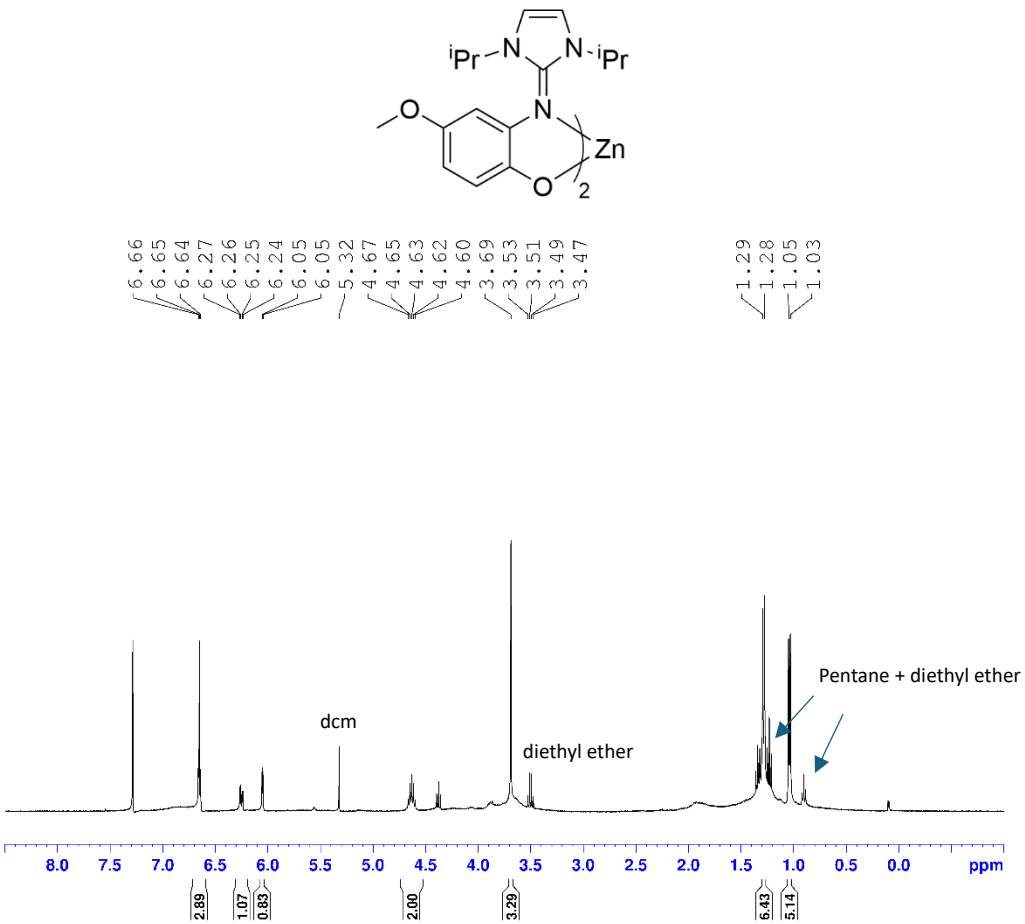

Figure A67 ^{1}H NMR spectrum of Zn[**L2d**]$_2$ (400 MHz, $CDCl_3$)

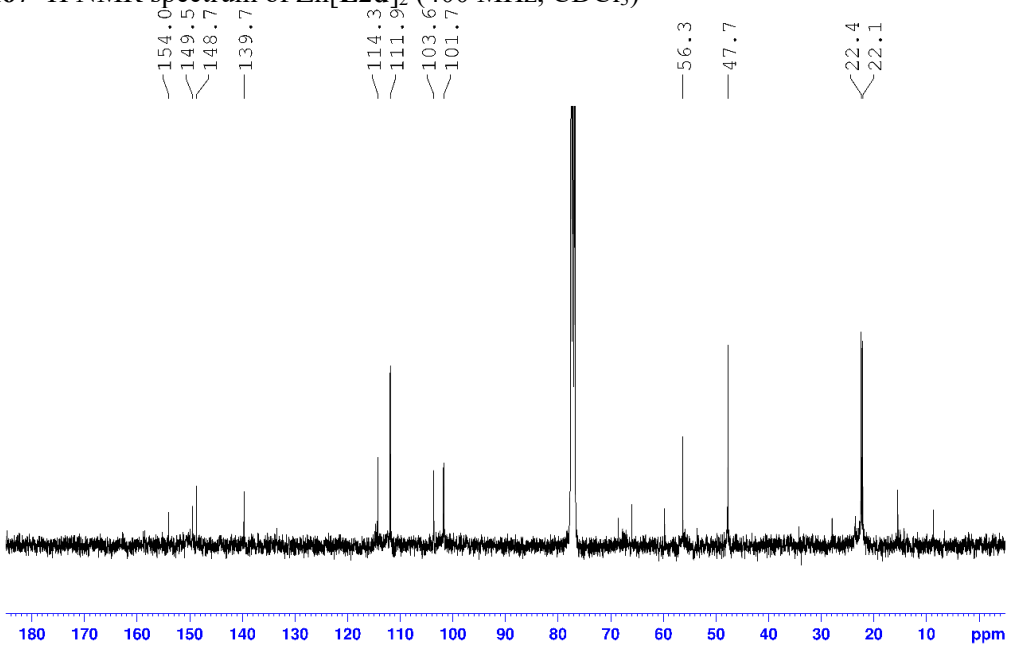

Figure A68 $^{13}C\{^{1}H\}$ NMR spectrum of Zn[**L2d**]$_2$ (100 MHz, $CDCl_3$)

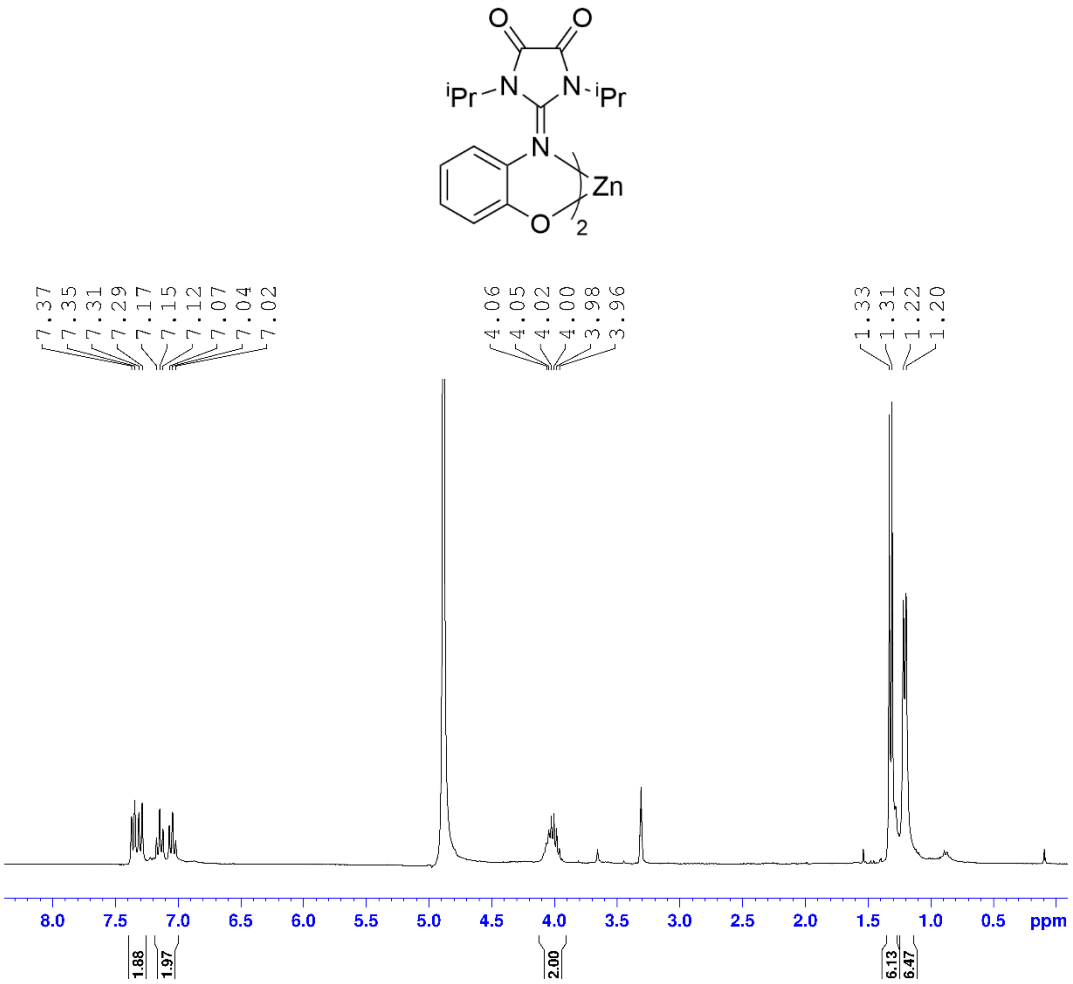

Figure A69 ^{1}H NMR spectrum of. Zn[**L5a**]$_2$ (400 MHz, CD_3OD)

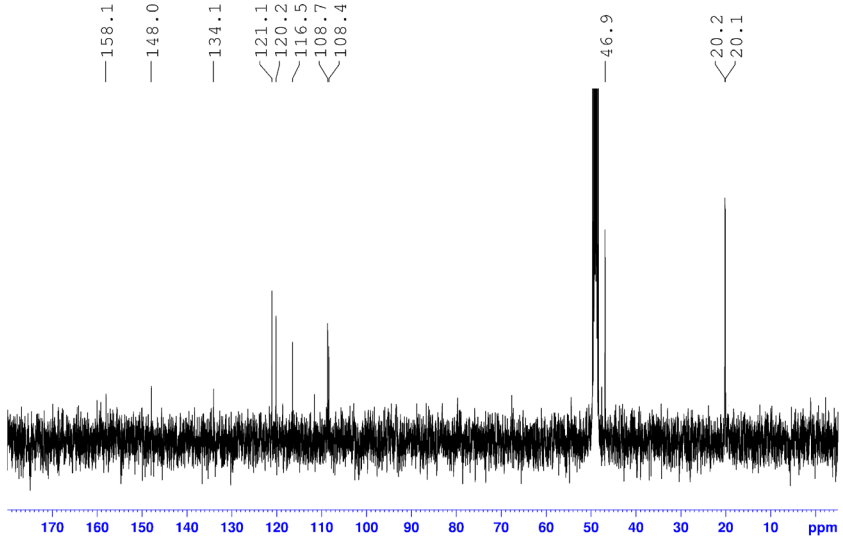

Figure A70 $^{13}C\{^{1}H\}$ NMR spectrum of Zn[**L5a**]$_2$ (100 MHz, CD_3OD)

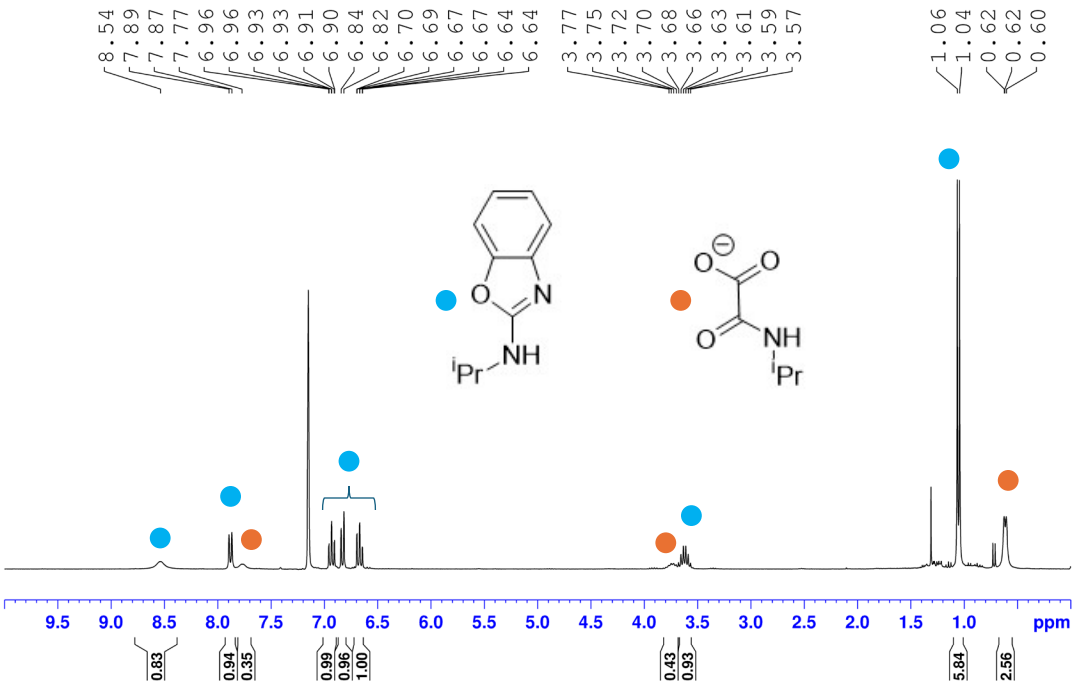

Figure A71 ^{1}H NMR spectrum of the Zn species containing the hydrolyzed **L5a** (300 MHz, $CDCl_3$)

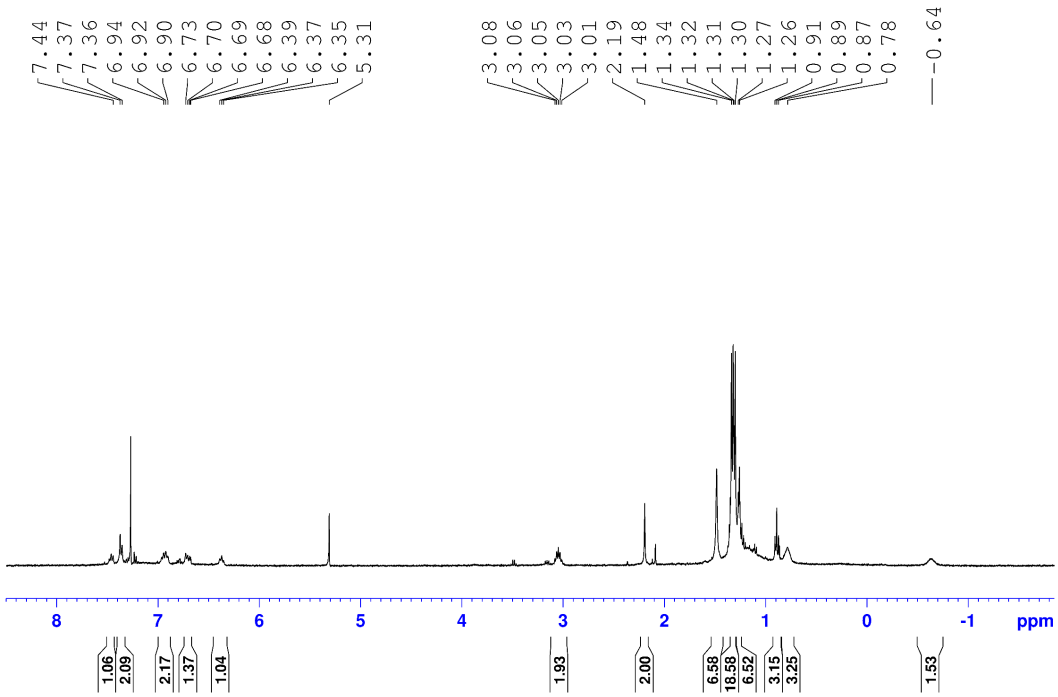

Figure A72 ^{1}H NMR spectrum of Zn[**L6a**]Et (400 MHz, $CDCl_3$)

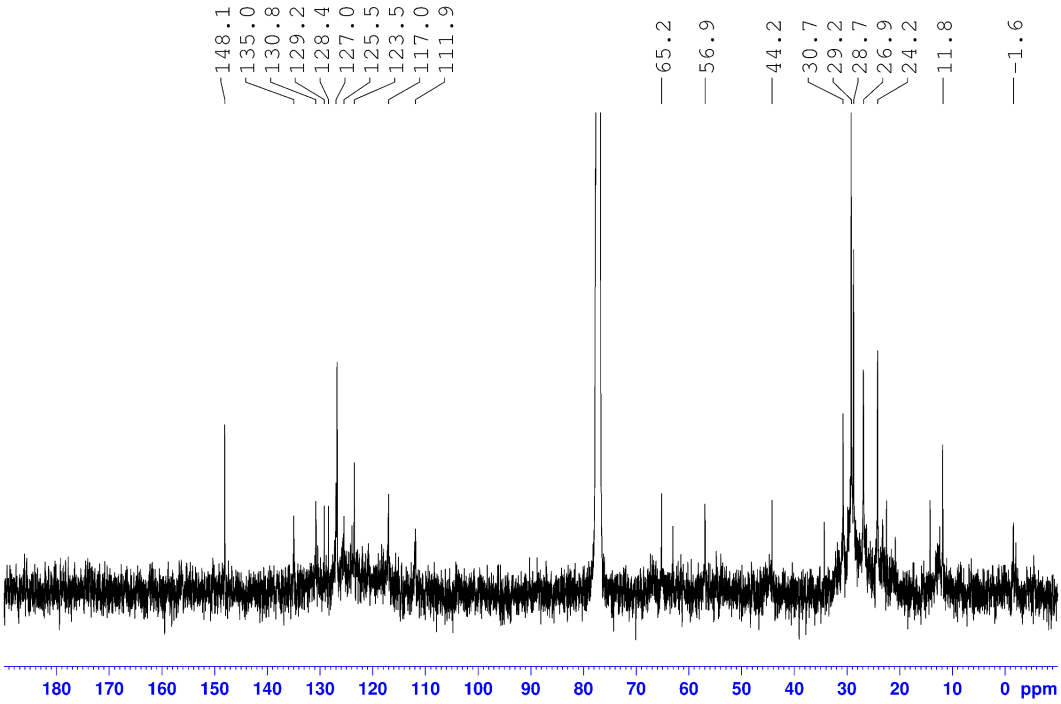

Figure A73 ^{13}C {^{1}H} NMR spectrum of Zn[**L6a**]Et (100 MHz, $CDCl_3$)

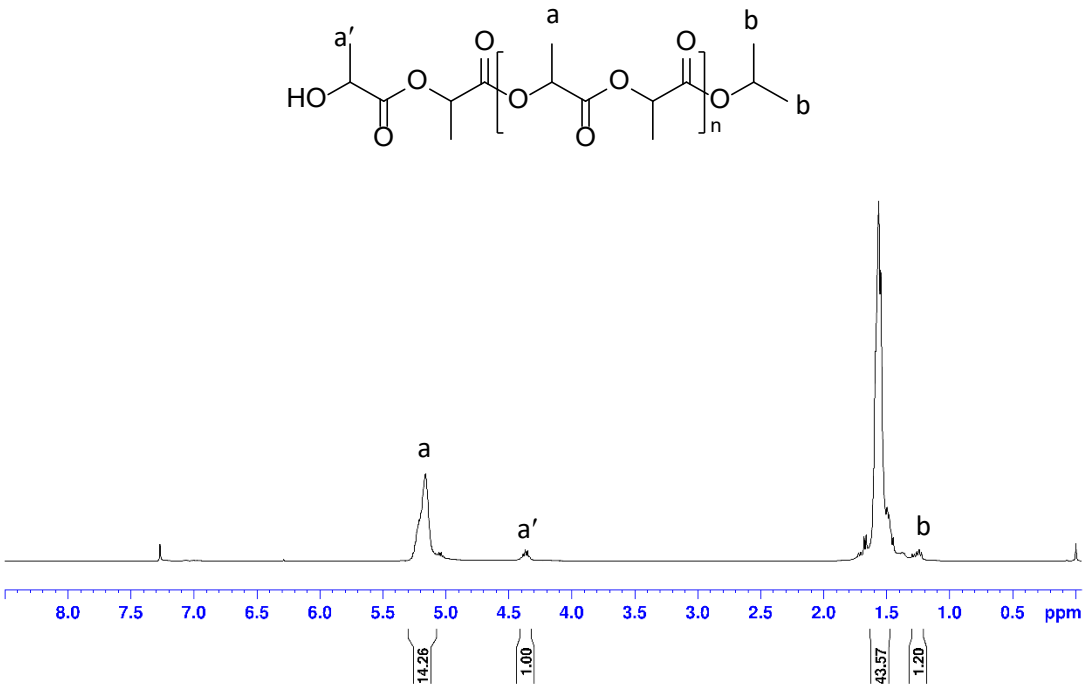

Figure A74.[1]H NMR spectrum of the polymer produced with Zr(**L2a**)$_2$(O^{i}Pr)$_2$ (400 MHz, $CDCl_3$)

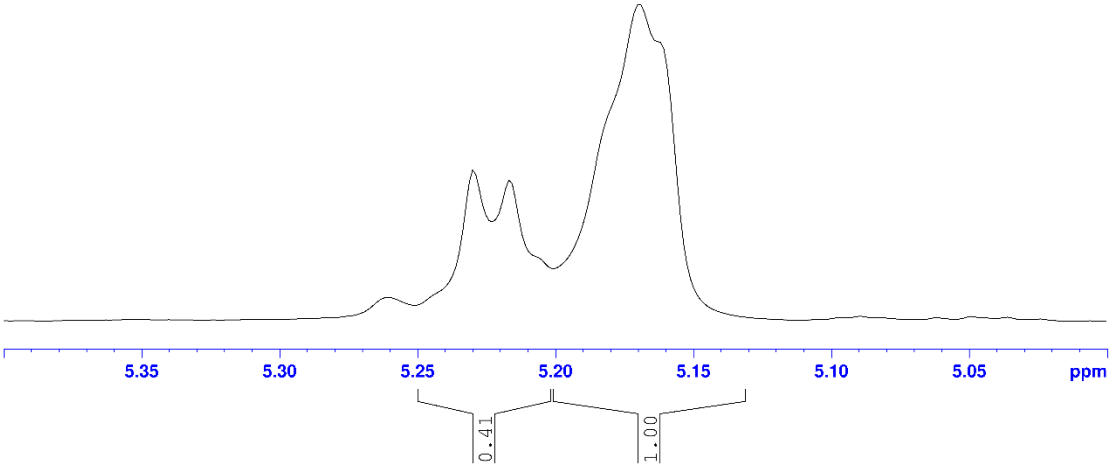

Figure A75.Homonuclear-decoupled [1]H NMR spectrum of the polymer produced with Zr(**L2a**)$_2$(O^{i}Pr)$_2$ (400 MHz, $CDCl_3$)

Figure A76. $^{13}C\{^{1}H\}$ NMR spectrum of the polymer produce with Zr(**L2a**)$_2$(O^{i}Pr)$_2$ (100 MHz, $CDCl_3$)

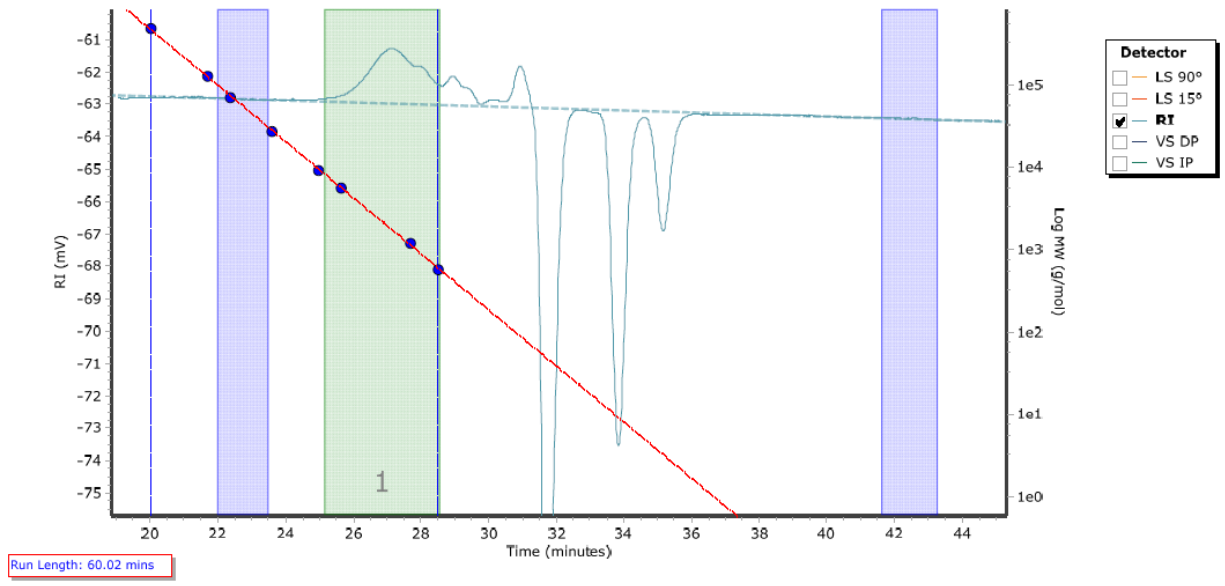

Figure A77. GPC chromatogram plot of the polymer obtained using complex Ti(**L1a**)$_2$(O^{i}Pr)$_2$ (Chapter 2, Table 7, entry 1)

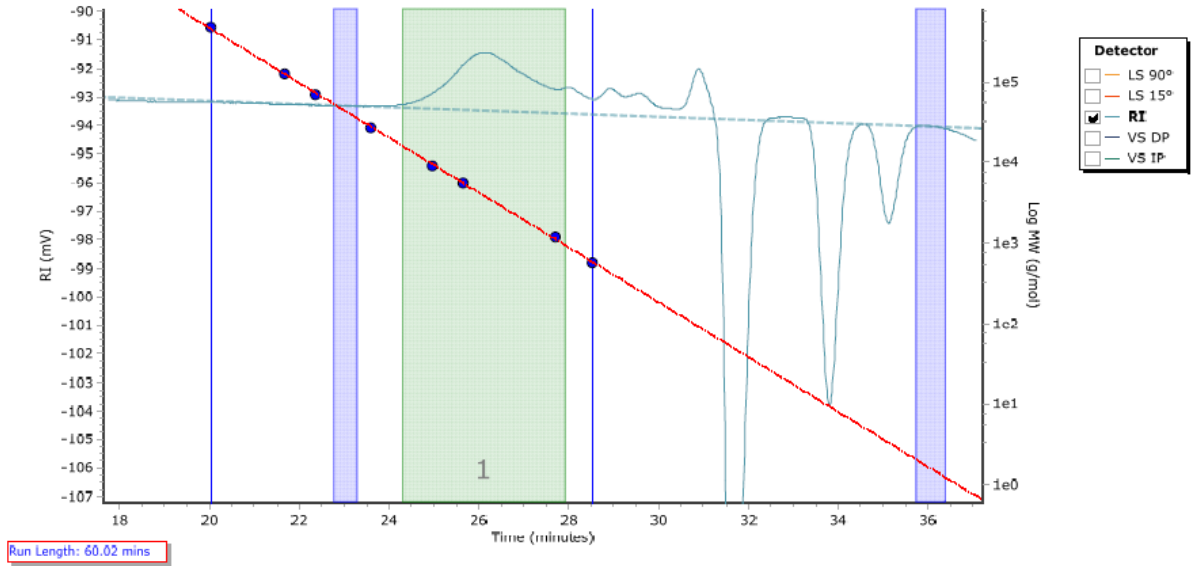

Figure A78. GPC chromatogram plot of the polymer obtained using complex Ti(**L1b**)$_2$(O^{i}Pr)$_2$ (Chapter 2, Table 7, entry 2)

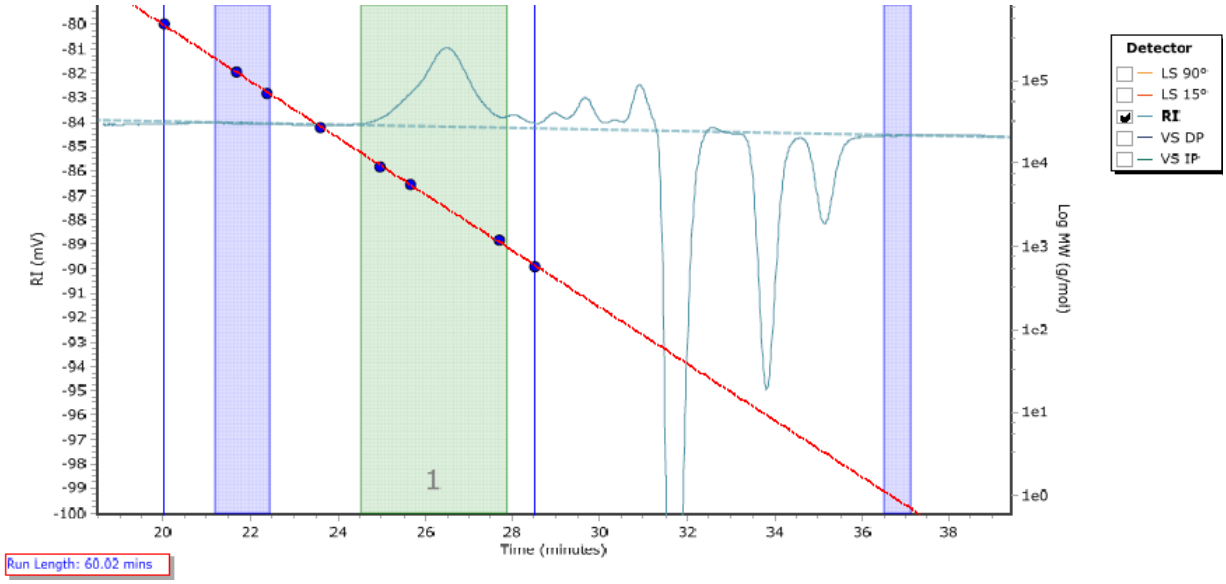

Figure A79. GPC chromatogram plot of the polymer obtained using complex Zr(**L1a**)$_2$(O^{i}Pr)$_2$ (Chapter 2, Table 7, entry 6)

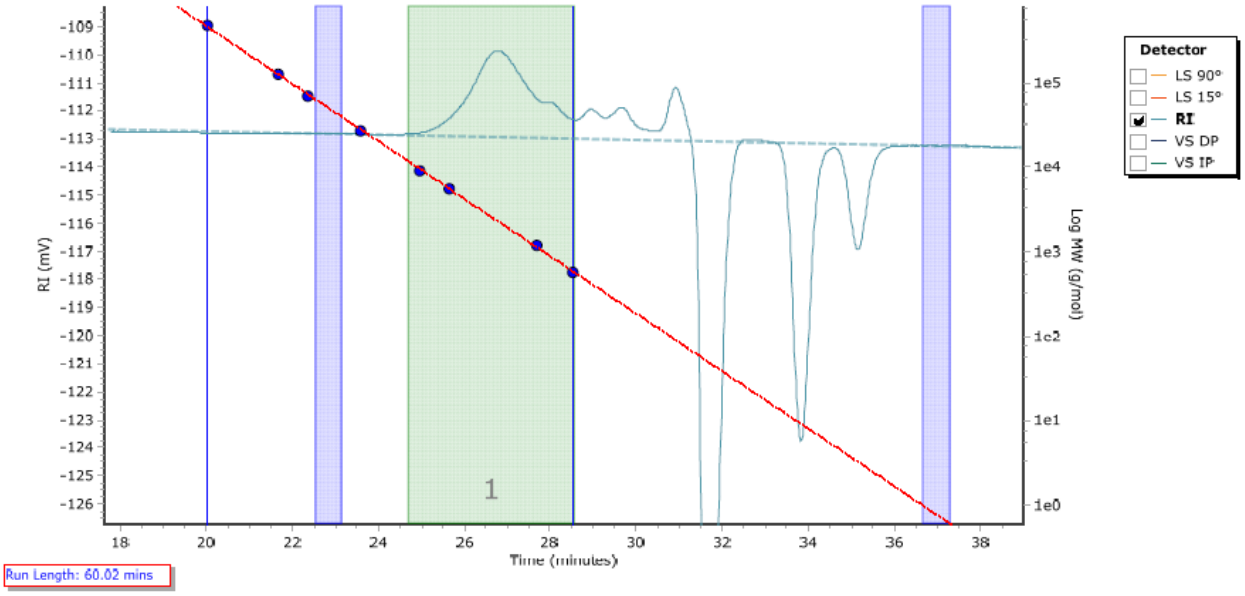

Figure A80. GPC chromatogram plot of the polymer obtained using complex Zr(**L1b**)$_2$(O^{i}Pr)$_2$ (Chapter 2, Table 7, entry 7)

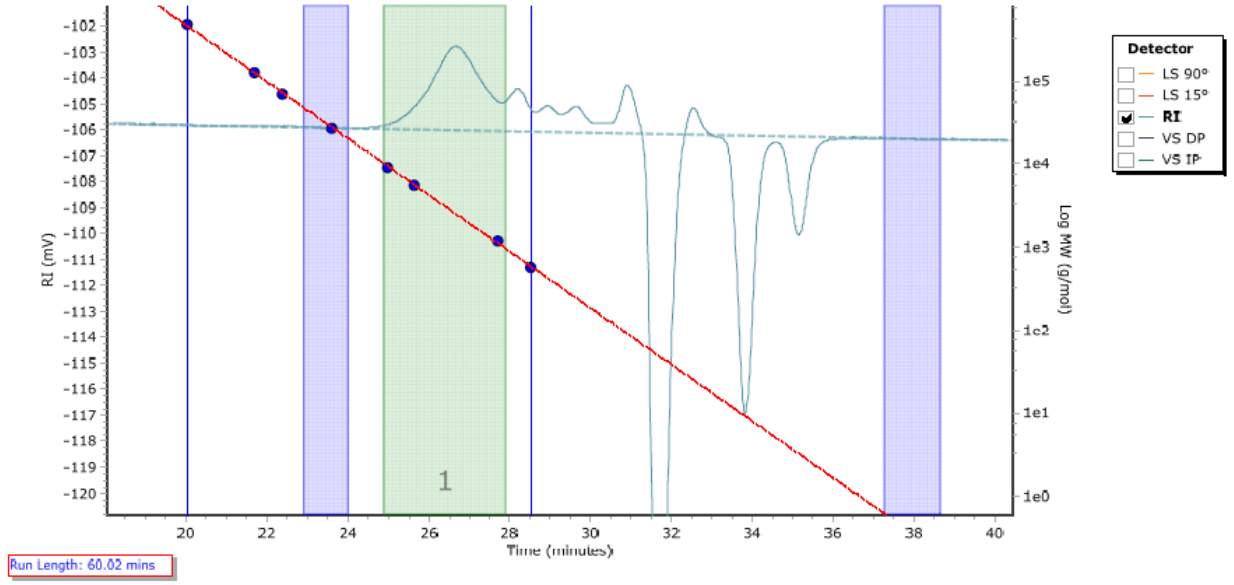

Figure A81. GPC chromatogram plot of the polymer obtained using complex **Ti(L2a)$_2$(O^{i}Pr)$_2$** (Chapter 2, Table 7, entry 3)

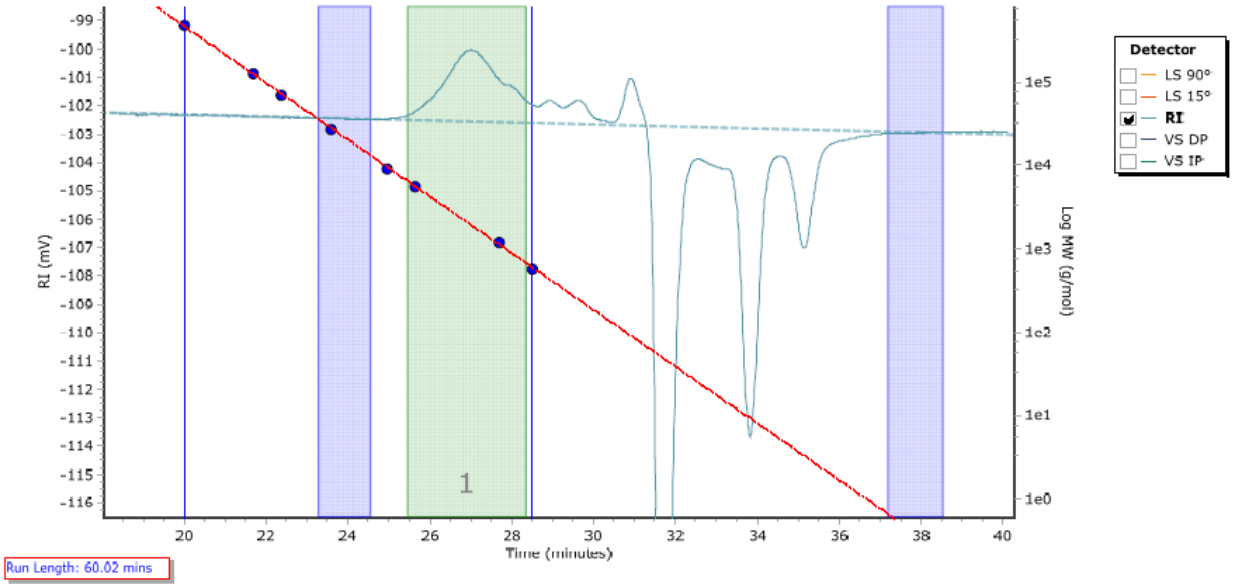

Figure A82. GPC chromatogram plot of the polymer obtained using complex Zr(**L2a**)$_2$(O^{i}Pr)$_2$ (Chapter 2, Table 7, entry 8)

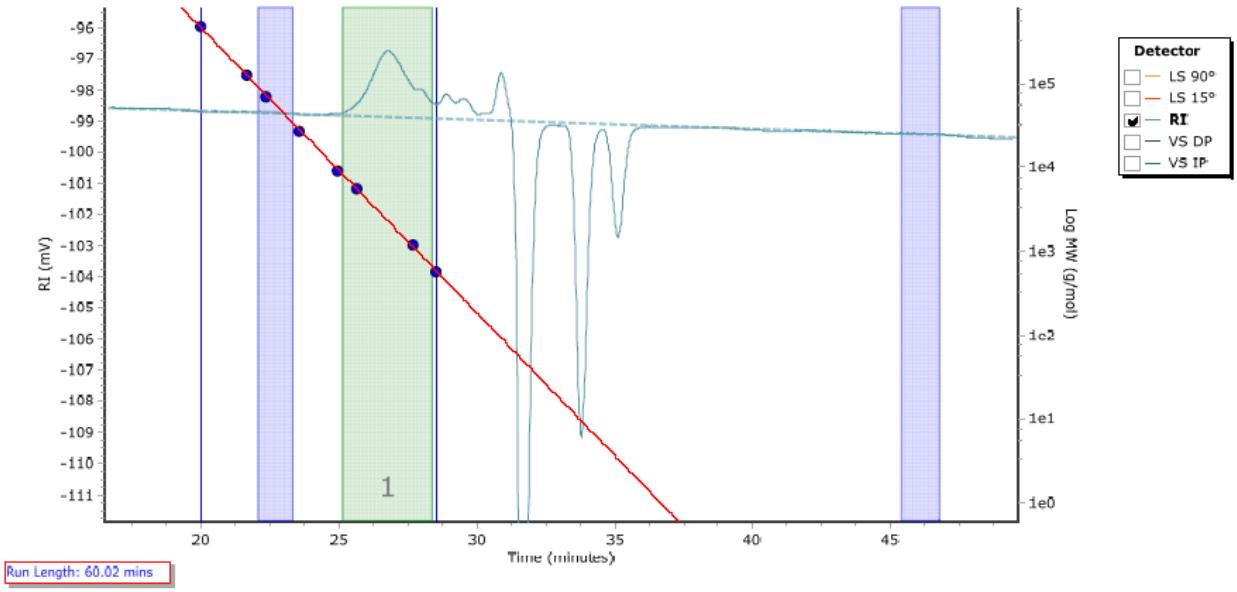

Figure A83. GPC chromatogram plot of the polymer obtained using complex Zr(**L2a**)$_2$(O^{i}Pr)$_2$ (Chapter 2, Table 7, purified LA, entry 9)

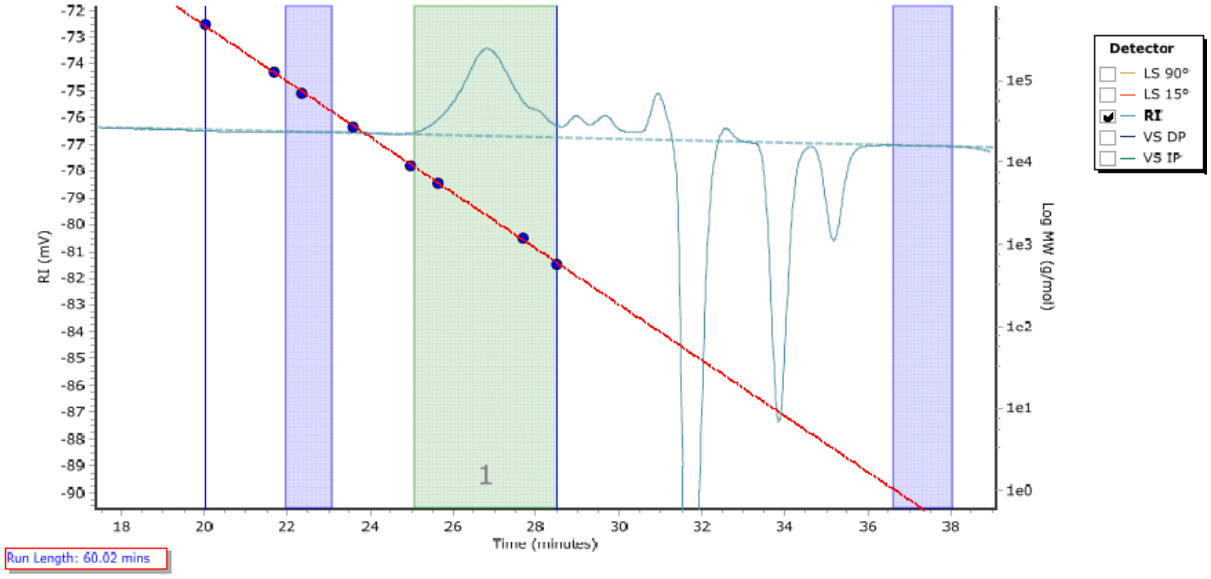

Figure A84. GPC chromatogram plot of the polymer obtained using complex Zr(**L2a**)$_2$(O^{i}Pr)$_2$ (Chapter 2, Table 7, 1 equiv. of ^{i}PrOH, entry 10)

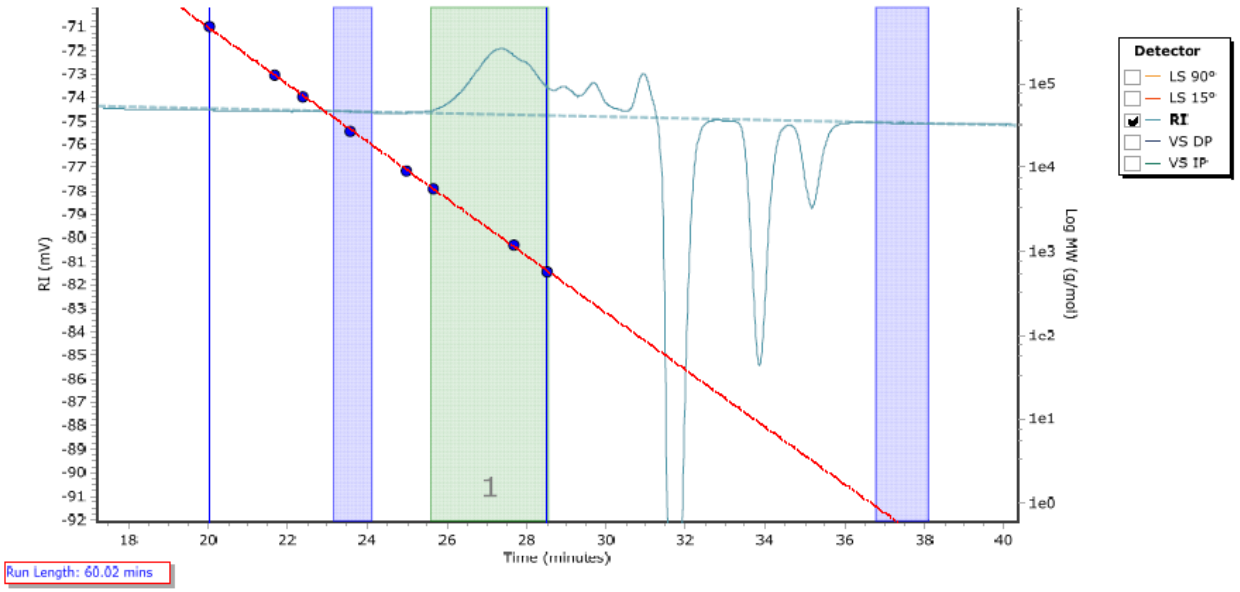

Figure A85. GPC chromatogram plot of the polymer obtained using complex Ti(**L3a**)$_2$(O^{i}Pr)$_2$ (Chapter 2, Table 7, entry 4)

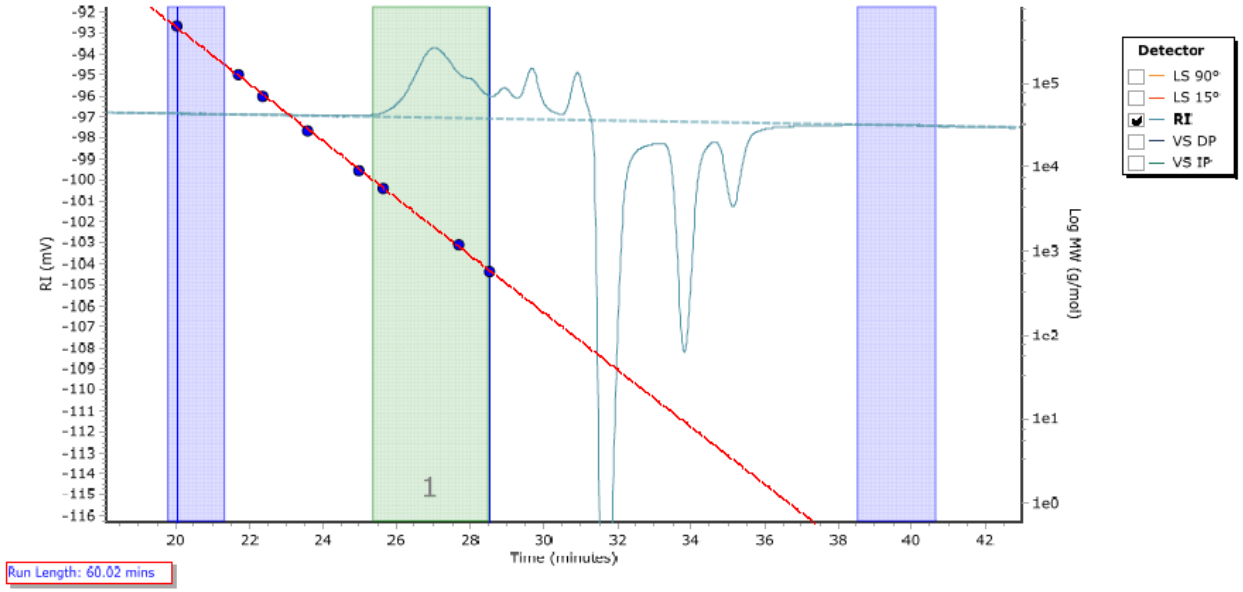

Figure A86. GPC chromatogram plot of the polymer obtained using complex Zr(**L3a**)$_2$(O^{i}Pr)$_2$ (Chapter 2, Table 7, entry 11)

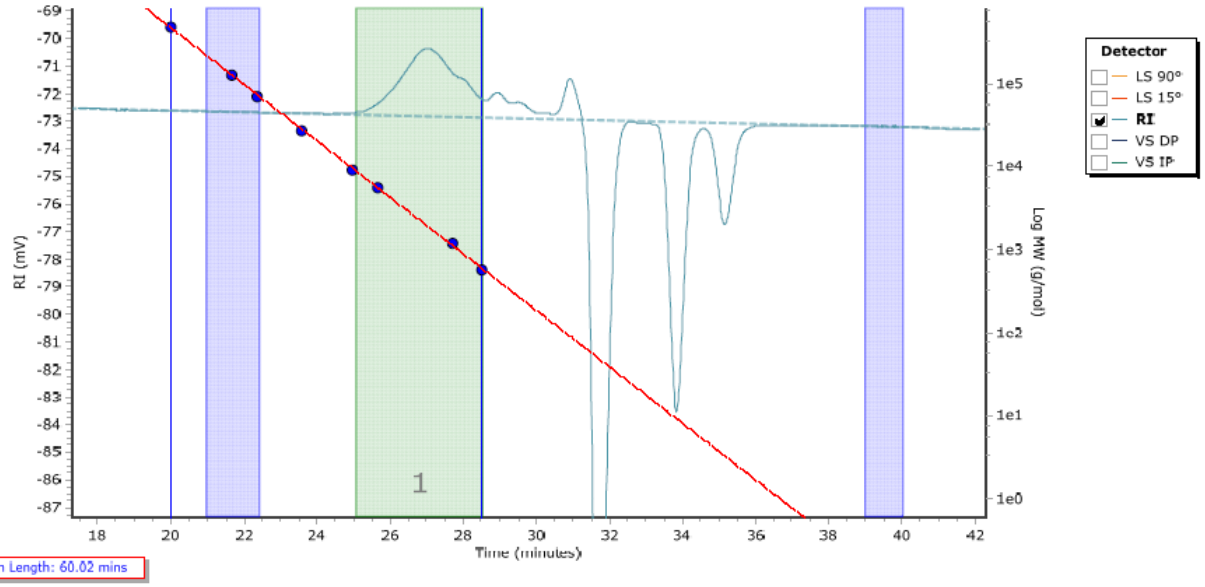

Figure A87. GPC chromatogram plot of the polymer obtained using complex Ti(**L4a**)$_2$(O^{i}Pr)$_2$ (Chapter 2, Table 7, entry 5)

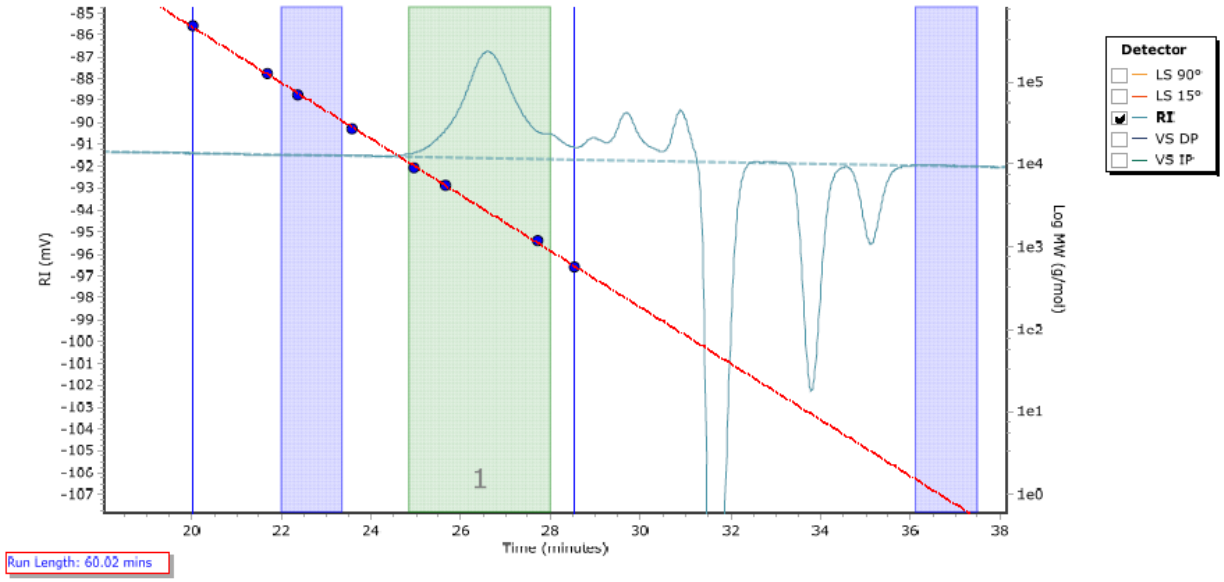

Figure A88. GPC chromatogram plot of the polymer obtained using complex Zr(**L4a**)$_2$(O^{i}Pr)$_2$ (Chapter 2, Table 7, entry 12)

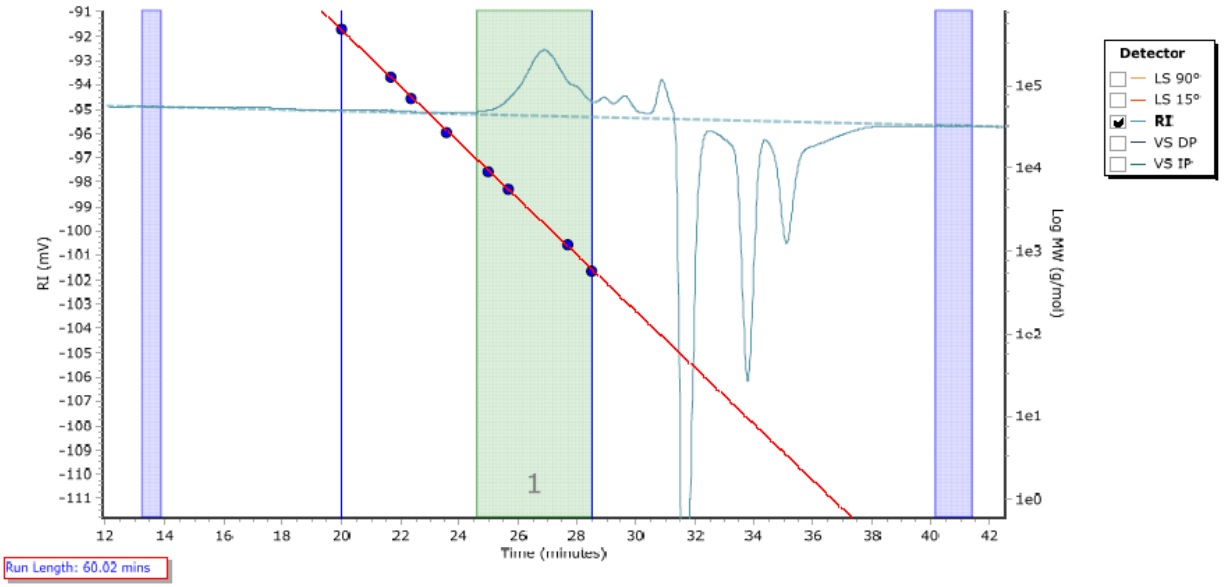

Figure A89. GPC chromatogram plot of the polymer obtained using complex **L2a**H (Chapter 2, Table 7, entry 13)

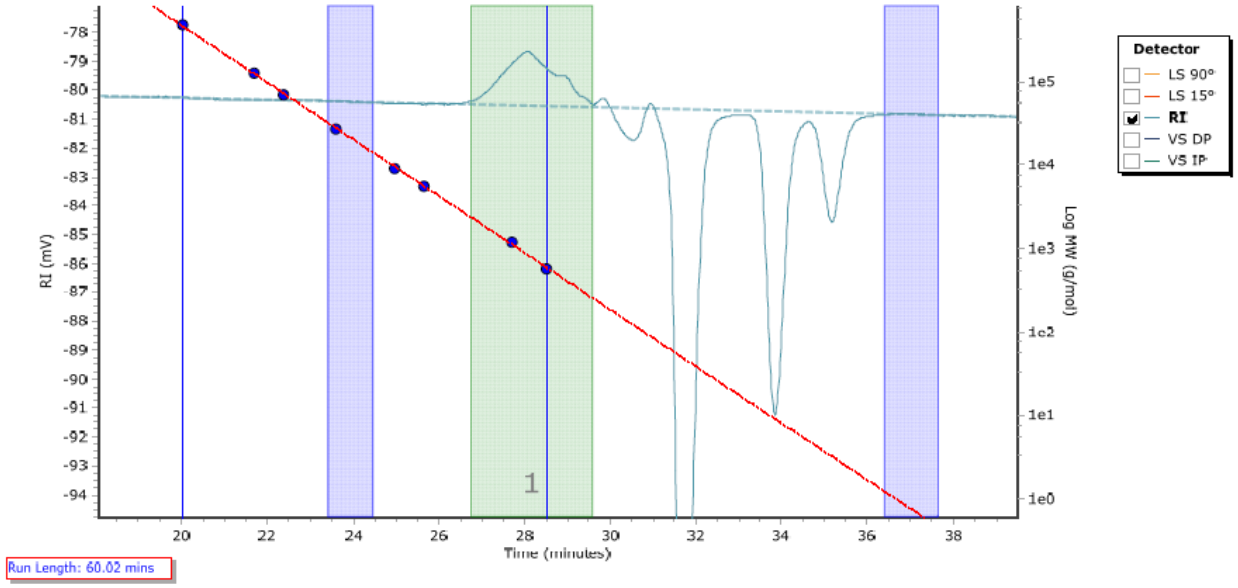

Figure A90. GPC chromatogram plot of the polymer obtained using complex **Ti(O^{i}Pr)$_4$** (Chapter 2, Table 7, entry 15)

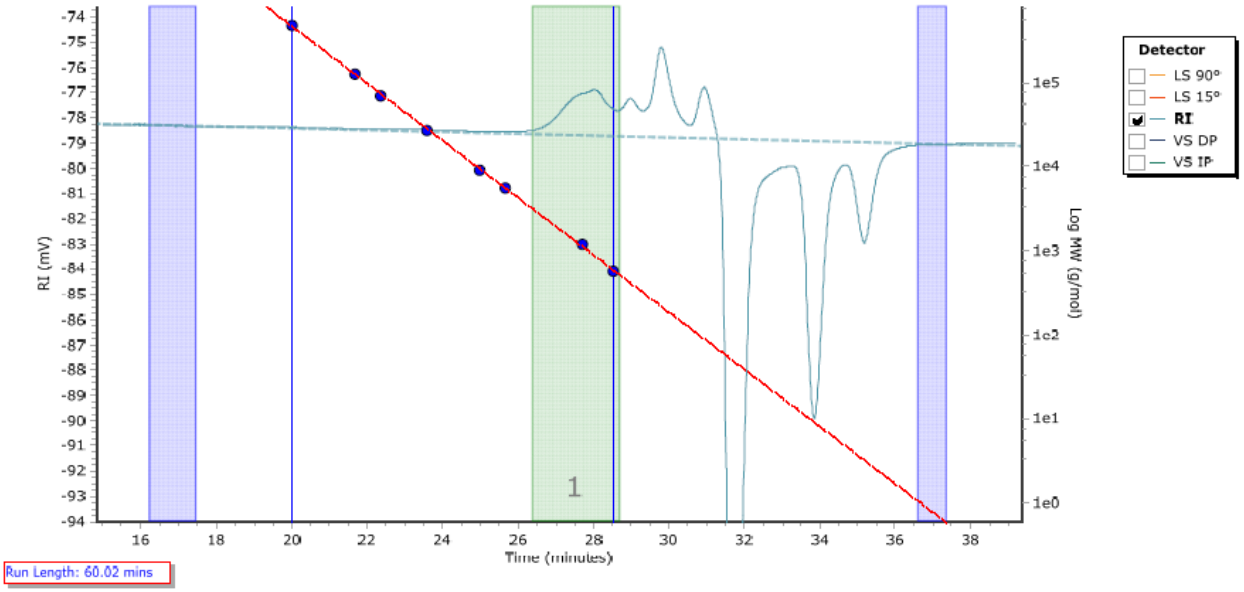

Figure A91. GPC chromatogram plot of the polymer obtained using complex **Zr(O^{i}Pr)$_4$·^{i}PrOH** (Chapter 2, Table 7, entry 16)

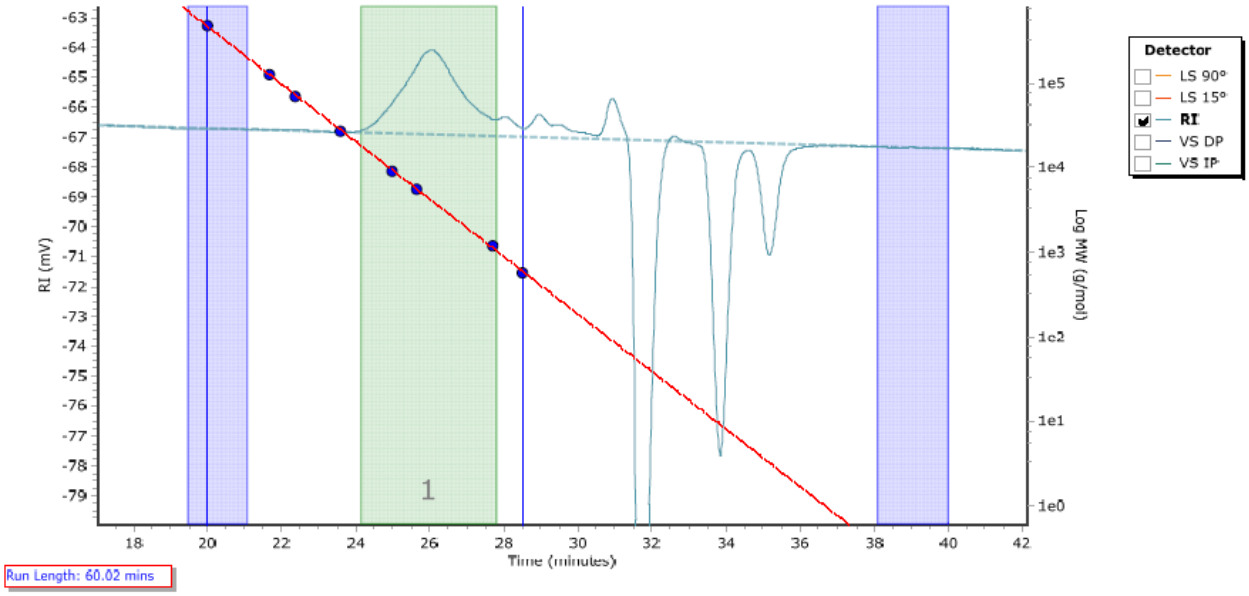

Figure A92. GPC chromatogram plot of the polymer obtained using **Sn(Oct)$_2$** (Chapter 2, Table 7, entry 14)

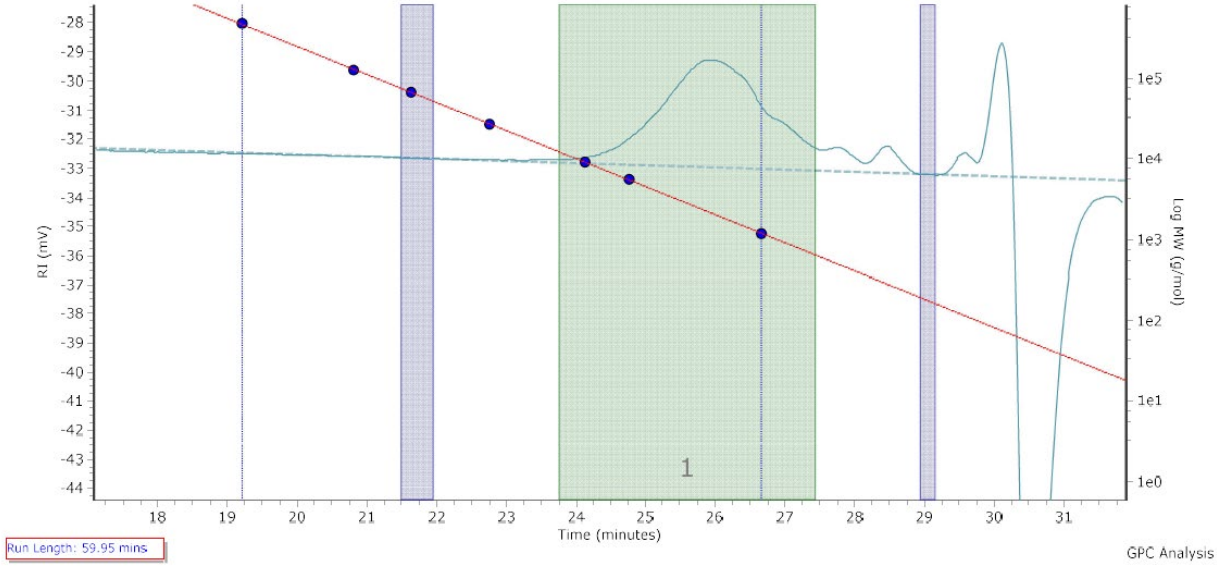

Figure A93 GPC chromatogram plot of a polymer sample, herein obtained using complex Zn[**L2a**]$_2$ (Chapter 3, Table 11, entry 1)

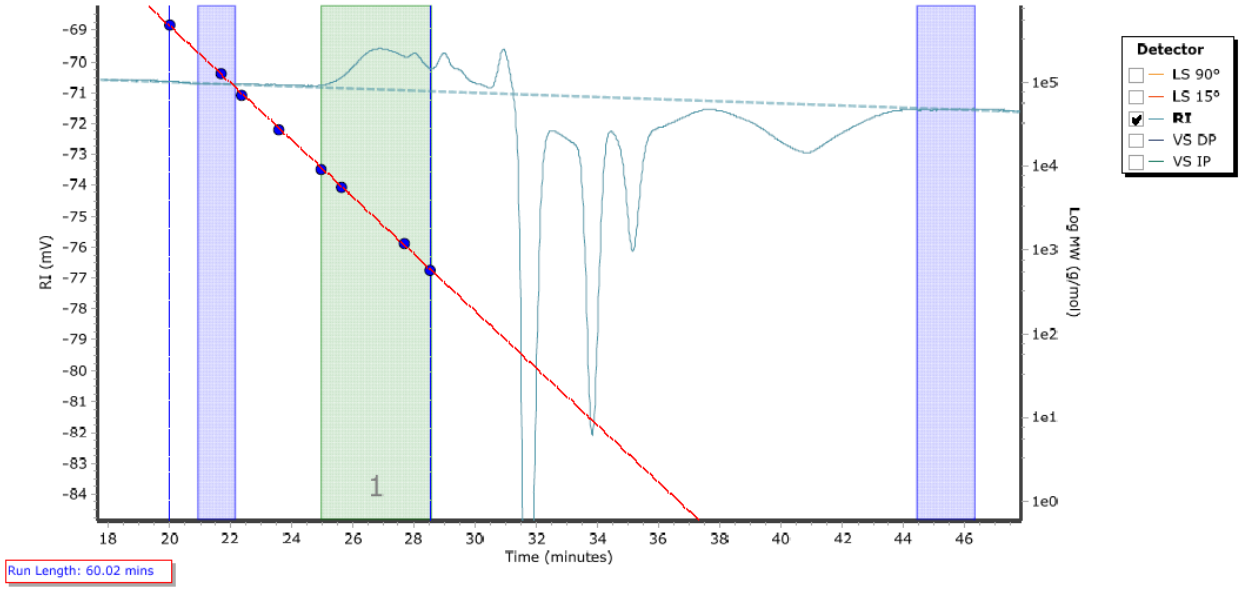

Figure A94 GPC chromatogram plot of a polymer sample, herein obtained using complex Zn[**L2a**]$_2$ with BnOH (Chapter 3, Table 11, entry 2)

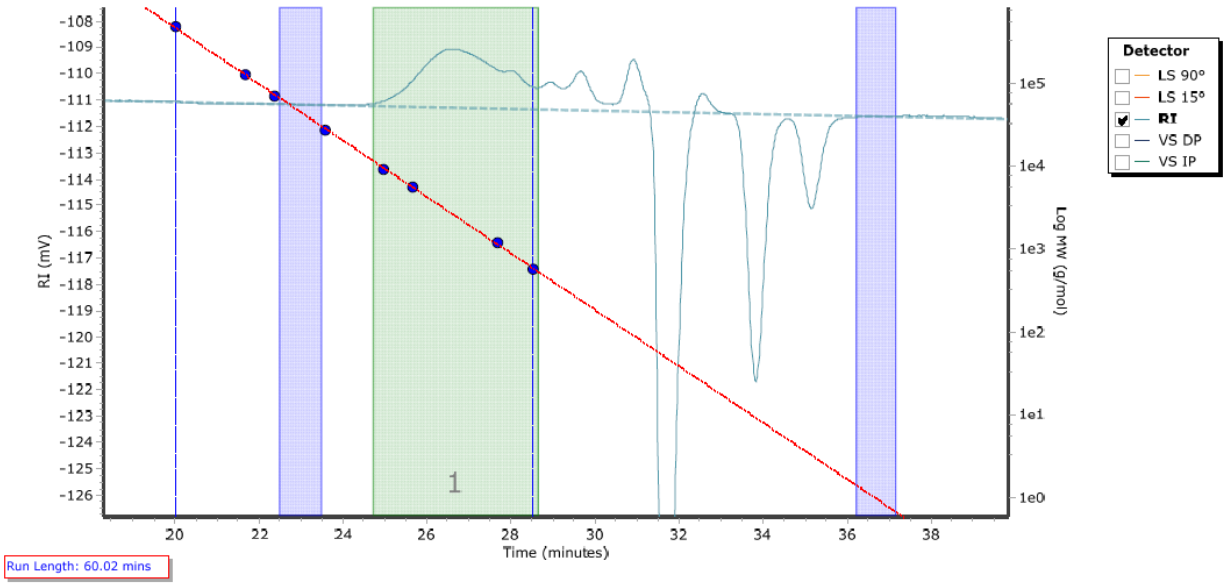

Figure A95 GPC chromatogram plot of a polymer sample, herein obtained using complex Zn[**L2a**]Et with BnOH (Chapter 3, Table 11, entry 3)

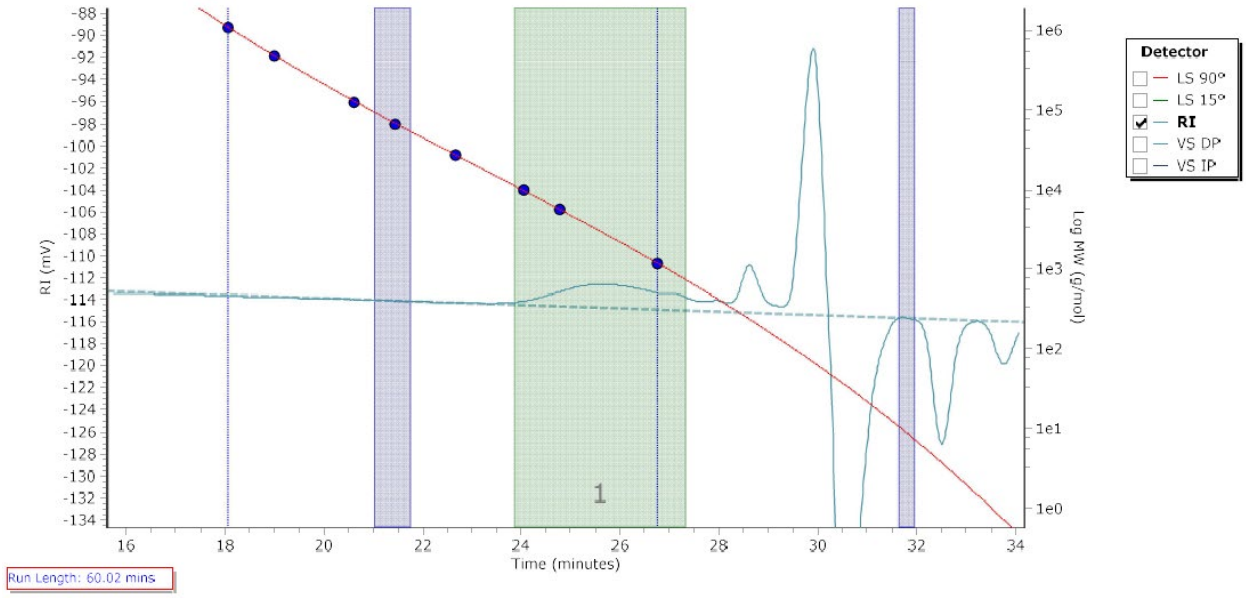

Figure A96 GPC chromatogram plot of a polymer sample, herein obtained using complex Zn[**L2a**]Et without BnOH (Chapter 3, Table 11, entry 4)

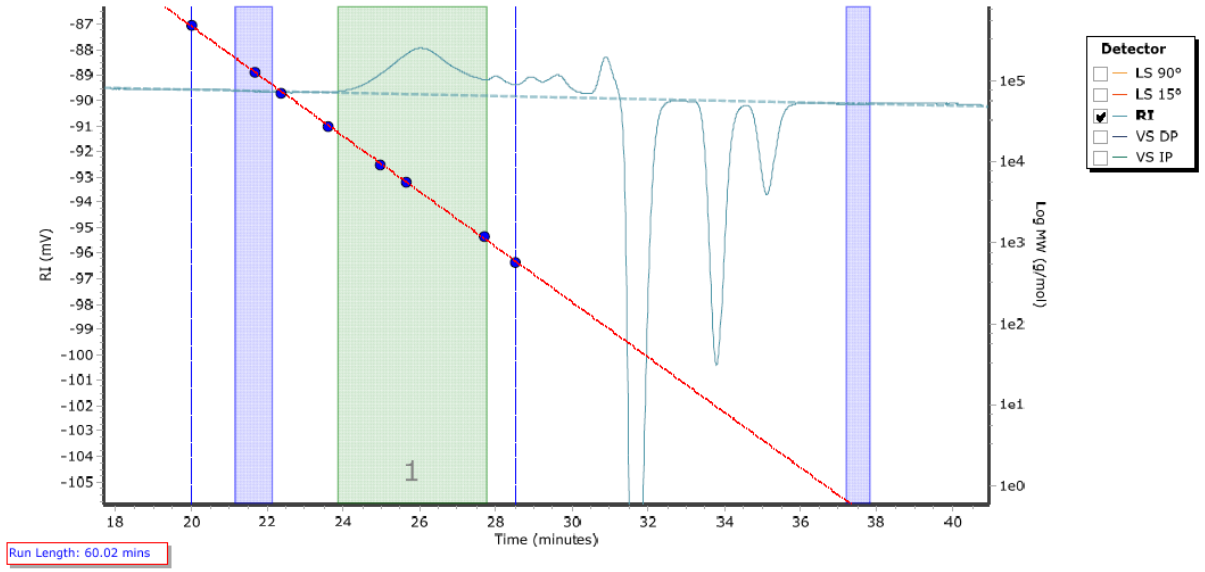

Figure A97 GPC chromatogram plot of a polymer sample, herein obtained using complex Zn[**L2b**]$_2$ (Chapter 3, Table 11, entry 5)

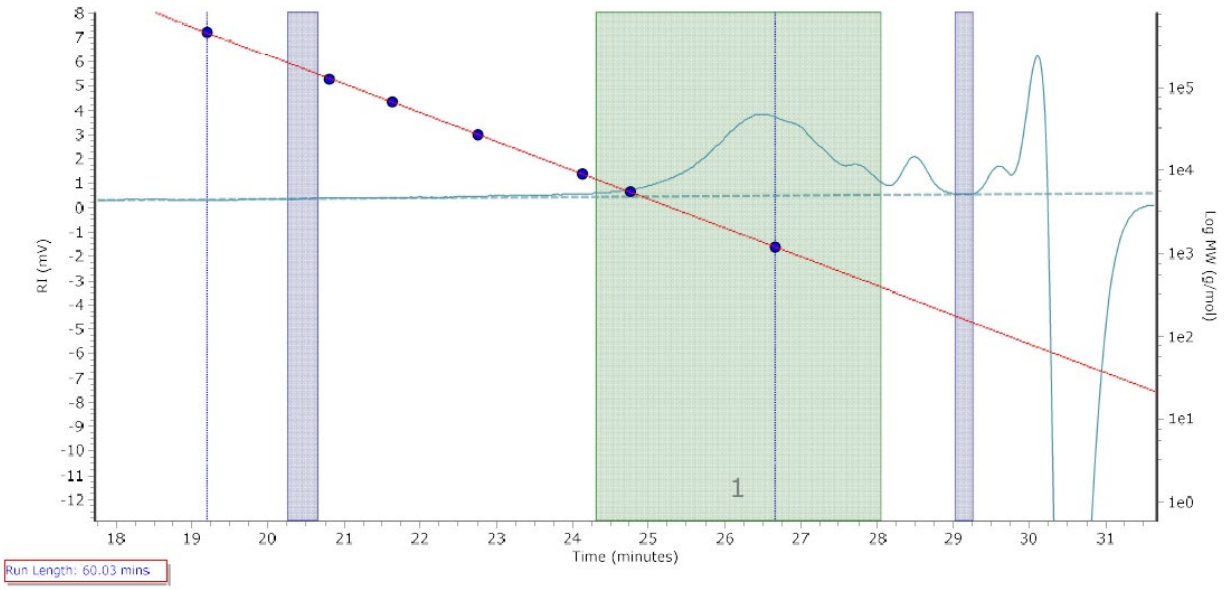

Figure A98 GPC chromatogram plot of a polymer sample, herein obtained using complex Zn[**L2b**]Et with BnOH (Chapter 3, Table 11, entry 6)

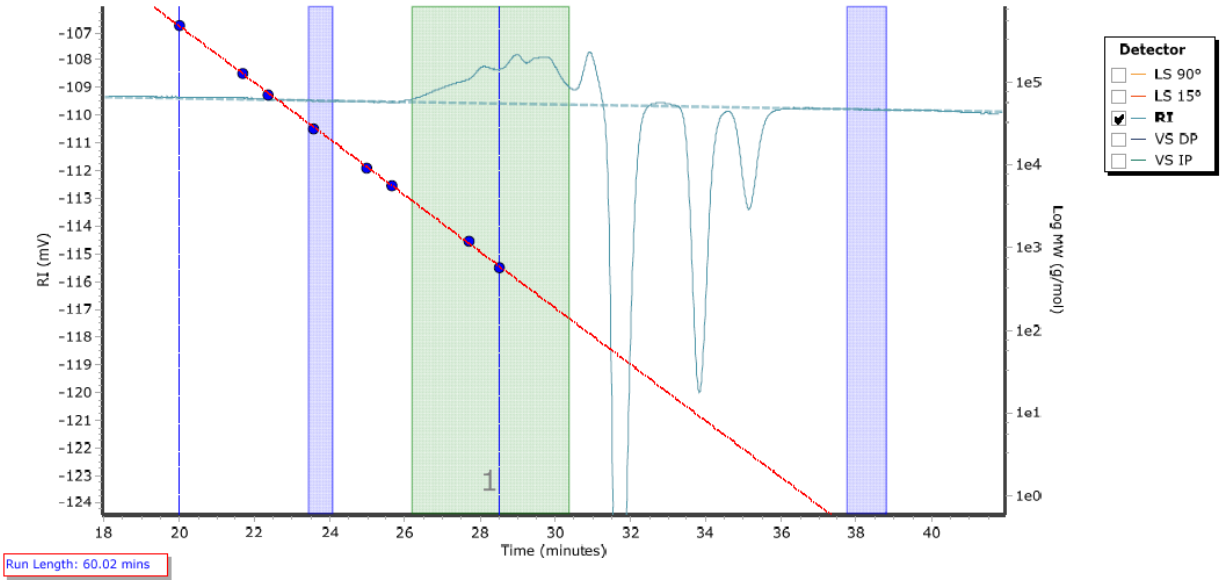

Figure A99 GPC chromatogram plot of a polymer sample, herein obtained using complex Zn[**L2c**]$_2$ (Chapter 3, Table 11, entry 7)

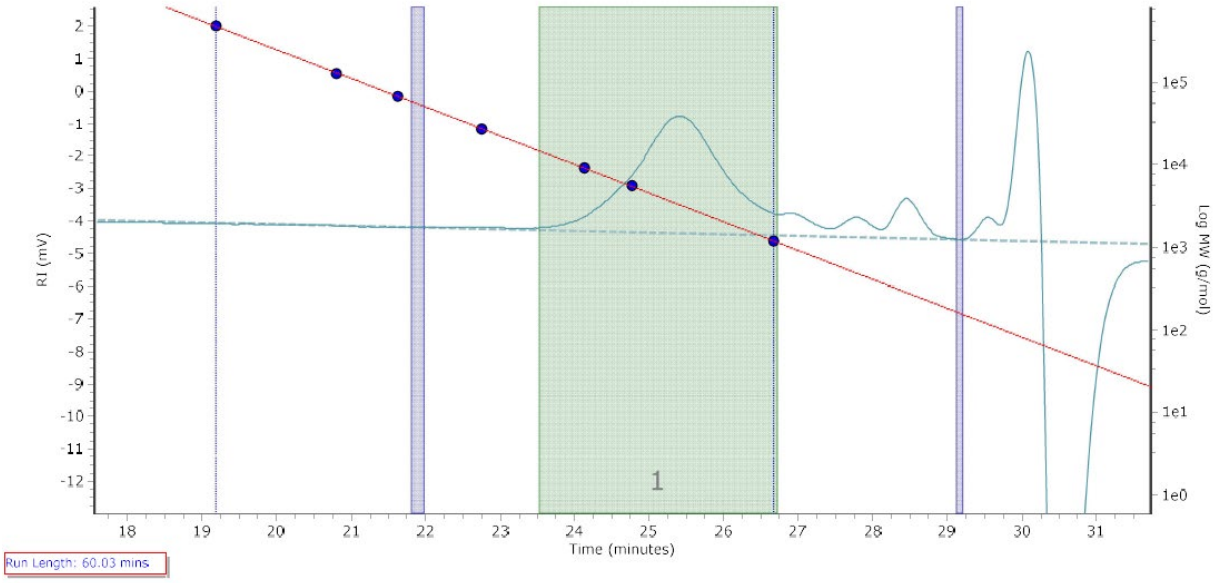

Figure A100 GPC chromatogram plot of a polymer sample, herein obtained using complex Zn[**L2d**]$_2$ (Chapter 3, Table 11, entry 8)

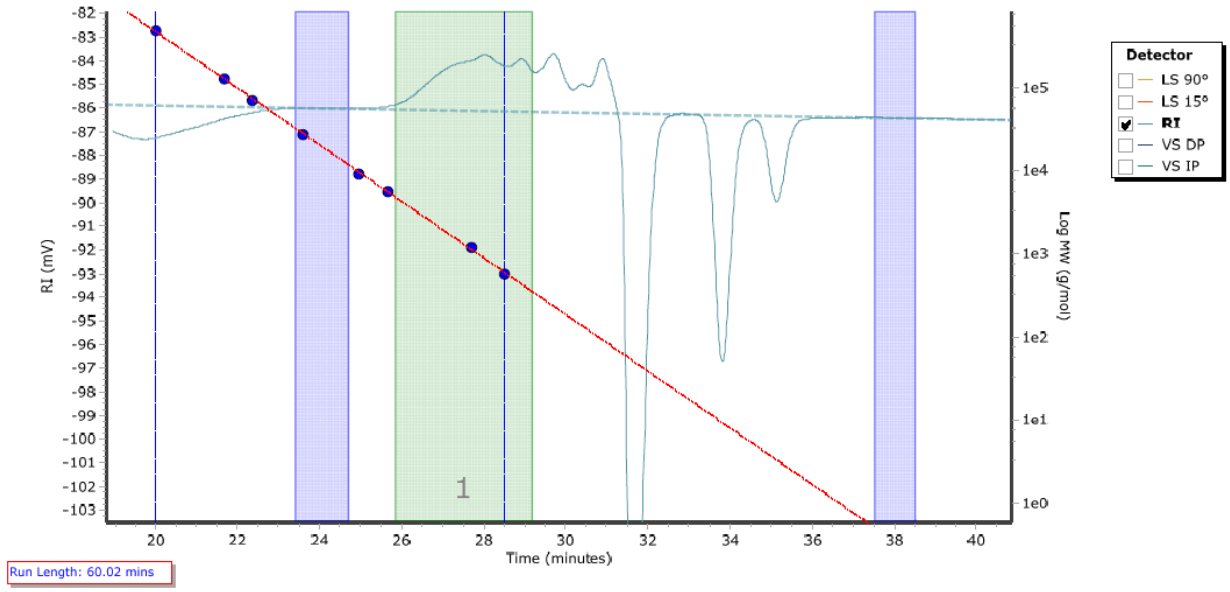

Figure A101 GPC chromatogram plot of a polymer sample, herein obtained using complex Zn[**L5a**]$_2$ (Chapter 3, Table 11, entry 9)

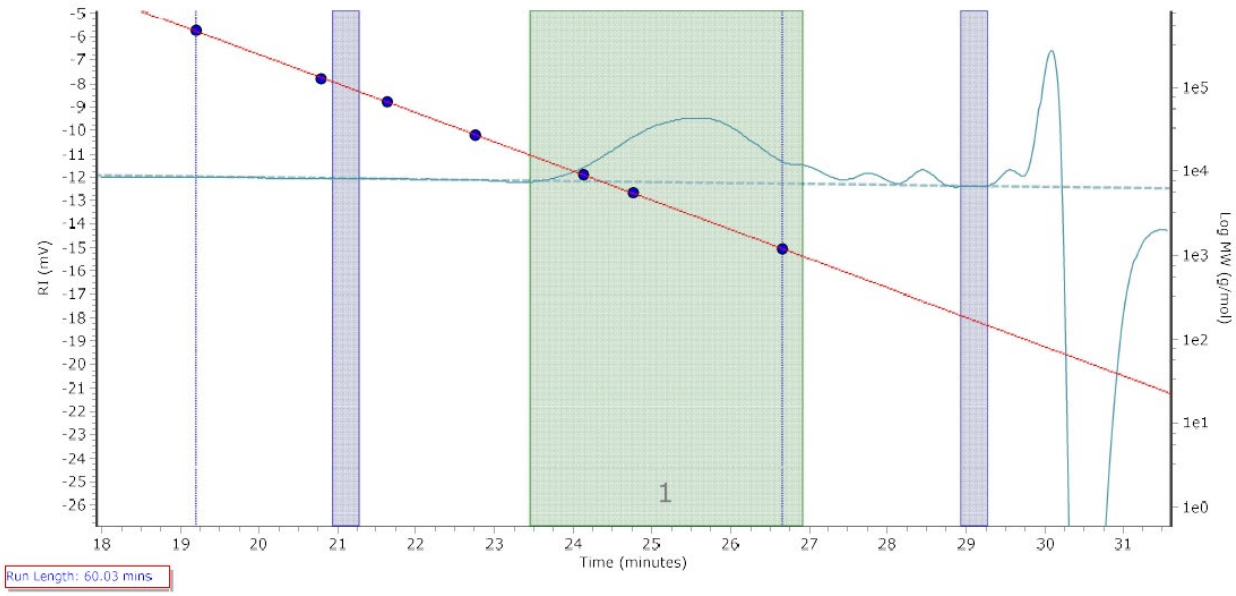

Figure A102 GPC chromatogram plot of a polymer sample, herein obtained using complex Zn[**L6a**]Et (Chapter 3, Table 11, entry 10)

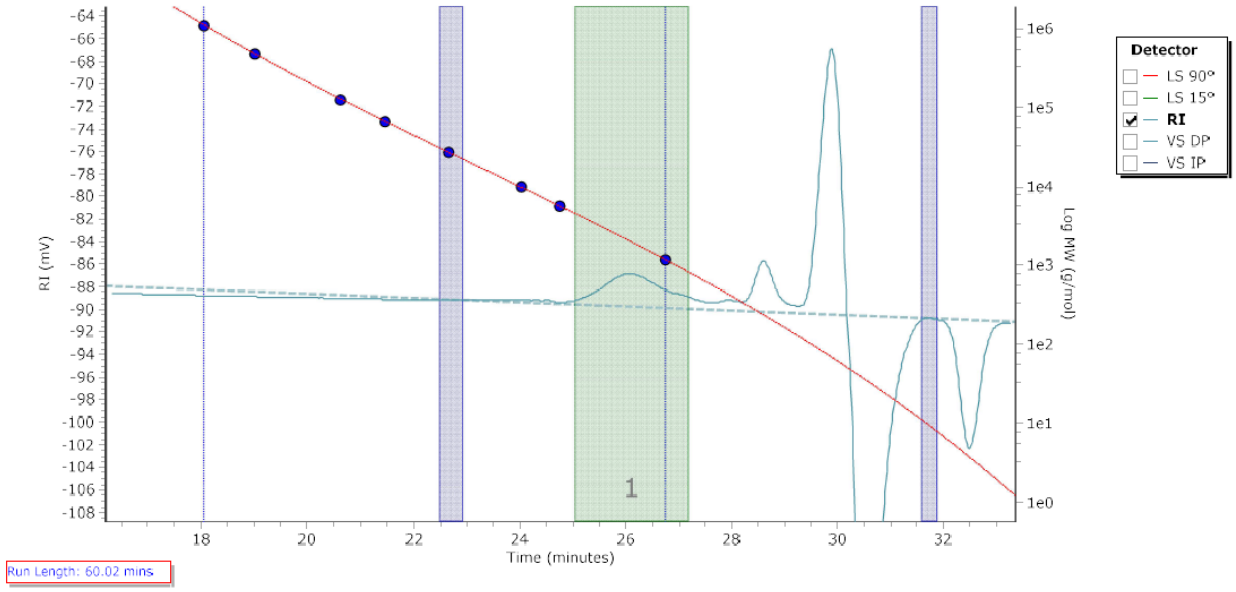

Figure A103 GPC chromatogram plot of a polymer sample, herein obtained using ligand **L2b**H (Chapter 3, Table 11, entry 12)

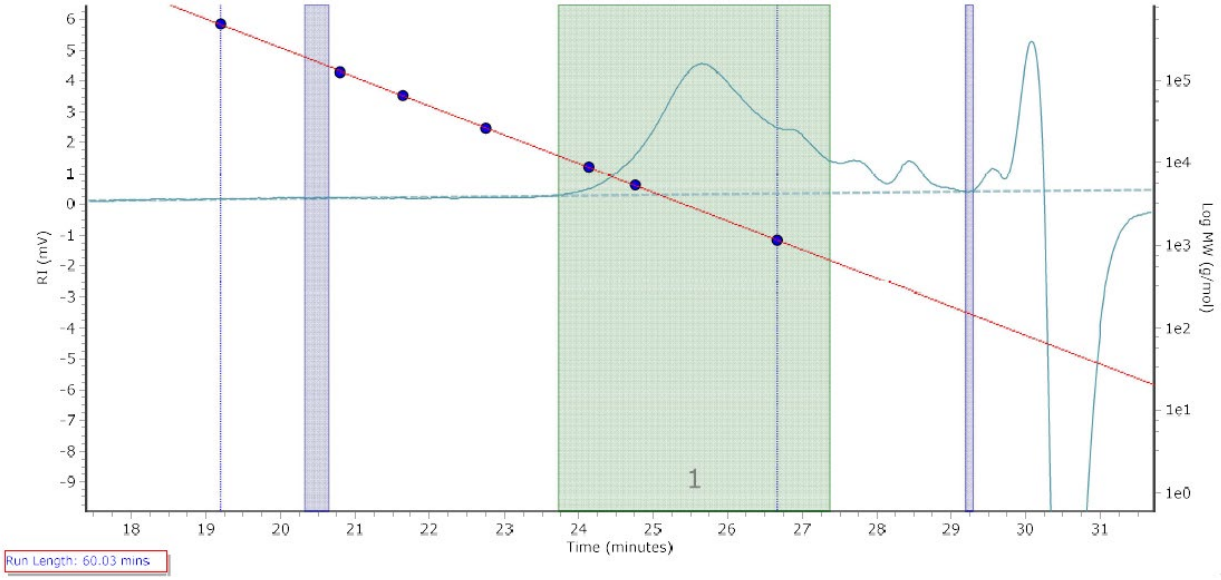

Figure A104 GPC chromatogram plot of a polymer sample, herein obtained using ligand **L2c**H (Chapter 3, Table 11, entry 13)

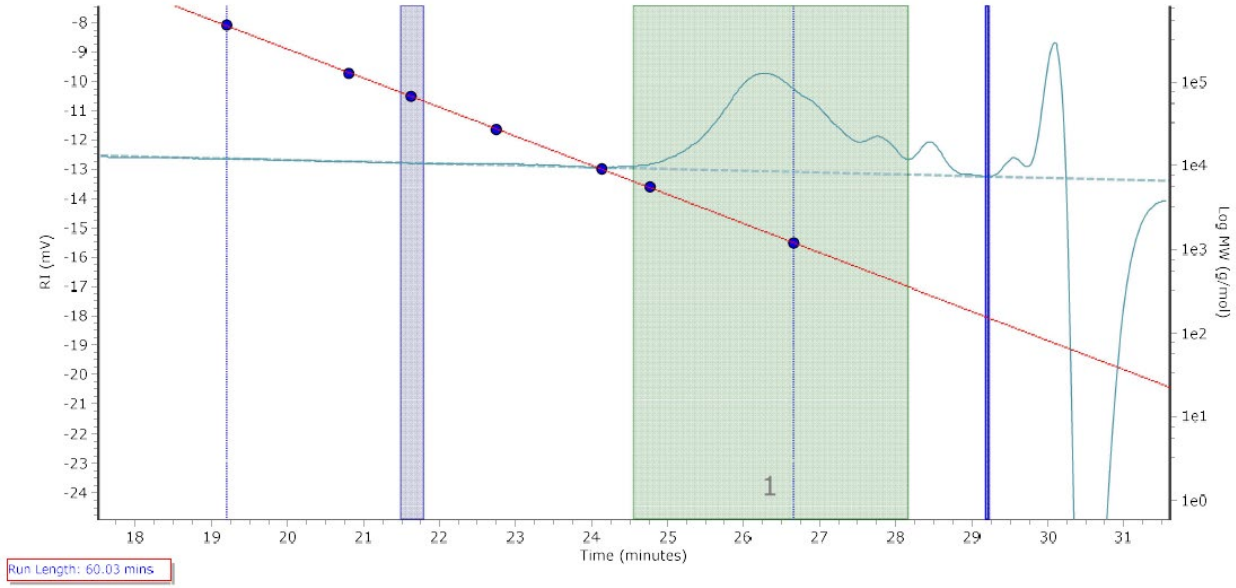

Figure A105 GPC chromatogram plot of a polymer sample, herein obtained using ligand **L2d**H (Chapter 3, Table 11, entry 14)

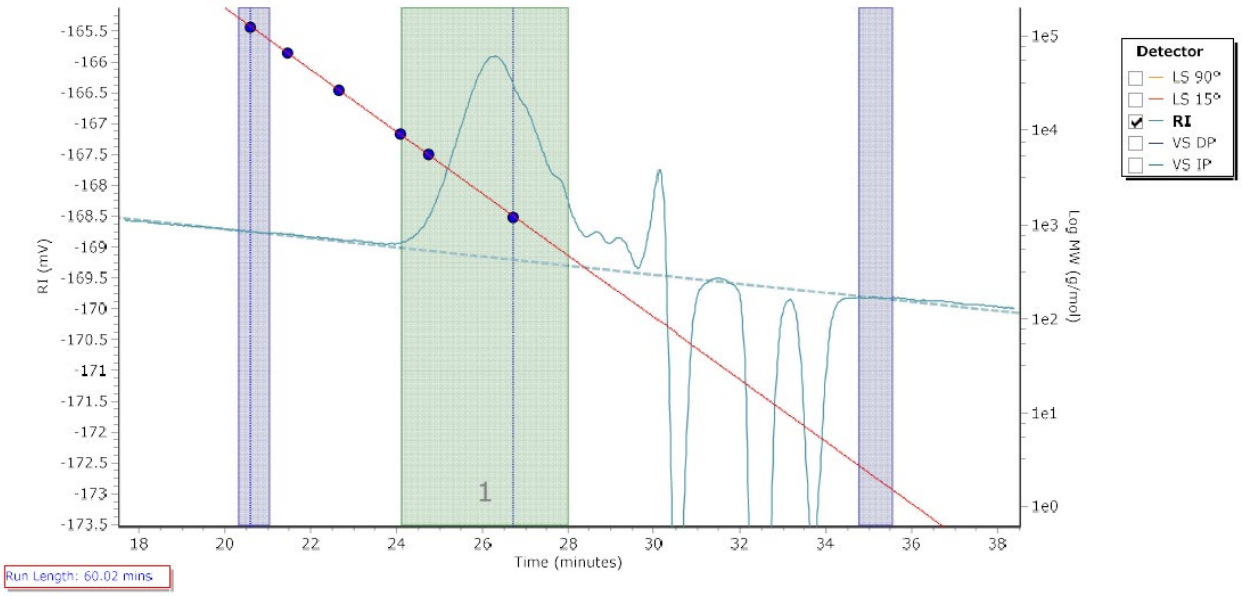

Figure A106 GPC chromatogram plot of a polymer sample, herein obtained using ligand **L5a′**H(Chapter 3, Table 11, entry 15)

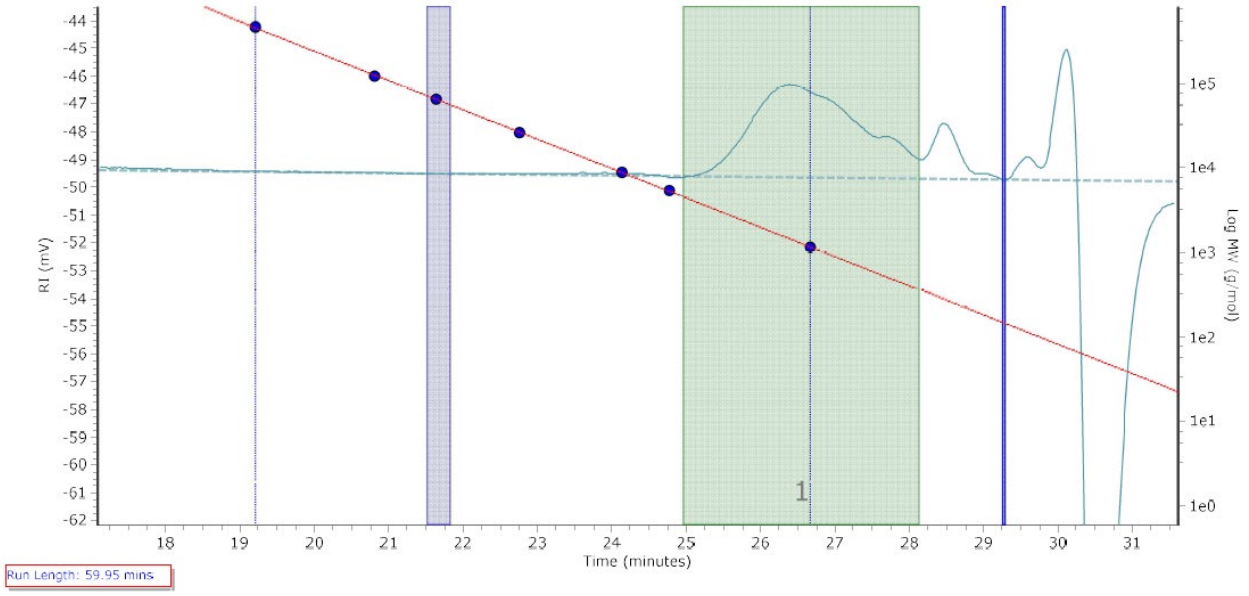

Figure A107 GPC chromatogram plot of a polymer sample, herein obtained using ligand **L6a**H (Chapter 3, Table 11, entry 16)

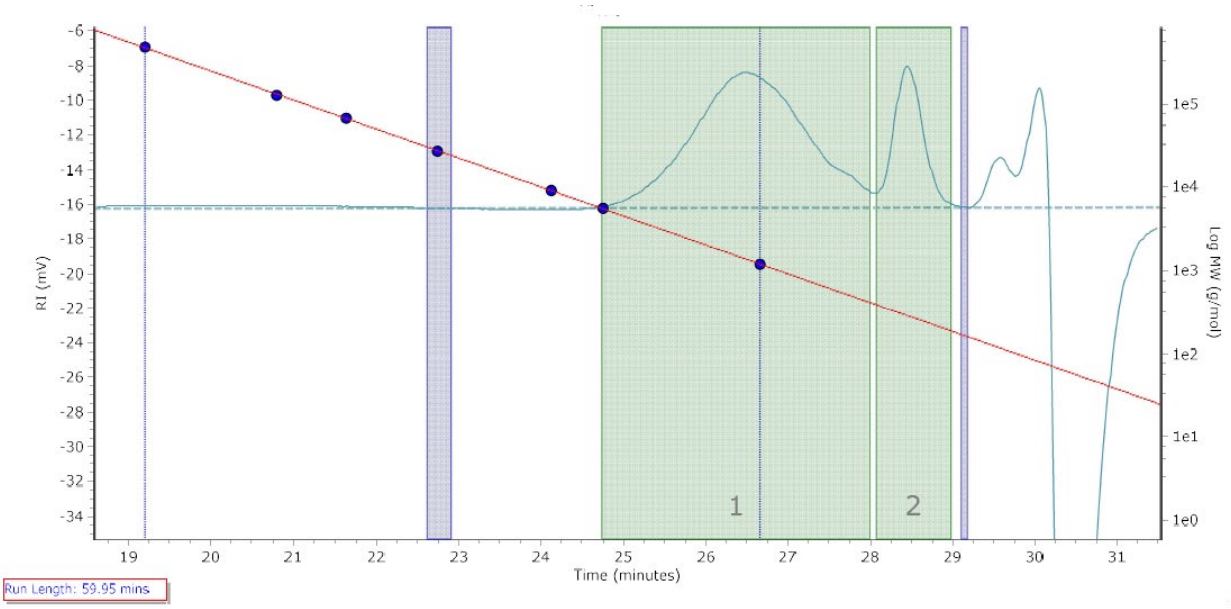

Figure A108 GPC chromatogram plot of a polymer sample, herein obtained using $ZnEt_2$(Chapter 3, Table 11, entry 17)

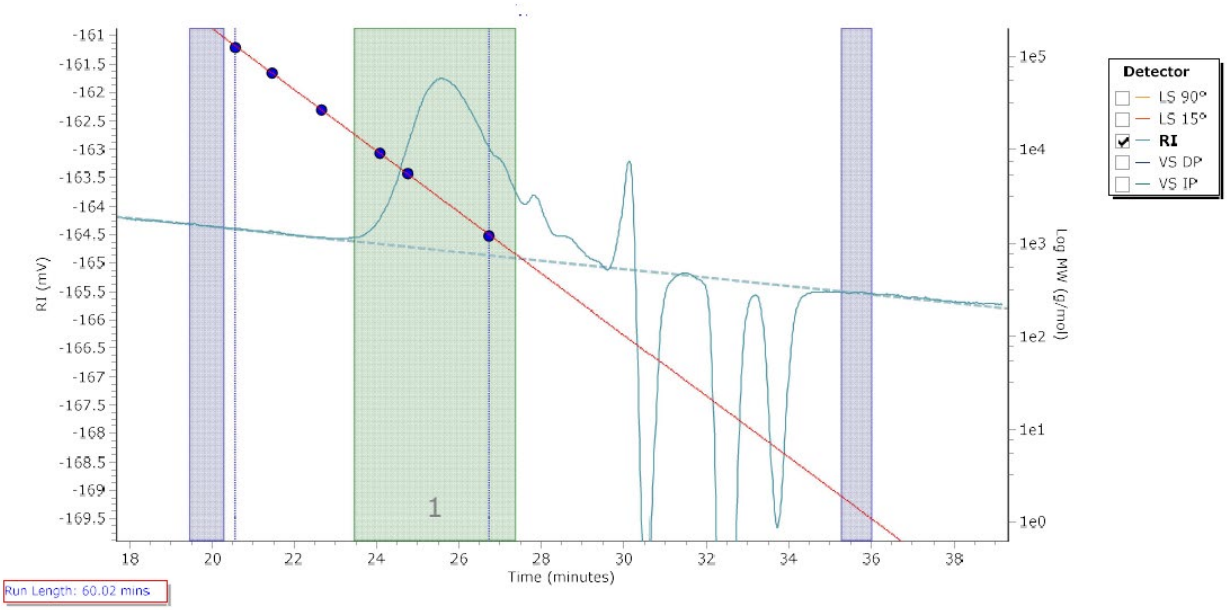

Figure A109 GPC chromatogram plot of a polymer sample, herein obtained using complex $Sn(Oct)_2$ with BnOH (Chapter 3, Table 11, entry 18)

Table A1 Crystal data for **L5a′**H

Empirical formula	$C_{15}H_{19}N_3O_3$
Formula weight	289.33
Temperature/K	174.00
Crystal system	Orthorhombic
Space group	$P2_12_12_1$
a/Å	15.8843(7)
b/Å	16.4411(7)
c/Å	17.7686(8)
α/°	90
β/°	90
γ/°	90
Volume/Å^3	4640.4(4)
Z	12
ρ_{calc}g/cm^3	1.242
μ/mm^{-1}	0.088
F(000)	1848.0
Crystal size/mm^3	0.2 × 0.2 × 0.1
Radiation	MoKα (λ = 0.71073)
2Θ range for data collection/°	4.238 to 55.064
Index ranges	$-20 \leq h \leq 20$, $-21 \leq k \leq 21$, $-23 \leq l \leq 23$
Reflections collected	61644
Independent reflections	10673 [R_{int} = 0.0687, R_{sigma} = 0.0484]
Data/restraints/parameters	10673/0/589
Goodness-of-fit on F^2	1.083
Final R indexes [I>=2σ (I)]	R_1 = 0.0494, wR_2 = 0.1154
Final R indexes [all data]	R_1 = 0.1103, wR_2 = 0.1535
Largest diff. peak/hole / e Å^{-3}	0.22/-0.23

Table A2 Bond lengths (Å) for **L5a′**H

O1A–C1A	1.436(4)	C2B–C3B	1.519(6)
O1A–C11A	1.396(5)	C4B–C5B	1.507(7)
O2A–C2A	1.230(5)	C4B–C6B	1.518(6)
O3A–C3A	1.227(5)	C7B–C8B	1.504(7)
N1A–C1A	1.420(5)	C7B–C9B	1.489(7)
N1A–C10A	1.390(5)	C10B–C11B	1.375(6)
N2A–C1A	1.452(5)	C10B–C15B	1.375(6)
N2A–C2A	1.342(5)	C11B–C12B	1.369(5)
N2A–C4A	1.481(5)	C12B–C13B	1.398(7)
N3A–C1A	1.448(5)	C13B–C14B	1.365(7)
N3A–C3A	1.350(5)	C14B–C15B	1.396(7)
N3A–C7A	1.465(5)	O1C–C1C	1.435(5)
C2A–C3A	1.508(6)	O1C–C11C	1.386(5)
C4A–C5A	1.506(6)	O2C–C2C	1.227(5)
C4A–C6A	1.514(6)	O3C–C3C	1.220(5)
C7A–C8A	1.519(7)	N1C–C1C	1.425(5)
C7A–C9A	1.499(7)	N1C–C10C	1.401(5)
C10A–C11A	1.378(6)	N2C–C1C	1.454(6)
C10A–C15A	1.368(6)	N2C–C2C	1.337(5)
C11A–C12A	1.368(6)	N2C–C4C	1.478(6)
C12A–C13A	1.385(7)	N3C–C1C	1.444(5)
C13A–C14A	1.378(8)	N3C–C3C	1.345(5)
C14A–C15A	1.406(7)	N3C–C7C	1.478(5)
O1B–C1B	1.436(4)	C2C–C3C	1.516(6)
O1B–C11B	1.387(5)	C4C–C5C	1.527(8)
O2B–C2B	1.223(5)	C4C–C6C	1.519(7)
O3B–C3B	1.221(5)	C7C–C8C	1.499(6)

N1B–C1B	1.439(5)	C7C–C9C	1.512(7)
N1B–C10B	1.399(5)	C10C–C11C	1.377(6)
N2B–C1B	1.453(5)	C10C–C15C	1.382(6)
N2B–C2B	1.343(5)	C11C–C12C	1.369(6)
N2B–C4B	1.469(5)	C12C–C13C	1.393(8)
N3B–C1B	1.440(5)	C13C–C14C	1.367(8)
N3B–C3B	1.351(5)	C14C–C15C	1.419(7)
N3B–C7B	1.481(5)		

Table A3 Bond Angles (°) of **L5a′**H

C11A	O1A	C1A	107.9(3)	O3B	C3B	C2B	123.8(4)
C10A	N1A	C1A	110.6(3)	N3B	C3B	C2B	106.2(3)
C1A	N2A	C4A	121.2(3)	N2B	C4B	C5B	110.4(4)
C2A	N2A	C1A	111.6(3)	N2B	C4B	C6B	111.1(3)
C2A	N2A	C4A	125.9(3)	C5B	C4B	C6B	113.1(4)
C1A	N3A	C7A	120.1(3)	N3B	C7B	C8B	110.9(4)
C3A	N3A	C1A	112.1(3)	N3B	C7B	C9B	111.6(4)
C3A	N3A	C7A	127.8(3)	C9B	C7B	C8B	115.1(5)
O1A	C1A	N2A	109.4(3)	C11B	C10B	N1B	106.8(3)
O1A	C1A	N3A	110.3(3)	C15B	C10B	N1B	132.3(4)
N1A	C1A	O1A	104.5(3)	C15B	C10B	C11B	120.9(4)
N1A	C1A	N2A	114.2(3)	C10B	C11B	O1B	110.6(3)
N1A	C1A	N3A	115.5(3)	C12B	C11B	O1B	126.0(4)
N3A	C1A	N2A	103.1(3)	C12B	C11B	C10B	123.4(4)
O2A	C2A	N2A	128.4(4)	C11B	C12B	C13B	116.0(4)
O2A	C2A	C3A	124.6(3)	C14B	C13B	C12B	120.8(4)
N2A	C2A	C3A	107.0(3)	C13B	C14B	C15B	122.7(4)
O3A	C3A	N3A	129.3(4)	C10B	C15B	C14B	116.2(4)
O3A	C3A	C2A	124.8(4)	C11C	O1C	C1C	107.9(3)
N3A	C3A	C2A	105.9(3)	C10C	N1C	C1C	109.1(4)
N2A	C4A	C5A	110.4(3)	C1C	N2C	C4C	121.5(3)
N2A	C4A	C6A	110.4(3)	C2C	N2C	C1C	111.9(3)
C5A	C4A	C6A	112.5(4)	C2C	N2C	C4C	126.6(4)
N3A	C7A	C8A	110.4(4)	C1C	N3C	C7C	121.4(3)
N3A	C7A	C9A	111.3(4)	C3C	N3C	C1C	112.3(3)
C9A	C7A	C8A	112.5(4)	C3C	N3C	C7C	126.1(3)
C11A	C10A	N1A	106.8(3)	O1C	C1C	N2C	109.4(3)

C15A	C10A	N1A	132.4(4)	O1C	C1C	N3C	109.7(3)
C15A	C10A	C11A	120.7(4)	N1C	C1C	O1C	105.1(3)
C10A	C11A	O1A	110.0(3)	N1C	C1C	N2C	114.6(3)
C12A	C11A	O1A	126.8(4)	N1C	C1C	N3C	114.9(4)
C12A	C11A	C10A	123.2(4)	N3C	C1C	N2C	103.1(3)
C11A	C12A	C13A	116.6(5)	O2C	C2C	N2C	128.8(4)
C14A	C13A	C12A	121.2(4)	O2C	C2C	C3C	124.5(4)
C13A	C14A	C15A	121.3(4)	N2C	C2C	C3C	106.7(3)
C10A	C15A	C14A	117.0(5)	O3C	C3C	N3C	128.7(4)
C11B	O1B	C1B	107.8(3)	O3C	C3C	C2C	125.4(4)
C10B	N1B	C1B	109.3(3)	N3C	C3C	C2C	105.9(3)
C1B	N2B	C4B	121.1(3)	N2C	C4C	C5C	109.9(4)
C2B	N2B	C1B	112.2(3)	N2C	C4C	C6C	110.1(4)
C2B	N2B	C4B	126.6(3)	C6C	C4C	C5C	113.0(5)
C1B	N3B	C7B	119.8(3)	N3C	C7C	C8C	111.3(4)
C3B	N3B	C1B	112.2(3)	N3C	C7C	C9C	110.3(4)
C3B	N3B	C7B	128.1(4)	C8C	C7C	C9C	111.6(5)
O1B	C1B	N1B	104.2(3)	C11C	C10C	N1C	107.4(4)
O1B	C1B	N2B	109.1(3)	C11C	C10C	C15C	120.6(4)
O1B	C1B	N3B	109.9(3)	C15C	C10C	N1C	132.0(5)
N1B	C1B	N2B	115.2(3)	C10C	C11C	O1C	110.0(3)
N1B	C1B	N3B	115.0(3)	C12C	C11C	O1C	125.7(4)
N3B	C1B	N2B	103.3(3)	C12C	C11C	C10C	124.3(4)
O2B	C2B	N2B	128.6(4)	C11C	C12C	C13C	115.8(5)
O2B	C2B	C3B	125.3(4)	C14C	C13C	C12C	121.0(5)
N2B	C2B	C3B	106.1(3)	C13C	C14C	C15C	122.8(5)
O3B	C3B	N3B	130.0(4)	C10C	C15C	C14C	115.5(5)

Table A4 Fractional Atomic Coordinates (×104) and Equivalent Isotropic Displacement Parameters (Å2×103) for **L5a′**H. Ueq is defined as 1/3 of the trace of the orthogonalized UIJ tensor.

Atom	*x*	*y*	*z*	U(eq)
O1A	6790.9(16)	401.6(17)	6626.8(15)	48.4(7)
O2A	5892.5(19)	2159.9(17)	4887.7(16)	51.9(7)
O3A	6296(2)	623.8(19)	4162.5(15)	55.6(8)
N1A	5396(2)	163(2)	6524.7(19)	52.0(9)
N2A	5986.4(19)	1371.3(19)	5965.0(17)	40.0(7)
N3A	6263(2)	161(2)	5401.4(18)	44.4(8)
C1A	6086(2)	512(3)	6132(2)	42.6(9)
C2A	6004(2)	1513(2)	5221(2)	41.3(9)
C3A	6207(2)	716(3)	4843(2)	44.3(9)
C4A	5717(3)	1956(3)	6552(2)	47.9(10)
C5A	4823(3)	2222(3)	6416(3)	63.9(13)
C6A	6323(3)	2665(3)	6591(3)	63.0(12)
C7A	6467(3)	-705(3)	5336(2)	51.9(10)
C8A	7365(3)	-814(3)	5060(3)	72.6(15)
C9A	5840(4)	-1141(3)	4853(3)	76.0(15)
C10A	5640(3)	-80(2)	7241(2)	42.1(9)
C11A	6494(3)	53(2)	7292(2)	43.3(9)
C12A	6957(3)	-131(3)	7919(3)	59.0(12)
C13A	6519(4)	-451(3)	8525(3)	68.4(14)
C14A	5663(4)	-578(3)	8490(3)	67.4(14)
C15A	5202(3)	-398(3)	7835(2)	55.9(11)
O1B	5453.8(17)	3212.6(16)	2491.0(14)	43.1(6)
O2B	6798(2)	4284(2)	4417.0(17)	59.1(8)
O3B	4994(2)	4403(2)	4660.8(17)	61.2(8)
N1B	5545(2)	2127(2)	3275.2(19)	42.6(8)

Atom	*x*	*y*	*z*	U(eq)
N2B	6375.4(19)	3349.0(19)	3521.0(17)	39.3(7)
N3B	4967(2)	3403(2)	3730.6(18)	43.5(8)
C1B	5584(2)	3002(2)	3267(2)	36.8(8)
C2B	6266(3)	3891(2)	4078(2)	42.4(9)
C3B	5322(3)	3940(3)	4210(2)	45.1(10)
C4B	7182(2)	3078(3)	3204(2)	47.1(10)
C5B	7655(3)	2566(4)	3767(4)	77.6(17)
C6B	7692(3)	3794(3)	2915(3)	56.0(11)
C7B	4065(3)	3197(3)	3647(3)	55.0(11)
C8B	3638(3)	3770(4)	3108(4)	79.3(17)
C9B	3644(4)	3108(4)	4391(3)	77.8(16)
C10B	5563(2)	1836(2)	2536(2)	40.0(9)
C11B	5489(2)	2502(2)	2072(2)	39.3(8)
C12B	5460(3)	2449(3)	1303(2)	52.2(11)
C13B	5516(3)	1666(3)	1001(3)	63.8(13)
C14B	5599(3)	1004(3)	1459(3)	63.8(13)
C15B	5626(3)	1064(3)	2242(3)	51.9(10)
O1C	7740.0(18)	6620.3(17)	5606.5(16)	49.9(7)
O2C	8656.7(19)	5625(2)	3471.9(16)	59.1(8)
O3C	9195.3(18)	4566.4(19)	4699.0(17)	57.2(8)
N1C	6710(2)	5708(2)	5338(2)	54.3(9)
N2C	7722(2)	6078(2)	4378.0(19)	48.0(9)
N3C	8166(2)	5279(2)	5341.3(18)	44.2(8)
C1C	7562(2)	5908(3)	5168(2)	46.2(10)
C2C	8350(3)	5623(3)	4106(2)	49.0(10)
C3C	8640(3)	5077(3)	4743(2)	45.1(9)

Atom	*x*	*y*	*z*	U(eq)
C4C	7240(3)	6704(3)	3965(3)	64.1(13)
C5C	7828(4)	7387(4)	3714(4)	85.9(18)
C6C	6765(4)	6317(4)	3315(3)	87.4(19)
C7C	8197(3)	4893(3)	6092(2)	51.2(10)
C8C	9027(3)	5041(3)	6469(3)	66.2(13)
C9C	8005(5)	3995(3)	6031(4)	96(2)
C10C	6362(3)	6324(3)	5785(2)	47.4(10)
C11C	6997(3)	6868(3)	5946(2)	47.8(10)
C12C	6899(4)	7548(3)	6381(2)	58.0(12)
C13C	6090(4)	7685(3)	6656(3)	74.6(16)
C14C	5448(4)	7156(3)	6503(3)	71.6(16)
C15C	5557(3)	6449(3)	6056(3)	60.2(12)

Table A5 Anisotropic Displacement Parameters (Å2×103) for **L5a′**H. The Anisotropic displacement factor exponent takes the form: -2π2[h2a*2U11+2hka*b*U12+…].

Atom	U_{11}	U_{22}	U_{33}	U_{23}	U_{13}	U_{12}
O1A	41.4(14)	60.8(18)	43.0(15)	13.7(13)	-8.3(12)	-3.9(13)
O2A	69.5(19)	45.2(16)	40.9(16)	12.6(13)	4.8(14)	6.9(14)
O3A	71.1(19)	59.2(18)	36.5(16)	1.4(14)	2.8(14)	12.0(16)
N1A	46.6(19)	70(2)	39.5(19)	15.7(18)	-5.7(15)	-14.5(17)
N2A	44.1(18)	42.3(18)	33.6(17)	6.5(14)	1.3(14)	-0.7(14)
N3A	56(2)	40.9(18)	36.8(18)	6.3(15)	-2.3(15)	1.1(15)
C1A	39(2)	51(2)	37(2)	10.7(18)	-2.9(16)	-7.1(17)
C2A	43(2)	47(2)	34(2)	4.3(18)	2.7(16)	0.5(17)
C3A	47(2)	49(2)	37(2)	6.1(19)	1.1(17)	1.8(19)
C4A	52(2)	53(2)	39(2)	-1.1(19)	0.7(18)	4(2)
C5A	47(2)	81(3)	64(3)	-11(3)	2(2)	8(2)
C6A	56(3)	62(3)	71(3)	-14(3)	-9(2)	-1(2)
C7A	64(3)	44(2)	48(2)	4(2)	-5(2)	4(2)
C8A	71(3)	60(3)	87(4)	8(3)	9(3)	13(3)
C9A	88(4)	48(3)	92(4)	-10(3)	-21(3)	4(3)
C10A	59(2)	34.6(19)	33(2)	3.8(16)	0.2(17)	-3.8(19)
C11A	57(2)	40(2)	33(2)	4.0(17)	-5.0(17)	-1.7(19)
C12A	73(3)	57(3)	47(3)	7(2)	-16(2)	-1(2)
C13A	109(5)	59(3)	37(2)	14(2)	-15(3)	-3(3)
C14A	114(4)	51(3)	37(2)	10(2)	7(3)	-6(3)
C15A	78(3)	44(2)	45(2)	2(2)	8(2)	-5(2)
O1B	52.9(15)	44.8(15)	31.5(14)	1.8(11)	-5.4(11)	2.5(13)
O2B	64.6(19)	62.8(19)	49.8(17)	-16.5(16)	-9.1(15)	-7.4(16)
O3B	76(2)	59.9(19)	47.3(17)	-8.6(16)	8.0(16)	15.2(17)

Atom	U_{11}	U_{22}	U_{33}	U_{23}	U_{13}	U_{12}
N1B	49.1(19)	40.1(18)	38.5(18)	1.5(15)	-3.2(15)	-0.1(15)
N2B	38.0(16)	43.1(17)	36.8(17)	-7.6(14)	-2.0(13)	0.8(14)
N3B	37.3(17)	53(2)	40.4(18)	-1.5(16)	1.2(14)	2.6(15)
C1B	37.5(19)	44(2)	28.9(18)	-1.1(16)	-2.2(15)	0.7(16)
C2B	51(2)	41(2)	35(2)	-4.3(17)	-8.9(18)	1.9(18)
C3B	56(2)	43(2)	36(2)	-1.1(18)	-0.4(18)	9.2(19)
C4B	41(2)	52(2)	49(2)	-7(2)	3.7(18)	-1.3(19)
C5B	46(3)	77(4)	110(5)	30(3)	10(3)	13(3)
C6B	55(3)	61(3)	51(3)	2(2)	8(2)	-3(2)
C7B	43(2)	62(3)	59(3)	2(2)	2(2)	-1(2)
C8B	46(3)	95(4)	97(4)	17(3)	-10(3)	3(3)
C9B	67(3)	98(4)	68(3)	-8(3)	19(3)	-20(3)
C10B	38.4(19)	45(2)	36(2)	-4.3(17)	-0.9(16)	-3.3(18)
C11B	38.1(19)	44(2)	36(2)	-8.4(17)	-1.3(16)	-1.0(17)
C12B	57(3)	65(3)	34(2)	0(2)	-5.0(18)	-2(2)
C13B	74(3)	76(3)	41(2)	-21(2)	-7(2)	0(3)
C14B	68(3)	64(3)	60(3)	-25(3)	-2(2)	-3(2)
C15B	51(2)	45(2)	59(3)	-5(2)	-3(2)	-7(2)
O1C	53.8(16)	48.3(16)	47.4(17)	-16.2(13)	2.0(13)	1.5(13)
O2C	58.4(17)	73(2)	45.4(17)	-4.1(16)	8.8(15)	9.9(16)
O3C	53.0(17)	59.4(18)	59.4(19)	-4.4(15)	6.0(14)	13.7(15)
N1C	40.1(18)	63(2)	60(2)	-23(2)	3.8(16)	3.6(18)
N2C	46.1(19)	60(2)	38.2(19)	-7.0(16)	1.2(15)	10.2(17)
N3C	44.1(18)	47.3(19)	41.2(18)	-4.4(15)	2.7(15)	2.3(15)
C1C	44(2)	50(2)	45(2)	-14.9(19)	1.6(18)	2.2(18)

Atom	U_{11}	U_{22}	U_{33}	U_{23}	U_{13}	U_{12}
C2C	44(2)	58(3)	45(2)	-8(2)	1.7(18)	2(2)
C3C	42(2)	44(2)	49(2)	-9.6(19)	4.1(18)	0.1(19)
C4C	66(3)	76(3)	50(3)	-8(2)	0(2)	26(3)
C5C	114(5)	68(4)	75(4)	7(3)	4(3)	18(3)
C6C	80(4)	119(5)	64(3)	-10(3)	-24(3)	27(4)
C7C	56(2)	57(3)	41(2)	-1(2)	0.5(19)	-4(2)
C8C	69(3)	76(3)	54(3)	2(3)	-10(2)	-13(3)
C9C	147(6)	67(4)	73(4)	15(3)	-27(4)	-50(4)
C10C	52(2)	54(2)	35(2)	3.5(18)	6.2(18)	18(2)
C11C	66(3)	45(2)	33(2)	2.4(18)	5.4(19)	11(2)
C12C	93(4)	40(2)	41(2)	1.2(19)	7(2)	15(2)
C13C	120(5)	49(3)	55(3)	9(2)	32(3)	24(3)
C14C	85(4)	74(3)	56(3)	19(3)	32(3)	40(3)
C15C	59(3)	74(3)	47(3)	13(2)	11(2)	18(2)

Table A6 Hydrogen Atom Coordinates (Å×104) and Isotropic Displacement Parameters (Å2×103) for **L5a′**H

Atom	***x***	***y***	***z***	**U(eq)**
H1A	4884.52	109.13	6340.21	62
H4A	5734.73	1668.26	7047.7	57
H5AA	4792.22	2527.56	5943.02	96
H5AB	4636.56	2569.8	6831.99	96
H5AC	4457.54	1743.07	6384.33	96
H6AA	6897.61	2460.16	6656.58	94
H6AB	6174.17	3014.06	7017.47	94
H6AC	6289.17	2979.51	6123.28	94
H7A	6432.78	-945.5	5852.29	62
H8AA	7405.97	-634.26	4535.99	109
H8AB	7522.04	-1389.59	5094.52	109
H8AC	7746.55	-489.68	5372.99	109
H9AA	5275.47	-1076.95	5067.25	114
H9AB	5983.5	-1720.6	4830.87	114
H9AC	5850.66	-912.02	4343.73	114
H12A	7547.49	-43.16	7938.54	71
H13A	6815.26	-585.95	8972.61	82
H14A	5377.9	-791.25	8916.75	81
H15A	4612.59	-493.41	7806.68	67
H1B	5800(30)	1820(30)	3680(30)	63(14)
H4B	7052.42	2722.49	2762.58	57
H5BA	7824.55	2906.08	4194.47	116
H5BB	8156.01	2334.77	3528.19	116
H5BC	7290.04	2125.91	3945.98	116

Atom	*x*	*y*	*z*	U(eq)
H6BA	7342.2	4123.18	2578.07	84
H6BB	8184.43	3593.26	2640.24	84
H6BC	7877.26	4127.58	3341.2	84
H7B	4045.61	2648.03	3405.49	66
H8BA	3612.88	4314.65	3330.96	119
H8BB	3065.17	3576.87	3006.28	119
H8BC	3956.75	3791.14	2636.67	119
H9BA	3950.47	2709.01	4695.84	117
H9BB	3063.46	2921.32	4316.59	117
H9BC	3639.65	3633.61	4650.49	117
H12B	5405.61	2917.29	993.57	63
H13B	5495.47	1593.3	471.22	77
H14B	5641.03	480.3	1235.34	77
H15B	5684.53	598.98	2554.94	62
H1C	6410(40)	5280(30)	5080(30)	85(17)
H4C	6817.04	6941.23	4318.48	77
H5CA	8126.28	7605.38	4152.96	129
H5CB	7497.89	7821.07	3477.85	129
H5CC	8237.04	7173.84	3351.75	129
H6CA	7166.24	6059.09	2970.06	131
H6CB	6446.8	6735.65	3045.18	131
H6CC	6376.23	5905.05	3510.52	131
H7C	7748.66	5148.18	6409.69	61
H8CA	9476.14	4782.22	6176.36	99
H8CB	9016.18	4810.43	6977.25	99

Atom	*x*	*y*	*z*	U(eq)
H8CC	9131.65	5627.78	6499.18	99
H9CA	7439.86	3921.32	5819.51	144
H9CB	8029.7	3746.78	6531.6	144
H9CC	8419.9	3735.26	5701.31	144
H12C	7353.62	7905.21	6488.52	70
H13C	5982.55	8152.58	6955.27	90
H14C	4905.91	7267.29	6704.56	86
H15C	5107.7	6085.33	5950.6	72

Table A7 Crystal data for **L5b′**H

Empirical formula	$C_{23}H_{35}N_3O_3$
Formula weight	401.54
Temperature/K	175.00
Crystal system	Orthorhombic
Space group	Pbca
a/Å	10.3388(5)
b/Å	18.8797(10)
c/Å	29.1252(15)
α/°	90
β/°	90
γ/°	90
Volume/Å^3	5685.0(5)
Z	8
ρ_{calc}g/cm^3	0.938
μ/mm^{-1}	0.062
F(000)	1744.0
Crystal size/mm^3	0.3 × 0.15 × 0.1
Radiation	MoKα (λ = 0.71073)
2Θ range for data collection/°	4.314 to 55.744
Index ranges	$-11 \leq h \leq 12$, $-23 \leq k \leq 23$, $-36 \leq l \leq 36$
Reflections collected	66131
Independent reflections	5793 [R_{int} = 0.0485, R_{sigma} = 0.0242]
Data/restraints/parameters	5793/3/303
Goodness-of-fit on F^2	1.145
Final R indexes [I>=2σ (I)]	R_1 = 0.0682, wR_2 = 0.2392
Final R indexes [all data]	R_1 = 0.0806, wR_2 = 0.2501
Largest diff. peak/hole / e Å^{-3}	0.37/-0.38

Table A8 Bond lengths (Å) for **L5b′**H

O1–C2	1.220(3)	C10–C11	1.385(3)
O2–C3	1.210(4)	C10–C15	1.385(4)
O3–C1	1.439(3)	C11–C12	1.376(3)
O3–C11	1.398(3)	C12–C13	1.409(4)
N1–C1	1.422(3)	C12–C16	1.542(3)
N1–C10	1.391(3)	C13–C14	1.399(4)
N2–C1	1.456(3)	C14–C15	1.400(4)
N2–C2	1.334(4)	C14–C20	1.538(4)
N2–C4	1.471(4)	C16–C17	1.535(4)
N3–C1	1.453(3)	C16–C18	1.526(4)
N3–C3	1.350(3)	C16–C19	1.528(4)
N3–C7	1.476(3)	C20–C21	1.580(6)
C2–C3	1.534(4)	C20–C22	1.505(6)
C4–C5	1.521(5)	C20–C23	1.466(7)
C4–C6	1.516(4)	C20–C21A	1.585(9)
C7–C8	1.506(5)	C20–C22A	1.604(9)
C7–C9	1.518(4)	C20–C23A	1.432(9)

Table A9 Bond angles (°) for **L5b′**H

C11	O3	C1	108.13(18)	C10	C11	O3	109.3(2)
C10	N1	C1	110.1(2)	C12	C11	O3	127.4(2)
C1	N2	C4	120.8(2)	C12	C11	C10	123.3(2)
C2	N2	C1	112.5(2)	C11	C12	C13	114.5(2)
C2	N2	C4	126.7(2)	C11	C12	C16	122.5(2)
C1	N3	C7	121.3(2)	C13	C12	C16	123.0(2)
C3	N3	C1	112.4(2)	C14	C13	C12	123.9(2)
C3	N3	C7	126.3(2)	C13	C14	C15	119.0(2)
O3	C1	N2	109.6(2)	C13	C14	C20	121.0(2)
O3	C1	N3	110.9(2)	C15	C14	C20	120.0(2)
N1	C1	O3	104.57(19)	C10	C15	C14	117.8(2)
N1	C1	N2	114.0(2)	C17	C16	C12	108.6(2)
N1	C1	N3	114.8(2)	C18	C16	C12	111.9(2)
N3	C1	N2	103.0(2)	C18	C16	C17	108.5(2)
O1	C2	N2	129.1(3)	C18	C16	C19	109.2(3)
O1	C2	C3	124.5(3)	C19	C16	C12	109.4(2)
N2	C2	C3	106.5(2)	C19	C16	C17	109.2(3)
O2	C3	N3	129.0(3)	C14	C20	C21	106.8(3)
O2	C3	C2	125.4(3)	C14	C20	C21A	112.6(4)
N3	C3	C2	105.6(2)	C14	C20	C22A	108.0(4)
N2	C4	C5	110.7(3)	C22	C20	C14	113.4(3)
N2	C4	C6	110.9(3)	C22	C20	C21	105.9(4)
C6	C4	C5	112.4(3)	C23	C20	C14	109.7(3)
N3	C7	C8	110.6(2)	C23	C20	C21	111.1(5)
N3	C7	C9	110.9(2)	C23	C20	C22	109.8(5)
C8	C7	C9	113.0(3)	C21A	C20	C22A	99.2(6)
C11	C10	N1	107.3(2)	C23A	C20	C14	113.9(5)

C15 C10 N1	131.2(2)	C23A C20 C21A	113.9(8)
C15 C10 C11	121.5(2)	C23A C20 C22A	107.9(8)

Table A10 Fractional Atomic Coordinates ($\times 10^4$) and Equivalent Isotropic Displacement Parameters ($Å^2 \times 10^3$) for **L5b′**H. U_{eq} is defined as 1/3 of the trace of the orthogonalized U_{IJ} tensor.

Atom	***x***	***y***	***z***	**U(eq)**
O1	8875(2)	7794.3(13)	4636.2(8)	50.2(6)
O2	8692(2)	6551.3(15)	5232.3(8)	55.5(6)
O3	6243.1(16)	6228.3(9)	4006.9(6)	26.5(4)
N1	4905(2)	6838.2(12)	4478.3(8)	31.4(5)
N2	7038(2)	7299.2(12)	4321.0(8)	31.4(5)
N3	6877(2)	6338.6(12)	4789.8(7)	30.9(5)
C1	6234(2)	6679.2(13)	4405.2(8)	27.0(5)
C2	8035(3)	7341.7(16)	4610.6(10)	35.8(6)
C3	7946(3)	6692.4(17)	4925.4(10)	36.7(6)
C4	6732(3)	7793.2(15)	3945.7(11)	40.0(7)
C5	7781(4)	7775.7(18)	3579.5(12)	50.4(8)
C6	6496(4)	8533.6(18)	4129.0(16)	62.2(11)
C7	6385(3)	5670.1(15)	4986.3(10)	35.7(6)
C8	7290(4)	5066.9(19)	4879.1(12)	56.6(9)
C9	6117(3)	5750.3(19)	5496.0(11)	46.1(8)
C10	4139(2)	6435.9(13)	4185.0(8)	25.8(5)
C11	4961(2)	6081.3(13)	3888.0(8)	23.7(5)
C12	4530(2)	5659.0(13)	3534.8(8)	25.6(5)
C13	3175(2)	5590.0(15)	3509.3(9)	30.7(6)
C14	2315(2)	5921.4(15)	3811.5(9)	30.3(6)
C15	2809(2)	6362.9(14)	4155.4(9)	29.5(6)
C16	5461(3)	5283.8(15)	3200.1(9)	31.3(6)
C17	6299(3)	5846.3(19)	2963.0(11)	46.5(8)
C18	4734(3)	4868(2)	2832.1(12)	53.9(9)

Atom	*x*	*y*	*z*	U(eq)
C19	6334(4)	4779(2)	3468.5(12)	53.5(9)
C20	848(3)	5797.7(17)	3774.6(10)	39.2(7)
C21	403(5)	6125(5)	3301(2)	68(2)
C22	83(5)	6178(4)	4138(2)	56(2)
C23	574(6)	5036(3)	3794(4)	71(3)
C21A	486(8)	5225(7)	3398(4)	65(3)
C22A	390(8)	5379(6)	4225(3)	64(3)
C23A	106(9)	6436(5)	3744(7)	88(5)

Table A11 Anisotropic Displacement Parameters ($Å^2 \times 10^3$) for .**L5b′**H The Anisotropic displacement factor exponent takes the form: $-2\pi^2[h^2a^{*2}U_{11}+2hka^*b^*U_{12}+\ldots]$.

Atom	U_{11}	U_{22}	U_{33}	U_{23}	U_{13}	U_{12}
O1	46.9(13)	58.3(14)	45.4(12)	-10.8(10)	-1.1(10)	-28.5(11)
O2	41.2(13)	85.0(18)	40.4(12)	4.0(12)	-14.1(10)	-13.4(12)
O3	21.0(8)	31.9(9)	26.6(9)	-7.0(7)	1.3(6)	-2.4(7)
N1	24.3(11)	35.5(12)	34.5(11)	-15.0(10)	2.6(9)	0.0(9)
N2	30.5(12)	30.7(12)	32.9(12)	-4.0(9)	-0.1(9)	-9.1(9)
N3	29.9(12)	35.8(12)	27.2(11)	-1.3(9)	-0.4(9)	-6.7(9)
C1	25.6(12)	28.9(12)	26.5(12)	-6.6(10)	1.2(9)	-4.2(10)
C2	30.8(14)	44.5(16)	32.0(14)	-10.3(12)	2.4(11)	-12.7(12)
C3	30.3(14)	49.9(17)	30.0(13)	-5.8(12)	-1.1(11)	-7.4(12)
C4	41.3(16)	29.5(14)	49.1(17)	4.2(12)	-2.5(13)	-3.2(12)
C5	66(2)	41.6(17)	44.0(17)	5.1(14)	8.2(16)	-3.4(16)
C6	65(2)	34.2(17)	87(3)	1.8(18)	28(2)	4.4(16)
C7	39.7(15)	35.3(14)	32.1(14)	2.1(11)	3.0(11)	-8.3(12)
C8	78(3)	42.3(18)	50(2)	3.0(15)	17.7(18)	6.8(17)
C9	51.9(19)	53.0(18)	33.3(15)	6.5(14)	9.1(13)	-1.5(15)
C10	25.3(12)	26.6(12)	25.3(12)	-0.7(9)	1.7(9)	-0.9(10)
C11	19.3(11)	28.2(12)	23.4(11)	1.7(9)	1.0(9)	-1.1(9)
C12	25.4(12)	30.2(12)	21.2(11)	0.2(9)	0.5(9)	-2.4(10)
C13	26.6(13)	39.6(15)	25.9(12)	-2.3(11)	-2.5(10)	-3.9(11)
C14	21.4(12)	39.6(14)	30.0(13)	2.5(11)	0.3(10)	-1.3(10)
C15	22.2(12)	36.8(14)	29.5(13)	-1.9(11)	3.1(9)	3.0(10)
C16	29.7(13)	37.5(14)	26.7(12)	-7.7(11)	3.5(10)	1.5(11)
C17	46.1(18)	55.7(19)	37.7(16)	-7.6(14)	16.0(13)	-5.7(15)
C18	44.9(18)	73(2)	44.2(18)	-30.1(17)	7.1(14)	-7.2(16)

Atom	U_{11}	U_{22}	U_{33}	U_{23}	U_{13}	U_{12}
C19	61(2)	58(2)	42.3(18)	-5.9(15)	4.7(15)	27.1(17)
C20	23.0(13)	55.5(18)	39.2(15)	-3.9(13)	-2.6(11)	-2.3(12)
C21	21(2)	140(7)	43(3)	8(4)	-9(2)	5(3)
C22	21(2)	97(5)	51(3)	-12(4)	4(2)	-3(3)
C23	28(3)	53(4)	133(9)	0(4)	2(4)	-12(3)
C21A	32(4)	106(9)	58(6)	-21(6)	-5(4)	-26(5)
C22A	34(4)	95(8)	63(6)	14(5)	0(4)	-26(5)
C23A	32(5)	55(6)	178(18)	7(8)	-6(7)	7(4)

Table A11 Hydrogen Atom Coordinates (Å×10^4) and Isotropic Displacement Parameters (Å^2×10^3) for **L5b′**H

Atom	*x*	*y*	*z*	U(eq)
H1	4611.18	7146.1	4679.6	38
H4	5910.74	7627.96	3799.64	48
H5A	8589.17	7961.89	3707.39	76
H5B	7515.1	8067.46	3317.69	76
H5C	7914.42	7286.48	3477.48	76
H6A	5841.22	8515.42	4372	93
H6B	6190.67	8839.13	3879.56	93
H6C	7303.86	8724.91	4254.1	93
H7	5541.37	5564.49	4832.77	43
H8A	7375.18	5017.62	4545.48	85
H8B	6941.83	4627	5008.22	85
H8C	8140.03	5163.57	5013.72	85
H9A	6933.87	5823.06	5660	69
H9B	5694.42	5320.93	5611.12	69
H9C	5549.33	6158.86	5546.09	69
H13	2824.43	5301.34	3272.82	37
H15	2250.38	6604.46	4361.67	35
H17A	5740.99	6186.69	2804.18	70
H17B	6872.19	5616.62	2740.04	70
H17C	6820.48	6094.63	3193.43	70
H18A	4197.46	4504.99	2978.4	81
H18B	5356.65	4641.61	2625.2	81
H18C	4182.35	5191.76	2656.38	81
H19A	6851.42	5049.5	3689.29	80

Atom	*x*	*y*	*z*	U(eq)
H19B	6910.07	4530.73	3255.25	80
H19C	5800.42	4433.27	3633.09	80
H21A	-510.43	6012.61	3248.17	102
H21B	927.29	5926.12	3052.45	102
H21C	514.77	6640.67	3309.21	102
H22A	220.74	6689.91	4109.33	85
H22B	367.13	6020.65	4442.5	85
H22C	-838.99	6072.24	4099.74	85
H23A	-363.75	4960.85	3789.1	107
H23B	935.51	4837.66	4076.89	107
H23C	966.78	4801.4	3528.04	107
H21D	-449.4	5141.72	3402.52	98
H21E	940.83	4781.35	3464.16	98
H21F	742.76	5398.42	3094.07	98
H22D	491.1	5684.15	4494.56	96
H22E	918.8	4951.92	4263.11	96
H22F	-520.88	5243.56	4192.4	96
H23D	368.04	6702.16	3470.72	132
H23E	257.11	6725.3	4018.57	132
H23F	-814.99	6318.15	3722.9	132

Table A12 Crystal data for **L6a**H

Empirical formula	$C_{26}H_{36}N_2O$
Formula weight	392.57
Temperature/K	173.00
Crystal system	Triclinic
Space group	P-1
a/Å	7.5708(3)
b/Å	10.0292(4)
c/Å	15.7497(6)
α/°	79.355(2)
β/°	82.900(2)
γ/°	82.858(2)
Volume/Å^3	1159.94(8)
Z	2
ρ_{calc}g/cm^3	1.124
μ/mm^{-1}	0.068
F(000)	428.0
Crystal size/mm^3	0.25 × 0.25 × 0.25
Radiation	MoKα (λ = 0.71073)
2Θ range for data collection/°	5.296 to 56.564
Index ranges	$-10 \leq h \leq 10$, $-13 \leq k \leq 13$, $-20 \leq l \leq 20$
Reflections collected	42507
Independent reflections	5744 [R_{int} = 0.0531, R_{sigma} = 0.0330]
Data/restraints/parameters	5744/0/301
Goodness-of-fit on F^2	1.105
Final R indexes [I>=2σ (I)]	R_1 = 0.0672, wR_2 = 0.1337
Final R indexes [all data]	R_1 = 0.0921, wR_2 = 0.1490
Largest diff. peak/hole / e Å^{-3}	0.40/-0.27

Table A13 Bond lengths (Å) for **L6a**H

O1–C22	1.362(2)	C9–C14	1.407(2)
N1–C1	1.287(2)	C10–C11	1.398(2)
N1–C21	1.414(2)	C10–C15	1.518(3)
N2–C1	1.362(2)	C11–C12	1.382(3)
N2–C2	1.498(2)	C12–C13	1.380(3)
N2–C9	1.439(2)	C13–C14	1.395(2)
C1–C4	1.538(2)	C14–C18	1.521(3)
C2–C5	1.523(3)	C15–C16	1.534(3)
C2–C6	1.517(3)	C15–C17	1.534(3)
C2–C3A	1.603(13)	C18–C19	1.537(3)
C2–C3	1.552(3)	C18–C20	1.533(3)
C4–C3A	1.549(15)	C21–C22	1.397(2)
C4–C7A	1.436(16)	C21–C26	1.392(3)
C4–C8A	1.614(15)	C22–C23	1.387(3)
C4–C3	1.548(3)	C23–C24	1.382(3)
C4–C7	1.551(4)	C24–C25	1.375(3)
C4–C8	1.518(4)	C25–C26	1.387(3)
C9–C10	1.406(2)		

Table A14 Bond angles (°) for **L6a**H

C1 N1 C21	123.35(15)	C10 C9 C14	120.96(15)
C1 N2 C2	115.04(14)	C14 C9 N2	119.81(15)
C1 N2 C9	122.14(14)	C9 C10 C15	122.49(16)
C9 N2 C2	122.51(14)	C11 C10 C9	118.28(16)
N1 C1 N2	120.25(15)	C11 C10 C15	119.07(16)
N1 C1 C4	131.16(16)	C12 C11 C10	121.12(17)
N2 C1 C4	108.56(14)	C13 C12 C11	119.91(17)
N2 C2 C5	112.15(16)	C12 C13 C14	121.26(17)
N2 C2 C6	111.90(17)	C9 C14 C18	123.04(16)
N2 C2 C3A	100.2(5)	C13 C14 C9	118.26(16)
N2 C2 C3	100.39(15)	C13 C14 C18	118.55(16)
C5 C2 C3A	134.6(7)	C10 C15 C16	110.37(16)
C5 C2 C3	107.8(2)	C10 C15 C17	113.34(17)
C6 C2 C5	107.30(18)	C16 C15 C17	109.23(17)
C6 C2 C3A	87.8(7)	C14 C18 C19	112.78(17)
C6 C2 C3	117.2(2)	C14 C18 C20	109.94(16)
C1 C4 C3A	103.3(4)	C20 C18 C19	109.99(18)
C1 C4 C8A	115.7(5)	C22 C21 N1	118.50(16)
C1 C4 C3	102.31(15)	C26 C21 N1	123.18(16)
C1 C4 C7	111.9(2)	C26 C21 C22	117.78(16)
C3A C4 C8A	106.3(8)	O1 C22 C21	120.19(16)
C7A C4 C1	107.5(6)	O1 C22 C23	118.64(17)
C7A C4 C3A	115.5(9)	C23 C22 C21	121.17(18)
C7A C4 C8A	108.8(9)	C24 C23 C22	119.76(19)
C3 C4 C7	109.5(2)	C25 C24 C23	119.96(19)
C8 C4 C1	110.5(2)	C24 C25 C26	120.3(2)
C8 C4 C3	112.3(2)	C25 C26 C21	121.0(2)

C8 C4 C7	110.2(2)	C4 C3A C2	104.2(8)
C10 C9 N2	119.23(15)	C4 C3 C2	106.74(19)

Table A15 Fractional Atomic Coordinates ($\times 10^4$) and Equivalent Isotropic Displacement Parameters ($Å^2 \times 10^3$) for **L6a**H. U_{eq} is defined as 1/3 of the trace of the orthogonalized U_{IJ} tensor.

Atom	*x*	*y*	*z*	U(eq)
O1	752(2)	6561.9(15)	3156.4(9)	41.7(4)
N1	2634.7(19)	4552.1(14)	2323.2(10)	23.2(3)
N2	4942.9(19)	3040.8(14)	2851.3(10)	22.9(3)
C1	4308(2)	4286.4(17)	2430.2(11)	20.9(3)
C2	6906(2)	2870(2)	2948.3(14)	31.9(4)
C4	5868(2)	5177.1(19)	2178.7(13)	29.6(4)
C5	7296(3)	2291(3)	3878.5(16)	47.3(6)
C6	7942(3)	1919(3)	2372.8(17)	50.8(6)
C9	3845(2)	1931.3(16)	3102.0(11)	20.3(3)
C10	3030(2)	1666.5(17)	3959.6(11)	22.4(3)
C11	2075(2)	526.1(19)	4206.3(12)	27.0(4)
C12	1924(2)	-319.7(19)	3624.6(13)	30.4(4)
C13	2659(2)	-10.6(18)	2774.1(13)	28.4(4)
C14	3607(2)	1124.7(17)	2490.9(11)	23.1(4)
C15	3035(3)	2625(2)	4601.0(12)	29.8(4)
C16	1197(3)	3446(2)	4713.6(14)	38.0(5)
C17	3550(3)	1892(3)	5494.0(14)	47.4(6)
C18	4218(3)	1490(2)	1527.5(12)	30.6(4)
C19	5366(4)	306(3)	1164.2(15)	50.1(6)
C20	2591(3)	1957(2)	1015.6(14)	41.4(5)
C21	1907(2)	5778.2(17)	1831.5(11)	23.1(4)
C22	896(2)	6749.6(18)	2272.5(12)	25.6(4)
C23	29(3)	7922.0(19)	1826.2(14)	33.6(4)

Atom	*x*	*y*	*z*	U(eq)
C24	135(3)	8128(2)	929.7(15)	41.0(5)
C25	1081(3)	7166(2)	484.7(14)	43.2(5)
C26	1946(3)	5993(2)	931.0(13)	34.9(4)
C3A	7545(17)	4121(14)	2234(13)	44(4)
C7A	5680(20)	6125(19)	2773(14)	45(4)
C8A	6010(20)	6020(20)	1199(10)	46(4)
C3	7308(4)	4383(3)	2751(3)	33.9(8)
C7	5362(5)	6617(4)	2419(4)	48.3(10)
C8	6484(5)	5290(5)	1216(2)	45.7(9)

Table A16 Anisotropic Displacement Parameters ($Å^2 \times 10^3$) for **L6a**H . The Anisotropic displacement factor exponent takes the form: $-2\pi^2[h^2a^{*2}U_{11}+2hka^*b^*U_{12}+\ldots]$.

Atom	U_{11}	U_{22}	U_{33}	U_{23}	U_{13}	U_{12}
O1	53.8(10)	36.0(8)	33.5(8)	-8.7(6)	-3.5(7)	6.1(7)
N1	22.0(7)	18.8(7)	27.3(8)	-1.4(6)	-2.3(6)	-0.9(6)
N2	15.8(7)	19.5(7)	32.1(8)	0.4(6)	-3.5(6)	-2.8(5)
C1	21.8(8)	18.6(8)	21.7(8)	-2.7(6)	0.5(6)	-3.8(6)
C2	16.0(8)	30.4(10)	47.1(12)	2.5(8)	-5.1(8)	-5.2(7)
C4	23.0(9)	23.1(9)	40.3(11)	2.6(8)	-0.6(8)	-8.0(7)
C5	25.7(10)	63.1(16)	54.3(14)	-8.8(12)	-18.3(10)	2.8(10)
C6	23.4(10)	69.6(17)	56.3(15)	-14.6(13)	-1.3(10)	10.4(10)
C9	15.3(7)	17.1(8)	26.4(9)	0.4(6)	-2.7(6)	0.2(6)
C10	16.7(8)	23.2(8)	25.9(9)	-1.6(7)	-4.6(6)	1.6(6)
C11	20.2(8)	29.0(9)	27.8(9)	3.7(7)	-0.6(7)	-1.5(7)
C12	26.2(9)	20.3(8)	42.4(11)	2.9(8)	-3.4(8)	-6.3(7)
C13	28.2(9)	21.4(9)	37.0(10)	-7.3(7)	-6.1(8)	-2.7(7)
C14	20.3(8)	21.1(8)	26.9(9)	-3.3(7)	-3.6(7)	1.6(6)
C15	27.3(9)	34.0(10)	28.3(9)	-7.8(8)	-3.8(7)	0.8(8)
C16	37.4(11)	38.7(11)	35.8(11)	-10.6(9)	-1.5(9)	8.8(9)
C17	52.5(14)	58.4(15)	32.6(11)	-12.9(10)	-15.7(10)	8.1(11)
C18	35.1(10)	30.5(10)	25.9(9)	-5.7(7)	-0.5(8)	-4.0(8)
C19	59.3(15)	51.5(14)	37.5(12)	-17.3(11)	5.3(11)	7.1(12)
C20	48.7(13)	44.1(12)	31.5(11)	-0.6(9)	-12.4(9)	-6.1(10)
C21	20.4(8)	19.5(8)	28.6(9)	0.0(7)	-3.9(7)	-3.6(6)
C22	23.4(9)	22.0(8)	31.5(9)	-3.4(7)	-3.3(7)	-4.3(7)
C23	25.5(9)	21.7(9)	52.6(13)	-4.4(8)	-4.9(9)	-0.6(7)
C24	34.5(11)	30.3(10)	52.5(13)	11.6(9)	-13.3(10)	-1.1(9)

Atom	U_{11}	U_{22}	U_{33}	U_{23}	U_{13}	U_{12}
C25	45.3(13)	47.9(13)	30.8(11)	7.8(9)	-8.9(9)	0.1(10)
C26	37.8(11)	34.9(11)	29.3(10)	-0.8(8)	-3.5(8)	-0.4(9)
C3A	34(6)	47(7)	52(10)	1(7)	-1(6)	-23(5)
C7A	32(8)	30(9)	80(13)	-25(8)	8(8)	-17(7)
C8A	44(9)	43(9)	47(8)	4(7)	13(6)	-20(7)
C3	23.2(12)	32.6(14)	46(2)	0.3(12)	-7.1(12)	-9.0(10)
C7	38.7(18)	22.1(18)	87(3)	-7.6(17)	-12.7(18)	-11.0(14)
C8	34.7(17)	50(2)	41.2(17)	15.0(17)	8.2(12)	-8.4(16)

Tables A17 Hydrogen Atom Coordinates (Å×10^4) and Isotropic Displacement Parameters (Å^2×10^3) for **L6a**H

Atom	***x***	***y***	***z***	**U(eq)**
H1	1282.35	5799.59	3349.02	63
H5A	6752.69	2932.51	4260.45	71
H5B	8592.79	2152.25	3907.04	71
H5C	6792.26	1417.49	4066.36	71
H6A	7524.35	1011.39	2540.92	76
H6B	9220.33	1855.5	2440.74	76
H6C	7749.04	2276.52	1765.2	76
H11	1520.09	329.38	4783.77	32
H12	1315.71	-1112.91	3809.77	36
H13	2516.89	-581.68	2373.88	34
H15	3932.87	3283.72	4355.23	36
H16A	823.48	3861.25	4141.53	57
H16B	1273.29	4162.94	5050.06	57
H16C	319.87	2836.87	5021.13	57
H17A	2622.3	1308.54	5774.5	71
H17B	3660.48	2567.96	5855.81	71
H17C	4695.66	1330.09	5422.12	71
H18	4960.45	2270.56	1446.6	37
H19A	4619.74	-424.49	1162.32	75
H19B	6337.95	-44.56	1528.98	75
H19C	5872.97	632.58	569.63	75
H20A	1855.47	1200.94	1075.45	62
H20B	2997.71	2245.71	401.03	62
H20C	1880.93	2724.01	1243.14	62

Atom	*x*	*y*	*z*	U(eq)
H23	-635.52	8580.76	2135.47	40
H24	-445.54	8934.66	621.23	49
H25	1142.66	7304.56	-131.04	52
H26	2574.98	5326.1	617.35	42
H3AA	8550.73	4504.95	2417.49	53
H3AB	7926.57	3829.72	1666.08	53
H7AA	4565.88	6725.05	2704.74	68
H7AB	6697.4	6673.62	2650.91	68
H7AC	5656.06	5622.01	3369.91	68
H8AA	5805.44	5425.68	797.19	69
H8AB	7196.95	6332.29	1045.57	69
H8AC	5096.04	6806.86	1158.2	69
H3A	7248.68	4748.3	3297.22	41
H3B	8518.51	4463.58	2439.13	41
H7A	4526.61	7146.78	2023.93	72
H7B	6444.47	7082.68	2366.49	72
H7C	4794.93	6532.75	3017.58	72
H8A	6676.13	4378.13	1059.65	69
H8B	7605.96	5716.08	1086.43	69
H8C	5567.5	5850.5	880.41	69

Table A18. Crystal data for Ti(**L3a**)$_2$(OiPr)$_2$

Empirical formula	$C_{28}H_{42}N_6O_4Ti$
Formula weight	574.57
Temperature/ K	173.0
Crystal system	monoclinic
Space group	P21/n
a/Å	23.2014(7)
b/Å	10.7004(3)
c/Å	24.3975(7)
α/°	90
β/°	95.7949(12)
γ/°	90
Volume/Å3	6026.1(3)
Z	8
ρcalcg/cm3	1.267
μ/mm-1	0.326
F(000)	2448.0
Crystal size/mm3	0.1 × 0.1 × 0.1
Radiation	MoKα (λ = 0.71073)
2Θ range for data collection/°	5.076 to 60.066
Index ranges	$-29 \leq h \leq 32$, $-15 \leq k \leq 15$, $-34 \leq l \leq 34$
Reflections collected	157194
Independent reflections	17589 [R_{int} = 0.0771, R_{sigma} = 0.0307]
Data/restraints/parameters	17589/0/779
Goodness-of-fit on F2	1.131
Final R indexes [I>=2σ (I)]	R1 = 0.0532, wR2 = 0.1254
Final R indexes [all data]	R1 = 0.0643, wR2 = 0.1316
Largest diff. peak/hole /	e Å-3 0.43/-0.60
CCDC	2345355

Table A19. Crystal data for Zr(**L3a**)$_2$(O^iPr)$_2$

Empirical formula	$C_{28}H_{42}N_6O_4Zr$
Formula weight	617.89
Temperature/K	173.00
Crystal system	monoclinic
Space group	$P2_1/n$
a/Å	9.6548(4)
b/Å	15.7838(6)
c/Å	19.7193(7)
α/°	90
β/°	90.246(2)
γ/°	90
Volume/Å^3	3005.0(2)
Z	4
ρ_{calc}g/cm^3	1.366
μ/mm^{-1}	0.408
F(000)	1296.0
Crystal size/mm^3	0.4 × 0.4 × 0.1
Radiation	MoKα (λ = 0.71073)
2Θ range for data collection/°	4.218 to 55.134
Index ranges	$-12 \leq h \leq 12$, $-20 \leq k \leq 20$, $-25 \leq l \leq 25$
Reflections collected	94441
Independent reflections	6938 [R_{int} = 0.1255, R_{sigma} = 0.0549]
Data/restraints/parameters	6938/0/371
Goodness-of-fit on F^2	1.049
Final R indexes [I>=2σ (I)]	R_1 = 0.0579, wR_2 = 0.0989
Final R indexes [all data]	R_1 = 0.0975, wR_2 = 0.1138
Largest diff. peak/hole / e Å^{-3}	1.10/-0.79
CCDC	2345357

Table A20. Crystal data for Ti(**L4a**)$_2$(O^iPr)$_2$

Empirical formula	$C_{30}H_{46}N_6O_4Ti$
Formula weight	602.63
Temperature/K	173.00
Crystal system	orthorhombic
Space group	$Pca2_1$
a/Å	14.5172(8)
b/Å	11.5840(6)
c/Å	19.1268(10)
α/°	90
β/°	90
γ/°	90
Volume/Å^3	3216.5(3)
Z	4
ρ_{calc}g/cm^3	1.244
μ/mm^{-1}	0.309
F(000)	1288.0
Crystal size/mm^3	0.2 × 0.2 × 0.1
Radiation	MoKα (λ = 0.71073)
2Θ range for data collection/°	4.498 to 55.106
Index ranges	-18 ≤ h ≤ 18, -14 ≤ k ≤ 15, -24 ≤ l ≤ 24
Reflections collected	39189
Independent reflections	7358 [R_{int} = 0.0835, R_{sigma} = 0.0610]
Data/restraints/parameters	7358/1/378
Goodness-of-fit on F^2	1.053
Final R indexes [I>=2σ (I)]	R_1 = 0.0481, wR_2 = 0.1066
Final R indexes [all data]	R_1 = 0.0924, wR_2 = 0.1296
Largest diff. peak/hole / e Å^{-3}	0.44/-0.35
CCDC	2345356

Table A21. Crystal data for Ti(**L4a**)$_2$Cl$_2$

Empirical formula	$C_{37}H_{48}Cl_2N_6O_2Ti$
Formula weight	727.61
Temperature/K	173.00
Crystal system	monoclinic
Space group	$P2_1/n$
a/Å	10.6343(7)
b/Å	30.9675(18)
c/Å	12.5823(8)
α/°	90
β/°	110.817(2)
γ/°	90
Volume/Å^3	3873.1(4)
Z	4
ρ_{calc}g/cm^3	1.248
μ/mm^{-1}	0.398
F(000)	1536.0
Crystal size/mm^3	0.1 × 0.025 × 0.025
Radiation	MoKα (λ = 0.71073)
2Θ range for data collection/°	4.304 to 61.016
Index ranges	$-15 \leq h \leq 15$, $-44 \leq k \leq 44$, $-17 \leq l \leq 17$
Reflections collected	150839
Independent reflections	11792 [R_{int} = 0.0482, R_{sigma} = 0.0239]
Data/restraints/parameters	11792/6/507
Goodness-of-fit on F^2	1.191
Final R indexes [I>=2σ (I)]	R_1 = 0.0600, wR_2 = 0.1306
Final R indexes [all data]	R_1 = 0.0700, wR_2 = 0.1352
Largest diff. peak/hole / e Å^{-3}	0.52/-0.53
CCDC	2345354

Table A22 Crystal data for Zn[**L2a**]$_2$

Empirical formula	$C_{30}H_{40}N_6O_2Zn$
Formula weight	582.05
Temperature/K	173.00
Crystal system	monoclinic
Space group	$P2_1/n$
a/Å	10.8813(5)
b/Å	17.2053(8)
c/Å	16.7369(8)
α/°	90
β/°	106.077
γ/°	90
Volume/Å^3	3010.9(2)
Z	4
ρ_{calc}g/cm^3	1.284
μ/mm^{-1}	0.852
F(000)	1232.0
Crystal size/mm^3	0.1 × 0.1 × 0.1
Radiation	MoKα (λ = 0.71073)
2Θ range for data collection/°	4.558 to 61.118
Index ranges	$-15 \leq h \leq 15$, $-24 \leq k \leq 24$, $-23 \leq l \leq 23$
Reflections collected	163292
Independent reflections	9224 [R_{int} = 0.0662, R_{sigma} = 0.0268]
Data/restraints/parameters	9224/0/360
Goodness-of-fit on F^2	1.017
Final R indexes [I>=2σ (I)]	R_1 = 0.0333, wR_2 = 0.0745
Final R indexes [all data]	R_1 = 0.0500, wR_2 = 0.0815
Largest diff. peak/hole / e Å^{-3}	0.36/-0.37

Table A23 Bond lengths (Å) for Zn[**L2a**]$_2$

Zn1–O1	1.9377(10)	C2–C3	1.338(2)
Zn1O2	1.9493(10)	C4–C5	1.520(2)
Zn1–N1	2.0017(11)	C4–C6	1.518(2)
Zn1–N4	1.9837(11)	C7–C8	1.520(2)
O1–C11	1.3280(17)	C7–C9	1.521(2)
O2–C26	1.3369(16)	C10–C11	1.4256(19)
N1–C1	1.3360(17)	C10–C15	1.3897(19)
N1–C10	1.4158(17)	C11–C12	1.3986(19)
N2–C1	1.3600(18)	C12–C13	1.387(2)
N2–C2	1.3935(18)	C13–C14	1.379(3)
N2–C4	1.4729(18)	C14–C15	1.398(2)
N3–C1	1.3609(18)	C17–C18	1.338(2)
N3–C3	1.3911(19)	C19–C20	1.519(2)
N3–C7	1.4812(19)	C19–C21	1.523(2)
N4–C16	1.3367(17)	C22–C23	1.522(2)
N4–C25	1.4105(17)	C22–C24	1.512(2)
N5–C16	1.3589(18)	C25–C26	1.4237(18)
N5–C17	1.3965(19)	C25–C30	1.3911(19)
N5–C19	1.475(2)	C26–C27	1.394(2)
N6–C16	1.3582(18)	C27–C28	1.392(2)
N6–C18	1.3926(18)	C28–C29	1.382(2)
N6–C22	1.4723(19)	C29–C30	1.388(2

Table A24 Bond Angles (°) for Zn[**L2a**]$_2$

O1	Zn1	O2	117.40(5)	N3	C7	C8	110.59(13)
O1	Zn1	N1	85.73(4)	N3	C7	C9	109.21(14)
O1	Zn1	N4	124.19(5)	C8	C7	C9	112.44(15)
O2	Zn1	N1	125.59(5)	N1	C10	C11	114.35(12)
O2	Zn1	N4	85.67(4)	C15	C10	N1	125.65(13)
N4	Zn1	N1	122.82(5)	C15	C10	C11	119.67(13)
C11	O1	Zn1	110.53(8)	O1	C11	C10	120.13(12)
C26	O2	Zn1	109.81(8)	O1	C11	C12	121.77(13)
C1	N1	Zn1	129.69(9)	C12	C11	C10	118.04(13)
C1	N1	C10	121.87(11)	C13	C12	C11	121.46(15)
C10	N1	Zn1	108.43(8)	C14	C13	C12	120.27(14)
C1	N2	C2	108.86(12)	C13	C14	C15	119.73(15)
C1	N2	C4	125.35(12)	C10	C15	C14	120.82(15)
C2	N2	C4	125.59(12)	N4	C16	N5	129.90(13)
C1	N3	C3	109.27(12)	N4	C16	N6	123.21(13)
C1	N3	C7	124.83(12)	N6	C16	N5	106.75(12)
C3	N3	C7	124.06(13)	C18	C17	N5	107.75(13)
C16	N4	Zn1	127.70(10)	C17	C18	N6	107.44(14)
C16	N4	C25	123.08(12)	N5	C19	C20	109.40(14)
C25	N4	Zn1	108.59(8)	N5	C19	C21	110.72(13)
C16	N5	C17	108.82(13)	C20	C19	C21	111.72(15)
C16	N5	C19	125.72(12)	N6	C22	C23	108.99(13)
C17	N5	C19	123.74(12)	N6	C22	C24	110.95(14)
C16	N6	C18	109.23(13)	C24	C22	C23	113.23(15)
C16	N6	C22	124.92(12)	N4	C25	C26	114.81(11)
C18	N6	C22	125.07(13)	C30	C25	N4	125.35(12)
N1	C1	N2	123.85(12)	C30	C25	C26	119.53(13)
N1	C1	N3	129.49(13)	O2	C26	C25	119.37(12)
N2	C1	N3	106.60(12)	O2	C26	C27	122.23(13)
C3	C2	N2	107.88(13)	C27	C26	C25	118.37(12)
C2	C3	N3	107.37(13)	C28	C27	C26	121.11(14)
N2	C4	C5	110.26(12)	C29	C28	C27	120.24(14)
N2	C4	C6	110.19(13)	C28	C29	C30	119.76(13)

Table A25 Fractional Atomic Coordinates ($\times 10^4$) and Equivalent Isotropic Displacement Parameters ($Å^2 \times 10^3$) for Zn[**L2a**]$_2$. U_{eq} is defined as 1/3 of the trace of the orthogonalized U_{IJ} tensor.

Atom	***x***	***y***	***z***	**U(eq)**
Zn1	3315.7(2)	2169.9(2)	6744.8(2)	18.13(5)
O1	1682.5(9)	1712.3(6)	6730.2(7)	25.0(2)
O2	4052.5(10)	1887.1(6)	5847.8(6)	23.9(2)
N1	2495.5(11)	3189.7(6)	6859.4(7)	19.6(2)
N2	3778.2(11)	4209.5(7)	6562.2(8)	22.3(2)
N3	2955.0(12)	4428.3(7)	7590.3(8)	23.8(2)
N4	4977.9(11)	1838.9(7)	7503.1(7)	20.7(2)
N5	6588.2(12)	2379.6(7)	8692.0(7)	23.8(2)
N6	4821.3(12)	1925.7(7)	8885.2(7)	24.5(2)
C1	3013.4(12)	3898.2(8)	6998.5(8)	19.5(3)
C2	4209.7(14)	4933.5(9)	6898.0(10)	28.1(3)
C3	3695.9(15)	5071.2(9)	7524.1(10)	28.7(3)
C4	4018.9(14)	3866.5(9)	5813.3(9)	24.3(3)
C5	3442.4(18)	4374.2(11)	5059.5(11)	38.3(4)
C6	5439.3(16)	3720.9(12)	5956.3(12)	40.9(4)
C7	2477.3(16)	4265.1(9)	8320.4(9)	29.3(3)
C8	1663(2)	4935.6(11)	8476.0(12)	44.4(5)
C9	3606(2)	4093.7(13)	9069.4(12)	48.7(5)
C10	1180.4(12)	3059.3(8)	6772.9(8)	19.2(2)
C11	809.9(13)	2262.1(8)	6687.0(8)	21.3(3)
C12	-491.8(14)	2086.8(10)	6519.8(10)	29.4(3)
C13	-1404.1(15)	2666.7(11)	6435.7(11)	34.8(4)
C14	-1040.8(15)	3436.7(11)	6520.1(11)	33.4(4)
C15	252.4(14)	3632.3(9)	6685.8(9)	26.0(3)
C16	5465.8(13)	2024.7(8)	8304.1(8)	20.8(3)

Atom	*x*	*y*	*z*	U(eq)
C17	6621.7(16)	2515.6(9)	9520.4(9)	29.7(3)
C18	5540.1(16)	2234.1(9)	9639.3(9)	30.6(3)
C19	7473.0(15)	2744.9(9)	8276.6(10)	26.9(3)
C20	7354(2)	3623.2(10)	8311.3(13)	44.2(4)
C21	8840.2(16)	2475.1(12)	8669.3(12)	39.2(4)
C22	3660.3(14)	1450.5(9)	8772.2(9)	26.7(3)
C23	3996.7(19)	717.0(11)	9295.7(12)	41.4(4)
C24	2597.9(18)	1916.5(12)	8962.7(13)	44.3(4)
C25	5688.4(12)	1458.5(8)	7030.9(8)	18.9(2)
C26	5135.5(13)	1488.6(8)	6154.6(8)	19.7(3)
C27	5729.4(15)	1078.7(9)	5646.3(10)	27.6(3)
C28	6826.0(15)	640.8(9)	5983.5(11)	30.9(3)
C29	7350.7(14)	607.6(9)	6835.2(10)	28.8(3)
C30	6777.7(13)	1011.2(8)	7354.8(9)	24.3(3)

Table A26. Anisotropic Displacement Parameters ($Å^2 \times 10^3$) for Zn[**L2a**]$_2$. The Anisotropic displacement factor exponent takes the form: $-2\pi^2[h^2a^{*2}U_{11}+2hka^*b^*U_{12}+\ldots]$.

Atom	U_{11}	U_{22}	U_{33}	U_{23}	U_{13}	U_{12}
Zn1	17.43(7)	17.85(8)	17.66(8)	0.16(6)	2.45(5)	2.55(6)
O1	22.3(5)	18.8(5)	32.2(6)	3.5(4)	4.7(4)	-1.7(4)
O2	24.8(5)	28.9(5)	16.9(5)	2.1(4)	3.7(4)	10.0(4)
N1	17.4(5)	17.0(5)	25.4(6)	-1.3(4)	7.3(4)	0.8(4)
N2	21.4(5)	19.1(5)	26.4(6)	-1.2(5)	6.7(5)	-2.4(4)
N3	27.8(6)	19.2(5)	24.2(6)	-2.6(5)	6.7(5)	1.8(5)
N4	19.3(5)	24.2(6)	15.8(5)	-2.2(4)	0.0(4)	2.9(4)
N5	24.7(6)	23.8(6)	18.6(6)	-1.0(4)	-0.8(5)	-3.0(5)
N6	26.8(6)	28.7(6)	15.3(5)	-1.6(5)	1.6(5)	-3.5(5)
C1	17.9(6)	18.0(6)	21.8(6)	0.3(5)	4.2(5)	2.8(5)
C2	25.5(7)	20.5(7)	36.0(8)	-1.7(6)	4.8(6)	-5.3(6)
C3	30.5(8)	19.8(7)	31.8(8)	-4.3(6)	1.9(6)	-2.0(6)
C4	24.8(7)	23.5(7)	27.1(7)	-0.2(5)	11.4(6)	-0.2(5)
C5	46.0(10)	39.2(9)	30.5(8)	4.0(7)	12.2(7)	8.7(8)
C6	28.0(8)	51.4(11)	46.7(10)	2.3(8)	15.8(8)	7.0(8)
C7	41.0(9)	25.7(7)	23.2(7)	-1.3(6)	12.0(6)	6.1(6)
C8	62.1(12)	36.9(9)	42.4(10)	-0.9(8)	28.2(9)	16.2(9)
C9	59.7(13)	52.4(12)	29.1(9)	3.5(8)	4.2(9)	11.6(10)
C10	16.9(6)	24.3(6)	17.2(6)	2.5(5)	5.8(5)	1.4(5)
C11	20.4(6)	24.9(7)	18.5(6)	4.7(5)	5.3(5)	-2.1(5)
C12	23.1(7)	35.0(8)	30.2(8)	3.8(6)	7.8(6)	-6.9(6)
C13	18.6(7)	51.6(10)	35.5(9)	4.5(7)	9.5(6)	-2.3(7)
C14	21.2(7)	43.9(9)	36.6(9)	4.9(7)	10.6(6)	9.8(7)
C15	24.3(7)	27.9(7)	26.8(7)	3.0(6)	9.0(6)	6.0(6)
C16	21.9(6)	18.9(6)	18.3(6)	0.6(5)	0.2(5)	1.0(5)

Atom	U_{11}	U_{22}	U_{33}	U_{23}	U_{13}	U_{12}
C17	33.8(8)	30.2(8)	18.3(7)	-2.3(6)	-3.9(6)	-2.9(6)
C18	37.1(8)	34.5(8)	15.9(6)	-2.7(6)	0.2(6)	-1.6(7)
C19	26.7(7)	25.2(7)	25.9(7)	0.2(6)	2.5(6)	-5.0(6)
C20	56.3(12)	25.9(8)	51.0(11)	1.3(8)	16.0(9)	-5.6(8)
C21	26.1(8)	46.0(10)	40.9(10)	1.4(8)	1.8(7)	-4.8(7)
C22	28.0(7)	30.0(7)	20.8(7)	2.6(6)	4.4(6)	-3.7(6)
C23	45.8(10)	33.4(9)	39.7(10)	9.4(7)	3.1(8)	-6.6(8)
C24	33.6(9)	46.4(10)	54.1(12)	-2.6(9)	14.2(8)	1.2(8)
C25	18.3(6)	16.4(6)	20.3(6)	-0.7(5)	2.8(5)	-0.6(5)
C26	19.7(6)	18.3(6)	20.4(6)	1.8(5)	4.3(5)	1.9(5)
C27	30.5(7)	29.7(7)	24.0(7)	-0.4(6)	9.8(6)	5.4(6)
C28	30.3(8)	27.2(7)	38.9(9)	-3.3(6)	15.8(7)	6.5(6)
C29	20.4(7)	21.5(7)	42.3(9)	-0.2(6)	5.0(6)	5.0(5)
C30	19.7(6)	21.4(6)	27.3(7)	-0.2(5)	-1.2(5)	1.4(5)

Table A27 Hydrogen Atom Coordinates (Å×10^4) and Isotropic Displacement Parameters (Å^2×10^3) for Zn[**L2a**]$_2$

Atom	***x***	***Y***	***z***	**U(eq)**
H2	4769.28	5269.67	6715	34
H3	3815.19	5524.4	7861.09	34
H4	3575.84	3351.7	5715.18	29
H5A	3625.64	4146.23	4568.27	57
H5B	3815.13	4896.02	5155.7	57
H5C	2514.7	4407.62	4968.59	57
H6A	5586.28	3484.5	5457.98	61
H6B	5746.2	3369.18	6430.29	61
H6C	5902.51	4215.02	6072.85	61
H7	1927.46	3790.15	8197.32	35
H8A	2198.06	5399.63	8632.97	67
H8B	1289.73	4797.39	8926.59	67
H8C	977.46	5041.91	7968.69	67
H9A	4134.7	3684.2	8926.9	73
H9B	3290.52	3920.65	9534.55	73
H9C	4119.22	4565.67	9229.22	73
H12	-756.94	1558.75	6462.71	35
H13	-2282.98	2532.74	6319.42	42
H14	-1666.86	3832.86	6465.76	40
H15	499.95	4163.49	6739.58	31
H17	7292.56	2763.75	9926.63	36
H18	5305.37	2242.86	10145.26	37
H19	7217.34	2581.91	7679.79	32
H20A	7885.01	3865.64	7993.7	66
H20B	7641.22	3796.6	8891.1	66

Atom	*x*	*Y*	*z*	U(eq)
H20C	6459.03	3774.09	8071.38	66
H21A	8891.62	1910.86	8605.44	59
H21B	9093.98	2608.25	9261.81	59
H21C	9414.79	2732.65	8393.43	59
H22	3367.31	1290.39	8175.04	32
H23A	3259.58	365.17	9166.36	62
H23B	4222.14	854.87	9886.7	62
H23C	4724.89	458.62	9171.18	62
H24A	2402.39	2368.91	8593.36	66
H24B	2869.47	2091.7	9542.27	66
H24C	1833.09	1591	8875.94	66
H27	5379.61	1098.52	5059.88	33
H28	7215.21	363.84	5627.02	37
H29	8100.72	309.61	7064.17	35
H30	7134.84	981.47	7940.09	29

Table A28 Crystal data for $Zn(BONHMe)_2(NIPOx)_2$ and $Zn(BONMe)_2Cl_2$

Empirical formula	$C_{50}H_{64}Cl_2N_{10}O_{10}Zn_2$
Formula weight	1166.75
Temperature/K	173.00
Crystal system	monoclinic
Space group	$P2_1/c$
a/Å	18.2107(8)
b/Å	21.2283(8)
c/Å	17.3620(7)
α/°	90
β/°	118.086(2)
γ/°	90
Volume/Å^3	5921.5(4)
Z	4
ρ_{calc}g/cm^3	1.309
μ/mm^{-1}	0.960
F(000)	2432.0
Crystal size/mm^3	0.25 × 0.25 × 0.15
Radiation	MoKα (λ = 0.71073)
2Θ range for data collection/°	4.6 to 53.36
Index ranges	$-22 \leq h \leq 22$, $-26 \leq k \leq 26$, $-21 \leq l \leq 21$
Reflections collected	86241
Independent reflections	12301 [R_{int} = 0.1018, R_{sigma} = 0.0653]
Data/restraints/parameters	12301/0/360
Goodness-of-fit on F^2	1.011
Final R indexes [I>=2σ (I)]	R_1 = 0.0624, wR_2 = 0.1563
Final R indexes [all data]	R_1 = 0.1128, wR_2 = 0.1861
Largest diff. peak/hole / e Å^{-3}	0.72/-0.94

Table A29 Bond lengths of $Zn(BONHMe)_2(NIPOx)_2$ and $Zn(BONMe)_2Cl_2$

Zn1–Cl1	2.275(2)	O4–C23	1.382(5)
Zn1–Cl2	2.217(2)	O5–C41	1.244(5)
Zn1–N1	2.033(4)	O6–C42	1.262(5)
Zn1–N3	2.027(4)	O7–C42	1.229(5)
O1–C1	1.363(5)	O8–C46	1.238(4)
O1–C3	1.383(6)	O9–C47	1.261(5)
O2–C11	1.369(6)	O10–C47	1.218(5)
O2–C13	1.396(5)	N5–C31	1.310(5)
N1–C1	1.314(6)	N5–C32	1.421(5)
N1–C2	1.398(6)	N6–C31	1.323(6)
N2–C1	1.315(6)	N6–C38	1.458(6)
N2–C8	1.476(6)	N7–C21	1.319(5)
N3–C11	1.315(6)	N7–C22	1.408(5)
N3–C12	1.403(6)	N8–C21	1.323(5)
N4–C11	1.319(6)	N8–C28	1.471(6)
N4–C18	1.473(7)	N9–C41	1.317(5)
C2–C3	1.387(7)	N9–C43	1.461(5)
C2–C7	1.368(7)	N10–C46	1.319(5)
C3–C4	1.381(7)	N10–C48	1.469(5)
C4–C5	1.376(8)	C22–C23	1.374(6)
C5–C6	1.390(9)	C22–C27	1.388(6)
C6–C7	1.386(8)	C23–C24	1.380(6)
C8–C9	1.502(8)	C24–C25	1.382(7)
C8–C10	1.525(8)	C25–C26	1.386(8)
C12–C13	1.381(6)	C26–C27	1.396(7)
C12–C17	1.372(7)	C28–C29	1.505(8)

C13–C14	1.368(7)	C28–C30	1.534(7)
C14–C15	1.392(7)	C32–C33	1.366(6)
C15–C16	1.379(8)	C32–C37	1.370(6)
C16–C17	1.394(8)	C33–C34	1.377(6)
C18–C19	1.469(9)	C34–C35	1.375(7)
C18–C20	1.512(9)	C35–C36	1.375(8)
Zn2–O5	2.228(3)	C36–C37	1.395(6)
Zn2–O6	2.063(3)	C38–C39	1.494(8)
Zn2–O8	2.161(3)	C38–C40	1.455(9)
Zn2–O9	2.076(3)	C41–C42	1.539(5)
Zn2–N5	2.084(3)	C43–C44	1.503(8)
Zn2–N7	2.147(3)	C43–C45	1.477(8)
O3–C31	1.366(5)	C46–C47	1.547(6)
O3–C33	1.396(5)	C48–C49	1.487(8)
O4–C21	1.363(5)	C48–C50	1.477(7)

Cl2 Zn1 Cl1	121.63(10)	C41 O5 Zn2	109.8(2)
N1 Zn1 Cl1	107.17(12)	C42 O6 Zn2	117.8(2)
N1 Zn1 Cl2	105.31(12)	C46 O8 Zn2	111.3(2)
N3 Zn1 Cl1	105.28(13)	C47 O9 Zn2	117.4(3)
N3 Zn1 Cl2	110.72(14)	C31 N5 Zn2	128.8(3)
N3 Zn1 N1	105.70(16)	C31 N5 C32	104.4(3)
C1 O1 C3	104.0(3)	C32 N5 Zn2	126.8(3)
C11 O2 C13	104.0(4)	C31 N6 C38	125.2(4)
C1 N1 Zn1	128.4(3)	C21 N7 Zn2	129.0(3)
C1 N1 C2	105.1(4)	C21 N7 C22	104.1(3)
C2 N1 Zn1	125.8(3)	C22 N7 Zn2	126.9(3)
C1 N2 C8	124.0(4)	C21 N8 C28	124.3(4)
C11 N3 Zn1	129.2(4)	C41 N9 C43	124.2(3)
C11 N3 C12	104.5(4)	C46 N10 C48	123.3(3)
C12 N3 Zn1	125.7(3)	N7 C21 O4	114.8(4)
C11 N4 C18	125.2(5)	N7 C21 N8	128.6(4)
N1 C1 O1	114.7(4)	N8 C21 O4	116.6(4)
N1 C1 N2	128.1(4)	C23 C22 N7	108.5(4)
N2 C1 O1	117.2(4)	C23 C22 C27	120.0(4)
C3 C2 N1	107.8(4)	C27 C22 N7	131.6(4)
C7 C2 N1	131.9(5)	C22 C23 O4	108.6(4)
C7 C2 C3	120.2(5)	C22 C23 C24	124.5(4)
O1 C3 C2	108.5(4)	C24 C23 O4	126.9(4)
C4 C3 O1	127.8(5)	C23 C24 C25	115.4(5)
C4 C3 C2	123.7(5)	C24 C25 C26	121.5(5)

C5 C4 C3	115.2(5)	C25 C26 C27	122.1(5)
C4 C5 C6	122.2(5)	C22 C27 C26	116.5(5)
C7 C6 C5	121.3(6)	N8 C28 C29	110.0(5)
C2 C7 C6	117.4(5)	N8 C28 C30	108.1(4)
N2 C8 C9	110.2(4)	C29 C28 C30	113.1(5)
N2 C8 C10	107.2(5)	N5 C31 O3	114.9(4)
C9 C8 C10	111.7(5)	N5 C31 N6	128.4(4)
N3 C11 O2	114.8(4)	N6 C31 O3	116.7(4)
N3 C11 N4	127.9(5)	C33 C32 N5	108.2(4)
N4 C11 O2	117.4(5)	C33 C32 C37	120.1(4)
C13 C12 N3	108.8(4)	C37 C32 N5	131.7(4)
C17 C12 N3	131.8(5)	C32 C33 O3	108.6(4)
C17 C12 C13	119.4(5)	C32 C33 C34	124.3(5)
C12 C13 O2	107.8(4)	C34 C33 O3	127.0(4)
C14 C13 O2	127.2(5)	C35 C34 C33	115.0(5)
C14 C13 C12	125.1(5)	C34 C35 C36	122.3(5)
C13 C14 C15	114.9(5)	C35 C36 C37	121.1(5)
C16 C15 C14	121.6(5)	C32 C37 C36	117.1(5)
C15 C16 C17	121.8(5)	N6 C38 C39	108.4(5)
C12 C17 C16	117.4(5)	C40 C38 N6	110.7(5)
N4 C18 C20	108.0(6)	C40 C38 C39	112.4(6)
C19 C18 N4	110.4(5)	O5 C41 N9	124.7(4)
C19 C18 C20	111.8(7)	O5 C41 C42	119.7(3)
O6 Zn2 O5	77.42(10)	N9 C41 C42	115.6(3)
O6 Zn2 O8	88.87(10)	O6 C42 C41	114.4(3)
O6 Zn2 O9	163.06(10)	O7 C42 O6	126.6(4)

O6 Zn2 N5	98.48(12)	O7 C42 C41	119.0(4)
O6 Zn2 N7	90.81(11)	N9 C43 C44	109.5(4)
O8 Zn2 O5	81.17(11)	N9 C43 C45	109.7(4)
O9 Zn2 O5	90.10(11)	C45 C43 C44	110.8(5)
O9 Zn2 O8	77.80(10)	O8 C46 N10	124.4(4)
O9 Zn2 N5	93.52(12)	O8 C46 C47	119.9(3)
O9 Zn2 N7	100.30(12)	N10 C46 C47	115.7(3)
N5 Zn2 O5	93.00(12)	O9 C47 C46	113.1(3)
N5 Zn2 O8	169.45(12)	O10 C47 O9	127.1(4)
N5 Zn2 N7	93.92(13)	O10 C47 C46	119.8(4)
N7 Zn2 O5	167.11(11)	N10 C48 C49	109.1(4)
N7 Zn2 O8	93.53(12)	N10 C48 C50	110.2(4)
C31 O3 C33	103.8(3)	C50 C48 C49	112.2(5)
C21 O4 C23	104.1(3)		

Table A30 Fractional Atomic Coordinates ($\times 10^4$) and Equivalent Isotropic Displacement Parameters ($Å^2 \times 10^3$) for $Zn(BONHMe)_2(NIPOx)_2$ and $Zn(BONMe)_2Cl_2$ U_{eq} is defined as 1/3 of the trace of the orthogonalized U_{IJ} tensor.

Atom	*x*	*y*	*z*	U(eq)
Zn1	3704.3(5)	1847.6(3)	5448.8(4)	70.2(2)
Cl1	4610.1(18)	1106.6(9)	5455.2(13)	126.7(9)
Cl2	2363.3(14)	1637.6(11)	4945.8(12)	123.3(9)
O1	3395(2)	3241.9(14)	3582(2)	51.1(8)
O2	5164(2)	2469.6(15)	8049(2)	53.3(8)
N1	3743(2)	2582.2(17)	4718(2)	47.8(9)
N2	2357(2)	2635.1(19)	3582(3)	54.3(10)
N3	4212(3)	2172.7(19)	6692(3)	57.3(10)
N4	5558(3)	1721(2)	7362(3)	71.7(13)
C1	3148(3)	2795(2)	3975(3)	45.6(10)
C2	4460(3)	2902.9(19)	4838(3)	47.1(11)
C3	4239(3)	3306(2)	4134(3)	51.1(11)
C4	4791(4)	3709(2)	4047(4)	65.3(15)
C5	5596(4)	3682(3)	4711(5)	73.6(17)
C6	5834(4)	3278(3)	5418(5)	74.7(17)
C7	5265(3)	2881(2)	5490(4)	62.0(13)
C8	1716(3)	2951(3)	2795(3)	64.1(14)
C9	1493(4)	3576(3)	3035(5)	90(2)
C10	966(4)	2511(3)	2389(4)	81.4(18)
C11	4973(3)	2101(2)	7332(3)	55.0(12)
C12	3844(3)	2609(2)	7012(3)	49.4(11)
C13	4425(3)	2791(2)	7841(3)	48.4(11)
C14	4284(3)	3211(2)	8355(3)	58.7(13)
C15	3482(4)	3458(3)	7982(4)	66.7(15)
C16	2882(3)	3279(3)	7161(4)	67.0(15)

Atom	*x*	*y*	*z*	U(eq)
C17	3052(3)	2850(3)	6658(3)	60.1(13)
C18	6415(4)	1687(3)	8084(4)	76.1(17)
C19	6958(5)	2121(4)	7926(5)	120(3)
C20	6707(6)	1012(4)	8161(7)	148(4)
Zn2	1509.3(3)	6113.7(2)	2729.8(3)	36.82(15)
O3	-364.3(19)	4688.3(14)	1570(2)	52.4(8)
O4	3751(2)	4967.8(13)	3987.6(19)	48.5(8)
O5	632.4(17)	6836.5(13)	1841.0(18)	40.5(7)
O6	1970.2(17)	6281.7(12)	1867.7(18)	38.2(6)
O7	1750(2)	6809.3(15)	670(2)	54.0(8)
O8	2145.4(17)	6949.8(12)	3440.3(18)	38.6(6)
O9	1017.6(18)	6232.0(12)	3583.2(18)	41.4(7)
O10	997(2)	6876.9(15)	4580(2)	63.0(10)
N5	711(2)	5371.5(15)	2068(2)	42.8(8)
N6	-282(3)	5411.1(19)	2586(3)	59.5(11)
N7	2543(2)	5507.2(15)	3494(2)	39.7(8)
N8	3419(2)	5629.0(17)	2831(2)	48.9(9)
N9	565(2)	7510.6(17)	796(2)	44.1(9)
N10	2075(2)	7663.6(15)	4371(2)	42.6(8)
C21	3209(3)	5388.4(18)	3403(3)	41.6(10)
C22	2646(3)	5126.9(18)	4202(3)	44.1(10)
C23	3385(3)	4805.7(19)	4499(3)	49.5(11)
C24	3693(4)	4394(2)	5196(3)	58.7(13)
C25	3194(4)	4304(2)	5588(3)	71.8(16)
C26	2436(4)	4609(2)	5291(4)	68.2(15)
C27	2141(3)	5030(2)	4591(3)	55.6(12)

Atom	*x*	*y*	*z*	U(eq)
C28	4114(3)	5400(2)	2699(4)	59.5(13)
C29	3806(4)	4916(4)	1981(5)	100(2)
C30	4522(4)	5970(3)	2512(4)	80.8(19)
C31	38(3)	5187.5(19)	2098(3)	46.2(11)
C32	785(3)	4947.5(19)	1476(3)	45.0(10)
C33	129(3)	4539(2)	1177(3)	48.7(11)
C34	3(3)	4057(2)	597(3)	62.8(14)
C35	600(4)	4004(2)	329(4)	66.8(15)
C36	1269(4)	4406(2)	616(4)	65.9(14)
C37	1376(3)	4891(2)	1202(3)	54.7(12)
C38	-1031(3)	5174(2)	2592(4)	64.0(15)
C39	-971(5)	5316(3)	3463(5)	104(3)
C40	-1772(4)	5445(3)	1877(6)	108(3)
C41	878(2)	7024.8(18)	1323(3)	36.6(9)
C42	1595(3)	6679.6(19)	1268(3)	38.6(9)
C43	-71(3)	7930(2)	795(3)	51.2(12)
C44	-779(4)	7984(3)	-117(5)	93(2)
C45	297(4)	8555(4)	1133(6)	125(3)
C46	1867(2)	7129.9(18)	3931(3)	35.8(9)
C47	1234(3)	6716.5(19)	4060(3)	39.5(9)
C48	2626(3)	8133.4(19)	4287(3)	46.2(11)
C49	2140(4)	8715(3)	3886(6)	119(3)
C50	3348(4)	8257(3)	5148(4)	86.0(19)

Table A31 Anisotropic Displacement Parameters ($Å^2 \times 10^3$) for $Zn(BONHMe)_2(NIPOx)_2$ and $Zn(BONMe)_2Cl_2$. The Anisotropic displacement factor exponent takes the form: $-2\pi^2[h^2a^{*2}U_{11}+2hka^*b^*U_{12}+\ldots]$.

Atom	U_{11}	U_{22}	U_{33}	U_{23}	U_{13}	U_{12}
Zn1	103.1(5)	49.2(4)	56.7(4)	4.4(3)	36.4(4)	-14.5(3)
Cl1	231(3)	69.1(11)	89.6(12)	16.6(9)	83.6(15)	47.4(14)
Cl2	132.5(16)	146.9(18)	77.6(11)	9.0(11)	38.8(11)	-87.4(14)
O1	66(2)	37.8(17)	65(2)	9.0(14)	43.4(18)	6.6(14)
O2	59(2)	51.6(19)	52.3(19)	4.2(15)	28.6(16)	4.5(16)
N1	54(2)	40(2)	53(2)	1.1(17)	29(2)	3.4(17)
N2	55(2)	50(2)	64(3)	4.8(19)	34(2)	1.4(19)
N3	70(3)	48(2)	58(2)	7.9(19)	33(2)	2(2)
N4	81(3)	61(3)	75(3)	0(2)	38(3)	14(2)
C1	56(3)	36(2)	55(3)	0(2)	35(2)	-1(2)
C2	56(3)	29(2)	63(3)	-6(2)	33(2)	1.7(19)
C3	58(3)	34(2)	74(3)	-8(2)	41(3)	0(2)
C4	83(4)	30(2)	112(5)	-4(3)	70(4)	1(2)
C5	68(4)	40(3)	128(5)	-25(3)	59(4)	-12(3)
C6	55(3)	56(3)	108(5)	-29(3)	34(3)	0(3)
C7	59(3)	45(3)	80(4)	-9(3)	32(3)	2(2)
C8	60(3)	74(4)	56(3)	4(3)	25(3)	8(3)
C9	81(4)	64(4)	106(5)	7(4)	29(4)	20(3)
C10	68(4)	103(5)	69(4)	-20(3)	29(3)	-7(3)
C11	66(3)	48(3)	57(3)	9(2)	33(3)	3(2)
C12	54(3)	47(3)	51(3)	13(2)	27(2)	-5(2)
C13	50(3)	47(3)	57(3)	12(2)	33(2)	-1(2)
C14	63(3)	61(3)	63(3)	2(3)	39(3)	-5(3)
C15	76(4)	65(3)	83(4)	12(3)	57(3)	9(3)
C16	59(3)	73(4)	78(4)	23(3)	39(3)	7(3)

Atom	U_{11}	U_{22}	U_{33}	U_{23}	U_{13}	U_{12}
C17	62(3)	63(3)	60(3)	12(3)	33(3)	-4(3)
C18	77(4)	75(4)	78(4)	11(3)	38(3)	23(3)
C19	94(5)	132(7)	125(7)	1(6)	44(5)	-24(5)
C20	142(8)	99(7)	176(9)	39(6)	52(7)	54(6)
Zn2	54.0(3)	23.7(2)	47.7(3)	-0.9(2)	36.3(2)	0.1(2)
O3	58.7(19)	37.6(17)	67(2)	-15.5(15)	34.7(17)	-6.7(14)
O4	70(2)	33.1(16)	54.6(18)	12.7(13)	39.4(17)	15.5(14)
O5	50.4(17)	35.9(15)	48.1(16)	3.9(13)	33.8(15)	3.6(13)
O6	53.2(17)	27.8(14)	47.9(16)	8.9(12)	35.5(14)	8.9(12)
O7	68(2)	55(2)	60.2(19)	23.1(16)	47.7(18)	20.4(16)
O8	49.2(17)	30.3(14)	49.0(16)	-3.8(12)	33.8(14)	-0.5(12)
O9	56.3(18)	29.6(15)	52.7(17)	-7.8(13)	37.6(15)	-6.5(12)
O10	88(2)	55(2)	82(2)	-31.8(18)	70(2)	-29.2(18)
N5	58(2)	28.7(18)	54(2)	-8.6(15)	36.7(19)	-1.1(16)
N6	70(3)	50(2)	81(3)	-30(2)	54(2)	-22(2)
N7	57(2)	24.3(16)	50(2)	3.7(14)	34.9(18)	2.2(15)
N8	63(2)	38(2)	64(2)	17.4(17)	44(2)	15.2(17)
N9	51(2)	44(2)	51(2)	17.8(17)	36.1(18)	16.3(17)
N10	59(2)	33.2(18)	50(2)	-8.8(16)	37.4(19)	-8.3(16)
C21	56(3)	26(2)	49(2)	4.1(18)	30(2)	5.0(18)
C22	72(3)	23(2)	49(2)	2.4(17)	38(2)	-1(2)
C23	78(3)	28(2)	56(3)	4.0(19)	43(3)	9(2)
C24	90(4)	36(2)	60(3)	13(2)	44(3)	16(2)
C25	129(5)	39(3)	64(3)	20(2)	60(4)	17(3)
C26	120(5)	42(3)	73(3)	11(3)	71(4)	2(3)
C27	83(4)	36(2)	68(3)	5(2)	53(3)	2(2)

Atom	U_{11}	U_{22}	U_{33}	U_{23}	U_{13}	U_{12}
C28	60(3)	60(3)	76(3)	23(3)	46(3)	20(2)
C29	105(5)	104(5)	116(6)	-25(4)	72(5)	21(4)
C30	69(4)	86(4)	107(5)	45(4)	58(4)	23(3)
C31	56(3)	30(2)	56(3)	-8.5(19)	30(2)	-2.9(19)
C32	61(3)	28(2)	50(3)	-4.5(18)	29(2)	5.4(19)
C33	59(3)	34(2)	56(3)	-6(2)	30(2)	3(2)
C34	68(3)	42(3)	70(3)	-23(2)	26(3)	-2(2)
C35	83(4)	48(3)	74(4)	-26(3)	41(3)	2(3)
C36	87(4)	50(3)	78(4)	-15(3)	53(3)	8(3)
C37	68(3)	39(3)	70(3)	-13(2)	43(3)	-1(2)
C38	65(3)	49(3)	102(4)	-23(3)	58(3)	-14(3)
C39	147(6)	83(5)	145(6)	-39(4)	121(6)	-42(4)
C40	83(5)	77(5)	162(7)	-13(5)	56(5)	6(4)
C41	41(2)	34(2)	41(2)	-0.2(17)	25(2)	1.8(17)
C42	47(2)	33(2)	46(2)	-1.3(18)	31(2)	0.9(18)
C43	57(3)	47(3)	63(3)	18(2)	40(3)	20(2)
C44	67(4)	86(5)	115(5)	-6(4)	33(4)	33(3)
C45	83(5)	102(6)	175(8)	-75(6)	48(5)	12(4)
C46	44(2)	30(2)	39(2)	3.8(17)	24(2)	2.7(17)
C47	51(2)	32(2)	47(2)	-1.5(18)	32(2)	-1.7(18)
C48	67(3)	33(2)	54(3)	-9.6(19)	42(2)	-15(2)
C49	84(5)	71(4)	171(8)	61(5)	35(5)	-6(4)
C50	62(4)	100(5)	90(4)	9(4)	31(3)	-25(3)

Table A32 Hydrogen Atom Coordinates (Å×104) and Isotropic Displacement Parameters (Å2×103) for $Zn(BONHMe)_2(NIPOx)_2$ and $Zn(BONMe)_2Cl_2$

Atom	*x*	*y*	*z*	U(eq)
H2	2201.06	2320.11	3800.64	65
H4	5426.08	1466.72	6915.31	86
H4A	4625.51	3984.73	3562.06	78
H5	6002.8	3949.1	4685.34	88
H6A	6398.39	3273.1	5860.98	90
H7	5428.15	2603.94	5972.9	74
H8A	1935.82	3019.45	2371.51	77
H9A	1293.13	3512.11	3463.25	135
H9B	1055.58	3776.08	2511.01	135
H9C	1986.59	3847.66	3286.54	135
H10A	1130.83	2112.6	2229.4	122
H10B	524.11	2708.13	1864.96	122
H10C	762.14	2430.19	2810.51	122
H14	4700.83	3324.54	8923.07	70
H15	3343.85	3757.33	8300.38	80
H16	2339.08	3452.7	6932.5	80
H17	2636.79	2728.23	6093.39	72
H18	6413.15	1810.73	8638.33	91
H19A	7002	1982.33	7410.4	180
H19B	7512.36	2123.95	8434.82	180
H19C	6722.11	2546.58	7825.88	180
H20A	6316.05	735.18	8238.6	222
H20B	7260.92	971.54	8665.03	222
H20C	6732.15	891.98	7628.85	222
H6	-22.33	5728.21	2935.41	71

Atom	*x*	*y*	*z*	U(eq)
H8	3124.07	5946.89	2508.88	59
H9	751.49	7587.25	420.35	53
H10	1874.05	7742.23	4733.31	51
H24	4213.73	4187.23	5393.82	70
H25	3373.29	4025.31	6071.66	86
H26	2107.18	4530.17	5572.62	82
H27	1622.29	5239.85	4391.75	67
H28	4533.36	5196.04	3251.69	71
H29A	3531.77	4572.3	2124.81	150
H29B	4277.38	4747.75	1920.69	150
H29C	3408	5112.36	1430.86	150
H30A	4113.21	6183.72	1982.41	121
H30B	4992.01	5828.93	2427.79	121
H30C	4722.87	6263.32	3005.87	121
H34	-462.31	3781.75	396.56	75
H35	548.98	3678.36	-68.88	80
H36	1666.46	4353.16	411.32	79
H37	1837.01	5170.01	1402.18	66
H38	-1051.27	4706.82	2514.8	77
H39A	-458.79	5131.13	3923.88	156
H39B	-1452.76	5136.03	3492.69	156
H39C	-961.51	5773.11	3545.04	156
H40A	-1790.28	5898.27	1974.29	162
H40B	-2268.62	5243.25	1848.82	162
H40C	-1758.03	5375.88	1326.31	162
H43	-284.52	7749.3	1182.84	61

Atom	*x*	*y*	*z*	U(eq)
H44A	-1191.77	8282.65	-122.25	140
H44B	-1039.13	7570.23	-313.14	140
H44C	-567.53	8134.13	-508.96	140
H45A	694.92	8520.86	1755.73	188
H45B	-145.04	8851.92	1055.27	188
H45C	584.87	8707.06	814.02	188
H48	2833.55	7960.41	3890.22	55
H49A	1943.86	8896.52	4275.41	178
H49B	1660.68	8610.12	3324.21	178
H49C	2494.24	9020.08	3793.93	178
H50A	3739.48	8536.35	5075.96	129
H50B	3625.49	7858.03	5407.78	129
H50C	3158.36	8457.5	5531.39	129